Towards Efficient and Accurate Description of Many-Electron Problems: Developments of Static and Time-Dependent Electronic Structure Methods

Feizhi Ding

A dissertation submitted in partial fulfillment
of the requirements for the degree of

Doctor of Philosophy

University of Washington

2015

Reading Committee:

Xiaosong Li, Chair

David Masiello

Stefan Stoll

Program Authorized to Offer Degree:
Chemistry

University of Washington

Abstract

Towards Efficient and Accurate Description of Many-Electron Problems: Developments of Static and Time-Dependent Electronic Structure Methods

Feizhi Ding

Chair of the Supervisory Committee:
Associate Professor Xiaosong Li
Department of Chemistry

Understanding electronic behavior in molecular and nano-scale systems is fundamental to the development and design of novel technologies and materials for application in a variety of scientific contexts from fundamental research to energy conversion. This dissertation aims to provide insights into this goal by developing novel methods and applications of first-principle electronic structure theory. Specifically, we will present new methods and applications of excited state multi-electron dynamics based on the real-time (RT) time-dependent Hartree-Fock (TDHF) and time-dependent density functional theory (TDDFT) formalism, and new development of the multi-configuration self-consist field theory (MCSCF) for modeling ground-state electronic structure. The RT-TDHF/TDDFT based developments and applications can be categorized into three broad and coherently integrated research areas: (1) modeling of the interaction between moleculars and external electromagnetic perturbations. In this part we will first prove both analytically and numerically the gauge invariance of the TDHF/TDDFT formalisms, then we will present a novel, efficient method for calculating molecular nonlinear optical properties, and last we will study quantum coherent plasmon in metal namowires using RT-TDDFT; (2) modeling of excited-state charge transfer in molecules. In this part, we will investigate the mechanisms of bridge-mediated electron transfer, and then we will introduce a newly developed non-equilibrium quantum/continuum embedding method for studying charge transfer dynamics in solution; (3) developments of

first-principles spin-dependent many-electron dynamics. In this part, we will present an *ab initio* non-relativistic spin dynamics method based on the two-component generalized Hartree-Fock approach, and then we will generalized it to the two-component TDDFT framework and combine it with the Ehrenfest molecular dynamics approach for modeling the interaction between electron spins and nuclear motion. All these developments and applications will open up new computational and theoretical tools to be applied to the development and understanding of chemical reactions, nonlinear optics, electromagnetism, and spintronics. Lastly, we present a new algorithm for large-scale MCSCF calculations that can utilize massively parallel machines while still maintaining optimal performance for each single processor. This will great improve the efficiency in the MCSCF calculations for studying chemical dissociation and high-accuracy quantum-mechanical simulations.

TABLE OF CONTENTS

LIST OF FIGURES

LIST OF TABLES

GLOSSARY

AA: : Adiabatic Approximation

AO: : Atomic Orbital

ASC: : Apparent Surface Charge

ATI: : Above Threshold Ionization

BOMD: : Born-Oppenheimer Molecular Dynamics

CASSCF: : Complete-Active-Space Self-Consistent Field

CC: : Coupled Cluster

CI: : Configuration Interaction

CO: : Carbon Monoxide

CP: : Coupled Perturbed

CSC: : Continuous Surface Charge

CSF: : Configuration State Function

CT: : Charge Transfer

DFT: : Density Functional Theory

DKH: : Douglas-Kroll-Hess

DMRG: : Density Matrix Renormalization Group

EOM: : Equation of Motion

ET: : Electron Transfer

DIIS: : Direct Inversion in the Iterative Subspace

FMM: : Fast Multipole Method

GGA: : Generalized Gradient Approximation

GIAO: : Gauge-Including Atomic Orbital

GVB: : Generalized Valence Bond

HF: : Hartree-Fock

HHG: : High-order Harmonic Generation

HOMO: : Highest Occupied Molecular Orbital

KS: : Kohn-Sham

LDA: : Local Density Approximation

LG: : Length Gauge

LR: : Linear-Response

LUMO: : Lowest Unoccupied Molecular Orbital

MCSCF: : Multi-Configuration Self-Consistent Field

MMUT: : Modified Midpoint and Unitary Transformation

MQC: : Mixed Quantum-Classical

MR: : Multi-Reference

NPA: : Natural Population Analysis

PCM: : Polarizable Continuum Model

RPA: : Random-Phase Approximation

RT: : Real-Time

SHG: : Second Harmonic Generation

SQ: : Sequential

SX: : Super-exchange

TDDFT: : Time-Dependent Density Functional Theory

TDHF: : Time-Dependent Hartree-Fock

TDN2C: : Time-Dependent Non-relativistic Two-Component Spinor

TDSE: : Time-Dependent Schrödinger Equation

VG: : Velocity Gauge

XC: : Exchange-Correlation

ACKNOWLEDGMENTS

I want to thank many people who have been supportive throughout my graduate study. These include:

My adviser, Xiaosong Li, to whom I am always grateful. He provided me with tremendous support in my research and beyond. He has been both a great mentor and a good friend to me.

My roommate and good friend Bo, from whom I learned many life lessons.

My old colleague and lunch partner Wenkel, from who I learned a lot about computer programming. I enjoyed many insightful discussions with him on various topics–not just about science!

Many thanks to my old colleague Joseph, who helped me a lot with latex editing and running jobs on clusters. I thank him for all the good work in organizing our group events.

My office-mate Sean, who offered many insights for my research through our discussions.

Other theory suite folks with whom I have had pleasure of working with daily: Craig, Phu, Erica, Alessio, Patrick, Josh, David Lingerfelt, David Williams-Young, Ben, Katia, Kerry, Hongbin and many others.

I thank my committee members, David Masiello, Lutz Maibaum, Stefan Stoll, Matthew Bush, and Jim Pfaendtner. Special thanks to David Masiello for offering me many scientific insights.

DEDICATION

To my loving parents.

To God.

Chapter 1

INTRODUCTION

The time-dependent Schrödinger equation governs all non-equilibrium quantum mechanical processes of a many-electron system. These processes are crucial driving forces in many advanced scientific research and technological developments. For example, tuning the excitonic dynamics (i.e. excited many-electron dynamics) at bulk heterojunctions is an important step toward achieving high-quantum yield photovoltaics; the spontaneous magnetization (i.e. many-electron spin-dynamics) in diluted magnetic semiconductors determines their suitability for spintronic applications, etc. All of these phenomena are underpinned by many-electron dynamics which have transcendent impact on the photovoltaic and photocatalytic systems.[1–13] Explicitly propagating the Schrödinger equation in time allows for probing the non-equilibrium kinetics and dynamics of many-electron systems that underlie these important processes.

One major area of my research conducted with Professor Xiaosong Li at the Univeristy of Washington focuses on the development of time-dependent many-electron theories and computational methods that can be applied to simulate realistic and experimentally relevant molecular systems and their responses to external driving forces (e.g. electromagnetic field, nuclear motion, and solvent). The basis of the many-electron dynamics development lies in the real-time integration of the time-dependent Hartree-Fock (TDHF)/time-dependent density functional theory (TDDFT) equations, which approximates the time-dependent electronic Schrödinger equation in terms of the one-particle density matrix.

Another area of my research was focused on the development of efficient computational strategies and algorithms for high-accuracy first-principles calculations, in particular, the multi-configuration self-consistent field (MCSCF) method.

The following documents collects major achievements of my research in these areas while working towards my doctorate degree. Most of the results shown here have been published

previously in a series of papers[14–29] The discussion will proceed as follows: In Chapter 2 we will review some basic theories and concepts that will be used in this dissertation, which include the Hartree-Fock (HF) theory, density functional theory (DFT), and their time-dependent counterparts, i.e. the TDHF/TDDFT theories. We will then briefly discuss the limitations of these methods and the concept of electron dynamic and static correlation effects, and ways to recover them. Specifically, we will introduce the multi-configuration self-consistent field method for treating static electron correlation. In Chapter 3, we will talk about some developments for modeling of the interaction between molecular systems and external electromagnetic fields within the RT-TDHF/TDDFT framework. There we will discuss the gauge invariance of the TDHF/TDDFT formalism. We will present a novel strategy for calculating molecular nonlinear optical properties, and lastly we will use RT-TDDFT to study quantum coherent plasmon in metal namowires. In Chapter 4 we will present some developments and applications for modeling of excited-state charge transfer in molecules. There we will investigate the mechanisms of bridge-mediated electron transfer, and then we will introduce a newly developed non-equilibrium quantum/continuum embedding method for studying charge transfer dynamics in solution. In Chapter 5 we will introduce some recent developments of first-principles spin-dependent many-electron dynamics. There we will present an *ab initio* non-relativistic spin dynamics method based on the two-component generalized Hartree-Fock wavefunction. Then we will generalize this approach to the two-component TDDFT framework and combine it with the Ehrenfest molecular dynamics scheme for modeling the interaction between electron spins and nuclear motion. Finally, in 6 we will present a new algorithm for large-scale MCSCF calculations that can utilize massively parallel machines while still maintaining optimal performance for each single processor. This will great improve the efficiency in the MCSCF calculations for studying chemical dissociation and high-accuracy quantum-mechanical simulations.

Chapter 2

BASIC THEORIES AND CONCEPTS

In this chapter, we aim to provide a brief outline of some basic theories, concepts, and algorithms that will be used in this thesis. Specifically, we will talk about the Hartree-Fock method, density functional theory, and their time-dependent counterparts, i.e. the time-dependent Hartree-Fock and time-dependent density functional theory. We will then briefly discuss the limitations of these methods and the concept of electron dynamic and static correlation effects, and ways to recover them. Specifically, we will introduce the multi-configuration self-consistent field method for treating static electron correlation.

2.1 The Hartree-Fock Theory

The Hartree-Fock theory is one of the fundamental building blocks of modern electronic structure theory. It is based on two approximations to the solution of the non-relativistic time-independent Schrödinger equation. The first approximation is the Born-Oppenheimer approximation, where one decouples nuclear motion from the electronic motion based on the fact that the nuclei are much heavier than electrons. This leads to the non-relativistic time-independent electronic Schrödinger equation:

$$\hat{H}_{\mathrm{el}}\Psi = E_{\mathrm{el}}\Psi \tag{2.1}$$

where Ψ is the electronic wavefunction of an N-electron system, E_{el} is the electronic energy of the system, and $\hat{H}_{\mathrm{el}}$ is the non-relativistic electronic Hamiltonian:

$$\hat{H}_{\mathrm{el}} = \sum_{i}^{N} \hat{h}(i) + \sum_{i \neq j}^{N} \frac{1}{r_{ij}} \tag{2.2}$$

where r_{ij} is the distance between electrons i and j. $\hat{h}(i)$ is the one-electron operator for electron i,

$$\hat{h}(i) = -\frac{1}{2}\nabla_i^2 - \sum_A \frac{Z_A}{r_{iA}} \tag{2.3}$$

where Z_A is the nuclear charge of nucleus A, and r_{iA} is the distance between electron i and nucleus A.

The second approximation is the so-called Hartree-Fock approximation, which simply replaces the N-electron wavefunction Ψ with an antisymmetrized product of single-particle wavefunctions, also known as a single Slater determinant Φ_{HF}:

$$\Phi_{\mathrm{HF}} = \frac{1}{\sqrt{N!}} \begin{vmatrix} \psi_1(\mathbf{x}_1) & \psi_2(\mathbf{x}_1) & \dots & \psi_N(\mathbf{x}_1) \\ \psi_1(\mathbf{x}_2) & \psi_2(\mathbf{x}_2) & \dots & \psi_N(\mathbf{x}_2) \\ \vdots & \vdots & \ddots & \vdots \\ \psi_1(\mathbf{x}_N) & \psi_2(\mathbf{x}_N) & \dots & \psi_N(\mathbf{x}_N) \end{vmatrix} \tag{2.4}$$

where $\psi_i(\mathbf{x})$ are single-particle wavefunctions, also called spin orbitals, which depend on the variable $\mathbf{x}$ of both the spatial coordinate $\mathbf{r}$ and the spin coordinate ω for one electron. In constructing the above single Slater determinant wavefunction, one assumes that the spin orbitals are orthonormal to each other:

$$\langle \psi_i | \psi_j \rangle = \int \mathrm{d}\mathbf{x} \psi_i^*(\mathbf{x}) \psi_j(\mathbf{x}) = \delta_{ij} \tag{2.5}$$

The Hartree-Fock ground state is obtained by applying the variation principle, i.e. minimizing the energy $E_0 = \langle \Phi_{\mathrm{HF}} | \Phi_{\mathrm{HF}} \rangle$ with respect to the spin orbitals, subject to the constraint that the spin orbitals remain orthonormal. The resulting equations are a set of effective one-particle eigenvalue equations, also known as the Hartree-Fock (HF) equations:

$$\hat{f}(\mathbf{x}_1)\psi_k(\mathbf{x}_1) = \varepsilon_k \psi_k(\mathbf{x}_1) \tag{2.6}$$

where ε_k are the energies of the spin-orbitals. $\hat{f}(\mathbf{x}_1)$ is the Fock operator defined by

$$\hat{f}(\mathbf{x}_1) = \hat{h}(\mathbf{x}_1) + \hat{J}(\mathbf{x}_1) - \hat{K}(\mathbf{x}_1) \tag{2.7}$$

where $\hat{h}(\mathbf{x}_1)$ is the one-electron operator defined in Eq. (2.3). $\hat{J}(\mathbf{x}_1)$ and $\hat{K}(\mathbf{x}_1)$ are the Coulomb and exchange operators, respectively. They are defined by:

$$\hat{J}(\mathbf{x}_1)\psi_k(\mathbf{x}_1) = \sum_j^N \left[\int d\mathbf{x}_2 \psi_j^*(\mathbf{x}_2) r_{12}^{-1} \psi_j(\mathbf{x}_2)\right] \psi_k(\mathbf{x}_1) \tag{2.8}$$

$$\hat{K}(\mathbf{x}_1)\psi_k(\mathbf{x}_1) = \sum_j^N \left[\int d\mathbf{x}_2 \psi_j^*(\mathbf{x}_2) r_{12}^{-1} \psi_k(\mathbf{x}_2)\right] \psi_j(\mathbf{x}_1) \tag{2.9}$$

Depending on the restrictions on the spin orbitals $\psi_i(\mathbf{x})$, the Hartree-Fock problem may be categorized into three major categories: (1) the restricted HF (RHF), (2) the unrestricted HF (UHF), and (3) the generalized HF (GHF). In both RHF and UHF, each spin orbital is a product of a spatial $\phi(\mathbf{r})$ and spin part $\sigma(\omega) = \alpha(\omega)$ or $\beta(\omega)$. Specifically, in RHF the spin orbitals take the form

$$\text{RHF:} \quad \psi_k(\mathbf{x}) = \begin{cases} \phi_i(\mathbf{r})\alpha(\omega) & \text{when } k = 2i-1 \\ \phi_i(\mathbf{r})\beta(\omega) & \text{when } k = 2i \end{cases} \tag{2.10}$$

In UHF the spatial parts that associates with α and β spin are different:

$$\text{UHF:} \quad \psi_k(\mathbf{x}) = \begin{cases} \phi_i^\alpha(\mathbf{r})\alpha(\omega) & \text{when } k = 2i-1 \\ \phi_i^\beta(\mathbf{r})\beta(\omega) & \text{when } k = 2i \end{cases} \tag{2.11}$$

In GHF, each spin orbital $\psi_k(\mathbf{x})$ is expanded in spin space over the two spin basis functions, $\alpha(\omega)$ and $\beta(\omega)$:

$$\psi_k(\mathbf{x}) = \phi_k^\alpha(\mathbf{r})\alpha(\omega) + \phi_k^\beta(\mathbf{r})\beta(\omega) \tag{2.12}$$

The most widely used approach to the solution of the HF equations, Eq. (2.6) is based on

the finite basis set expansion technique, i.e. linear combination of atomic orbitals (LCAO), as proposed by Roothaan.[30] In the LCAO approach, the spatial part of the spin orbitals are expanded in terms of a set of M atomic orbital (AO) basis functions $\{\chi_\mu(\mathbf{r})\}$.

$$\phi_k(\mathbf{r}) = \sum_{\mu}^{M} C_{\mu k}\chi_\mu(\mathbf{r}) \tag{2.13}$$

where $C_{\mu k}$ are called molecular orbital (MO) coefficients.

Here in this section, we show the matrix formalism of the HF equation for the restricted close-shell HF case. Generalization to UHF and GHF is straightforward. With the expansion of spin orbitals into atomic orbital basis, the problem of calculating the HF molecular orbitals is recast into the solution of a generalized matrix eigenvalue problem, also called the Roothaan equation:

$$\mathbf{FC} = \mathbf{SC}\boldsymbol{\varepsilon} \tag{2.14}$$

where $\mathbf{F}$ is called the Fock matrix and for RHF its elements are

$$F_{\mu\nu} = h_{\mu\nu} + \sum_{\lambda\kappa} P_{\lambda\kappa}\left[\left(\mu\nu|\kappa\lambda\right) - \frac{1}{2}\left(\mu\lambda|\kappa\nu\right)\right] \tag{2.15}$$

where $\mathbf{P}$ is called the density matrix and is defined by

$$P_{\mu\nu} = 2\sum_{i}^{N/2} C_{\mu i}C_{\nu i}^{*} \tag{2.16}$$

$\mathbf{S}$ is the overlap matrix,

$$S_{\mu\nu} = \langle\mu|\nu\rangle \tag{2.17}$$

and $\boldsymbol{\varepsilon}$ is the diagonal matrix of the MO energies.

The Roothaan equation Eq. (2.14) is a nonlinear system equation since the Fock matrix depends on the MO coefficient matrix, and it needs to be solved in an iterative fashion. Therefore the HF method is also called a self-consistent field (SCF) method.

The Hartree-Fock method has proved to be of crucial importance in physics and chemistry since it provides a reasonable description of the electronic structure of atoms and molecules at a low cost. Even when the HF method does not give desirable accuracy, the HF wavefunction is often a useful and convenient starting point for more accurate methods.

2.2 Density Functional Theory

The density functional theory (DFT) is a conceptually different approach to the solution of the non-relativistic time-independent electronic Schrödinger equation given in Eq. (2.1). The development of DFT is based on the theorem of Hohenberg and Kohn[31] and the clever implementation by Kohn and Sham.[32] The basic concept of DFT is the use of the electron density $\rho(\mathbf{r})$ for the calculation of ground-state energy and other physical properties, instead of using the electronic wavefunction which depends on $4N$ variables, N being the number of electrons.

2.2.1 The Hohenberg-Kohn Theorem

The Hohenberg-Kohn theorem provides a rigorous foundation of DFT. It consists of two sub-theorems. The first Hohenberg-Kohn theorem states that the external potential $v_{\text{ext}}(\mathbf{r})$ is (to within a constant) a unique functional of density $\rho(\mathbf{r})$. Therefore, the ground-state density uniquely determines the Hamiltonian operator and thus all the properties of the system. The proof is done by the method of *reductio ad absurdum*:

Assume that there were two external potential $v_{\text{ext}}(\mathbf{r})$ and $v'_{\text{ext}}(\mathbf{r})$ differing by more than a constant, both giving the same ground-state density $\rho(\mathbf{r})$. Then the two Hamiltonians $\hat{H}$ and $\hat{H}'$ would be different, and therefore the ground-state wavefunctions Ψ and Ψ' , and energies E and E' would be different. From the minimal property of the ground state,

$$E' = \langle \Psi' | \hat{H}' | \Psi' \rangle < \langle \Psi | \hat{H}' | \Psi \rangle = \langle \Psi | \hat{H} + v'_{\text{ext}} - v_{\text{ext}} | \Psi \rangle = E + \int [v'_{\text{ext}}(\mathbf{r}) - v_{\text{ext}}(\mathbf{r})] \rho(\mathbf{r}) \mathrm{d}\mathbf{r} \tag{2.18}$$

Similarly,

$$E = \langle \Psi | \hat{H} | \Psi \rangle < \langle \Psi' | \hat{H} | \Psi' \rangle = \langle \Psi' | \hat{H}' + v_{\text{ext}} - v'_{\text{ext}} | \Psi' \rangle = E' + \int [v_{\text{ext}}(\mathbf{r}) - v'_{\text{ext}}(\mathbf{r})] \rho(\mathbf{r}) \mathrm{d}\mathbf{r} \tag{2.19}$$

Adding Eq. (2.18) and Eq. (2.19), we would obtain

$$E + E' < E + E' \tag{2.20}$$

which is a contradiction. Therefore there cannot be two different external potentials that give the same ground-state density.

Since $v_{\text{ext}}(\mathbf{r})$ fixes the Hamiltonian $\hat{H}$ which fixes the wavefunction Ψ. The ground-state wavefunction is a unique functional of the density $\rho(\mathbf{r})$. Therefore the kinetic energy T, interaction energy E_{ee}, and the total energy E are also unique functionals of the density:

$$E[\rho] = \int v_{\text{ext}}(\mathbf{r})\rho(\mathbf{r})\mathrm{d}\mathbf{r} + T[\rho] + E_{\text{ee}}[\rho] \tag{2.21}$$

The fact that $T[\rho]$ and $E_{\text{ee}}[\rho]$ are universal functionals of density, valid for any number of particles and any external potential, builds the foundation of DFT.

The second Hohenberg-Kohn theorem states that for a given external potential $v_{\text{ext}}(\mathbf{r})$, the total energy functional $E[\rho]$ assumes its minimum value if and only if the input density is the true ground-state density. The proof of this theorem makes use of the variation principle with respect to the wavefunction. Since any trial density $\tilde{\rho}$ defines its own Hamiltonian $\tilde{H}$ and hence it own wavefunction $\tilde{\Psi}$. This wavefunction $\tilde{\Psi}$ can now be taken as the trial wavefunction for the Hamiltonian generated by the true external potential $v_{\text{ext}}(\mathbf{r})$. From the variation principle:

$$\langle\tilde{\Psi}|H|\tilde{\Psi}\rangle = \int v_{\text{ext}}(\mathbf{r})\tilde{\rho}(\mathbf{r})\mathrm{d}\mathbf{r} + T[\tilde{\rho}] + E_{\text{ee}}[\tilde{\rho}] = E[\tilde{\rho}] \geq \langle\Psi|H|\Psi\rangle = E[\rho] \tag{2.22}$$

2.2.2 The Kohn-Sham Equation

From the Hohenberg-Kohn theorems, we have seen that the ground-state energy of a system can be obtained as a minimization of the energy functional defined in Eq. (2.21). However, since the exact forms of the kinetic energy functional $T[\rho]$ and the electron-electron interaction energy functional $E_{\text{ee}}[\rho]$ are not known, direct minimization is not possible. In order to solve this problem, Kohn and Sham[32] suggested to calculate the exact kinetic energy of

a non-interacting reference system with the same density as the real, interacting one. The kinetic energy of this non-interacting reference system is given by

$$T_s = -\frac{1}{2}\sum_i^N \langle\psi_i|\nabla^2|\psi_i\rangle \tag{2.23}$$

and the density is given by

$$\rho_s(\mathbf{r}) = \sum_i^N \psi_i^*\psi_i \equiv \rho(\mathbf{r}) \tag{2.24}$$

where ψ_i are the wavefunctions (orbitals) of the non-interacting electrons.

Since T_s is not equal to the true kinetic energy of the system, Kohn and Sham introduced the following separation of the functional

$$F[\rho] = T[\rho] + E_{\text{ee}}[\rho] = T_s[\rho] + J[\rho] + E_{\text{xc}}[\rho] \tag{2.25}$$

where $J[\rho]$ is the classical Coulomb energy and is given by

$$J[\rho] = \frac{1}{2}\iint \frac{\rho(\mathbf{r}_1)\rho(\mathbf{r}_2)}{r_{12}}\mathrm{d}\mathbf{r}_1\mathrm{d}\mathbf{r}_2 \tag{2.26}$$

$E_{\text{xc}}[\rho]$ is the so-called exchange-correlation energy and is defined as

$$E_{\text{xc}}[\rho] = \big(T[\rho] - T_s[\rho]\big) + \big(E_{\text{ee}}[\rho] - J[\rho]\big) \tag{2.27}$$

The total energy of the interacting system is thus given by

$$E[\rho] = \int v_{\text{ext}}(\mathbf{r})\rho(\mathbf{r})\mathrm{d}\mathbf{r} + T_s[\rho] + J[\rho] + E_{\text{xc}}[\rho] \tag{2.28}$$

In order to find the minimum energy of the actual system that has the same density as the non-interacting system, one apply the variation principle with respect to the change of

the single-particle orbitals. The resulting equations are the so-called Kohn-Sham equations:

$$\hat{f}^{\mathrm{KS}}\psi_i = \varepsilon_i\psi_i \tag{2.29}$$

where $\hat{f}^{\mathrm{KS}}$ is the so-called Kohn-Sham operator and is given by

$$\hat{f}^{\mathrm{KS}} = -\frac{1}{2}\nabla^2 + \int \frac{\rho(\mathbf{r}_2)}{r_{12}}\mathrm{d}\mathbf{r}_2 + v_{\mathrm{ext}}(\mathbf{r}_1) + v_{\mathrm{xc}}(\mathbf{r}_1) \tag{2.30}$$

where v_{xc} is the exchange-correlation potential and is defined by the functional derivative of exchange-correlation energy $E_{\mathrm{xc}}[\rho]$ with respect to the density:

$$v_{\mathrm{xc}} = \frac{\delta E_{\mathrm{xc}}[\rho]}{\delta\rho(\mathbf{r})} \tag{2.31}$$

The Kohn-Sham equations, Eq. (2.29), provide an elegant route to the exact solution of the many-body Schrödinger equation, given that the exact form of the energy functional $E_{\mathrm{xc}}[\rho]$ is known. Unfortunately, the explicit form of this functional is not known, nor is there any systematic procedure for finding such functional. During the last few decades, extensive effort has been put to the approximations of the functional. So far, most of the widely used density functional approximations consist of the local density approximation (LDA), the generalized gradient approximation (GGA) and the hybrid functionals that mix in some Hartree-Fock exchange.

2.3 Time-Dependent Hartree-Fock and Time-Dependent Density Functional Theory

While HF and DFT are routinely used for calculating the static electronic structure of atoms and molecules, there are growing interests in the simulation of dynamical processes such as electron transfer, molecular dynamics, and interaction of molecules with electromagnetic fields. In order to achieve this, one starts with the time-dependent Schrödinger equation (TDSE). However, exact solution of the full molecular TDSE is prohibitive except for very small systems. One of the widely used approach toward affordable computations is the mixed quantum-classical (MQC) scheme in which the electronic degrees of freedom is treated quantum mechanically and the nuclei move as classical particles. Within such framework, two general approaches, namely the surface hopping[33,34] and Ehrenfest dynamics[35–38] have emerged. Both approaches incorporate electronic nonadiabaticity and both include quantum coherence effects. The surface hopping method describes nonadiabaticity by allowing stochastic electronic transitions subject to a time- and momenta-dependent hopping probability, while the Ehrenfest method does so by propagating the classical nuclei in a superposition of adiabatic states. In the following, we will derive the equations of motion for the Ehrenfest dynamics, and then we will talk about two widely used approximations to solving the equation of motion for the electronic degrees of freedom: the time-dependent Hartree-Fock (TDHF) method and the time-dependent density functional theory (TDDFT).

2.3.1 Ehrenfest Dynamics

The starting point is the time-dependent Schrödinger equation for a molecular system described by the total wavefunction $\Psi(\mathbf{x}, \mathbf{R}; t)$:

$$i\hbar\Psi(\mathbf{x}, \mathbf{R}; t) = \hat{H}\Psi(\mathbf{x}, \mathbf{R}; t) \tag{2.32}$$

where $\mathbf{x} = (\mathbf{r}, \sigma)$ denotes the electronic coordinates of both spatial $\mathbf{r}$ and spin σ of all electrons. $\mathbf{R}$ denotes the spatial coordinates of all nuclei. The molecular Hamiltonian is

defined as

$$\hat{H} = -\sum_I \frac{\hbar^2}{2M_I}\nabla_I^2 - \sum_i \frac{\hbar^2}{2m_e}\nabla_i^2 + V_{\rm ne}(\mathbf{r},\mathbf{R}) \tag{2.33}$$

where M_I is the mass of the I-th nucleus and m_e the electron mass. $V_{\rm ne}(\mathbf{r},\mathbf{R})$ contains the nuclei-nuclei, nuclei-electron, and electron-electron interaction potentials.

In the Ehrenfest molecular dynamics model, one uses a product ansatz for the total wavefunction:

$$\Psi\left(\mathbf{x},\mathbf{R};t\right) \approx \Phi\left(\mathbf{x};t\right)\Theta\left(\mathbf{R};t\right)\exp\left[\frac{i}{\hbar}\int_{t_0}^{t} E_{\rm el}(t')\mathrm{d}t'\right] \tag{2.34}$$

$\Phi\left(\mathbf{x};t\right)$ is the electronic wavefunction and $\Theta\left(\mathbf{R};t\right)$ the nuclear wavefunction. $E_{\rm el}(t')$ is a phase factor that is defined by

$$E_{\rm el}(t) = \int \Phi^*\left(\mathbf{x};t\right)\Theta^*\left(\mathbf{R};t\right)\hat{H}_{\rm el}\Phi\left(\mathbf{x};t\right)\Theta\left(\mathbf{R};t\right)\mathrm{d}\mathbf{x}\mathrm{d}\mathbf{R} \tag{2.35}$$

where $\hat{H}_{\rm el}$ is the electronic Hamiltonian. Inserting this product ansatz for the total wavefunction into the Schrödinger equation and after some straigtforward algebra, on obtains the coupled equations of motion for the electronic and nuclear wavefunctions:

$$i\hbar\frac{\partial\Phi}{\partial t} = -\sum_i \frac{\hbar^2}{2m_e}\nabla_i^2\Phi + \left[\int \Theta^*\left(\mathbf{R};t\right)V_{\rm ne}\Theta\left(\mathbf{R};t\right)\mathrm{d}\mathbf{R}\right]\Phi \tag{2.36}$$

$$i\hbar\frac{\partial\Theta}{\partial t} = -\sum_I \frac{\hbar^2}{2M_I}\nabla_I^2\Theta + \left[\int \Phi^*\left(\mathbf{x};t\right)H_{\rm el}\Phi\left(\mathbf{x};t\right)\mathrm{d}\mathbf{x}\right]\Theta \tag{2.37}$$

where $V_{\rm ne}$ includes the electron-electron repulsion, electron-nuclei attraction and nuclei-nuclei repulsion. Evident from Eqs. (2.36) and (2.37), both electronic and nuclear degrees of freedom evovle in a time-dependen mean-field potential generated by each other. If one further takes the Eikonal representation of the nuclear wavefunction,

$$\Theta\left(\mathbf{R};t\right) = A\left(\mathbf{R};t\right)\exp\left[\frac{i}{\hbar}S\left(\mathbf{R};t\right)\right] \tag{2.38}$$

substituting this polar respresentation for the nuclear wavefunction in Eq. (2.37) and separating the real and imaginary parts, and taking the classical limit $\hbar \to 0$ for the phase S, one gets the classical Hamilton-Jacobi equation:

$$\frac{\partial S}{\partial t} = -\sum_I \frac{\hbar^2}{2M_I}(\nabla_I S)^2 - \int \Phi^* \left(\mathbf{x};t\right) H_{\mathrm{el}} \Phi \left(\mathbf{x};t\right) \mathrm{d}\mathbf{x} \tag{2.39}$$

where the phase S is identified as the classical action. By making the connection to the classical momentum $\mathbf{P}_I = \nabla_I S$, one can obtain Newtonian equation of motion as an equivalent representation of the Hamilton-Jacobi equation Eq. (2.39):

$$\begin{aligned} M_I \ddot{\mathbf{R}}_I &= -\nabla_I \int \Phi^* \left(\mathbf{x};t\right) H_{\mathrm{el}} \Phi \left(\mathbf{x};t\right) \mathrm{d}\mathbf{x} \\ &\equiv -\nabla_I \langle \Phi | H_{\mathrm{el}} | \Phi \rangle \end{aligned} \tag{2.40}$$

With the classical point nuclei approximation, the eqaution of motion for the electronic wavefunction Eq. (2.36) reduces to

$$\begin{aligned} i\hbar \frac{\partial \Phi}{\partial t} &= -\sum_i \frac{\hbar^2}{2m_e} \nabla_i^2 \Phi + V_{\mathrm{ne}}(\mathbf{r},\mathbf{R})\Phi \\ &\equiv H_{\mathrm{el}} \Phi \end{aligned} \tag{2.41}$$

Eqs. (2.40) and (2.41) are the equations of motions for Ehrenfest dynamics, where the nuclei move classically according to a mean-field potential generated by the electronic wavefunction, and the electrons are treated quantum mechanically and depends parametrically on the classical nuclear positions.

The solution to the Newtonian equation of motion for the nuclei, Eq. (2.40), can be carried out using a number of standard integration techniques, such as the velocity Verlet algorithm.

The solution to the electronic Schrödinger equation, Eq. (2.41), is not trivial, since it corresponds to the solution of the N-electron problem. Exact solutions are only possible for very few electron systems. For many-electron systems, approximations have to be made in order to achieve an affordable computation. As HF and DFT introduced in the previous sec-

tions provide a good compromise between computational cost and accuracy for the ground state problem, it seems reasonable to extend these approaches to the time-dependent regime. This will lead to the time-dependent Hartree-Fock (TDHF) method and the time-dependent density functional theory (TDDFT).

2.3.2 Time-Dependent Hartree-Fock

The time-dependent Hartree-Fock (TDHF) equations were first derived in 1930 by Dirac.[39] Since then several different formalism have been given, most notably the one by Frenkel using a time-dependent variation principle.[40] The TDHF equations were an approximation to the the time-dependent electronic Schrödinger equation, by assuming that an N-electron system can at all times be represented by a single Slater determinant composed of N time-dependent orthonormal spin orbitals, $\{\psi_k(\mathbf{x}, t)\}$

$$\Phi(t) = \frac{1}{\sqrt{N!}} \begin{vmatrix} \psi_1(\mathbf{x}_1, t) & \psi_2(\mathbf{x}_1, t) & \dots & \psi_N(\mathbf{x}_1, t) \\ \psi_1(\mathbf{x}_2, t) & \psi_2(\mathbf{x}_2, t) & \dots & \psi_N(\mathbf{x}_2, t) \\ \vdots & \vdots & \ddots & \vdots \\ \psi_1(\mathbf{x}_N, t) & \psi_2(\mathbf{x}_N, t) & \dots & \psi_N(\mathbf{x}_N, t) \end{vmatrix} \tag{2.42}$$

where the variable $\mathbf{x}$ includes both the spatial coordinate $\mathbf{r}$ and the spin coordinate ω for one electron.

Applying the Dirac-Frenkel time-dependent variational principle to this approximate wavefunction,

$$\langle \delta\Phi | i\frac{\partial}{\partial t} - \hat{H}_{\text{el}} | \Phi \rangle = 0 \tag{2.43}$$

one obtains the TD-HF equation:

$$i\frac{\partial}{\partial t}\psi_k(t) = \hat{f}(t)\psi_k(t) \tag{2.44}$$

where the time-dependent Fock operator $\hat{f}(t)$ has the same form as that given in Eq. (2.7), except that all the terms are now time-dependent because of the time-dependent spin or-

bitals.

Equivalently, one can also write the Liouville-von Neumann type equation:

$$i\frac{\partial\hat{\gamma}(t)}{\partial t} = \left[\hat{f}(t), \hat{\gamma}(t)\right] \tag{2.45}$$

where $\hat{\gamma}(t)$ is the one-particle reduced density matrix (1-RDM) defined by

$$\hat{\gamma}(t) = \sum_{i}^{N} |\psi_k(t)\rangle\langle\psi_k(t)| \tag{2.46}$$

Here in this section, we use a general spin orbital approach without referring specifically to RHF, UHF or GHF. Expanding the spin orbitals in a set of M AO basis functions,

$$\psi_i(t) = \sum_{\mu}^{M} C_{\mu i}(t)\chi_\mu \tag{2.47}$$

The resulting AO density matrix $\mathbf{P'}(t)$ is

$$P'_{\mu\nu}(t) = \sum_{i}^{N} C_{\mu i}(t)C^*_{\nu i}(t) \tag{2.48}$$

The Fock matrix in the AO basis is defined as

$$F'_{\mu\nu}(t) = \langle\mu|\hat{f}(t)|\nu\rangle \tag{2.49}$$

Since the AO basis functions are in general not orthonormal, we will need to orthonormalize the basis in order to obtain a matrix equation of similar form to Eq. (2.45).

The orthonormal transformation is a similarity transformation that brings the overlap matrix to identiy. There are two widely used orthonormalization methods: the Löwdin orthonormalization method and the Cholesky decomposition method. In the Löwdin orthonormalization method, the transformation matrix $\mathbf{V}$ is

$$\mathbf{V} = \mathbf{S}^{1/2} \tag{2.50}$$

whereas in the Cholesky decomposition, the transformation matrix $\mathbf{V}$ is upper triangular and is defined by

$$\mathbf{S} = \mathbf{V}^T\mathbf{V} \tag{2.51}$$

With the orthonormal transformation matrix $\mathbf{V}$, the density matrix and Fock matrix can be transformed from the AO basis to the orthonormal basis:

$$\mathbf{P} = \mathbf{V}\mathbf{P}'\mathbf{V}^T \tag{2.52}$$

$$\mathbf{F} = \mathbf{V}^{-T}\mathbf{F}'\mathbf{V}^{-1} \tag{2.53}$$

In an orthonormal basis, the Liouville-von Neumann equation, Eq. (2.45) can be rewritten as

$$i\frac{\partial}{\partial t}\mathbf{P}(t) = \big[\mathbf{F}(t), \mathbf{P}(t)\big] \tag{2.54}$$

which is the matrix form of the TDHF equation.

The integration of the TDHF equation, Eq. (2.54), can be achieved using a number of standard methods such as 4^{th}-order Runge-Kutta, and unitary propagation methods such as the Crank-Nicolson method,[41] the high-order Magnus method,[42] the exponential midpoint method. The efficiency of these methods are comparable since the most expensive step is the formation of the Fock matrix. In the present work, we use a modified version of the exponential midpoint method which is called the modified midpoint and unitary transformation (MMUT) algorithm.[43,44]

In the MMUT method, the density matrix is propagated from time t_{n-1} to t_{n+1} through the unitary time-evolution operator $\mathbf{U}(t_n)$, according to the Baker-Campbell-Hausdorff formula:

$$\mathbf{P}(t_{n+1}) = e^{\hat{\mathcal{L}}(t_n)}\mathbf{P}(t_{n-1}) = \mathbf{U}(t_n)\cdot\mathbf{P}(t_{n-1})\cdot\mathbf{U}^{\dagger}(t_n) \tag{2.55}$$

where $\hat{\mathcal{L}}(t)$ is the Liouville super operator, is defined as

$$\hat{\mathcal{L}}(t_n)\mathbf{P}(t_{n-1}) = -i \cdot 2\Delta t \left[\mathbf{F}(t_n), \mathbf{P}(t_{n-1})\right] \tag{2.56}$$

where Δt is the time step for the MMUT integrator.

The unitary time-evolution operator $\mathbf{U}(t_n)$ is then given by

$$\mathbf{U}(t_n) = \exp\left[-i \cdot 2\Delta t \cdot \mathbf{F}(t_n)\right] \tag{2.57}$$

By computing the Fock matrix at the midpoint of the step, the MMUT method accounts for linear changes in the density matrix during the time step. The MMUT algorithm can be used with a larger step size, while still maintaining very good control of numerical noise and integration errors.

There are several ways to construct the unitary matrix $\mathbf{U}(t_n)$. One common approach is to express $\mathbf{U}(t_n)$ in the eigenvector basis of the Fock matrix:

$$\mathbf{C}^\dagger(t_n) \cdot \mathbf{F}(t_n) \cdot \mathbf{C}(t_n) = \boldsymbol{\epsilon}(t_n) \tag{2.58}$$

$$\mathbf{U}(t_n) = \mathbf{C}(t_n) \cdot \exp\left[-i \cdot 2\Delta t \cdot \boldsymbol{\epsilon}(t_n)\right] \cdot \mathbf{C}^\dagger(t_n) \tag{2.59}$$

where $\mathbf{C}(t_n)$ is the eigenvector matrix and $\boldsymbol{\epsilon}(t_n)$ the eigenvalue matrix of the Fock matrix at time t_n.

Another approach is to expand $\mathbf{U}(t_n)$ in a Chebychev series:

$$\mathbf{U}(t_n) = \exp\left[-i \cdot 2\Delta t \cdot \mathbf{F}(t_n)\right] \approx \sum_{i=0}^{L} a_n \varphi_n \left[-i \cdot 2\Delta t \cdot \mathbf{F}(t_n)\right] \tag{2.60}$$

where a_n are the expansion coefficients and φ_n are the complex Chebychev polynomials. Because of the uniform character of the Chebychev expansion, the error decreases exponentially once the expansion length L is large enough. One advantage of using the Chebychev expansion method is that it only involves a few number of matrix multiplies for the calculation of $\mathbf{U}(t_n)$, which makes it easier to parallelize as compared to the full diagonalization of the Fock matrix when the dimension of the Fock matrix becomes very large.

2.3.3 Time-Dependent Density Functional Theory

Compared to the TDHF theory, the time-dependent density functional theory (TDDFT) is a rather different approach to the solution of the electronic TDSE equation, Eq. (2.41). Formally, it can be viewed as an exact reformulation of the time-dependent quantum mechanics, with the density being the fundamental variable instead of the many-body wavefunction, in the same spirit as the ground-state DFT. The foundation of TDDFT was made by Runge and Gross[45] in 1984, who proved the existence of the universal, time-dependent density functional.

The essential part of the Runge-Gross theorem states that there is a one-to-one correspondence between the external, time-dependent potential $v_{\text{ext}}(\mathbf{r}, t)$, and the electron density $\rho(\mathbf{r}, t)$, for a many-electron system evolving from a fixed initial state. The proof of this theorem is more involved than that of the ground-state Hohenberg-Kohn theorem, since there is no minimum principle available in the time-dependent case. The proof was done in two steps: in the first step, they showed that two different external potentials $v_{\text{ext}}(\mathbf{r}, t)$ and $v'_{\text{ext}}(\mathbf{r}, t)$, differing by more than a time-dependent function, generates two different current densities $\mathbf{j}(\mathbf{r}, t)$ and $\mathbf{j}'(\mathbf{r}, t)$; in the second step, it is showed that if the two systems have different current densities, they must also have different electron densities $\rho(\mathbf{r}, t)$ and $\rho'(\mathbf{r}, t)$.

Since the electron density uniquely defines the external potential, which in turn determines the time-dependent Hamiltonian which in turn defines the many-body wavefunction, the action integral

$$A[\rho] = \int_{t_0}^{t_1} \langle \Phi(t) | i \frac{\partial}{\partial t} - \hat{H}(t) | \Phi(t) \rangle \mathrm{d}t \tag{2.61}$$

can be represented as a unique functional of the density. And the following action integral, $B[\rho]$, is defined

$$B[\rho] = \int_{t_0}^{t_1} \langle \Phi(t) | i \frac{\partial}{\partial t} - \hat{T} - \hat{G} | \Phi(t) \rangle \mathrm{d}t \tag{2.62}$$

where $\hat{T}$ is the kinetic energy operator, and $\hat{G}$ is the electron-electron interaction operator.

$B[\rho]$ is a universal functional of the density in the sense that the same dependence on $\rho(\mathbf{r}, t)$ holds for all external potentials $v_{\text{ext}}(\mathbf{r}, t)$.

Further, $A[\rho]$ has a stationary point at the exact density of the system, i.e. the exact density can be computed from

$$\frac{\delta A[\rho]}{\delta \rho} = 0 \tag{2.63}$$

Finally, in order to derive a computation scheme similar to the ground-state Kohn-Sham equations, Runge and Gross introduced an auxiliary system of non-interacting electrons. In analogy to the stationary case, the exchange-correlation action integral is defined as

$$A_{\text{xc}}[\rho] = \int_{t_0}^{t_1} \langle \Phi(t)|\hat{G}|\Phi(t)\rangle \mathrm{d}t - \frac{1}{2}\int \frac{\rho(\mathbf{r}_1)\rho(\mathbf{r}_2)}{r_{12}} \mathrm{d}\mathbf{r}_1 \mathrm{d}\mathbf{r}_2 + \int_{t_0}^{t_1} \langle \Phi(t)|\hat{T} - \hat{T}_s|\Phi(t)\rangle \mathrm{d}t \tag{2.64}$$

where $\hat{T}_s$ is the kinetic energy of the non-interacting system.

This non-interacting system is subject to an effective local potential v_{eff}:

$$v_{\text{eff}}(\mathbf{r}_1, t) = v_{\text{ext}}(\mathbf{r}_1, t) + \int \frac{\rho(\mathbf{r}_2)}{r_{12}} \mathrm{d}\mathbf{r}_2 + v_{xc}[\rho](\mathbf{r}_1, t) \tag{2.65}$$

where $v_{xc}[\rho](\mathbf{r}_1, t)$ is the time-dependent exchange-correlation (xc) potential and is defined by

$$v_{xc}[\rho](\mathbf{r}_1, t) = \frac{\delta A_{\text{xc}}[\rho]}{\delta \rho} \tag{2.66}$$

such that the density of this non-interacting system is the same as the density of the interacting system. The single-particle orbitals fulfill the time-dependent Kohn-Sham (TDKS) equation:

$$i\frac{\partial}{\partial t}\psi(\mathbf{r}_1, t) = \hat{f}^{\text{KS}}(\mathbf{r}_1, t)(\mathbf{r}_1, t) \tag{2.67}$$

where

$$\hat{f}^{\mathrm{KS}}(\mathbf{r}_1, t) = -\frac{1}{2}\nabla^2 + v_{\mathrm{eff}}(\mathbf{r}_1, t) \tag{2.68}$$

The time-dependent xc potential $v_{xc}[\rho]$ includes all nontrivial many-body effects and is nonlocal, both in space and time. Unfortunately, the exact form of this functional is unknown and approximations to it are still in their infancy. The simplest and widely used approach is the so-called adiabatic approximation (AA), in which the exact time-dependent xc functional is approximated as some ground-state xc functional, $\tilde{v}_{xc}$

$$v_{xc}^{\mathrm{adiabatic}}[\rho](\mathbf{r}, t) = \tilde{v}_{xc}[\rho](\mathbf{r})|_{\rho=\rho(\mathbf{r},t)} \tag{2.69}$$

When expressed in a set of orthonormal set of basis functions, the TDKS equation, Eq. (2.67), can be rewritten as:

$$i\frac{\partial}{\partial t}\mathbf{P}(t) = \big[\mathbf{F}(t), \mathbf{P}(t)\big] \tag{2.70}$$

which has the same form as the TDHF equation, Eq. (2.54), except that the HF exchange potential is replaced by the xc potential in TDDFT.

2.4 Electron Correlation

While the Hartree-Fock method and the density functional theory, as well as their time-dependent counterparts have been successful in the study of many molecular properties and dynamical processes, they have their own limitations. Being a single configuration wavefunction method, the HF and TDHF lack the so-called electron correlation. The electron correlation energy is defined as the energy difference between the exact non-relativistic ground-state energy (E_{exact}) and the Hartree-Fock ground-state energy (E_{HF}):

$$E_{\text{corr}} = E_{\text{exact}} - E_{\text{HF}} \tag{2.71}$$

DFT and TDDFT, on the other hand, are formally exact provided that the true density functional is used. However, the exact form of the functional is not known. So far, practical applications of DFT and TDDFT exploit approximations to the functional, and there is no systematic way of improving the accuracy or choosing a particular approximation. As a result, at current stage DFT and TDDFT are still far from being a reliable predictive tool for many chemical applications, especially when high accuracy is desired.

The term "electron correlation", may be divided into two categories: the so-called "dynamical correlation" and "nondynamical correlation" (or static correlation). Dynamical correlation comes from the instantaneous Coulomb repulsion between electrons of opposite spin. HF theory is a mean-field theory, in which each electron experiences an average field of all the other electrons in the system. Although HF theory accounts for the instantaneous repulsion between electrons of same spin via anti-symmetry of the single Slater determinant, it cannot describe the instantaneous repulsion between two electrons of the opposite spin. Thus dynamic correlation is missing in HF theory.

Static correlation arises from degeneracy or near-degeneracy between configurations (i.e. Slater determinants). This type of correlation becomes more pronounced when the HF ground state determinant and excited determinants are close in energy.

Different from DFT, in wavefunction theory systematic improvement in the description of the electron correlation can be accomplished by extending the HF single-particle, single-

determinant description. Since these methods usually use HF wavefunction as a starting point, they are often referred as post-Hartree-Fock methods.

The most straightforward way of including both dynamical and static correlations is the so-called configuration interaction (CI) method. In the CI method, a linear combination of HF determinant and excited determinants is used to provide a better approximation to the exact many-electron wavefunction. Then variation principle is used to find the upper bounds to the exact eigen-states within the CI expansion space. If the expansion space is complete, i.e. all possible excited determinants are included, the method gives the exact solution within the space spanned by a given atomic orbital basis set, and is called full CI. Unfortunately, the size of the full CI expansion grows exponentially with the size of system, and thus not practical for quantum chemical calculations except for very small systems.

The HF wavefunction usually provides qualitatively correct description of the electronic structure when the molecule is near its equilibrium geometry. In this case, what is missing is primarily the dynamical correlation, which can be included by treating the electron correlation as a small perturbation to the HF Hamiltonian. A widely used perturbation method is given by Møller and Plesset,[46] and is referred as the MPn ($n \geq 2$) method. Another way of treating dynamical correlation is done by the coupled cluster (CC) method, where a cluster expansion of the wavefunction is performed using the HF single Slater determinant as the reference.

However, when the molecules are far away from their equilibrium geometries, i.e. when the bonds are stretched or broken, the HF wavefunction does not give even qualitatively correct description of the electronic structure. For example, the RHF method cannot describe the dissociation of molecules into open-shell fragments (e.g., $H_2 \rightarrow 2H$). In this case, static correlation is the major missing piece rather than dynamical correlation, and the HF wavefunction cannot be used as a zero-order approximation for perturbation treatments or CC methods. There are several methods that can treat the static correlation, namely the generalized valence bond (GVB) method,[47] the multi-configuration self-consistent field (MCSCF) method, and the density matrix renormalization group (DMRG)[48] method. Among these, the MCSCF method has been widely used for exploring the potential energy surfaces of molecules and as a starting point for high accuracy wavefunction approaches such

as multireference (MR) perturbation theory, MR-CI, and MR-CC theory . In the following section, we will provide a brief introduction of the MCSCF theory, in particular, the complete-active-space self-consistent field (CASSCF) method.

2.5 Multi-Configuration Self-Consistent Field Theory

As discussed in the previous section, the MCSCF method is aimed to recover the static correlation effects. Instead of using one single Slater determinant as in HF theory, the MCSCF wavefunction consists of a small number of selected determinants or configuration state functions (CSFs). A configuration state function is a linear combination of several Slater determinants and is a spin eigen-function. In order to obtain the lowest possible energy within this truncated CI space, the variation principle is applied to both the expansion coefficients and the spin orbitals of which the determinants are composed.

In the MCSCF approach, one writes the approximate wavefunction as a truncated CI expansion:

$$|\Phi_{\mathrm{MC}}\rangle = \sum_I c_I |\Phi_I\rangle \tag{2.72}$$

where c_I are the expansion coefficients, $|\Phi_I\rangle$ are the HF and excited Slater determinants, composed of orthonormal spin orbitals ψ_i, as given in Eq. (2.4).

The task is to minimize the energy $\langle\Phi_{\mathrm{MC}}|\hat{H}|\Phi_{\mathrm{MC}}\rangle$ by varying both the expansion coefficients c_I and the orbitals ψ_i, using the variation principle:

$$E_{\mathrm{MC}} = \min_{\{c_I\},\{\psi_i\}} \frac{\langle\Phi_{\mathrm{MC}}|\hat{H}|\Phi_{\mathrm{MC}}\rangle}{\langle\Phi_{\mathrm{MC}}|\Phi_{\mathrm{MC}}\rangle} \tag{2.73}$$

This flexibility in the variation space allows for a better description of the electronic structure of bonded molecular systems compared to the HF method. Most importantly, it is one of the few options that can give qualitatively correct description of bond breaking and molecular dissociation processes.

One of the greatest difficulties in a MCSCF calculation is the selection of the expansion space. For very simple systems, the selection can be done by inspection of individual configuration and choosing the ones that will likely give most important contributions to the energy. For more complicated molecules, however, the selection of the expansion space can be very difficult and sometimes the selected space is not flexible enough to properly describe

the physical process. In order to overcome these problems, Roos[49] introduced the complete-active-space (CAS) self-consistent field (SCF) approach. In this approach, one only needs to select a set of active orbitals and the expansion space is automatically determined by collecting all possible configurations of the active electrons in the active orbitals. All the rest orbitals are kept doubly occupied or unoccupied. The CAS wavefunction can be regarded as a full CI wavefunction within the variationally optimized active orbital space. Of course, when the active orbital space comprises all the orbitals in the system, the true full CI wavefunction is recovered; on the other hand, when the active orbital space is empty, the CAS wavefunction reduces to the HF wavefunction.

There are also variants of the CASSCF approach, to name a few, the restricted active space (RAS) SCF and the general active space (GAS) SCF methods. These methods were developed to further reduce the size of the CASSCF expansion, by subdividing the active space into groups of orbitals with certain occupancy restrictions.

Because the configuration expansion that can be managed within MCSCF approaches is usually small, it is in general impossible to recover dynamical correlation. Thus MCSCF methods alone are usually not appropriate for applications that require high accuracy. However, since MCSCF methods are one of the few options that can treat the static correlation effects, they may provide a good zero-order wavefunction for subsequent treatment of dynamical correlation such as in the framework of multireference CI (MR-CI), multireference coupled-cluster, or multi-configuration perturbation theory.

In Chapter 6, we will give a detailed exposition of MCSCF theory, in particular the CASSCF method. New developments in the optimization of the CI coefficients will be presented.

Chapter 3

MODELING SYSTEM-ELECTROMAGNETIC INTERACTIONS WITH RT-TDHF/TDDFT

3.1 Gauge Invariance of TDHF and TDDFT Equations

Nonperturbative electronic dynamics using the time-dependent Hartree-Fock (TDHF) and time-dependent Kohn-Sham (TDKS) theory with the adiabatic approximation is a powerful tool in obtaining insights into the interaction between a many-electron system and an external electromagnetic field. In practical applications of TDHF/TDKS using an incomplete basis set, electronic dynamics and molecular properties become gauge-dependent. Numerical simulations in incomplete basis sets are carried out in the length gauge and velocity gauge to verify the extent of gauge-dependence using incomplete basis sets. Electronic dynamics of two many-electron systems, a Helium atom and a carbon monoxide molecule in high-intensity linearly polarized radiation fields are performed using the TDHF and TDKS with two selected adiabatic exchange-correlation (xc) functionals. The time evolution of the expectation values of the dipole moment and harmonic spectra are calculated in the two gauges, and the basis set dependence on the gauge-invariance of these properties is investigated.

3.1.1 Introduction

Ever since the first treatment of radiation problems in quantum mechanics, there have been numerous arguments[50–63] concerning the equivalence of quantum mechanical observables in different gauges. It is well known[62–65] that the time-dependent Schrödinger equation (TDSE) is formally invariant upon a gauge transformation of the electromagnetic potentials in space and time. As a result, all physical observables do not depend on the choice of gauge. For instance, using grid methods to integrate the TDSE, Han *et al.*[66] calculated the high-order harmonic generation (HHG) spectra of the hydrogen atom in a laser

field. By performing calculations in two different gauges, the length gauge and the velocity gauge, they showed that the two gauges gave identical time-dependent expectation values of the dipole, dipole velocity and dipole acceleration. However, TDSE cannot be solved exactly except for very small systems.[66–72] Various approximations have been introduced with the aim of achieving reliable results at lower costs. In a perturbative treatment,[73–75] the interaction between the system and radiation is treated as a perturbation to the system Hamiltonian in the absence of the radiation field. Such perturbative approaches, however, do not preserve gauge invariance.[57,58,60,63] For example, Lamb[56] noted that when treating the interaction of an electromagnetic field with matter perturbatively, the probability amplitudes calculated in different gauges were not the same and only one particular form of the perturbation (so-called "length form") gave results that were in better agreement with experiment. In addition to the problem of gauge dependence, the perturbative approach is insufficient when a high intensity radiation field is applied to the system.

One possible alternative to the TDSE is the time-dependent Hartree-Fock (TDHF)[43,76–78] approach, which approximates the TDSE with a time-dependent single Slater determinant wavefunction. A conceptually different approach is the time-dependent density functional theory (TDDFT),[45,79–83] which can be viewed as an exact reformulation of the TDSE given an exact exchange-correlation (xc) functional. The Runge-Gross (RG) theorem[45] and its modifications[79,80] ensure a unique one-to-one mapping between the time-dependent single-particle external potential $v(\mathbf{r},t)$ and the time-dependent single-particle density $\rho(\mathbf{r},t)$. However, the RG theorem is restricted to scalar potentials and excludes situations involving vector potentials. To describe the interaction of electromagnetic radiation with matter, Ghosh and Dhara[84] developed the time-dependent current density functional formalism (TDCDFT), in which the single-particle current density $\mathbf{j}(\mathbf{r},t)$ determines uniquely the time-dependent scalar and vector potentials that characterize the system. Given the exact xc functional, both TDDFT and TDCDFT can be reformulated into a set of coupled time-dependent single-particle Kohn-Sham equations (TDKS). The TDKS equations can be equivalently written in matrix form[44,85–88] using a single Slater determinant wave function projected onto a basis.

Depending on the strength of external perturbation, applications of TDHF/TDKS treat-

ment of the interaction between electromagnetic radiation and matter can be classified into two categories.[81] When the intensity of the external radiation is small, a linear response description of the TDHF/TDKS equations can be used, as exemplified by the random-phase approximation (RPA)[89,90] for TDHF and linear-response time-dependent density functional theory (LR-TDDFT)[81,91–93] for TDKS. The RPA and LR-TDDFT have been widely used for calculations of excitation energies and oscillator strengths. However, this approach does not give any dynamical information as the system evolves over time. More importantly, when the external field is strong, neither RPA nor LR-TDDFT is sufficient to describe the problem. Within this strong field regime, the real-time TDHF and TDKS propagations have been implemented in calculations of the multiphoton ionization,[70,76,77] the high-order harmonic generation (HHG),[94–98] and the above threshold ionization (ATI).[99]

Within the perturbation limit, the gauge behavior of TDHF/TDKS has been mathematically evaluated,.[61,100,101] However, gauge behaviors of TDHF/TDKS in the perturbative regime can not be simply translated into the real-time dynamics in the nonperturbative regime. In the perturbative regime, the RPA and LR-TDDFT equations are essentially time-independent. Analyses of gauge behaviors are based on the time-independent ground state orbital space, and focus on linear absorption spectra and oscillator strengths. In the nonperturbative regime, real-time TDHF/TDKS dynamics propagate a time-dependent coherent electronic state, and the HF/KS orbital space is time-dependent. Such a nonperturbative treatment is often associated with applications of high-order harmonic spectra or intense-laser controlled molecular reactions.

This section addresses gauge behaviors for real-time electronic dynamics driven by an external field within the TDHF/TDKS framework beyond the perturbative regime.

3.1.2 Gauge invariance of the TDHF and TDKS equations

A. The many-body TDSE in a classical electromagnetic field.

In a conventional non-relativistic approach for the interaction of an electromagnetic field with a quantum mechanical electronic system, the field is treated classically and characterized by a vector potential $\mathbf{A}(\mathbf{r},t)$ and a scalar potential $U(\mathbf{r},t)$. The electronic Hamiltonian

can be obtained from the Lagrangian approach[65,102]

$$H(\mathbf{A},U)=\sum_{k}^{N}\left(\frac{1}{2}[\mathbf{p}_k+\mathbf{A}(\mathbf{r}_k,t)]^2-U(\mathbf{r}_k,t)\right)+V_{Ne}+V_{ee} \tag{3.1}$$

and the time-dependent Schrödinger (TDSE) equation is

$$i\frac{\partial}{\partial t}\Psi(\mathbf{A},U)=H(\mathbf{A},U)\Psi(\mathbf{A},U) \tag{3.2}$$

where $\mathbf{p}_k=-i\nabla_k$ and $\mathbf{r}_k$ are the momentum and position operators for the k-th electron, respectively. V_{Ne} and V_{ee} are nuclear-electron, and electron-electron interaction potentials, respectively. Atomic units are used throughout and the atomic units of the scalar and vector potentials are converted from SI units.

Given a gauge function $\chi(\mathbf{r},t)$, which is an arbitrary differentiable real function of position and time, the vector potential $\mathbf{A}(\mathbf{r},t)$ and scalar potential $U(\mathbf{r},t)$ can be transformed to generate a new set of potentials,

$$\mathbf{A}'(\mathbf{r},t)=\mathbf{A}(\mathbf{r},t)+\nabla\chi(\mathbf{r},t) \tag{3.3a}$$

$$U'(\mathbf{r},t)=U(\mathbf{r},t)-\frac{\partial}{\partial t}\chi(\mathbf{r},t) \tag{3.3b}$$

It has been shown[57,65,102] that the TDSE, Eq. (3.2) is formally invariant upon the gauge transformation defined in Eq. (3.3). The wavefunction $\Psi'(\mathbf{A}',U')$ in this new gauge is related to $\Psi(\mathbf{A},U)$ by a phase factor

$$\Psi'(\mathbf{A}',U')=\exp\left[-i\sum_{k}^{N}\chi(\mathbf{r}_k,t)\right]\Psi(\mathbf{A},U) \tag{3.4}$$

where χ is the same gauge function used in Eq. (3.3). As a result, the expectation values of the single-particle position operator $\mathbf{r}$ and mechanical momentum operator $\boldsymbol{\pi}=\mathbf{p}+\mathbf{A}$ are also gauge invariant.[65,102]

It should be noted that the classically inferred Hamiltonian in Eq. (3.1) is still incomplete in a sense that it omits all the interactions associated with the spin of the particles,

which include the spin-spin interactions, spin-orbital couplings, and spin-magnetic field interactions. In the present work, these terms are not included due to the fact that they are essentially non-classical in origin and their magnitudes are much smaller compared to the other terms.

B. Gauge invariance of the TDHF formalism.

The TDHF formalism, as an approximation to the exact time-dependent Schrödinger equation, makes use of the assumption that the exact solution can be represented by a single Slater determinant composed of time-dependent single-particle wavefunctions, ϕ_k

$$\Phi(\mathbf{r}_1, \mathbf{r}_2, \ldots, \mathbf{r}_N, t) = \frac{1}{\sqrt{N!}} \left| \; \phi_1(\mathbf{r}, t)\phi_2(\mathbf{r}, t) \ldots \phi_N(\mathbf{r}, t) \; \right| \tag{3.5}$$

and the resulting TDHF equations are obtained as

$$i\frac{\partial}{\partial t}\phi_k(\mathbf{r}, t) = \hat{F}(\mathbf{r}, t)\phi_k(\mathbf{r}, t) \tag{3.6}$$

where, the Fock operator $\hat{F}(\mathbf{r}, t)$ is defined as

$$\hat{F}(\mathbf{r}, t) = \hat{h}(\mathbf{r}, t) + \hat{J}(\mathbf{r}, t) - \hat{K}(\mathbf{r}, t) \tag{3.7}$$

For a many-electron system interacting with a time-dependent electromagnetic field characterized by the scalar potential $U(\mathbf{r}, t)$ and vector potential $\mathbf{A}(\mathbf{r}, t)$, the one-electron term $\hat{h}(\mathbf{r}, t)$ is written as

$$\hat{h}(\mathbf{r}, t) = \frac{1}{2}[\mathbf{p} + \mathbf{A}(\mathbf{r}, t)]^2 + V(\mathbf{r}) - U(\mathbf{r}, t) \tag{3.8}$$

where $V(\mathbf{r})$ is the electron-nuclei interaction potential. The Coulomb operator $\hat{J}(\mathbf{r}, t)$ and exchange operator $\hat{K}(\mathbf{r}, t)$ in Eq. (3.7) describe the average electron-electron interactions,

$$\hat{J}(\mathbf{r}, t)\phi_k(\mathbf{r}, t) = \left[\sum_j^N \int d\mathbf{r}' \frac{\phi_j^*(\mathbf{r}', t)\phi_j(\mathbf{r}', t)}{|\mathbf{r} - \mathbf{r}'|}\right]\phi_k(\mathbf{r}, t) \tag{3.9}$$

$$\hat{K}(\mathbf{r},t)\phi_k(\mathbf{r},t) = \left[\sum_j^N \int d\mathbf{r}' \frac{\phi_j^*(\mathbf{r}',t)\phi_k(\mathbf{r}',t)}{|\mathbf{r}-\mathbf{r}'|}\right]\phi_j(\mathbf{r},t) \tag{3.10}$$

It is shown (see Appendix) that, upon a gauge transformation of the electromagnetic potentials, the TDHF equations are essentially form-invariant,

$$i\frac{\partial}{\partial t}\phi_k'(\mathbf{r},t) = \hat{F}'(\mathbf{r},t)\phi_k'(\mathbf{r},t) \tag{3.11}$$

where the vector and scalar potentials ($\mathbf{A}'$, U') in the new gauge are used in Eq. (3.8). The one-electron orbitals in the new gauge can be obtained via a unitary transformation similar to Eq. (3.4),

$$\phi_k'(\mathbf{r},t) = e^{-i\chi(\mathbf{r},t)}\,\phi_k(\mathbf{r},t) \tag{3.12}$$

With the relation (3.12), it is easy to show that expectation values of the single-particle position operator $\mathbf{r}$ and mechanical momentum operator $\boldsymbol{\pi} = \mathbf{p} + \mathbf{A}$ are gauge invariant in the TDHF framework.

The expectation value of the electric dipole moment, $\boldsymbol{\mu}_e$, and the time-dependent electron charge density, $\rho(\mathbf{r},t)$, can be evaluated as,

$$\boldsymbol{\mu}_e(t) = -\langle\Phi(t)|\mathbf{r}|\Phi(t)\rangle = -\sum_k^N \langle\phi_k(t)|\mathbf{r}|\phi_k(t)\rangle \tag{3.13}$$

$$\rho(\mathbf{r},t) = \sum_k^N |\phi_k(\mathbf{r},t)|^2 \tag{3.14}$$

Using Eq. (3.12), it follows that both the expectation value of the dipole moment and the time-dependent charge density are invariant under gauge transformations.

C. The Ghosh-Dhara theorem and gauge invariance of the TDKS equations with adiabatic approximation.

The Ghosh-Dhara theorem[84] can be viewed as an extension of the RG theorem[45] to time-dependent problems involving the interaction of electromagnetic radiation with matter. It states that the exact single-particle current density $\mathbf{j}(\mathbf{r},t)$ uniquely determines the time-dependent scalar potential $U(\mathbf{r},t)$ and vector potential $\mathbf{A}(\mathbf{r},t)$, as well as the exact single-

particle density $\rho(\mathbf{r},t)$. It has been shown that there exists a universal xc functional $E_{xc}[\rho,\mathbf{j}]$ that does not dependent on the external scalar and vector potentials. This ensures that for a many-electron system subject to an external scalar and vector potentials $U(\mathbf{r},t)$ and $\mathbf{A}(\mathbf{r},t)$, the exact single-particle density $\rho(\mathbf{r},t)$ and current density $\mathbf{j}(\mathbf{r},t)$ can be obtained from the single-particle TDKS equations:

$$i\frac{\partial}{\partial t}\phi_k(\mathbf{r},t) = \left\{\frac{1}{2}[\mathbf{p}+\mathbf{A}_{\text{eff}}]^2 + U_{\text{eff}}(\mathbf{r},t)\right\}\phi_k(\mathbf{r},t) \tag{3.15}$$

where the effective scalar and vector potentials U_{eff} and $\mathbf{A}_{\text{eff}}$ are given by

$$\mathbf{A}_{\text{eff}}(\mathbf{r},t) = \mathbf{A}(\mathbf{r},t) + \int d\mathbf{r}'\frac{\mathbf{j}(\mathbf{r}',t)}{|\mathbf{r}-\mathbf{r}'|} + \frac{\delta E_{xc}[\rho,\mathbf{j}]}{\delta \mathbf{j}} \tag{3.16}$$

$$U_{\text{eff}}(\mathbf{r},t) = V(\mathbf{r}) - U(\mathbf{r},t) + \int d\mathbf{r}'\frac{\rho(\mathbf{r}',t)}{|\mathbf{r}-\mathbf{r}'|} + \frac{\delta E_{xc}[\rho,\mathbf{j}]}{\delta \rho} + \frac{1}{2}(\mathbf{A}_{\text{eff}}^2 - \mathbf{A}^2) \tag{3.17}$$

Ghosh and Dhara[84] have shown that the TDKS equations, Eq. (3.15) are essentially gauge invariant under the transformation of the electromagnetic potentials U and $\mathbf{A}$ defined in Eq. (3.3).

The Ghosh-Dhara theorem provides a scheme to model the interaction of a many-electron system with electromagnetic radiation through the solution of the TDKS equations. Unfortunately, the exact form of the time-dependent xc functional $E_{xc}[\rho,\mathbf{j}](\mathbf{r},t)$ is unknown and approximations to it are still in their infancy. The simplest and widely used approach is the adiabatic approximation, in which the exact time-dependent xc functional is approximated as some ground-state xc functional, $\tilde{E}_{xc}$

$$E_{xc}^{\text{adiabatic}}[\rho,\mathbf{j}](\mathbf{r},t) = \tilde{E}_{xc}[\rho](\mathbf{r})|_{\rho=\rho(\mathbf{r},t)} \tag{3.18}$$

With this approximation, the second and third terms in Eq. (3.16), and consequently the last term in Eq. (3.17), are ignored.[103] We also note here the ground-state xc functionals available today are not explicit functionals of the current density $\mathbf{j}$. By further ignoring the

current-current interaction, the TDKS equations become

$$i\frac{\partial}{\partial t}\phi_k(\mathbf{r},t) = \left\{\frac{1}{2}[\mathbf{p}+\mathbf{A}(\mathbf{r},t)]^2 + V(\mathbf{r}) - U(\mathbf{r},t) + \int d\mathbf{r}'\,\frac{\rho(\mathbf{r}',t)}{|\mathbf{r}-\mathbf{r}'|} + \frac{\delta\tilde{E}_{xc}[\rho]}{\delta\rho}\right\}\phi_k(\mathbf{r},t) \quad (3.19)$$

where $\tilde{E}_{xc}[\rho]$ is some ground-state xc functional and ρ is given by Eq. (3.14).

Since the adiabatic approximation is trivially included in the Ghosh-Dhara theorem, the TDKS equations with adiabatic approximation, Eq. (3.19), are also gauge invariant. The resulting single-particle wavefunctions $\{\phi_k\}$ undergo a unitary transformation similar to Eq. (3.12). In the next section, we will carry out the numerical solution of the TDKS equations using two commonly used adiabatic xc functionals, the Becke-Lee-Yang-Parr (BLYP) generalized gradient approximation (GGA) functional[104–106] and the Becke-3-parameter-Lee-Yang-Parr (B3LYP) hybrid functional,[105,107–109] and examine their gauge behaviors. The results obtained therein will be the first step toward building nonadiabatic xc functionals for real-time electronic dynamics.

3.1.3 Gauge properties of TDHF and TDKS electronic dynamics in incomplete basis sets

We have seen that TDHF and TDKS equations are formally invariant in the sense that a gauge transformation of electromagnetic potentials gives rise to a unitary transformation on the single-particle wavefunctions. As a result, molecular properties such as the dipole moment and charge density are gauge invariant. In practical calculations, a finite incomplete basis set is often used to expand the single-particle wavefunctions. With an incomplete basis set, the TDHF/TDKS equations may not be gauge invariant. The proof is by *reductio ad absurdum*: Given a finite incomplete set of M basis functions $\varphi_k(\mathbf{r})$, the solutions to the TDHF equations in a particular gauge, Eq. (3.6), are linear combinations of these basis functions,

$$\phi_k(\mathbf{r},t) = \sum_{\mu}^{M} c_{\mu,k}(t)\varphi_\mu(\mathbf{r}) \quad (3.20)$$

Assume gauge invariance can be achieved in this incomplete basis set, that is, under an arbitrary gauge transformation of the electromagnetic potentials, the new solutions, $\phi'_k(\mathbf{r},t)$,

are related to the old ones, $\phi_k(\mathbf{r},t)$, by Eq. (3.12). In terms of the basis functions, we have

$$\phi'_k(\mathbf{r},t) = \sum_{\mu}^{M} c_{\mu,k}(t)\, e^{-i\chi(\mathbf{r},t)}\varphi_\mu(\mathbf{r}) \tag{3.21}$$

On the other hand, the solutions in the new gauge are also linear combinations of the basis functions,

$$\phi'_k(\mathbf{r},t) = \sum_{\nu}^{M} c'_{\nu,k}(t)\varphi_\nu(\mathbf{r}) \tag{3.22}$$

By equating Eqs. (3.21) and (3.22), it requires that the product $e^{-i\chi(\mathbf{r},t)}\varphi_\mu(\mathbf{r})$ must be expanded by the same basis

$$e^{-i\chi(\mathbf{r},t)}\varphi_\mu(\mathbf{r}) = \sum_{k}^{M} B_{k,\mu}(t)\varphi_k(\mathbf{r}) \tag{3.23}$$

However, since the gauge function $\chi(\mathbf{r},t)$ can be arbitrary, there exists some $\chi(\mathbf{r},t)$ such that the products $e^{-i\chi(\mathbf{r},t)}\varphi_\mu(\mathbf{r})$ do not fall into the subspace expanded by the incomplete basis $\varphi_k(\mathbf{r})$. In this case, relation (3.12) is no longer valid, which is in contradiction to our assumption. As a result, the TDHF/TDKS equations in the incomplete basis are not form-invariant, and the calculated molecular properties will depend on the gauge used to describe the electromagnetic field.

One could introduce a pseudo-gauge function to recover a certain amount of invariance in an incomplete basis set. Such an idea has been applied to resolve the gauge-origin issue in the self-consistent field (SCF) calculations of nuclear magnetic shielding[110–112] and magnetically induced current densities.[113] In these approaches the so-called gauge-including atomic orbitals (GIAOs) are constructed by adding a time independent phase factor to the atomic basis functions.[110] However, the use of GIAOs does not necessarily lead to true gauge invariance.[114] In addition, due to the exponential nature of the phase factor, full evaluation of the two-electron integrals using GIAOs is computationally formidable. In practical calculations, the phase factor is usually Taylor-expanded to the first-order,[110] which again would lead to gauge dependence of the results.

3.1.4 Numerical methods

To examine the gauge properties of TDHF/TDKS electronic dynamics, we consider two different electronic systems, a Helium atom and a carbon monoxide (CO) molecule, interacting with high-intensity linearly polarized sine-squared envelope laser pulses. In both cases, the laser wavelength is chosen to be 456 nm, which is much larger than the atomic/molecular size. Thus we invoke the long-wavelength approximation, in which the spatial variation of the electromagnetic field is neglected. As a consequence, the electric field becomes purely time-dependent and the magnetic field vanishes.[63] With this approximation, the electric field of the laser pulse is written as:

$$\mathbf{E}(t) = \begin{cases} \mathbf{E}_0 \sin^2(\pi t/T)\cos(\omega t + \phi), & 0 \leq t \leq T \\ 0, & t > T \end{cases} \tag{3.24}$$

where $\mathbf{E}_0$ and ω are the amplitude and angular frequency of the electric field, respectively, T is the pulse duration, and ϕ is the phase.

For problems of atoms/molecules interacting with intense laser fields, there are three commonly used gauges or representations: the length gauge (or called electric field gauge), the velocity gauge (or called Coulomb gauge), and the acceleration gauge (or called Bloch-Nordsieck representation).[115] Each representation has been used with varying degrees of success.[66,116–119] The length and velocity gauges can be obtained from the usual transformation of the electromagnetic potentials defined in Eq. (3.3). On the other hand, the Bloch-Nordsieck representation is obtained through a unitary transformation of the momentum operator and hence cannot be considered as a gauge transformation.[120] The equivalence of the three gauges or representations exists only between exact eigenstates of respective Hamiltonians. In numerical simulations on large grids, it is the eigenstates of the grid which form the basis for gauge invariant results, a well known principle in strong field simulations where the grid initial state must be obtained by integrating TDSE initially backward in imaginary time.[95]

In this work, we compare numerical results in the length gauge (LG) and the velocity

gauge (VG), within the long-wavelength approximation. The LG is defined using:

$$\mathbf{A}^{LG} = 0 \tag{3.25a}$$

$$\mathbf{U}^{LG} = -\mathbf{r} \cdot \mathbf{E}(t) \tag{3.25b}$$

and the VG takes the form:

$$\mathbf{A}^{VG} = -\int_0^t \mathbf{E}(t')dt' \tag{3.26a}$$

$$\mathbf{U}^{VG} = 0 \tag{3.26b}$$

It can be seen that both the LG and VG describe the same electromagnetic field and are related by a gauge transformation using the function

$$\chi(\mathbf{r}, t) = \mathbf{r} \cdot \mathbf{A}^{VG} = -\mathbf{r} \cdot \int_0^t \mathbf{E}(t')dt' \tag{3.27}$$

Numerical integrations of the TDHF and TDKS equations in both the LG and the VG are performed in the density matrix formulation. In an orthonormal basis $\{|\mu\rangle\}$, the TDHF/TDKS equation for the density matrix is:

$$i\frac{d}{dt}\mathbf{P}(t) = \mathbf{F}(t)\mathbf{P}(t) - \mathbf{P}(t)\mathbf{F}(t) \tag{3.28}$$

where $\mathbf{P}(t)$ is the density matrix and is constructed from the product of the single-particle wavefunction coefficients

$$\mathbf{P}_{\mu\nu}(t) = \sum_k^N c_{\mu,k}(t)c^*_{\nu,k}(t) \tag{3.29}$$

The Fock/Kohn-Sham matrix is given by

$$\mathbf{F}_{\mu\nu}(t) = \langle\mu|\hat{F}(t)|\nu\rangle \tag{3.30}$$

where $\hat{F}(t)$ is defined in Eq. (2.7) and Eq. (3.19), correspondingly.

The elements of the Fock/Kohn-Sham matrices in the length and velocity gauges are

$$\mathbf{F}_{\mu\nu}(t) = \begin{cases} \mathbf{F}^{LG}_{0,\mu\nu}(t) + \langle\mu|\mathbf{r}|\nu\rangle \cdot \mathbf{E}(t) & \text{(LG)} \\ \mathbf{F}^{VG}_{0,\mu\nu}(t) - i\langle\mu|\boldsymbol{\nabla}|\nu\rangle \cdot \mathbf{A}^{VG} + \frac{1}{2}\Big(A^{VG}\Big)^2\langle\mu|\nu\rangle & \text{(VG)} \end{cases} \tag{3.31}$$

where $\mathbf{F}_0(t)$ is the Fock/Kohn-Sham matrix without the electromagnetic field.

With the Fock/Kohn-Sham matrices given above, the TDHF/TDKS equation, Eq. (3.28) is integrated with a modified midpoint and unitary transformation (MMUT) algorithm.[43,44,121] In the MMUT method, the time-evolution operator is a unitary transformation matrix $\mathbf{U}(t_n)$ that is constructed from the eigenvector matrix $\mathbf{C}(t_n)$ and eigenvalue matrix $\boldsymbol{\epsilon}(t_n)$ of the Fock matrix at time t_n:

$$\mathbf{C}^\dagger(t_n) \cdot \mathbf{F}(t_n) \cdot \mathbf{C}(t_n) = \boldsymbol{\epsilon}(t_n) \tag{3.32}$$

$$\begin{aligned} \mathbf{U}(t_n) &= \exp\big[i \cdot 2\Delta t \cdot \mathbf{F}(t_n)\big] \\ &= \mathbf{C}(t_n) \cdot \exp\big[i \cdot 2\Delta t \cdot \boldsymbol{\epsilon}(t_n)\big] \cdot \mathbf{C}^\dagger(t_n) \end{aligned} \tag{3.33}$$

where Δt is the time step for the MMUT integrator. The density matrix is then propagated from time t_{n-1} to t_{n+1} through the time-evolution operator $\mathbf{U}(t_n)$:

$$\mathbf{P}(t_{n+1}) = \mathbf{U}(t_n) \cdot \mathbf{P}(t_{n-1}) \cdot \mathbf{U}^\dagger(t_n) \tag{3.34}$$

By computing the Fock matrix at the midpoint of the step, the MMUT method accounts for linear changes in the density matrix during the time step. The MMUT algorithm can be used with a larger step size, while still maintaining very good control of numerical noise and integration errors.

The TDHF/TDKS electronic dynamics in both the LG and the VG is implemented using the development version of the GAUSSIAN series of programs[122] with the addition of the MMUT algorithm discussed above. For TDKS, two widely used adiabatic xc functionals, the BLYP and B3LYP functionals, are chosen to study their gauge behaviors. In the case of the He atom, we compare the time-dependent expectation values of the dipole $\langle z\rangle$, dipole velocity $\langle \dot{z}\rangle$, and dipole acceleration $\langle \ddot{z}\rangle$ in the LG and the VG. For the CO molecule, we

compute the expectation values of the dipole and the corresponding harmonic spectra, and compare the results in the LG and the VG. The harmonic spectra can be obtained by the Fourier transformation of the respective time-dependent expectation values of the dipole moment:

$$|d(\omega)|^2 = \left| \frac{1}{T} \int_0^T \mu_e(t) e^{-i\omega t} dt \right|^2 \tag{3.35}$$

3.1.5 Results and discussion

A. Helium Atom

To model the electronic dynamics of a He atom in a strong laser field, we use a laser pulse with a wavelength of 456 nm (0.10 au) and an intensity of $I = 8.75 \times 10^{13}$ W/cm^2 ($|E|_{max} = 0.05$ au). The pulse duration T is set to 5 optical cycles, i.e. $T = 5 \times 2\pi t/\omega$. The polarization direction of the electric field is along the z-direction of the atomic coordinates. Figs. 3.1–3.3 show the time-evolution of the expectation values of the dipole $\langle z \rangle$, dipole velocity $\langle \dot{z} \rangle$, and dipole acceleration $\langle \ddot{z} \rangle$ calculated by TDHF equations and TDKS with BLYP and B3LYP xc functionals in both the LG and the VG. We consider three atom-centered Gaussian-type basis sets: the d-aug-cc-pVQZ basis with 62 basis functions, the aug-cc-pVTZ basis with 23 basis functions and the 6-311++G** basis with 7 basis functions for the He atom. Continuum functions are not included in all basis sets and the simulations are not intended to model ionization processes. The dipole velocity $\langle \dot{z} \rangle$ and dipole acceleration $\langle \ddot{z} \rangle$ are obtained by numerical differentiations of the time-dependent expectation values of the dipole. As can be seen from Fig. 3.1, with the largest d-aug-cc-pVQZ basis the dipole oscillations are nearly identical in both the LG and VG for all methods considered herein. Convergence is retained for TDHF for both the dipole velocity and dipole acceleration. For TDBLYP and TDB3LYP, there are small deviations near the end of the pulse duration. These small differences can be examined using the dipole acceleration, as indicated in panels 1(f) and 1(i). This discrepancy may be due to the use of finite grid points for the xc functionals, or the numerical differentiation error. Time-evolutions of dipole velocity and dipole acceleration are known to be more sensitive than the dipole moment to the choice of gauge.[94,95] Although TDBLYP and TDB3LYP show significant difference in the dipole

acceleration in the two gauges, the deviation is only on the order of <0.0005 a.u. and the overall oscillation patterns are similar. Note that this difference will become much smaller when a weaker field is used or the perturbative limit is approached. To further investigate gauge dependence upon incompleteness of the basis, we now present results for two smaller basis sets. Fig. 3.2 shows the results obtained using a smaller aug-cc-PVTZ basis. We note first that convergence of the dipole oscillations is still retained for all methods and the length gauge gives smooth oscillations of the dipole, dipole velocity and dipole acceleration. Unlike in the d-aug-cc-pVQZ basis, there is apparent discrepancy in both the dipole velocity and dipole acceleration of the two gauges. Moreover, the dipole acceleration in VG exhibits large-amplitude, high-frequency oscillations shortly after the beginning of the pulse and continue to oscillate after the passage of the pulse, which may be due to the basis incompleteness, or the error caused by numerical differentiation. Results for the smallest 6-311++G** basis are demonstrated in Fig. 3.3. It can be seen that now the amplitude of the dipole moment starts to deviate between the two gauges, although they seem to have the same oscillating frequency. Similar to the aug-cc-PVTZ basis, the dipole velocity and dipole acceleration in the two gauges are not converged and there are high-frequency oscillations in the dipole acceleration in VG.

B. CO molecule

For modeling CO in an electric field, a laser pulse with $\lambda = 456$ nm (0.10 au) and $I = 1.4 \times 10^{13}$ W/cm^2 is used and the pulse duration is set to 3 optical cycles . The direction of the polarization of the electric field is aligned along the C-O axis. The simulations are carried out with a fixed carbon-oxygen bond length of 1.1215 Å. In this study, we focus on the gauge behavior of the dipole oscillation as the size of basis set increases. Three atom-centered Gaussian-type basis sets, the 6-311++G** basis with 44 basis functions, the aug-cc-pVTZ basis with 92 basis functions and the d-aug-cc-pVQZ basis with 210 basis functions are investigated. Figs. 3.4–3.6 show the expectation values of the dipole and harmonic spectra calculated from TDHF, TDBLYP and TDB3LYP, respectively. The time-dependent dipole oscillations in LG and VG tends to converge as the size of the basis set increases. As indicated in Figs. 3.5 and 3.6, there is small discrepancy near the end

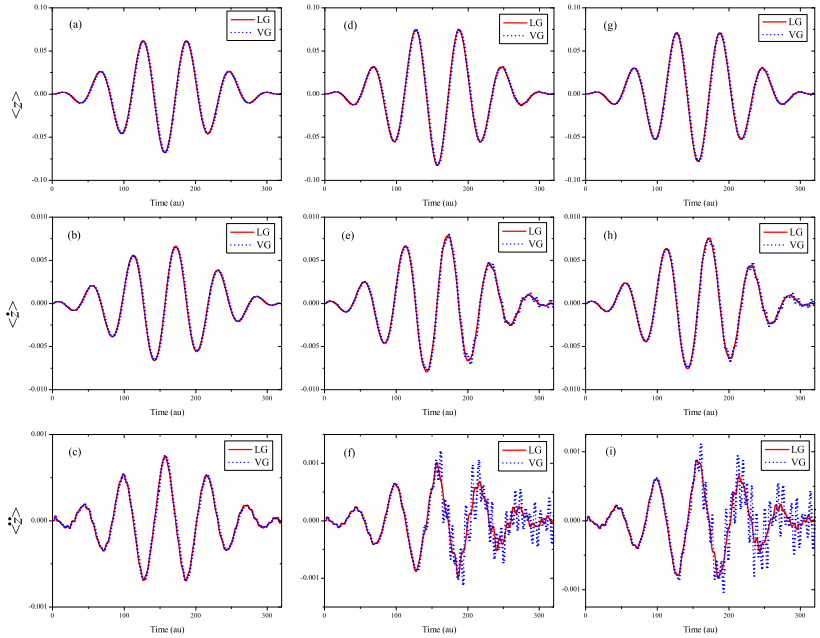

Figure 3.1: Time-dependent expectation values (in atomic units) of the dipole (first row panels), dipole velocity (second row panels) and dipole acceleration (third row panels) of the He atom in the basis of d-aug-cc-pVQZ, obtained from TDHF ((a)-(c)), TDBLYP ((d)-(f)), and TDB3LYP ((g)-(i)). The red solid and blue dashed lines refer to the length gauge (LG) and the velocity gauge (VG), respectively.

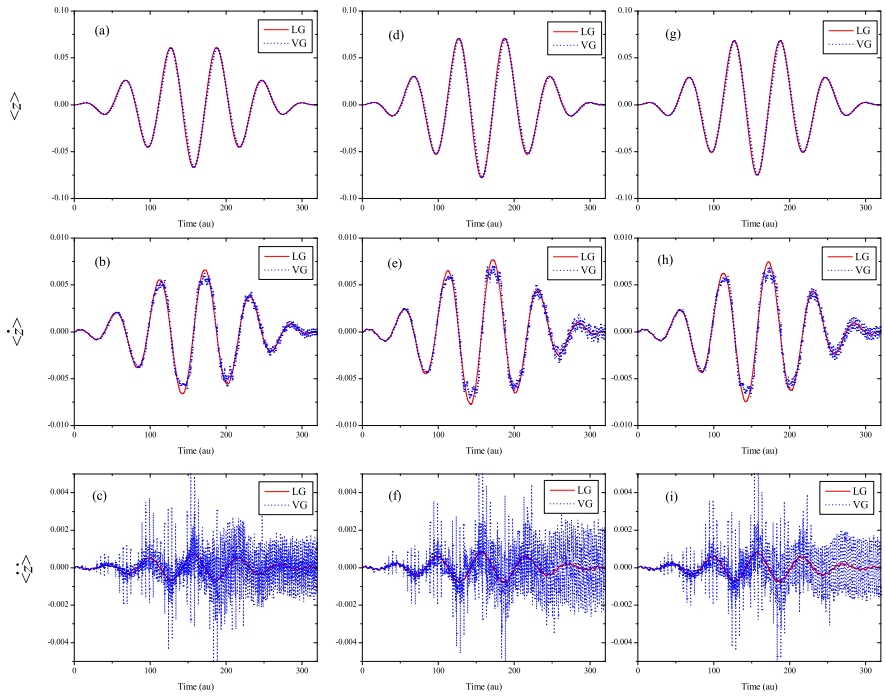

Figure 3.2: Same as Fig. 3.1, except that the results are obtained using aug-cc-pVTZ basis.

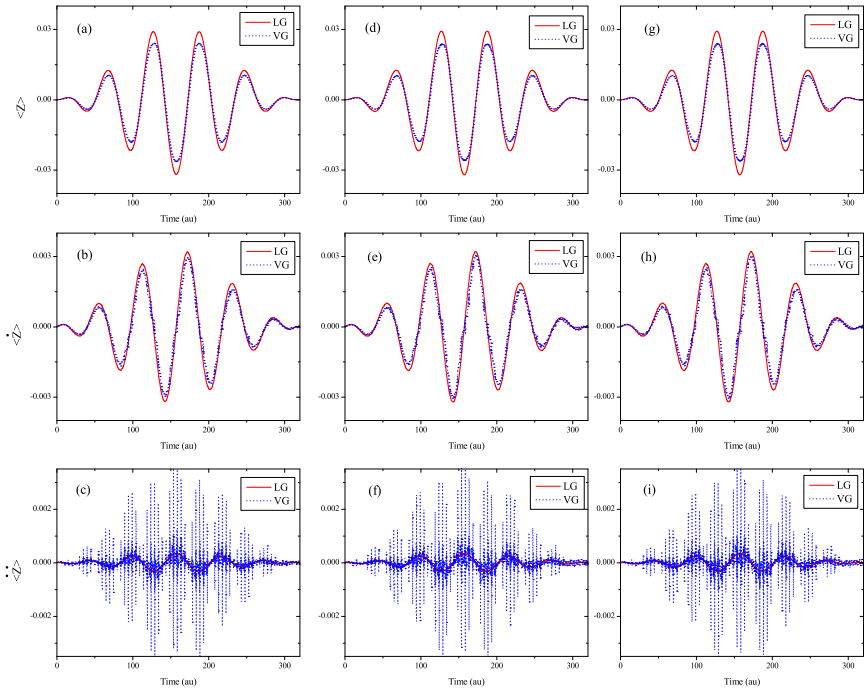

Figure 3.3: Same as Fig. 3.1, except that the results are obtained using 6-311++G** basis.

of the dipole oscillations for TDBLYP and TDB3LYP calculations, which again may be caused by the use of finite grid points for the xc functionals or the numerical differentiation error. The harmonic spectrum is a powerful tool in examining the gauge dependence in incomplete basis. For both TDHF and TDKS, the lower-order harmonic spectrum peaks (with frequency < 5 au) converge rapidly with the increase of basis size, while higher-order peaks are still unconverted even with the largest d-aug-cc-pVQZ basis. Since the amplitude of higher-order peaks are very small (usually $< 10^{-8}$), there are two possible causes of the deviations: (1) the incompleteness of the basis, and (2) the numerical noise from both simulation and data analysis.

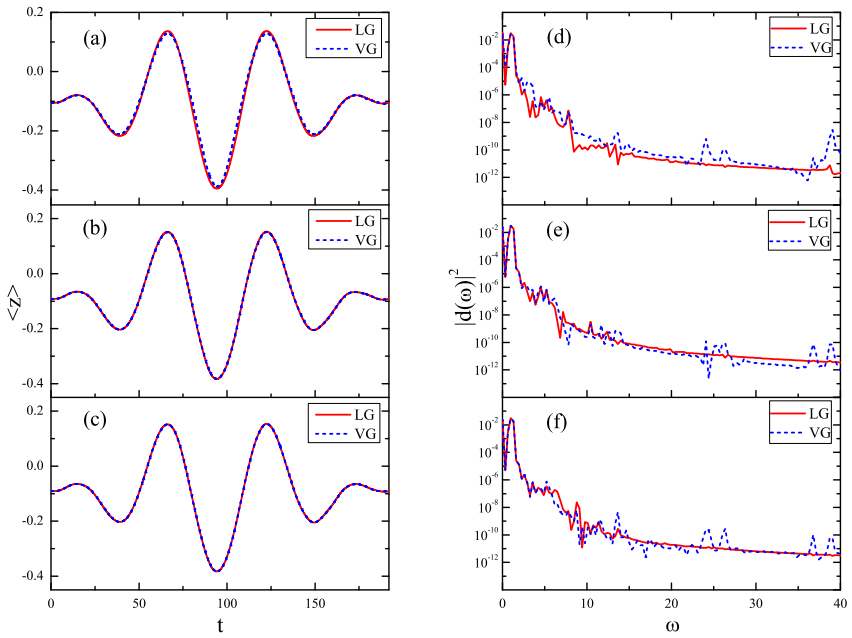

Figure 3.4: TDHF simulations of expectation values (in atomic units) of the dipole moment of the CO molecule in the basis of (a) 6-311++G**, (b) aug-cc-pVTZ, and (c) d-aug-cc-pVQZ, and the corresponding harmonic spectra (d)-(f). The red solid and blue dashed lines refer to the length gauge (LG) and the velocity gauge (VG), respectively.

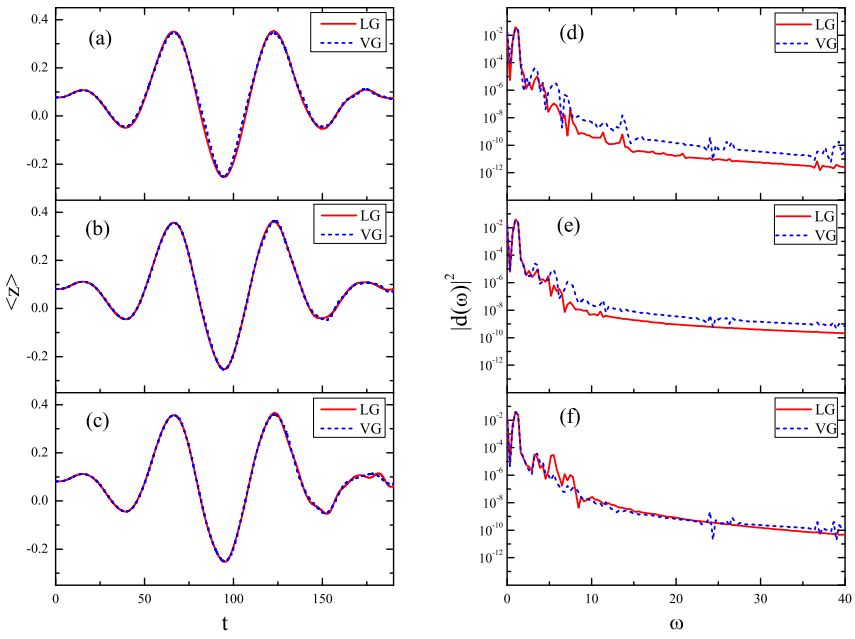

Figure 3.5: Same as Fig. 3.4, except that the results are obtained by TDBLYP simulation

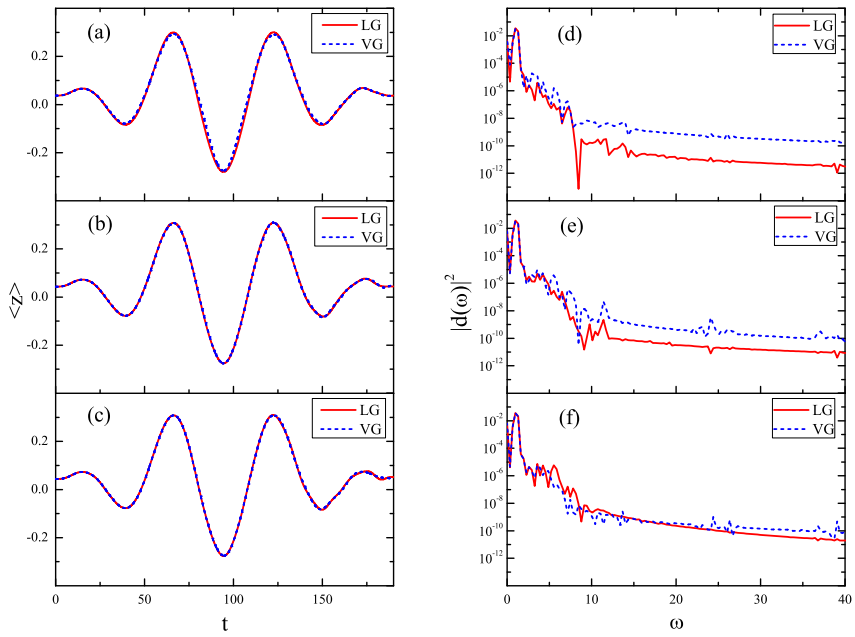

Figure 3.6: Same as Fig. 3.4, except that the results are obtained by TDB3LYP simulation

3.1.6 Conclusion

In this section, we have investigated the gauge-invariance properties of the time-dependent Hartree-Fock (TDHF) and the time-dependent Kohn-Sham (TDKS) theory with the adiabatic approximation for modeling many-body electronic dynamics in an electromagnetic field. The wavefunction solutions of the TDHF/TDKS equations in two different gauges are related by a unitary transformation. As a result, physical observables such as dipole moment and charge density are independent of the choice of gauge as well.

When an incomplete basis set is used for wavefunction expansion in practice, the gauge-invariance property of the TDHF/TDKS equations breaks down. Numerical simulations of TDHF and TDKS electronic dynamics were carried out to investigate the physical properties under gauge transformation in an incomplete basis. We used a helium atom and a carbon monoxide molecule interacting with strong linearly polarized electromagnetic fields as an example. For all methods considered herein, the length and velocity gauges tend to give identical electronic dynamics as the basis approaches completeness.

Appendix: Gauge invariance of the TDHF equations

We show herein the form invariance of the TDHF equations under gauge transformations. The proof is done by the *abduction* method: Consider the following unitary transformation of the solutions to the TDHF equations, Eq. (3.7) in section 2.2:

$$\phi'_k(\mathbf{r},t) = e^{-iT(\mathbf{r},t)}\phi_k(\mathbf{r},t) \tag{3.36}$$

where $T(\mathbf{r},t)$ is an abitrary differentiable real function of position $\mathbf{r}$ and time t.

Substituting Eq. (3.36) into the TDHF equations, the left hand side of Eq. (2.7) becomes

$$i\frac{\partial}{\partial t}\phi_k(\mathbf{r},t) = e^{iT(\mathbf{r},t)}\cdot\left\{-\frac{\partial T(\mathbf{r},t)}{\partial t}\phi'_k(\mathbf{r},t) + i\frac{\partial}{\partial t}\phi'_k(\mathbf{r},t)\right\} \tag{3.37}$$

The right hand side of Eq. (2.7) is

$$\hat{F}(\mathbf{r},t)\phi_k(\mathbf{r},t) = \left\{\frac{1}{2}[\mathbf{p}+\mathbf{A}(\mathbf{r},t)]^2 + V(\mathbf{r}) - U(\mathbf{r},t)\right\}\phi_k(\mathbf{r},t) + \left[\sum_j^N \int d\mathbf{r}' \frac{\phi_j^*(\mathbf{r}',t)\phi_j(\mathbf{r}',t)}{|\mathbf{r}-\mathbf{r}'|}\right]\phi_k(\mathbf{r},t) - \left[\sum_j^N \int d\mathbf{r}' \frac{\phi_j^*(\mathbf{r}',t)\phi_k(\mathbf{r}',t)}{|\mathbf{r}-\mathbf{r}'|}\right]\phi_j(\mathbf{r},t) \tag{3.38}$$

Note that $\mathbf{p} = -i\boldsymbol{\nabla}$ and does not generally commute with $T(\mathbf{r},t)$. Using Eq. (3.36), the first term of Eq. (3.38) becomes,

$$\begin{aligned}
&\left\{\frac{1}{2}[\mathbf{p}+\mathbf{A}(\mathbf{r},t)]^2 + V(\mathbf{r}) - U(\mathbf{r},t)\right\}\phi_k(\mathbf{r},t) \\
&= \frac{1}{2}[\mathbf{p}+\mathbf{A}(\mathbf{r},t)]\left\{e^{iT(\mathbf{r},t)}\,[\mathbf{p}+\mathbf{A}(\mathbf{r},t)+\boldsymbol{\nabla}T(\mathbf{r},t)]\phi_k'(\mathbf{r},t)\right\} \\
&\quad + \; e^{iT(\mathbf{r},t)}\cdot\Big[V(\mathbf{r}) - U(\mathbf{r},t)\Big]\phi_k'(\mathbf{r},t) \\
&= e^{iT(\mathbf{r},t)}\cdot\left\{\frac{1}{2}[\mathbf{p}+\mathbf{A}(\mathbf{r},t)+\boldsymbol{\nabla}T(\mathbf{r},t)]^2 + V(\mathbf{r}) - U(\mathbf{r},t)\right\}\phi_k'(\mathbf{r},t)
\end{aligned} \tag{3.39}$$

Since the unitary transformation defined in Eq. (3.36) applies to all single-particle wavefunctions, it is easy to show that in terms of the new wavefunctions ϕ_i' the second and third terms in Eq. (3.38) are

$$\left[\sum_j^N \int d\mathbf{r}' \frac{\phi_j^*(\mathbf{r}',t)\phi_j(\mathbf{r}',t)}{|\mathbf{r}-\mathbf{r}'|}\right]\phi_k(\mathbf{r},t) = e^{iT(\mathbf{r},t)}\cdot\left[\sum_j^N \int d\mathbf{r}' \frac{\phi_j'^*(\mathbf{r}',t)\phi_j'(\mathbf{r}',t)}{|\mathbf{r}-\mathbf{r}'|}\right]\phi_k'(\mathbf{r},t) \tag{3.40}$$

and

$$\left[\sum_j^N \int d\mathbf{r}' \frac{\phi_j^*(\mathbf{r}',t)\phi_k(\mathbf{r}',t)}{|\mathbf{r}-\mathbf{r}'|}\right]\phi_j(\mathbf{r},t) = e^{iT(\mathbf{r},t)}\cdot\left[\sum_j^N \int d\mathbf{r}' \frac{\phi_j'^*(\mathbf{r}',t)\phi_k'(\mathbf{r}',t)}{|\mathbf{r}-\mathbf{r}'|}\right]\phi_j'(\mathbf{r},t) \tag{3.41}$$

We can now rewrite the TDHF equations in terms of the new single-particle wavefunctions ϕ_k'. By collecting the terms in Eqs. (3.37), (3.39), (3.40) and (3.41) and rearrange-

ments, we obtain

$$
\begin{aligned}
i\frac{\partial}{\partial t}\phi'_k(\mathbf{r},t) &= \left\{\frac{1}{2}\big[\mathbf{p}+\mathbf{A}(\mathbf{r},t)+\boldsymbol{\nabla}T(\mathbf{r},t)\big]^2+V(\mathbf{r})\right\}\phi'_k(\mathbf{r},t) \\
&- \left[U(\mathbf{r},t)-\frac{\partial T(\mathbf{r},t)}{\partial t}\right]\phi'_k(\mathbf{r},t) \\
&+ \left[\sum_j^M \int d\mathbf{r}'\frac{\phi'^*_j(\mathbf{r}',t)\phi'_j(\mathbf{r}',t)}{|\mathbf{r}-\mathbf{r}'|}\right]\phi'_k(\mathbf{r},t) - \left[\sum_j^M \int d\mathbf{r}'\frac{\phi'^*_j(\mathbf{r}',t)\phi'_k(\mathbf{r}',t)}{|\mathbf{r}-\mathbf{r}'|}\right]\phi'_j(\mathbf{r},t) \\
&= \left\{\frac{1}{2}\big[\mathbf{p}+\mathbf{A}'(\mathbf{r},t)\big]^2+V(\mathbf{r})-U'(\mathbf{r},t)\right\}\phi'_k(\mathbf{r},t) \\
&+ \left[\sum_j^M \int d\mathbf{r}'\frac{\phi'^*_j(\mathbf{r}',t)\phi'_j(\mathbf{r}',t)}{|\mathbf{r}-\mathbf{r}'|}\right]\phi'_k(\mathbf{r},t) - \left[\sum_j^M \int d\mathbf{r}'\frac{\phi'^*_j(\mathbf{r}',t)\phi'_k(\mathbf{r}',t)}{|\mathbf{r}-\mathbf{r}'|}\right]\phi'_j(\mathbf{r},t)
\end{aligned}
\tag{3.42}
$$

where $\mathbf{A}'$ and U' are defined as

$$\mathbf{A}'(\mathbf{r},t) = \mathbf{A}(\mathbf{r},t)+\boldsymbol{\nabla}T(\mathbf{r},t) \tag{3.43a}$$

$$U'(\mathbf{r},t) = U(\mathbf{r},t)-\frac{\partial}{\partial t}T(\mathbf{r},t) \tag{3.43b}$$

Now it is clear that upon a gauge transformation of the electromagnetic potentials in Eqs. (3.43), the solutions to the TDHF equations can be related to the old ones by a unitary transformation described in Eq. (3.36) up to a constant phase factor $e^{i\,a}$.

3.2 Obtaining Molecular Nonlinear Optical Properties

In this section, we present a time-domain time-dependent density functional theory (TDDFT) approach to calculate frequency-dependent polarizability and hyperpolarizabilities. In this approach, the electronic degrees of freedom are propagated within the density matrix based TDDFT framework using the efficient modified midpoint and unitary transformation algorithm. We use monochromatic waves as external perturbations and apply the finite field method to extract various orders of the time-dependent dipole moment. By fitting each order of time-dependent dipole to sinusoidal waves with harmonic frequencies, one can obtain the corresponding (hyper)polarizability tensors. This approach avoids explicit Fourier transform and therefore does not require long simulation time. The method is illustrated with application to the optically active organic molecule *para*-nitroaniline, of which the frequency-dependent polarizability $\alpha(-\omega;\omega)$, second-harmonic generation $\beta(-2\omega;\omega,\omega)$, optical rectification $\beta(0;-\omega,\omega)$, third-harmonic generation $\gamma(-3\omega;\omega,\omega,\omega)$, and degenerate four-wave mixing $\gamma(-\omega;\omega,\omega,-\omega)$ are calculated.

3.2.1 Introduction

Materials with strong optical response characteristics have important applications in electro-optics and opto-electronics.[123–127] Recently, an increasing effort has been devoted to the design of π-conjugated organic materials because of their high performance as a result of relatively large susceptibilities. Because the microscopic (hyper)polarizabilities are closely related to the bulk susceptibilities of conjugated organic materials,[128] the computational design of organic nonlinear optical materials has focused on calculating polarizability and hyperpolarizabilities of single oriented molecules using *ab initio* quantum mechanical methods.

The static properties may be obtained using the finite field method[129–134] or the analytic derivative method.[135–139] The finite field method is based on a Taylor expansion of the total energy (or dipole moment) in powers of the external electric field. By calculating the energies (or dipole moments) of the molecule at various field strengths, one can obtain the static (hyper)polarizabilities using numerical differentiation. This method is easy to

implement and can be used at any level of theory. It requires a careful choice of field strengths and a high precision energy evaluation. The analytic derivative method calculates the derivatives of the total energy with respect to the static field directly and does not suffer from the numerical precision problems. So far both the finite field method and the analytic derivative method are mainly implemented for calculations of static properties.

Since experimental measurements of hyperpolarizabilities usually involve oscillating electric fields, it is of great importance to determine frequency-dependent properties theoretically. A widely used approach is the direct use of the sum-over-states (SOS) expressions[140] for the frequency-dependent (hyper)polarizabilities. Applications of the SOS method usually require accurate calculations for excited states and transition dipole moments, and thus involve the use of correlated wave function methods, such as configuration interaction[141] and coupled-cluster methods.[142]

Frequency-dependent (hyper)polarizabilities can also be obtained by an iterative solution of the coupled perturbed time-dependent Hartree-Fock (CP-TDHF)[143–145] or the time-dependent density functional theory (CP-TDDFT)[146–156] equations. These methods can be viewed as a generalization of the analytic derivative method to the frequency domain. The CP-TDHF/CP-TDDFT method is equivalent to the SOS method in the realm of single Slater determinant approaches.

In the CP-TDHF/TDDFT approach, a small, external time-dependent electric field is added to the effective single-particle Fock/KS Hamiltonian. This perturbation induces deviations of the single-particle wavefunctions from the unperturbed solutions. Using perturbation theory, the single-particle wavefunctions and Fock/KS operators are expanded in various orders of the electric field. Then the first order and higher order equations are obtained in which quantities with the same frequency dependence are taken together. The solution to these equations will yield the first and higher-order density matrices which are needed for the calculation of the frequency-dependent (hyper)polarizabilities.

The major drawback of CP-TDHF is the lack of electron correlations, which are usually crucial for an accurate determination of nonlinear response properties.[143] On the other hand, the CP-TDDFT method, which takes into account electron correlation, at least in an approximate way, has become a routine method for calculation of frequency-dependent

(hyper)polarizabilities. The equations used in CP-TDDFT are similar to those used in CP-TDHF. The major difference enters through the Fock/Kohn-Sham (KS) operator, where the Hartree-Fock (HF) exchange potential is replaced by an (approximate) exchange-correlation (xc) potential. This difference complicates the implementation of CP-TDDFT for higher order response calculations due to the difficulties in the evaluation of the functional derivatives. Furthermore, the CP-TDHF/CP-TDDFT fails at near-resonant frequencies due to the divergence of the response functions at resonant frequencies.[156]

Alternatively, one can integrate the TDDFT equations in the time domain. This approach has several advantages over the CP-TDDFT method. First of all, the time-domain approach is easier to implement since the evaluation of the functional derivatives is avoided. Second, it does not suffer from the divergence problem that arises in CP-TDDFT at resonant frequencies. Further, it provides a straightforward, meticulous elucidation on the real-time dynamics of the system subjected to a time-evolving field, which can lead to a wealth of useful information. The use of time-domain TDDFT for molecular electric responses has been put forward in several studies[157–161] which, however, were mainly focused on the linear response. The major difficulty of extracting nonlinear response properties from time-domain TDDFT is the presence of all orders of response in one time signal. Recently, calculations of first hyperpolarizabilities using time-domain TDDFT have been carried out by Chen *et al.*[156] and Rehr *et al.*[162] Upon a careful choice of the field strength, Chen *et al.*[156] succeeded in extracting the first hyperpolarizability tensor components using the filter diagonalization method.[163] Rehr *et al.*[162] applied the finite field method to the time domain and used Gaussian-enveloped external field together with the so-called quasimonochromatic approximation to obtain the second-order response properties.

We introduce a time-domain TDDFT approach that uses a monochromatic wave as the external perturbation and the finite field method to extract various orders of the time-dependent dipole response. The TDDFT equation is integrated using the modified midpoint and unitary transformation (MMUT) algorithm[43,44] within the density matrix based TDDFT scheme. By fitting each order of time-dependent dipole response to appropriate sinusoidal functions, one can obtain the corresponding hyperpolarizability tensors. This approach avoids explicit Fourier transforms and therefore does not require long simulation

time. Furthermore, our approach presents the first implementation of the time-domain TDDFT method for the calculation of third-order time-dependent properties.

3.2.2 Theory

The TDKS/TDHF equation in an orthonormal basis is given by:

$$i\frac{d\mathbf{P}(t)}{dt} = [\mathbf{K}(t), \mathbf{P}(t)] \tag{3.44}$$

where $\mathbf{P}(t)$ is the time-dependent density matrix.

Within the electric-dipole approximation, the time-dependent KS/Fock matrix $\mathbf{K}(t)$ in an external electric field $\mathbf{E}(t)$ is given by

$$\mathbf{K}(t) = \mathbf{K}_0(t) - \boldsymbol{\mu} \cdot \mathbf{E}(t) \tag{3.45}$$

where $\mathbf{K}_0(t)$ is the unperturbed KS/Fock matrix, and $\boldsymbol{\mu}$ is the dipole matrix in the length form.[14]

The TDKS/TDHF equation, Eq. (3.44) is integrated with a modified midpoint and unitary transformation (MMUT) algorithm.[43,44] In the MMUT method, the time-evolution operator is a unitary transformation matrix $\mathbf{U}(t_n)$ that is constructed from the eigenvectors $\mathbf{C}(t_n)$ and eigenvalues $\boldsymbol{\epsilon}(t_n)$ of the Kohn-Sham/Fock matrix at time t_n:

$$\mathbf{C}^\dagger(t_n) \cdot \mathbf{K}(t_n) \cdot \mathbf{C}(t_n) = \boldsymbol{\epsilon}(t_n) \tag{3.46}$$

$$\begin{aligned}\mathbf{U}(t_n) &= \exp\big[i \cdot 2\Delta t \cdot \mathbf{K}(t_n)\big] \\ &= \mathbf{C}(t_n) \cdot \exp\big[i \cdot 2\Delta t \cdot \boldsymbol{\epsilon}(t_n)\big] \cdot \mathbf{C}^\dagger(t_n)\end{aligned} \tag{3.47}$$

where Δt is the time step. The density matrix is then propagated from time t_{n-1} to t_{n+1} using the time-evolution operator $\mathbf{U}(t_n)$:

$$\mathbf{P}(t_{n+1}) = \mathbf{U}(t_n) \cdot \mathbf{P}(t_{n-1}) \cdot \mathbf{U}^\dagger(t_n) \tag{3.48}$$

The time-dependent expectation value of of the electric dipole moment or the optical

polarization, $\boldsymbol{\mu}(t)$, is calculated using Eq. (3.49)

$$\boldsymbol{\mu}(t) = -\mathrm{Tr}\,[\boldsymbol{\mu}\mathbf{P}(t)] \tag{3.49}$$

At any given time, the time-dependent dipole moment can be Taylor-expanded to all orders of response,[164]

$$\begin{aligned}\mu_i(t) = \mu_i^0 &+ \sum_j \int_{-\infty}^{+\infty} dt_1 \alpha_{ij}(t-t_1) E_j(t_1) \\ &+ \frac{1}{2!}\sum_{jk} \iint_{-\infty}^{+\infty} dt_1 dt_2 \beta_{ijk}(t-t_1, t-t_2) E_j(t_1) E_k(t_2) \\ &+ \frac{1}{3!}\sum_{jkl} \iiint_{-\infty}^{+\infty} dt_1 dt_2 dt_3 \gamma_{ijkl}(t-t_1, t-t_2, t-t_3) E_j(t_1) E_k(t_2) E_l(t_3) \\ &+ \cdots\end{aligned} \tag{3.50}$$

where i, j, k are Cartesian coordinates x, y, or z. μ_i^0 is the permanent dipole moment in the absence of the external field. $\alpha(t-t_1)$, $\beta(t-t_1, t-t_2)$ and $\gamma(t-t_1, t-t_2, t-t_3)$ are time-domain response functions of first, second and third order, respectively, which are equivalent to widely used response properties in the frequency domain, known as frequency-dependent (hyper)polarizabilities.

We consider an electronic system interacting with a time-dependent external monochromatic field,

$$\mathbf{E}(t) = \mathbf{A}\cos(\omega t) \tag{3.51}$$

where ω is the frequency and $\mathbf{A}$ the constant magnitude vector of the field. Embedded in Eq. (3.51) is a Fourier component of $\cos(\omega t)$, which implicitly encodes frequency-dependent information in the time-domain. Upon observing this property of the external field of choice,

Eq. (3.50) is rearranged to obtain,

$$\begin{aligned}\mu_i(t) = \mu_i^0 &+ \sum_j \alpha_{ij}(-\omega;\omega)\cos(\omega t)A_j \\ &+ \frac{1}{4}\sum_{jk}\left\{\beta_{ijk}(-2\omega;\omega,\omega)\cos(2\omega t) + \beta_{ijk}(0;\omega,-\omega)\right\}A_jA_k \\ &+ \frac{1}{24}\sum_{jkl}\left\{\gamma_{ijkl}(-3\omega;\omega,\omega,\omega)\cos(3\omega t) + 3\bar{\gamma}_{ijkl}(-\omega;\omega,\omega,-\omega)\cos(\omega t)\right\}A_jA_kA_l \\ &+ \cdots \end{aligned} \tag{3.52}$$

where $\alpha(-\omega;\omega)$ is the frequency-dependent polarizability and is related to the linear refractive index; $\beta(-2\omega;\omega,\omega)$ and $\beta(0;\omega,-\omega)$ are the frequency-dependent first hyperpolarizabilities, which are related to the second-harmonic generation (SHG) and optical rectification (OR), respectively; $\gamma(-3\omega;\omega,\omega,\omega)$ and $\gamma(-\omega;\omega,\omega,-\omega)$ are the frequency-dependent second hyperpolarizabilities, which are related to the third-harmonic generation (THG) and degenerate four-wave mixing (DFWM) coefficient.

$\bar{\gamma}_{ijkl}(-\omega;\omega,\omega,-\omega)$ is the averaged DFWM coefficient and is expressed as

$$\bar{\gamma}_{ijkl}(-\omega;\omega,\omega,-\omega) = \frac{1}{3}\left[\gamma_{ijkl}(-\omega;\omega,\omega,-\omega) + \gamma_{ijkl}(-\omega;\omega,-\omega,\omega) + \gamma_{ijkl}(-\omega;-\omega,\omega,\omega)\right] \tag{3.53}$$

Equation (3.52) implies that in the presence of a monochromatic wave, the time-dependent dipole can be expressed as a sum of sinusoidal waves of resonant frequencies and the magnitude of each frequency component corresponds to the (hyper)polarizability tensors. This equation is similar in spirit to the dipole expansion in the frequency-domain, but is directly related to the dipole moment in the time-domain. In principle, one can extract all components of the (hyper)polarizability tensors from only one or a few simulations, given that the simulation is exact and a highly accurate analysis method is used. However, it is particularly difficult to resolve high-order responses using standard signal processing techniques, because the high-order terms in the Taylor expansion are usually several orders smaller in magnitude than the linear response. In addition, because several terms in Eq. (3.52), such as the polarizability $\alpha(-\omega;\omega)$ and the DFWM $\bar{\gamma}(-\omega;\omega,\omega,-\omega)$ are associated with the same

Fourier component $\cos(\omega t)$, different orders of time-dependent dipole response need to be separated for analysis.

In the current approach, we apply the finite field method to the time-domain calculations and extract the frequency-dependent dipole responses. The (hyper)polarizability tensor components are determined from a least-squares fitting to the corresponding time-domain signals. To achieve this, Eq. (3.52) is rewritten as

$$\mu_i(t) = \mu_i^0 + \sum_j \mu_{ij}^{(1)}(t) A_j + \sum_{jk} \mu_{ijk}^{(2)}(t) A_j A_k + \sum_{jkl} \mu_{ijkl}^{(3)}(t) A_j A_k A_l + \cdots \tag{3.54}$$

where

$$\mu_{ij}^{(1)}(t) = \alpha_{ij}(-\omega;\omega)\cos(\omega t) \tag{3.55}$$

$$\mu_{ijk}^{(2)}(t) = \frac{1}{4}\left[\beta_{ijk}(-2\omega;\omega,\omega)\cos(2\omega t) + \beta_{ijk}(0;\omega,-\omega)\right] \tag{3.56}$$

$$\mu_{ijkl}^{(3)}(t) = \frac{1}{24}\left[\gamma_{ijkl}(-3\omega;\omega,\omega,\omega)\cos(3\omega t) + 3\bar{\gamma}_{ijkl}(-\omega;\omega,\omega,-\omega)\cos(\omega t)\right] \tag{3.57}$$

$\mu_{ij}^{(1)}(t)$, $\mu_{ijk}^{(2)}(t)$, and $\mu_{ijkl}^{(3)}(t)$ are time-dependent optical responses which encode frequency-dependent responses. They can be obtained by time-domain electronic dynamics simulations at various (small) field strengths. Using the finite field method,[129–134] the first, second and third-order time-dependent dipole responses $\mu_{ij}^{(1)}(t)$, $\mu_{ijj}^{(2)}(t)$ and $\mu_{ijjj}^{(3)}(t)$ are determined as

$$\mu_{ij}^{(1)}(t) = \frac{2}{3A_j}\left[\mu_i(t,A_j) - \mu_i(t,-A_j)\right] - \frac{1}{12A_j}\left[\mu_i(t,2A_j) - \mu_i(t,-2A_j)\right] + \mathcal{O}(A_j^4) \tag{3.58}$$

$$\mu_{ijj}^{(2)}(t) = \frac{2}{3A_j^2}\left[\mu_i(t,A_j) + \mu_i(t,-A_j)\right] - \frac{1}{24A_j^2}\left[\mu_i(t,2A_j) + \mu_i(t,-2A_j)\right] - \frac{5}{4A_j^2}\mu_i^0 + \mathcal{O}(A_j^4) \tag{3.59}$$

$$\mu_{ijjj}^{(3)}(t) = -\frac{13}{48A_j^3}\left[\mu_i(t,A_j) - \mu_i(t,-A_j)\right] + \frac{1}{6A_j^3}\left[\mu_i(t,2A_j) - \mu_i(t,-2A_j)\right] - \frac{1}{48A_j^3}\left[\mu_i(t,3A_j) - \mu_i(t,-3A_j)\right] + \mathcal{O}(A_j^4) \tag{3.60}$$

where $\mu_i(t,\pm A_j)$, $\mu_i(t,\pm 2A_j)$ or $\mu_i(t,\pm 3A_j)$ are the i-th component of the time-dependent dipole moment when a cosine field with strength of A_j, $2A_j$ or $3A_j$ in the $\pm j$-th direction

is applied.

As suggested by Eqs. (3.55)–(3.57), the frequency dependent (hyper)polarizabilities are encoded in these time-dependent optical responses to a monochromatic field. Given the time-dependent signals of different orders of dipole response in Eqs. (3.58)–(3.60), many signal processing technique can be used to resolve the (hyper)polarizabilities. In this section, we use a least-squares wave fitting to extract the frequency-dependent response properties from the time-dependent form:

- The polarizability $\alpha(-\omega;\omega)$ is determined by fitting the time signal $\mu^{(1)}(t)$ calculated using Eq. (3.58) to a cosine wave with a fixed frequency of ω. According to Eq. (3.55), the amplitude of the fitted cosine wave is the $\alpha(-\omega;\omega)$ term.

- The first hyperpolarizabilities $\beta(-2\omega;\omega,\omega)$ and $\beta(0;\omega,-\omega)$ are calculated by fitting the time signal $\mu^{(2)}(t)$ obtained using Eq. (3.59) to a shifted cosine wave with a fixed frequency of 2ω. According to Eq. (3.56), the amplitude and the offset (shift) of the fitted cosine wave are directly related to $\beta(-2\omega;\omega,\omega)$ and $\beta(0;\omega,-\omega)$, respectively.

- The second hyperpolarizabilities $\gamma(-3\omega;\omega,\omega,\omega)$ and $\bar{\gamma}(-\omega;\omega,\omega,-\omega)$ can be obtained by fitting the time signal $\mu^{(3)}(t)$ computed using Eq. (3.60) to a superposition of two cosine waves with frequencies of 3ω and ω. According to Eq. (3.57), the amplitudes of the two fitted cosine waves correspond to $\gamma(-3\omega;\omega,\omega,\omega)$ and $\bar{\gamma}(-\omega;\omega,\omega,-\omega)$

In this approach, no explicit Fourier transform is required. The following numerical tests show that a simulation time of no more than four cycles of the incident wave is enough for a reliable fitting and increasing the simulation time does not give much improvement on the accuracy. The computational cost for the time-domain approach formally scales as $\mathcal{O}(mN^4)$, where N is the number of basis functions and m the number of simulation steps. With linear scaling techniques, the RT-TDDFT method can be reduced to nearly linear scaling $\mathcal{O}(mN)$.[165] The linear response TDDFT equations for calculations of (hyper)polarizabilities using the sum-of-state technique formally scales as $\mathcal{O}(N^6)$, which can be reduced to $\mathcal{O}(N^{2-4})$ using iterative eigensolver.[166,167] For calculations of lower order response properties, the

large prefactor (number of time-integration steps) dominates the computational cost, and therefore the RT-TDDFT is not necessarily computationally cost effective. Although the overall scaling does not increase when higher order properties are concerned, the prefactor of the computational scaling using the RT-TDDFT method does not increase as the order of response property increases, whereas it increases significantly for the CP-TDDFT method. As a result, we expect the RT-TDDFT method will become more advantageous in terms of computational cost as the order of response properties increases.

3.2.3 Results and Discussion

Integration of the TDDFT equation with the modified mid-point and unitary transformation (MMUT) algorithm, as well as the calculation of frequency-dependent hyper-polarizabilities using the finite field method are implemented in the development version of GAUSSIAN program.[122] The B3LYP functional is used to construct the adiabatic TDDFT exchange-correlation potential. Although there are general concerns regarding the accuracy of the B3LYP method for dipole moments and hyperpolarizabilities,[168,169] a recent study has shown that the B3LYP method is reliable for chromophores with fewer than six single-double bond pairs,[170–172] and has also shown consistent assessment of relative properties of similar chromophore systems. In addition, a basis set with diffuse functions is recommended for studies of non-linear optical properties. In this section, we also include calculations and comparisons using range-separated HSE1PBE functional[173,174] and the time-dependent Hartree-Fock. To test the performance of our time-domain method, we calculate the frequency-dependent (hyper)polarizabilities, α, β and γ tensors of a test molecule, at the incident field frequencies of 0.0428 a.u. ($\lambda = 1064$ nm) and 0.0656 a.u. ($\lambda = 695$ nm). The 6-31G(d) basis set is used for all calculations. To further test the basis set effect, we have also tested the 6-31+G(d) basis, where one additional set of *sp* diffuse functions are added to the 6-31G(d) basis, and the aug-cc-pVDZ basis. A time step of 50 a.u. (0.0012 fs) and a total propagation time of 4 cycles of the incident field are used in the time domain TDDFT simulations. Results are compared with those obtained from an analytical solution of the CP-TDDFT equations at the same geometries and level of theories.

Table 3.1: Frequency-dependent (hyper)polarizabilities (a.u.) of pNA.

		$\omega = 0.0428$ a.u.		$\omega = 0.0656$ a.u.	
		Time Domain	Frequency Domain	Time Domain	Frequency Domain
			6-31G(d)		
$\alpha(-\omega;\omega)$	α_{xx}	143.82	143.59	152.08	151.43
	α_{yy}	90.58	90.55	92.02	91.97
	α_{zz}	29.54	29.53	29.62	29.62
$\beta(0;\omega,-\omega)$	β_{xxx}	1755.39	1709.13	2415.62	2149.37
	β_{xyy}	-136.40	-140.82	-151.55	-142.02
	β_{xzz}	-3.66	-4.85	-4.91	-5.03
	β_{zxx}	47.18	46.69	56.85	54.01
	β_{zzz}	0.95	0.97	1.01	1.02
$\beta(-2\omega;\omega,\omega)$	β_{xxx}	2602.56	2442.47	8010.35	8157.06
	β_{xyy}	189.24	198.77	-540.99	-544.38
	β_{xzz}	-5.96	-6.08	-12.53	-13.11
	β_{zxx}	58.19	56.14	119.85	121.43
	β_{zzz}	1.04	1.05	1.20	1.19
$\bar{\gamma}(-\omega;\omega,\omega,-\omega)$	$\bar{\gamma}_{xxxx}$	117000.81		378965.51	
	$\bar{\gamma}_{zxxx}$	1047.77		4449.24	
	$\bar{\gamma}_{xzzz}$	-27.80		-38.90	
	$\bar{\gamma}_{zzzz}$	42.71		44.88	
$\gamma(-3\omega;\omega,\omega,\omega)$	γ_{xxxx}	428557.48		-735195.83	
	γ_{zxxx}	4267.92		-3154.79	
	γ_{xzzz}	-70.85		-19.87	
	γ_{zzzz}	47.17		69.11	
			6-31+G(d)		
$\alpha(-\omega;\omega)$	α_{xx}	161.29	161.21	171.48	171.41
	α_{yy}	100.77	100.74	102.63	102.59
	α_{zz}	51.04	51.02	51.53	51.52
$\beta(0;\omega,-\omega)$	β_{xxx}	2307.22	2279.72	2946.86	2934.58
	β_{xyy}	-150.25	-150.76	-155.57	-153.79
	β_{xzz}	-70.99	-73.44	-75.55	-78.08
	β_{zxx}	28.89	28.21	36.10	35.35
	β_{zzz}	16.36	17.03	17.50	17.91
$\beta(-2\omega;\omega,\omega)$	β_{xxx}	3399.84	3390.17	17052.53	16151.70
	β_{xyy}	-225.03	-221.60	-898.13	-855.51
	β_{xzz}	-88.42	-82.55	-239.89	-239.51
	β_{zxx}	42.49	41.94	209.05	195.84
	β_{zzz}	1.04	1.05	1.20	1.19
$\bar{\gamma}(-\omega;\omega,\omega,-\omega)$	$\bar{\gamma}_{xxxx}$	177517.45		912461.54	
	$\bar{\gamma}_{zxxx}$	1760.36		10084.76	
	$\bar{\gamma}_{xzzz}$	-365.04		-496.73	
	$\bar{\gamma}_{zzzz}$	12866.28		14926.49	
$\gamma(-3\omega;\omega,\omega,\omega)$	γ_{xxxx}	941148.58		-1505440.00	
	γ_{zxxx}	12512.18		-82758.97	
	γ_{xzzz}	-587.20		-3120.25	
	γ_{zzzz}	14918.44		22774.66	

Based on the finite field expressions, Eqs. (3.58)–(3.60), we apply electric fields with strengths $\pm A$, $\pm 2A$ and $\pm 3A$ to obtain time-dependent dipole moment of a molecular system. As in any application using the finite difference technique, the choice of the field requires scrutiny. If the field strength is too weak, numerical error can be drastically amplified for higher order properties. On the other hand, if the perturbation strength is too large, the numerical truncation error can become dominant and electronic nonadiabaticity can also affect the dynamics. As a result, the finite difference approach fails. We have tested several different field strengths ranging from 0.0005 a.u. to 0.005 a.u., and we find that a unit field strength A of 0.002 a.u. gives the best fit to the time signal for the case studied here (see Appendix for detailed discussion). The electric field is applied along each of the three axes and the time-dependent dipole moment is evaluated at each time step. The monochromatic electric field is turned on with a linear ramping envelop:

$$\mathbf{E}(t) = \begin{cases} \frac{\omega t}{2\pi}\mathbf{A}\cos(\omega t) & 0 \leqslant t < \frac{2\pi}{\omega} \\ \mathbf{A}\cos(\omega t) & t \geqslant \frac{2\pi}{\omega} \end{cases} \tag{3.61}$$

We choose pNA (Fig. 3.7) as a test molecule to showcase the performance of the method introduced herein. The pNA molecule is a prototype test case because it has a large first hyperpolarizability and has been widely used for theoretical studies.[134,146,149,154,170] In this study, the molecule is first optimized at the B3LYP/6-31G(d) level of theory, and is then placed in the xy-plane of a fixed Cartesian coordinate system, with its largest dipole component aligned with the x axis. We have computed the time-domain first, second, and third-order dipole responses of pNA at the two incident frequencies $\omega = 0.0428$ a.u. and 0.0656 a.u., using both 6-31G(d) and 6-31+G(d) basis sets. The finite field expressions, Eqs. (3.58)–(3.60), are employed to extract time signals from calculations of the dipole moments at different field strengths. As the main features of the time signals do not change significantly with the incident frequencies and basis sets, we only present in Figs. 3.8–3.10 the time-evolution of the time-dependent optical responses for the incident frequency of $\omega = 0.0428$ a.u. using 6-31G(d) basis. Note that in the least-squares fitting process, the first period of time-evolution is ignored because of the linear ramping of the incident field

during the turn-on period. For the calculated frequency-dependent (hyper)polarizability tensors using Eqs. (3.55)–(3.57), we list in Tab. 1 the results for both incident frequencies and the two basis sets used.

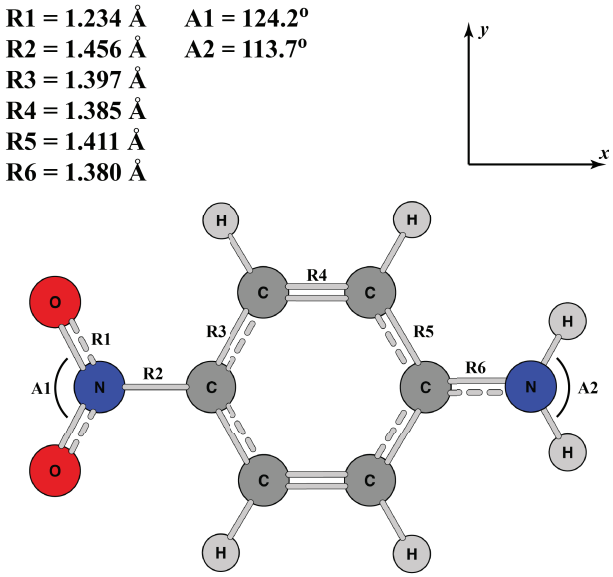

Figure 3.7: Optimized structure of pNA at the B3LYP/6-31G(d) level of theory and the Cartesian axes.

Figure 3.8 shows the diagonal elements of the first-order (linear) dipole responses $\mu_{ii}^{(1)}(t)$ and the least-squares fittings of the real-time signals to the analytical expression given in Eq. (3.55). The polarizability tensors, $\alpha_{ii}(-\omega;\omega)$, are extracted from the fittings and are compared to the CP-TDDFT results, listed in Tab. 1. The two approaches yield almost identical results for the polarizability tensor.

Figure 3.9 displays the xxx, zxx, and xzz components of the time-domain second-order dipole responses. The fitted curves using Eq. (3.56) are in good agreement with the real-time signals which feature shifted sinusoidal oscillations at twice the incident frequency. There are noticeable small deviations of the truncated analytical expression from the RT-TDDFT simulations. The deviation pattern, as characterized by high-frequency oscillations, appear in all nonlinear time signals obtained at the two selected incident frequencies. This

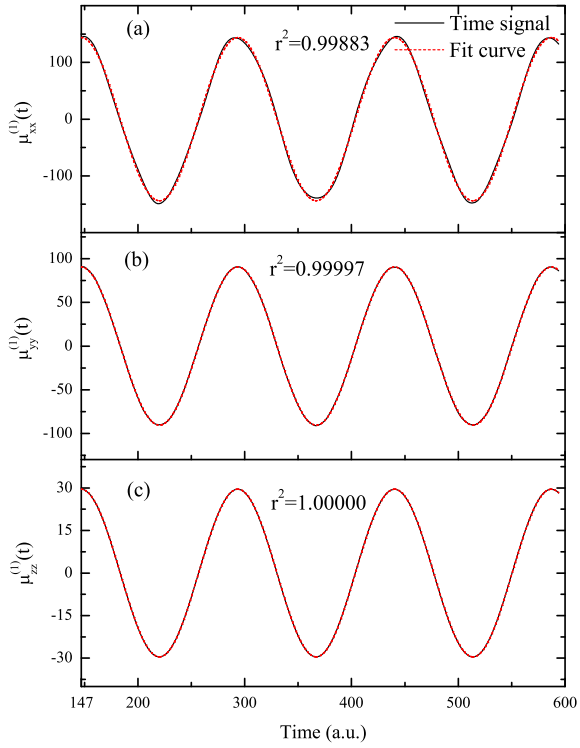

Figure 3.8: Time evolution of the first-order dipole responses, $\mu_{ii}^{(1)}(t)$.

phenomenon arises from the absence of higher-order corrections in the analytical expressions. Although reducing the field strength could in principle lead to a smaller truncation error and a better agreement, it will also give rise to a larger numerical error using the finite field approach. The choice of a unit field strength A of 0.002 a.u. in our tests seems to be a good compromise for these errors under consideration.

Table 1 lists the values of selected β components computed using the time-domain method introduced here and compared with the CP-TDDFT results. The results from the time-domain method are in excellent agreement with analytical CP-TDDFT approach.

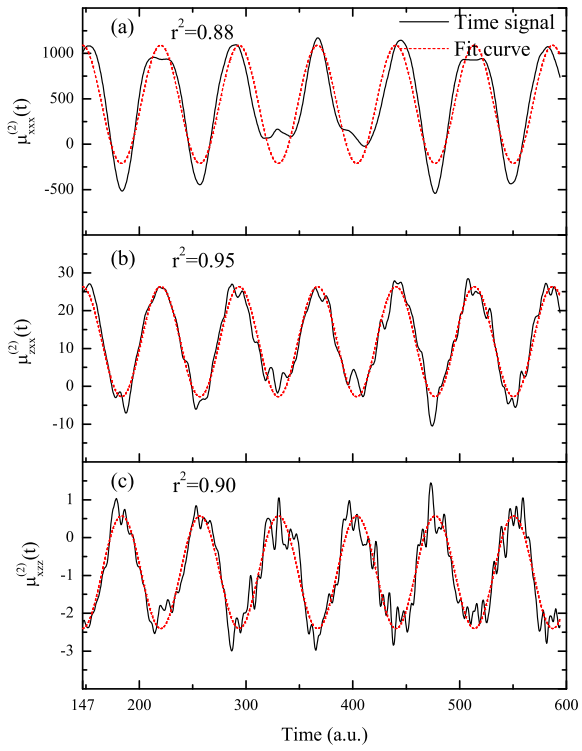

Figure 3.9: Time evolution of some second-order dipole responses, $\mu^{(2)}_{ijj}(t)$.

Figure 3.10 shows the dominant component of the third-order response, γ_{xxxx}, which is at least two orders in magnitude larger than the second largest component, γ_{zxxx}. As Fig. 3.10 suggests, the agreement between the time signal and the truncated analytical expression in

Eq. (3.57) is reasonably good with $r^2 = 0.72$. Two kinds of second hyperpolarizability tensors, i.e. the third-harmonic generation (THG) $\gamma(-3\omega;\omega,\omega,\omega)$, and degenerate four-wave mixing (DFWM) $\gamma(-\omega;\omega,\omega,-\omega)$ can be extracted from the curve fitting. Table 1 lists the calculated $xxxx$ as well as three other components of the second hyperpolarizability tensors. Due to the complexity of the implementation, the CP-TDDFT calculations for $\gamma(-3\omega;\omega,\omega,\omega)$ and $\gamma(-\omega;\omega,\omega,-\omega)$ are not widely available in electronic structure packages. Therefore, direct comparison of our time-domain values with the CP-TDDFT results is not available.

Table 1 also shows the results obtained at a different incident frequency, $\omega = 0.0656$ a.u. ($\lambda = 695$ nm). The time-domain results are consistent with those computed from CP-TDDFT. It is also interesting to observe the frequency dependence of the polarizability and hyperpolarizabilities: there is a significant increase in the values of most components. For example, the xxx component of the SHG $\beta(-2\omega;\omega,\omega)$ increases by a factor of ~ 2 when the frequency of the incident field goes from 0.0428 a.u. ($\lambda = 1064$ nm) to 0.0656 a.u.($\lambda = 695$ nm).

The accuracy of computed (hyper)polarizability tensors is known to be sensitive to the quality of basis set of choice.[170] To verify the quality of the time-domain approach, we have carried out calculations using the 6-31+G(d) basis with one additional set of *sp* diffuse functions, and the results are listed in Tab. 1. Compared to the results obtained using 6-31G(d) basis, a better agreement can be found between the time-domain method and the CP-TDDFT for the first hyperpolarizabilities $\beta(-2\omega;\omega,\omega)$ and $\beta(0;-\omega,\omega)$. Furthermore, we note that the addition of the diffuse functions leads to a significant change of the calculated polarizability and the hyperpolarizabilities.

Since the approach introduced here does not require functional derivatives, we can easily apply it to complex density functionals such as the range-separated HSE1PBE hybrid functional, and the time-dependent Hartree-Fock. We also extend our test to the use of the aug-cc-pVDZ basis, which was shown to perform as well as the much larger aug-cc-pVTZ basis in the polarizability calculations.[175] Section 3.2.3 lists the x-components of the (hyper)polarizability tensors obtained from the time-domain TDDFT (B3LYP and HSE1PBE) and TDHF, at the field frequency $\omega = 0.0428$ a.u., compared to previously obtained results

Table 3.2: Comparison of the x-components of the tensors obtained from the time-domain TDDFT (B3LYP and HSE1PBE) and TDHF, at the field frequency $\omega = 0.0428$ a.u..

	B3LYP/6-31G(d)	B3LYP/6-31+G(d)	B3LYP/aug-cc-pVDZ
$\alpha_{xx}(-\omega;\omega)$	143.82	161.29	167.81
$\beta_{xxx}(0;\omega,-\omega)$	1748.32	2307.22	2118.81
$\beta_{xxx}(-2\omega;\omega,\omega)$	2601.88	3399.84	3147.40
$\bar{\gamma}_{xxxx}(-\omega;\omega,\omega,-\omega)$	117000.81	177517.45	175905.19
$\gamma_{xxxx}(-3\omega;\omega,\omega,\omega)$	428557.48	941148.58	932821.06
	HSE1PBE/aug-cc-pVDZ	HF/aug-cc-pVDZ	
$\alpha_{xx}(-\omega;\omega)$	165.91	141.11	
$\beta_{xxx}(0;\omega,-\omega)$	2065.14	1178.64	
$\beta_{xxx}(-2\omega;\omega,\omega)$	3096.81	1444.73	
$\bar{\gamma}_{xxxx}(-\omega;\omega,\omega,-\omega)$	179849.99	93894.64	
$\gamma_{xxxx}(-3\omega;\omega,\omega,\omega)$	789528.41	189329.60	

using the smaller 6-31G(d) and 6-31+G(d) basis. As suggested by Sec. 3.2.3, the 6-31G(d) basis underestimates all orders of response properties and the deviation becomes larger for higher-order responses. Surprisingly, the results using the 6-31+G(d) basis are comparable to those obtained using the larger aug-cc-pVDZ basis. Section 3.2.3 also shows that the range-separated HSE1PBE yields similar (hyper)polarizabilities compared to the B3LYP results. As expected, the TDHF method gives poor predictions of all the response properties, due to the lack of electron correlations.

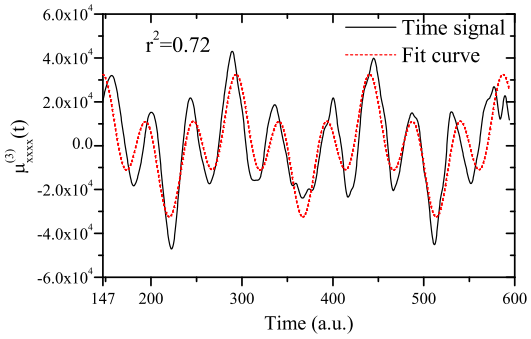

Figure 3.10: Time evolution of the dominant component of the third-order dipole responses, $\mu^{(3)}_{xxxx}(t)$.

3.2.4 Conclusions

In this section we presented a time-domain TDDFT method for an efficient and accurate calculation of the frequency-dependent polarizability and hyperpolarizabilities. This approach is completely done in the time-domain. It avoids explicit Fourier transform by taking advantage of the implicit Fourier component in the monochromatic electric field perturbation. We have derived analytical equations for time-dependent (hyper)polarizabilities that implicitly encode frequency-dependent components. Using the finite field method and least-squares curve fitting, we are able to resolve the frequency-dependent (hyper)polarizabilities directly from time-domain TDDFT electronic dynamics without Fourier transformation. The method has been applied to the calculations of the frequency-dependent polarizability (α), first hyperpolarizability (β) and second hyperpolarizability (γ) tensors for pNA. The results are in good agreement with those obtained from analytical solutions using the CP-TDDFT equations. The advantage of this method lies in that it does not require long simulation time and the integration method is rather efficient. In addition, it does not require implementation of analytically complex second- or third-derivatives.

Appendix: Finite Difference Method for Time-Dependent Dipole Response

Several applications using the finite difference method for calculations of static hyperpolarizabilities with a constant field have been presented by various research groups[129–134] and they differ by the truncation error that is resulted from the number of applied fields. In this section, we apply the finite difference method to analyze dynamical (hyper)polarizabilities where the frequency-dependent perturbation is an oscillatory field.

When a monochromatic field (Eq. (3.51)) with strength $\pm mA$ ($m = 0, 1, 2, 3$) is applied along the j-th axis of the system, the i-th componenet of the time-dependent dipole expansion (Eq. (3.54)) becomes

$$\begin{aligned}\mu_i(t, \pm mA) = \mu_i^0 \pm \mu_i^{(1)}(t)mA + \mu_{ij}^{(2)}(t)(mA)^2 \pm \mu_{ijj}^{(3)}(t)(mA)^3 \\ + \mu_{ijjj}^{(4)}(t)(mA)^4 \pm \mu_{ijjjj}^{(5)}(t)(mA)^5 + \cdots\end{aligned} \tag{3.62}$$

In order to derive an expression to analyze the first order response where the truncation error comes from the fourth order and above, four different time-dependent dipole equations are needed, $\mu_i(t, \pm A)$ and $\mu_i(t, \pm 2A)$. We can construct two linear combinations, $\mu_i(t, A) - \mu_i(t, -A)$ and $\mu_i(t, 2A) - \mu_i(t, -2A)$,

$$\mu(t, A) - \mu(t, -A) = 2\mu^{(1)}(t)A + 2\mu^{(3)}(t)A^3 + 2\mu^{(5)}(t)A^5 + \cdots \tag{3.63}$$

$$\mu(t, 2A) - \mu(t, -2A) = 4\mu^{(1)}(t)A + 16\mu^{(3)}(t)A^3 + 64\mu^{(5)}(t)A^5 + \cdots \tag{3.64}$$

where we have dropped the indices of direction for the sake of brevity. In order to eliminate the A^3 term to minimize the numerical error, we multiply Eq. (3.63) by a factor of eight and subtract it by Eq. (3.64),

$$8[\mu(t, A) - \mu(t, -A)] - [\mu(t, 2A) - \mu(t, -2A)] = 12\mu^{(1)}(t)A - 48\mu^{(5)}(t)A^5 + \cdots \tag{3.65}$$

Reorganize Eq. (3.65), we then have the time-dependent first-order response equation,

$$\mu^{(1)}(t) = \frac{1}{12A}\Big(8\left[\mu(t, A) - \mu(t, -A)\right] - \left[\mu(t, 2A) - \mu(t, -2A)\right]\Big) + 4\mu^{(5)}(t)A^4 \cdots \tag{3.66}$$

Similarly, higher order responses $\mu^{(n)}(t)A^n$ can be obtained:

$$\begin{aligned}\mu^{(2)}(t) = \frac{1}{24A^2}\Big(16\left[\mu(t, A) + \mu(t, -A)\right] - \left[\mu(t, 2A) + \mu(t, -2A)\right] - 30\mu^0\Big) \\ + 4\mu^{(6)}(t)A^4 + \cdots \end{aligned} \tag{3.67}$$

$$\begin{aligned}\mu^{(3)}(t) = \frac{1}{48A^3}\Big(-13\left[\mu(t, A) - \mu(t, -A)\right] + 8\left[\mu(t, 2A) - \mu(t, -2A)\right] \\ - \left[\mu(t, 3A) - \mu(t, -3A)\right]\Big) + 49\mu^{(7)}(t)A^4 + \cdots \end{aligned} \tag{3.68}$$

We note that the perturbation expansion Eq. (3.62) as a function of the field strength is convergent given a sufficiently small value of A so that $\lim_{n\to\infty}(\mu^{(n)}A^n) = 0$.[176,177] The convergence radius depends on the system under study and in principle one should use as small field strength as possible. However, it is impossible to derive an appropriate field strength so that $\lim_{n\to\infty}(\mu^{(n)}A^n) = 0$ is satisfied without information regarding how the higher

order response property grows as n approaches infinity. On the other hand, the field strength appropriate for calculations of $\mu^{(n)}(t)$ is also limited by numerical stabilities of the finite difference method. As a result, there are no well-defined rules of choosing appropriate field strength and it is largely based on experience. The suggested field strengths used in the finite field applications are between 0.001 a.u. and 0.005 a.u.,[133] to be compared with the maximum field strength of 100 V/μm ($\sim 2\times10^{-4}$ a.u.) used in the attenuated total reflection (ATR) electrooptic coefficient measurements of nonlinear optical chromophores.[178,179]

3.3 Quantum Coherent Plasmon in Silver Nanowires

A plasmon-like phenomenon, arising from coinciding resonant excitations of different electronic characteristics in 1D silver nanowires, has been proposed based on theoretical linear absorption spectra. Such a molecular plasmon holds the potential for applications of anisotropic nanoplasmon. However, its dynamical nature remains unexplored. Quantum dynamics of longitudinal and transverse excitations in 1D silver nanowires are carried out within the real-time time-dependent density functional theory framework. The anisotropic electron dynamics confirm that the transverse transitions of different electronic characteristics are collective in nature and oscillate in-phase with respect to each other. Analysis of time evolutions of participating one-electron wave functions suggest that the transverse transitions form a coherent wave packet that gives rise to a strong plasmon resonance at the molecular level.

3.3.1 Introduction

When a gold or silver nanoparticle is subjected to an electromagnetic field with a photon frequency corresponding to a natural frequency of the valence electrons collectively oscillating against the restoring force of the positive nuclei, a strong peak appears in the absorption spectrum.[180–182] This collective oscillation leads to an enhanced and confined electric field around the particle.[182–184] This phenomenon, called surface plasmon resonance (SPR), has been intensively studied both experimentally[185–189] and theoretically.[190–195] Applications include high-sensitivity chemical and biological sensing[196–204] as well as energy conversion and storage.[205] Anisotropic systems such as nanorods and nanowires are especially useful for certain applications such as photothermal cancer therapy.[206,207]

Noble metal nanorods have two main plasmon modes: the longitudinal mode (along the main axis of the nanorod) and the transverse mode (in the plane perpendicular to the main axis).[201,208–212] The longitudinal peak observed in the excitation spectrum shifts to lower energy with increasing aspect ratio whereas the transverse peak remains at nearly constant energy.[208–212] Recent linear response time-dependent density functional theory (LR-TDDFT) calculations performed on noble metal clusters suggest that a plasmon may

be identified when there is a constructive addition of the dipole moments of one-electron transitions and does not only occur in large nanoparticles (from a few to several hundred nanometers) but also in small clusters (less than 2 nm).[212–218] The frontier orbitals of silver and gold clusters are linear combinations of the valence s-orbitals of the metal atoms and are delocalized over the entire structure.[191,215,219]

Linear chains of noble metal atoms (nanowires) have been studied as model systems using TDDFT.[215,217,220–223] While the frequency domain LR-TDDFT method has been routinely used for studying plasmon excitations in small metal clusters, it becomes cumbersome as the system becomes large since large number of excited states have to be computed. On the other hand, the real-time TDDFT method has emerged as a powerful tool due to its better scalability. Further, it provides a straightforward, meticulous elucidation on the time evolution of the system subjected to an external electric field, which can lead to a wealth of useful information. For example, using real-time TDDFT, Yan *et al.*[221,222] identified the end and central plasmon resonances in linear sodium and silver chains. Gao *et al.*[223] studied the formation and size-evolution of electronic excitations in copper, silver and gold chains with up to 26 atoms. In both studies, the collective nature of the longitudinal and transverse excitations was deduced by the length dependence of the dipole strength. Induced density response was also analyzed to understand the nature of the two resonance modes.

Due to the symmetry of the nanowires, the delocalized frontier orbitals have cylindrical symmetry and can be labeled with the greek letters Σ, Π, Δ, etc. The longitudinal peak of these systems corresponds to the HOMO $\rightarrow$ LUMO transition ($\Sigma \rightarrow \Sigma$). The transverse peak corresponds to a superposition of $\Sigma \rightarrow \Pi$ transitions whose dipole moments add up constructively (a plasmon according to the identification scheme mentioned above).[215] However, the dynamical nature of such a superposition of single-particle transitions (i.e. molecular orbital transitions) is still unknown. How this superposition affects the time-dependence of the electron density in the plasmonic excitation remains unexplored.

To this end, we use the real-time TDDFT method developed in our group to study the interplay between the time evolution of the superposition of the single-particle transitions and the plasmonic excitations in silver chains. Formation and length-dependence of the longitudinal and transverse excitations are investigated by probing the dipole response to

an external step function electric field. In particular, we explore the superposition nature of the transverse excitation by analyzing the time evolution of the molecular orbital occupations. We observe a collective oscillation of single-particle transitions that are in-phase and coherent. This phenomenon is linked to the collective nature of plasmon resonance.

3.3.2 Methodology

The plasmon excitations of the silver nanowires are examined by performing the RT-TDDFT calculations, in which the electronic density matrix is propagated according to the TDDFT equation:

$$i\frac{d\mathbf{P}(t)}{dt} = [\mathbf{K}(t), \mathbf{P}(t)] \tag{3.69}$$

where $\mathbf{P}$ and $\mathbf{K}$ are density and Kohn-Sham matrices in orthonormal basis. Eq. (3.69) is integrated with a modified midpoint and unitary transformation (MMUT) algorithm,[43,44] where the density matrix is propagated using a unitary time evolution operator $\mathbf{U}(t_n)$:

$$\mathbf{P}(t_{n+1}) = \mathbf{U}(t_n) \cdot \mathbf{P}(t_{n-1}) \cdot \mathbf{U}^{\dagger}(t_n) \tag{3.70}$$

where $\mathbf{U}(t_n)$ is constructed from the eigenvectors $\mathbf{C}(t_n)$ and eigenvalues $\boldsymbol{\epsilon}(t_n)$ of the Kohn-Sham matrix at time t_n:

$$\begin{aligned}\mathbf{U}(t_n) &= \exp\big[-i \cdot 2\Delta t \cdot \mathbf{K}(t_n)\big] \\ &= \mathbf{C}(t_n) \cdot \exp\big[-i \cdot 2\Delta t \cdot \boldsymbol{\epsilon}(t_n)\big] \cdot \mathbf{C}^{\dagger}(t_n)\end{aligned} \tag{3.71}$$

with Δt denoting the time step.

To probe the time-dependent response of the silver chains to external electric field perturbations, we apply a step-function electric field either along the longitudinal or along the

transverse direction:

$$\mathbf{E}(t) = \begin{cases} \mathbf{E}_0 & t < 0 \\ 0 & t > 0 \end{cases} \tag{3.72}$$

Computationally this is equivalent to the following scheme: (1) prepare the initial electronic density by a self-consistent-field (SCF) calculation in the presence of the static electric field $\mathbf{E}_0$; (2) turn off the field and propagate the electronic system using the RT-TDDFT method outlined above.

The time-dependent dipole moment $\boldsymbol{\mu}(t)$ is calculated at each time step according to

$$\boldsymbol{\mu}(t) = \mathrm{Tr}\left[\mathbf{DP}(t)\right] \tag{3.73}$$

where $\mathbf{D}$ is the dipole matrix in the orthonormal basis. With the dipole response in real time, one can compute the dipole strength function $S(\omega)$, which is given by

$$S(\omega) = \frac{4\pi\omega}{3c}\mathrm{Tr}\left[\mathrm{Im}\boldsymbol{\alpha}(\omega)\right] \tag{3.74}$$

where $\boldsymbol{\alpha}(\omega)$ is the polarizability in the frequency domain and it can be obtained by the Fourier transform of the dipole moment and the step field through the following relation:

$$\mu_i(\omega) = \alpha_{ii}(\omega)E_i(\omega) \tag{3.75}$$

where i stands for x, y, z Cartesian coordinates.

At the weak perturbation limit, the time-domain approach generates the same excitation energies and relative dipole strengths as the frequency-domain LR-TDDFT.[224] On the other hand, the time-domain method can reveal insightful dynamical information about the interplay between the system and the external field, as will be discussed in the following section.

To find the relationship between the transverse excitation and single-particle transitions, we analyze the time evolutions of the molecular orbital occupations, which are calculated

by the projection of the time-dependent density matrix onto the initial ground state orbital space:[43]

$$n_i(t_k) = \mathbf{C}_i^{\dagger}(t_0)\mathbf{P}(t_k)\mathbf{C}_i(t_0) \tag{3.76}$$

where n_i is the occupation of the i-th molecular orbital.

The RT-TDDFT simulations were carried out using the development version of the GAUSSIAN series of programs.[122] A series of silver chains, with the number of atoms from 4, 6, and up to 12 were investigated. In all calculations, the BP86 density functional and the LanL2DZ[225–227] effective core potential were used. For real time simulations, the electronic wavepacket was evolved for 100 fs with an integration step size of 0.5 a.u. ($\sim$1.2 attoseconds). The strength of the external static field was chosen to be 0.001 a.u. In doing the Fourier transform of the time-dependent dipole moments, we added a damping factor of 0.2 eV which can physically account for the experimental broadening the dipole strength. The molecular geometries of the studied silver linear chains were taken from Ref. 215.

3.3.3 Results and Discussion

The dipole response of the silver chains due to the external step-function field perturbation along the longitudinal and transverse directions is shown in Fig. 3.11. Two main peaks are observed within the energy range of 0-8 eV for all chains. The peak L at low energy corresponds to the longtudinal excitation and arises from the dipole response to the electric field perturbation along the chain, and the peak T at high energy corresponds to the transverse excitation and arises from the dipole response to the perturbation perpendicular to the chain. This is consistent with the linear response TDDFT calculations in Ref. 215. However, there are slight differences between our results and those reported in Ref. 223 and 222, where multiple longitudinal and transverse peaks were present. This might be due to the use of different density functionals and basis sets, and bond lengths. It might also be a result of implementation differences. Despite those discrepancies, same trends can be observed: the longitudinal peak L is red-shifted when the chain length increases whereas the energy of the transverse peak T remains relatively constant, only slightly blue-shifting,

as clearly seen in Fig. 3.12. Fig. 3.12 also plots the evolution of the dipole strength as a function of the number of silver atoms. The dipole strength of both the longitudinal and transverse excitations increases as the chain length increases. This might be an indication of the collective nature of the two excitations. Note that there is a slight oscillation in the dipole strength of the transverse peak for Ag_8 and Ag_{10}, which is consistent with the results reported in Refs. 215 and 222.

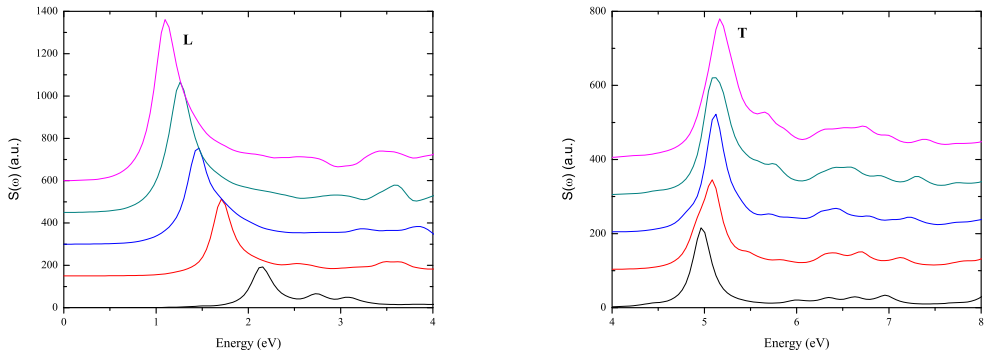

Figure 3.11: Dipole strength spectra of the linear silver chains $Ag_n (n = 4, 6, 8, 10, 12)$ to an external step field polarized in the longitudinal (L) and transverse (T) directions.

As shown in linear response TDDFT calculations,[215] the longitudinal excitation is predominated by a single-particle transition (i.e. HOMO $\rightarrow$ LUMO transition), which is assigned as a plasmon excitation.[215,222,223] However in classical solid-state physics, there is a clear distinction between single-particle excitations and plasmon excitations.[217] The seeming contraction lies in the fact that for systems consisting of a few to hundreds of atoms, classical electrodynamics is no longer applicable due to the existence of discrete energy levels in small clusters, and the distinction between single-particle excitations and plasmon excitations becomes less obvious. Identification of plasmon excitations in cases where the excitaion is dominated by a single-particle transition is not trivial. Rencently Bernadotte *et al.*[217] have proposed an approach to identify plasmons in small systems by scaling the electron repulsion integrals in the linear response TDDFT working equation.

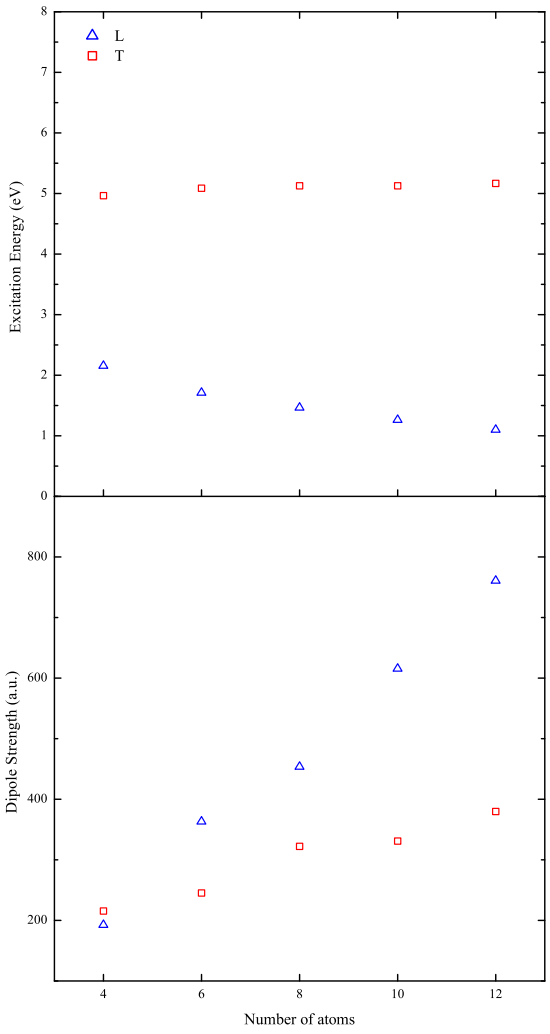

Figure 3.12: Excitation energy (top) and dipole strength (bottom) as functions of the number of atoms for the longitudinal (L) and transverse (T) plasmon resonant peaks shown in Fig. 3.11.

The transverse excitation, on the other hand, can be characterized by a superposition of multiple single-particle transitions, i.e. $\Sigma_m \rightarrow \Pi_m$ for Ag_{2m}, as indicated by linear response calculations.[215] As these transitions occur at a similar frequency, they can form the so-called "excited state plasmon"[228] if the interactive nature of these different electronic transitions is constructive and coherent.

To probe the nature of the interplay between these single-particle transitions, the time evolution of each involved molecular orbital is analyzed using the time-dependent occupation number of pertinent orbitals (Eq. (3.76)). The phase relationship between different time evolutions of occupation number will provide information regarding the constructive or destructive nature of related electronic transitions. On the other hand, if excited state wave functions are quantum mechanically coherent, the non-zero off-diagonal probability density $(\rho_{ij} \cdot e^{-i(\omega_j - \omega_i)t})$ will give rise to an additional peak in the spectrum of population density at the frequency that corresponds to the frequency difference $(\omega_j - \omega_i)$ of coherent states. As a result, any component (e.g. participating MO occupation number) of the state population density also bears the same signature of coherence. Therefore, frequency analysis of time evolution of orbital occupation can be used to probe the coherence of electronic excited states.

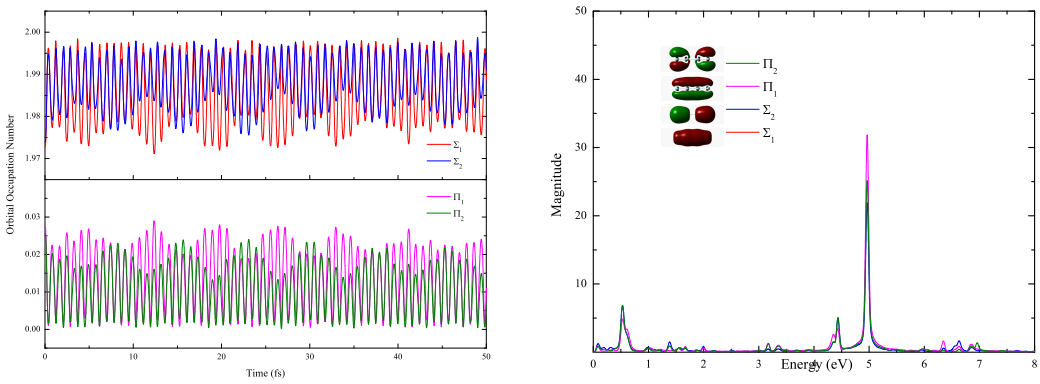

Figure 3.13: Orbital occupation analysis for the Ag_4 chain: (a) time-dependent oscillation-sand (b) the corresponding Fourier transformed spectra.

For Ag_4, the transverse excitation consists of two single-particle transitions: $\Sigma_1 \rightarrow \Pi_1$ and $\Sigma_2 \rightarrow \Pi_2$. Fig. 3.13 shows the time evolution of the occupation numbers (MO population density) of the four single-particle orbitals. Fourier transforms of these oscillations resolved a strong peak at ∼5 eV, agreeing with the transverse peak in the dipole strength spectrum in Fig. 3.11, as well as a small peak at ∼4.5 eV. The oscillations of the four orbitals are in phase and constructively interfere with each other. Further, the oscillations Σ_1 (Σ_2) and Π_1 (Π_2) exhibit the same amplitude, indicating a pairwise transition between Σ_1 (Σ_2) and Π_1 (Π_2) . The phase-relationship of these oscillations is well-maintained throughout simulations of much longer time scale (longer time simulation, >100 fs, is not shown here). This implies that the transverse excitation is composed of constructive oscillations of two single-particle transitions with no interference from other excited states. Different from the dipole strength spectrum, an additional peak appears at ∼0.5 eV in the spectrum of the time evolution of population density. The frequency of this peak (∼0.5 eV) is equal to the frequency difference between the two peaks at ∼5 eV. As discussed previously, this arises from the coherence of the $\Sigma_1 \rightarrow \Pi_1$ and $\Sigma_2 \rightarrow \Pi_2$ transitions.

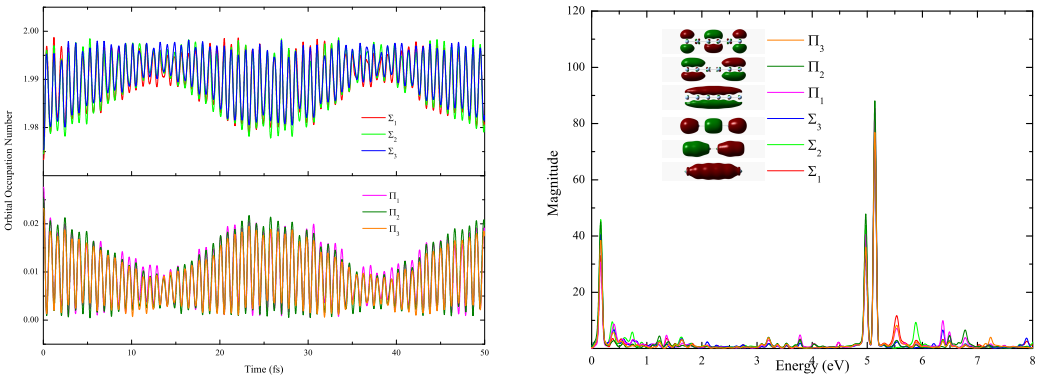

Figure 3.14: Orbital occupation analysis for the Ag_6 chain: (a) time-dependent oscillation-sand (b) the corresponding Fourier transformed spectra.

For Ag_6, the transverse peak consists of three single-particle transitions: $\Sigma_1 \rightarrow \Pi_1$, $\Sigma_2 \rightarrow \Pi_2$ and $\Sigma_3 \rightarrow \Pi_3$. Fig. 3.14 shows the time evolution of the occupation numbers of

the six orbitals and the corresponding Fourier transform. The oscillations of the six orbitals are in phase and constructively interfere with each other, and the phase relationship is well maintained throughout the simulation. Slightly different from Ag_4, all six orbitals oscillate with comparable amplitude. Pairwise transitions may still be identified from the character of the molecular orbitals, as depicted in Fig. 3.14. Fourier transform of the six oscillations gives almost the same spectrum. The two strong peaks at ∼5 eV correspond to the broadened transverse peak in the dipole strength spectrum, confirming that the transverse excitation is a collective oscillation of three single-particle transitions. The appearance of an additional peak at ∼0.2 eV results from the frequency difference between the two close-spaced peaks at ∼5 eV, indicating a coherence nature of the three single-particle transitions. These analyses suggest that the in-phase and quantum coherent single-particle transitions in the transverse direction can lead to an excited state plasmon at the molecular level.

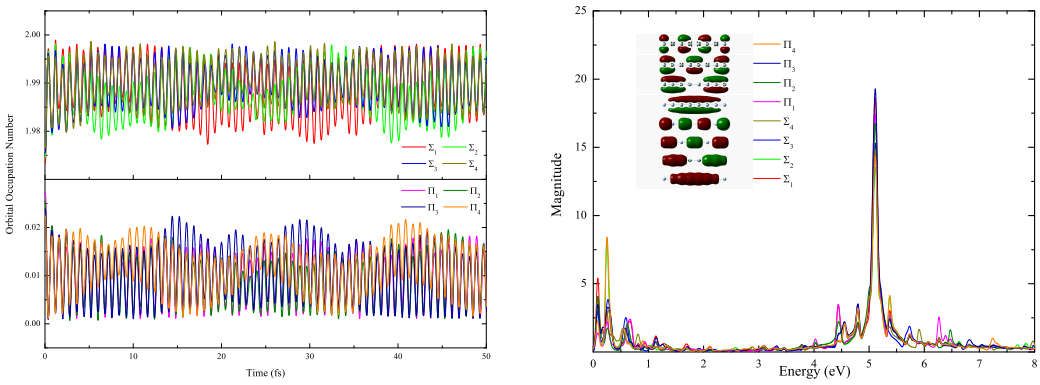

Figure 3.15: Orbital occupation analysis for the Ag_8 chain: (a) time-dependent oscillation-sand (b) the corresponding Fourier transformed spectra.

Starting at Ag_8, d-transitions start to mix with the $\Sigma \rightarrow \Pi$ transitions for the transverse excitation.[215] Although the single-particle transitions $\Sigma \rightarrow \Pi$ still make major contributions to the transverse excitation, the participation of the d-transitions will certainly complicate the analysis. In addition, broad absorption peak will show up in the transverse spectra because of the d-transitions, as shown in Ref. 222. In Fig. 3.15 we plot the occupation

number oscillations of the orbitals involved in the four single-particle transitions in Ag_8. These oscillations are of similar frequency and constructively interfere with each other, confirming the collective nature of this excitation. Compared to Ag_4 and Ag_6, the Ag_8 chain exhibits a larger variation in the amplitude of orbital oscillations and identification of the pairwise transitions becomes less trivial. Fourier transform of the orbital oscillations shows a broadened peak at ∼5 eV, which is consistent with the observation made in Ref. 222. Further, the Fourier spectrum exhibits a more complex pattern in the low frequency regime, which is a direct result of the amplitude variations in the time domain.

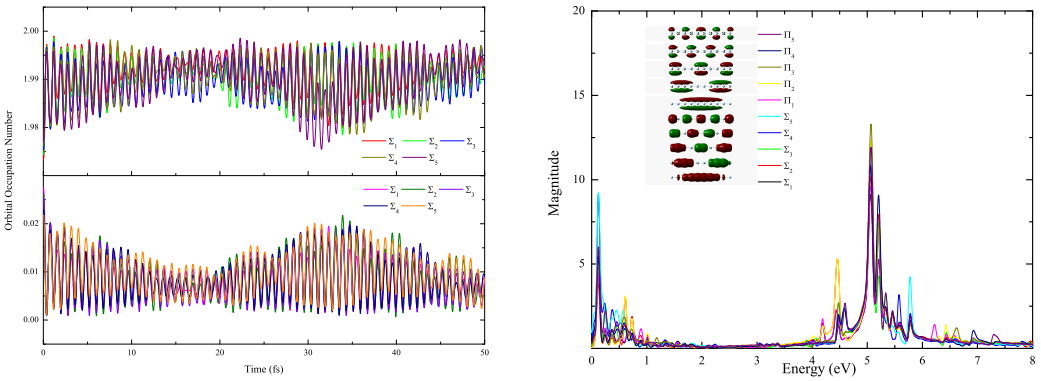

Figure 3.16: Orbital occupation analysis for the Ag_{10} chain: (a) time-dependent oscillation-sand (b) the corresponding Fourier transformed spectra.

For longer chains such as Ag_{10} and Ag_{12}, there is more mixing of d-transitions with the single-particle transitions $\Sigma \rightarrow \Pi$.[215] As a result, the transverse peak will be more broadened. Fig. 3.16 and Fig. 3.17 show the occupation number oscillations of the orbitals involved in the four single-particle transitions and the Fourier transformed spectra for Ag_{10} and Ag_{12}, respectively. Compared to the shorter chains, a large variation in the amplitude of the orbital oscillations is observed, and the Fourier spectra show a broad transverse peak at ∼5 eV and a complex pattern in the low frequency regime. In spite of these complications, in both cases we observe oscillations of the single-particle transitions that are in-phase and constructively interfere with each other.

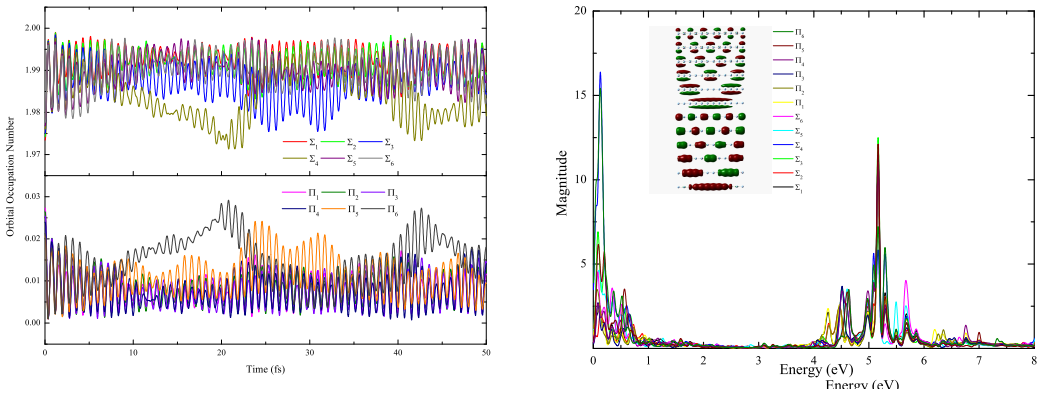

Figure 3.17: Orbital occupation analysis for the Ag_{12} chain: (a) time-dependent oscillationsand (b) the corresponding Fourier transformed spectra.

3.3.4 Conclusion

Using the real-time TDDFT method, we have studied the electronic excitations in a series of 1D silver nanowires. Length-dependence of the excitation energies and dipole strengths is investigated by analyzing the dipole response of the system to an external step function field in the longitudinal and transverse directions. We would like to place a special emphasis on the uniqueness of the transverse transitions from the point of view of dynamics. We analyze the time evolution of the population density of orbitals associated with the transverse excitation. In-phase and coherent plasmon type oscillations of the associated transitions are observed. The fact that these transitions occur at a similar frequency does not necessarily give rise to a plasmonic oscillation. It is the strong quantum coherence among these characteristic electronic oscillations that leads to molecular-scale plasmonics and nanoplasmonics, and our work herein provide the theoretical evidence. We also believe this feature could also exist in many quantum confined systems, such as quantum confined semiconductor nanocrystals and conjugated polymers.

Chapter 4

MODELING EXCITED STATE CHARGE TRANSFER DYNAMICS WITH RT-TDHF/TDDFT

4.1 Mechanisms of Bridge-Mediated Electron Transfer

We present a time-dependent density functional theory approach for probing the dynamics of electron transfer (ET) on a donor-bridge-acceptor polyene dye scaffold. Two kinds of mechanisms, namely, the superexchange mechanism and the sequential mechanism, may be involved in the electron transfer process. In this section, we focus on the crossover between these two charge transfer mechanisms on a series of donor-bridge-acceptor polyene dye systems with varying lengths of conjugated bridges. A number of methods and quantities are used to assist in the analysis, including the phase relationship of charge evolution, frequency domain spectra of the time-dependent dipole, and first-order rate kinetics. Our simulations show that the superexchange mechanism plays a dominant role in the electron transfer from donor to acceptor when the bridge length is small, and the sequential mechanism becomes more important as the polyene bridge is lengthened. However, the coherent electron transfer rate shows little dependence on the bridge length. Full Ehrenfest dynamics with nuclear motion show that molecular vibrations play a very small role in such ultrafast charge transfer processes.

4.1.1 Introduction

Charge transfer (CT) reactions are among the most fundamental and increasingly important processes in physics, chemistry and biology.[229–232] Recent advances in experimental and theoretical techniques are able to directly probe the mechanisms of electron-transfer kinetics and related chemical processes in bulk heterojunction or dye-sensitized solar cells,[233–235] bacterial photosynthetic reactions[236,237] and organic second-order nonlinear optical (NLO) materials.[171,238–241] The primary chemical event common amongst all of these physical

systems, and the one that must be exploited for most exciting new materials to be practically employed using their light harvesting or optical properties, is the generation of a long-lived, tunable charge separation. Bulk heterojunction and dye-sensitized solar cells make use of a photoexcitation to create a local electron-hole pair that can subsequently undergo long-range separation. Then the separated charges are transferred to electrodes, thus generating current. Similarly, in bacterial photosynthesis, a charge-separated state is generated via CT from the special pair to a bacteriopheophytin following the initial photoexcitation. This charge-separated state has been found to be created in $\sim$ 3 ps, and relies on a spatially intermediate bacteriochlorophyl to regulate the electron transfer.

There are two mechanisms commonly used to explain electron transfer in such bridge-mediated donor–acceptor systems, superexchange (SX) and sequential (SQ). The SX mechanism, as first invoked by McConnell,[242] relies on one or more high-lying virtual bridge states, and is a commonly employed description when the energy of the bridge state is relatively high or there is insufficient thermal energy available to the system to induce a ET event. This unistep process proceeds directly from donor to acceptor, with the bridge only acting to mediate the D and A wavefunctions. On the other hand, in SQ a composite bridge state is occupied during the ET reaction. When the bridge state is occupied an electron can be distributed among a number of localized sites whose number and nature depends on the nuclear composition and geometry of the backbone. The ET sequence within SQ can be described as donor $\rightarrow$ bridge $\rightarrow$ acceptor. In SQ, the lifetime of an electron in the bridge state can be longer than the characteristic time of the dephasing among phonons interacting with the transferring electron and the thermalization of phonons.[243] While the initial donor $\rightarrow$ bridge step can be unistep process the overall transfer is generally stepwise due to the interaction of multiple bridge sites with the donor and acceptor, and the thermalization of phonons from the bridge state. SQ is commonly used to describe reaction kinetics when the energy of the bridge state is sufficiently low or there is sufficient thermal energy in the system.

The transition between the SX and SQ mechanisms has invoked increasing interest from both experimental[244–247] and theoretical[243,248–262] perspectives. Experimentally, Miller *et al.*[245] succeeded in bridging the SX and SQ mechanisms in a single molecular sys-

tem by lowering the free energy of the bridge state. While the semiclassical rate theories[243,248,250,252,253] have been proven successful in understanding the SX and SQ mechanisms, a unified theoretical approach that accounts for both mechanisms is desired. In particular, Bixon and Jortner[249] studied the effects of the donor-bridge energy gap on the switching of the two mechanisms in a Franck-Condon system characterized by three multidimensional displaced harmonic potential surfaces. Simulations of ET were based on the exact diagonalization of the entire Hamiltonian of the system, revealing a transition from SQ to SX ET with increasing donor-bridge energy gap. The reduced density matrix formulism[254,256–261] is also widely used to study to the switching between the two mechanisms. In this approach, only the dynamics of the electronic degrees of freedom is treated explicitly and the rest part of the overall system (typically including the vibrational modes of the molecule and the solvent) is approximated by a harmonic bath coupled to the electronic degrees of freedom. Along this line, Hu and Mukamel[254] first incorporated both mechanisms into a single unified theoretical framework using the reduced density matrix approach with higher-order correlation functions for the system-bath coupling. Ratner and coworkers[259,260] studied the distance dependence of ET in model donor-bridge-acceptor (DBA) systems using a steady-state description of the reduced density matrix formulism. They observed several different regimes of distance dependence, ranging from fairly rapid exponential decay in the SX regime to an inverse length dependence in the SQ regime. Compared to approaches where all degrees of freedom are treated explicitly, such as Ehrenfest method[37,263] and the surface hopping method,[33,34] the reduced density matrix approach is more computationally efficient.[264] However, this approach usually relies on simplified model Hamiltonians with parameterized electronic energies and couplings, and cannot be easily generalized to simulate real systems.

In this section, we present an *ab initio* dynamics study of gas-phase ultrafast ET processes on real DBA polyene dye molecules, keeping the donor and the acceptor groups unchanged but varying the length of the polyene bridge. The molecular structure of the shortest DBA triad is shown in Figure 4.2. The electronic degrees of freedom are treated quantum mechanically using the time-dependent density functional theory (TDDFT). Numerical integration of TDDFT equations is carried out with an efficient modified mid-point

and unitary transformation (MMUT)[43] algorithm. In the first stage, we investigate the limiting case where the coupling between the electronic and nuclear degrees of freedom is negligible and the dynamics of ET is described as a coherent propagation of the superposition of the electronic states. This is possible for systems where ultrafast ET takes place on a femtosecond time scale and quantum coherence is observed.[265] To check the validity of this approximation we then perform Ehrenfest dynamics with TDDFT on the DBA triad with intermediate bridge length. In Ehrenfest dynamics, the quantum-mechanical equations-of-motion (EOM) for electrons are coupled with the classical EOM for nuclei via a mean-field electronic potential surface.[37,263]

We will discuss the modeling procedure for the initialization of the ET dynamics and briefly describe our TDDFT electronic and Ehrenfest dynamics method. We simulate the ET dynamics under two different initial conditions, the voltage-bias-induced ET and the photoinduced ET. In the former case, we create an initially polarized electronic state by applying an external electric field before the propagation of the electron density, and analyze the charge evolution on the D, B, and A groups. In the latter case, we create the initial donor state by a Koopman excitation of one electron from the HOMO to some low-lying donor-localized unoccupied MO and monitor the population evolution of the corresponding D/B/A states. We will discuss in both cases the transition between the SX and SQ mechanisms. We would like to emphasize that in our discussions the SX and SQ mechanisms are defined with respect to the temporal (charge or electron density) population on the donor, bridge and acceptor groups, which might differ from the definition of Bixon and Jortner[249] and that of Sumi and Kakitani.[252] Bixon and Jortner[249] defined the two mechanisms in the context of vibronic manifold D/B/A states, while in our simulations only electronic wavefunctions are considered. Sumi and Kakitani[252] considered the SQ mechanism in terms of vibrational relaxation in the bridge manifold state, whereas we distinct between SX and SQ simply based on the analysis of the population on the bridge group.

4.1.2 Review of the SX and SQ mechanisms

The SX and SQ mechanisms for charge transfer have been discussed by various groups with different notations. Here we follow Jortner and coworkers[244,250] and briefly describe the two mechanisms within a diabatic electronic state framework. For a charge transfer event in a D-B_i-A system where B_i =B_1,B_2,$\cdots$,B_N are the N adjacent, repeating bridge units, the relevant diabatic electronic states are $|D^* B_1 B_2 \cdots B_N A\rangle$, $|D^+ B_1^- B_2 \cdots B_N A\rangle$, $|D^+ B_1 B_2^- \cdots B_N A\rangle$, $\cdots$, $|D^+ B_1 B_2 \cdots B_N^- A\rangle$, and $|D^+ B_1 B_2 \cdots B_N A^-\rangle$. Here we assume the bridge states $|D^+\{B_i\}^- A\rangle$ are degenerate. In what follows, we consider the transfer of an electron from donor to acceptor. A similar approach can also be used to describe hole transfer.

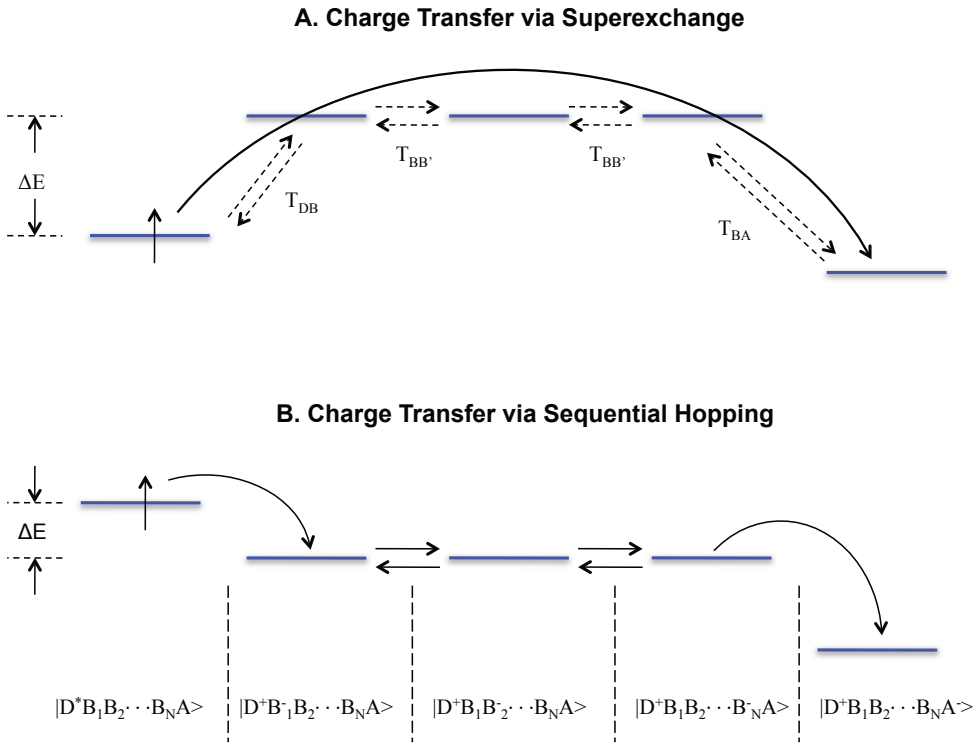

Figure 4.1: Schematic representation of the superexchange and sequential hopping mechanisms

A. Superexchange (SX)

In the SX mechanism, the electron/hole transfer is dictated by the off-resonance coupling T_{DB} between the initial $|D^*B_1B_2\cdots B_NA\rangle$ state and the bridge state $|D^+B_1^-B_2\cdots B_NA\rangle$, with a large energy gap ($\Delta E \gg k_BT$), as shown in Figure 4.1A. The overall transfer can be described as a unit step reaction:

$$|D^*B_1B_2\cdots B_NA\rangle \xrightarrow{k} |D^+B_1B_2\cdots B_NA^-\rangle. \tag{4.1}$$

Using the nearest-neighbor (NN) perturbation theory model of McConnel,[242] the superexchange coupling between donor and acceptor is

$$V_{DA} = (T_{DB}T_{BA}/\Delta E)(T_{BB'}/\Delta E)^{N-1} \tag{4.2}$$

where T_{DB}, $T_{BB'}$ and T_{BA} are nearest-neighbor couplings with

$$T_{DB} = \langle D^*B_1B_2\cdots B_NA|\hat{H}|D^+B_1^-B_2\cdots B_NA\rangle \tag{4.3a}$$

$$T_{BB'} = \langle D^+B_1\cdots B_i^-B_{i+1}\cdots A|\hat{H}|D^+B_1\cdots B_iB_{i+1}^-\cdots A\rangle \tag{4.3b}$$

$$T_{BA} = \langle D^+B_1B_2\cdots B_N^-A|\hat{H}|D^+B_1B_2\cdots B_NA^-\rangle \tag{4.3c}$$

where $\hat{H}$ is the electronic Hamiltonian of the system.

Using Marcus theory, the rate for the SX electron transfer can be expressed as

$$k = \frac{2\pi}{\hbar}V_{DA}^2F_{DA} \tag{4.4}$$

where F_{DA} is the thermally averaged nuclear Franck-Condon overlap between the donor $|D^*B_1B_2\cdots B_NA\rangle$ state and the acceptor $|D^+B_1B_2\cdots B_NA^-\rangle$. By defining

$$\beta = 2\ \ln(\Delta E/T_{BB'}) \tag{4.5a}$$

$$V_0 = T_{DB}T_{BA}/\Delta E \tag{4.5b}$$

one obtains the the Marcus-Levich-Jortner equation:

$$k = \frac{2\pi}{\hbar} V_0^2 F_{DA} \exp\{-\beta(N-1)\} \tag{4.6}$$

Since $N-1$ is proportional to the length of the bridge and hence the donor-acceptor distance, Eq. 4.6 indicates that for the SX mechanism the rate of electron transfer exhibits an exponential fall-off with the D-A distance.

B. Sequential hopping (SQ)

The SQ electron transfer occurs when the energy gap between the donor state $|D^* B_1 B_2 \cdots B_N A\rangle$ and the bridge states $|D^+ \{B_i\}^- A\rangle$ is relatively low, i.e., $\Delta E \ll k_B T$ or $\Delta E \leq 0$ (Figure 4.1B). The overall transfer can be expressed as a first-order consecutive reaction:

$$\begin{aligned} |D^* B_1 B_2 \cdots B_N A\rangle \xrightarrow{k_{DB}} |D^+ B_1^- B_2 \cdots B_N A\rangle \underset{k_{21}}{\overset{k_{12}}{\rightleftarrows}} \\ |D^+ B_1 B_2^- \cdots B_N A\rangle \underset{k_{32}}{\overset{k_{23}}{\rightleftarrows}} \cdots \underset{k_{N,N-1}}{\overset{k_{N-1,N}}{\rightleftarrows}} \\ |D^+ B_1 B_2 \cdots B_N^- A\rangle \xrightarrow{k_{BA}} |D^+ B_1 B_2 \cdots B_N A^-\rangle. \end{aligned} \tag{4.7}$$

Based on the nature of the electron transfer, the above reaction can be divided into three microscopic processes: (1) the charge injection from the donor to the bridge, (2) the charge migration between the bridge units, and (3) the charge trapping at the acceptor site.

The charge injection rate can be expressed as

$$k_{DB} = \frac{2\pi}{\hbar} V_{DB}^2 F_{DB} \tag{4.8}$$

where V_{DB} is the electronic coupling between the donor and bridge states and is given by Eq. 4.3a. F_{DB} is the thermally averaged nuclear Franck-Condon density for the donor-bridge vibronic coupling.

The rate of charge migration between adjacent bridge units is

$$k_{BB'} = \frac{2\pi}{\hbar} V_{BB'}^2 F_{BB'} \tag{4.9}$$

where $V_{BB'}$ is the nearest-neighbor coupling between two (near) degenerate bridge states and is given by Eq. 4.3b. $F_{BB'}$ is the thermally averaged nuclear Franck-Condon density for the vibronic coupling between two bridge states.

Finally, the charge trapping rate is given by

$$k_{BA} = \frac{2\pi}{\hbar} V_{BA}^2 F_{BA} \tag{4.10}$$

where V_{BA} is the electronic coupling between the bridge and acceptor states and is given by Eq. 4.3c. F_{BA} is the thermally averaged nuclear Franck-Condon density between the bridge and acceptor vibronic manifold states.

For an acceptor-direction-biased hopping, as depicted in Figure 4.1B, a simple diffusion model with biased random walk gives the following rate expression for the SQ transfer:

$$k \approx k_{BB'} N^{-\eta} \tag{4.11}$$

where $k_{BB'}$ is given by Eq. 4.9 and $1 \leq \eta \leq 2$. This indicates a weak D/A distance dependence for the electron transfer rate.

In the frozen-nuclei approximation the state populations of the electronic part of the system does not affect the nuclear configuration so that the thermally averaged nuclear Franck-Condon density $F = 1$. As a result, Eqs. 4.6 and 4.11 can be used to describe the pure electronic dynamics.

4.1.3 Modeling and methodology

The ET process can be initiated under different conditions. A voltage-bias-induced ET, as can be found in molecular junctions, uses an external voltage to populate a manifold of excited electronic states of the linkage molecule. The transfer from the donor to the acceptor through the bridge can then commence along many coupled electron transfer channels.

Photoinduced ET can also proceed, but is initiated by inducing an excitation of an electron from the ground state to a low-lying donor-localized excited state. This state can be coupled to bridge-localized states and can, depending on several factors such as temperature and energy level distribution, induce long-range ET through a single channel. We consider both types of bridge-mediated ET in a range of DBA-n triads (n=2,4,6,8,10,12), with n representing the number of double bonds along the polyene bridge (see Figure 4.2).

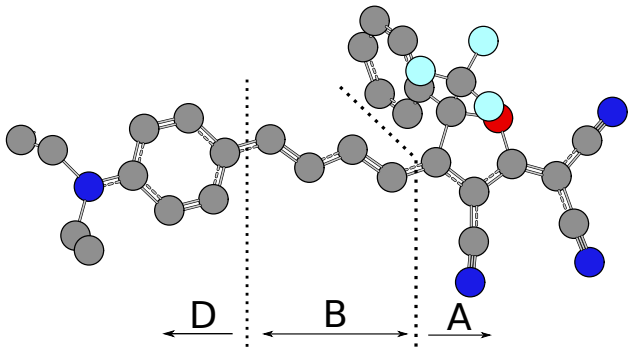

Figure 4.2: Equilibrium geometry of the DBA-2 triad. Carbon atoms are shown as grey circles, nitrogen as dark blue, fluorine as light blue, and oxygen as red. Hydrogens are omitted for clarity. Dashed lines indicate the NPA boundaries between D, B, and A.

A. Modeling the bias-induced electron transfer

To create an initial electronic state that represents the polarized $|D^-[BA]^+\rangle$ state, a static electric field polarized along the molecular axis from D to A is included in the SCF procedure for each of the triads with varying field strengths. The applied external field strengths and equilibrated molecular dipole moments are given in Table 4.1. For each molecule, the applied DC field strength is chosen to produce a charge difference of $\sim$1 electron charge between the donor and the rest of the molecule. This method of initial state preparation mimics what would be found in a molecular junction where D (A) is attached to a voltage sink (reservoir), and a polarization of the junction is allowed to be maintained. Upon removal of the voltage bias the polarized electron density will decay to its equilibrium configuration through an intramolecular charge transfer. By tracking the localized charge on the D, B,

and A groups while the initially prepared electron density proceeds toward equilibrium we can observe the crossover from SX to SQ with increasing n. In this study we employ a closed-system formulation of DFT in which environmental degrees of freedom are neglected, including nuclear motion. This discounts the possibility of irreversible decoherence. As such the initially prepared nonequilibrium electronic density matrix does not relax to a global minimum, but will redistribute according to its energetic constraints and follow the most active electron transfer channels.

Table 4.1: Applied external field strengths and finally equilibrated total dipole moments for the range of polyene bridge lengths.

n	Field Strenght (au)	μ (Debye)
2	0.016	21.8202
4	0.012	26.2463
6	0.010	30.1208
8	0.009	33.4565
10	0.008	36.2427
12	0.007	38.6010

B. Modeling the photoinduced electron transfer

The initial state created by applying a static electric field generally consists of a superposition of excited states and the dynamics is a result of ET via multiple ET pathways. In order to obtain a simple ET dynamics, we seek to model the process via the lowest transfer pathway. The initial state is created using a single-photoexcited-electronic state localized on the donor group. We consider the cationic radicals of the DBA triads. The unpaired cationic electron is promoted from the highest occupied molecular orbital (HOMO), localized primarily on the acceptor, to an unoccupied molecular orbital (MO) that is localized on the donor. An electron density prepared in this way can be thought of as resulting from photoexcitation of the donor by visible light. Figure 4.3 shows selected molecular orbitals (MO's) for the cationic radicals of DBA-2, 6 and 10. For DBA-2, an electron is promoted from the acceptor-dominant HOMO to the donor-dominant LUMO. For DBA-6 and

DBA-10, the initial state is prepared by promoting an electron from the acceptor-dominant HOMO to the lowest lying unoccupied MO with electron density localized on donor.

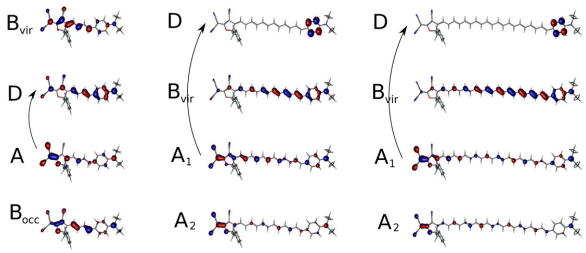

Figure 4.3: One-electron orbitals for the cations of DBA-2, 6, and 10. Characters indicate the localization site of the density: A = acceptor, B = bridge, D = donor. The arrows represent the initial excitation from the acceptor-dominant MO to the donor-dominant MO.

C. TDDFT Electronic Dynamics and Ehrenfest Dynamics

We use the MMUT algorithm to propagate the electronic density matrix to simulate the pure electronic dynamics. As the methodology is well established, we refer readers to our previous publications,[43,165] and only present a brief summary of the method herein. The electronic density matrix is propagated using a modified mid-point unitary transformation algorithm, according to which the TDDFT equation:

$$i\frac{d\mathbf{P}}{dt} = [\mathbf{K}, \mathbf{P}] \tag{4.12}$$

is implemented as:

$$\mathbf{P}(t_{k+1}) = \mathbf{U}(t_k) \cdot \mathbf{P}(t_{k-1}) \cdot \mathbf{U}^{\dagger}(t_k), \tag{4.13}$$

where $\mathbf{P}$ is the electronic density matrix, $\mathbf{K}$ is the Kohn-Sham matrix, and the unitary propagator $\mathbf{U}$ is constructed from the eigenvalues and eigenvectors of the Kohn-Sham matrix

$\mathbf{C}^{\dagger}(t_k) \cdot \mathbf{K}(t_k) \cdot \mathbf{C}(t_k) = \varepsilon(t_k)$ as

$$\mathbf{U}(t_k) = \mathbf{C}(t_k) \exp[i2\Delta t \varepsilon(t_k)] \mathbf{C}^{\dagger}(t_k), \tag{4.14}$$

with $\Delta t = t_{k+1} - t_k$.

Computational time was significantly reduced using a dynamical active space screening for the electron density, based on incremental Fock builds in the time domain wherein only the contribution to the two-electron integral of portions of the electron density that are perturbed above a predetermined threshold are recalculated at each time step.[165]

To address the effect of nulcear motion on the charge transfer process, classical nuclei are propagated on the real-time TDDFT potential energy surface using the Ehrenfest dynamics approach. The TDDFT Ehrenfest dynamics[37,44] is implemented with a triple-split-operator scheme with three different integrators: the velocity Verlet[266] algorithm for classical nuclear motion, a nuclear position coupled midpoint Kohn-Sham integrator, and the MMUT-TDDFT algorithm for electronic degrees of freedom. Because the electronic wave function changes much faster than the nuclear motion, the nuclear position coupled midpoint Kohn-Sham propagator updates integrals required in the Kohn-Sham matrix with a time step of Δt_{Ne}, which encompasses some integer number m of the MMUT electronic dynamics steps, $m\Delta t_e$. The integrals are recomputed at the midpoint of every Δt_{Ne} time step, $t' + \Delta t_{Ne}/2$, and are used in the Kohn-Sham matrix for the m MMUT steps between t' and $t' + \Delta t_{Ne}$,

$$\mathbf{K}(t) = \mathbf{h}\left[x\left(t' + \frac{\Delta t_{Ne}}{2}\right)\right] + \mathbf{G}\left[x\left(t' + \frac{\Delta t_{Ne}}{2}\right), \mathbf{P}(t)\right] \tag{4.15}$$

where $\mathbf{h}$ and $\mathbf{G}$ are one- and two-electron matrices, respectively. The nuclear position is updated for some integer number n of the midpoint Kohn-Sham steps, $n\Delta t_{Ne}$ before the gradient is recalculated, which occurs in the time step $\Delta t_N = n\Delta t_{Ne}$. The standard velocity Verlet algorithm is used to propagate the nuclear coordinates,

$$p(t_{k+\frac{1}{2}}) = p(t_k) - \frac{1}{2} g(t_k) \Delta t_N, \tag{4.16}$$

$$x(t_{k+1}) = x(t_k) - \frac{p(t_{k+\frac{1}{2}})}{M}\Delta t_N, \tag{4.17}$$

$$p(t_{k+1}) = p(t_{k+\frac{1}{2}}) - \frac{1}{2}g(t_{k+1})\Delta t_N, \tag{4.18}$$

where p is the linear momentum and g is the energy gradient.

We focus on charge transfer processes with frozen-nuclei approximation using the real-time TDDFT electronic dynamics. Due to the computational cost, only a single Ehrenfest dynamics is simulated to illustrate the effect of nulcear motion on the charge transfer process. The computational scheme of the electron transfer dynamics is as follows: (1) The electron density that corresponds to a donor state is prepared either by applying a static electric field or by promoting an electron from HOMO to some unoccupied donor-dominant MO. This step create an electron density that is not stationary but represents a coherent wave packet composed of the ground state and excited states of interest. (2) The coherent state is propagated using the real-time MMUT-TDDFT electronic dynamics. (3) For the static field approach, a natural population analysis is performed at each time step to analyze the charge on the D, B, and A groups. The time-dependent dipole moment or charge distribution is also calculated. For the photoinduced ET dynamics simulations, we project the total electron density on to the ground state molecular orbital space and analyze the orbital occupation numbers $n_i(t_k)$ at each time step k:

$$n_i(t_k) = \mathbf{C}_i^{\dagger}(t_0)\mathbf{P}(t_k)\mathbf{C}_i(t_0) \tag{4.19}$$

where $\mathbf{C}_i(t_0)$ is the i-th eigenvector of the ground state Kohn-Sham matrix. In the one-electron orbital approximation, the time-dependent occupation numbers describe the population evolution of the corresponding donor/bridge/acceptor states.

4.1.4 Results and Discussion

A. Bias-induced ET

The TDDFT electronic and Ehrenfest dynamics described above has been implemented within the development version of the GAUSSIAN series of program.[122] We first simulate

the bias-induced ET dynamics with the neglection of coupling between the electronic and nuclear degrees of freedom. The B3LYP functional[104,105] with the 6-31G(d) basis set is used for calculations of ground-state properties, the excited states within the linear response framework, as well as for the electronic dynamics simulations. The electronic dynamics is invetigated at the equilibrium geometries of the neutral triads after the external electric field is turned off. A step size of $\Delta t_e = 0.0012$ fs is used for the propagation of the electronic density matrix. We perform a natural population analysis (NPA)[267] at each time point to determine the charge on the donor, bridge, and acceptor groups. Figures 4.4(a)-4.9(a) plot the time evolution of the natural charge on each of the D, B, and A groups for polyenes varying from 2 to 12 double bonds and the corresponding Fourier transformed spectra. All of the molecules studied show a prominent fast oscillation in the natural charges as well as a slower average decay, with the long-time average charge distribution approaching that found at equilibrium. Figures 4.4(b)-4.9(b) plot the time evolution of the dipole moment of the molecules and the corresponding frequency domain spectra. Figures 4.4(c)-4.9(c) show the calculated linear absorption spectra using linear-response TDDFT. It is well known that TDDFT with standard approximate xc functionals may yield substantial errors for the excitation energies of long range charge-transfer excited states, due to their incorrect asymptotic behavior. With regard to our study of ET dynamics, the approximate xc functionals may affect the ordering of the excited states, which in turn may give rise to unreliable predictions for the superexchange mechanism in molecules with long conjugated bridge. On the other hand, the SQ mechanism consists of a sequence of short-ranged ET steps, which can be properly modeled by conventional practice of DFT.

For DBA-2, the oscillations on the D and A groups are large in amplitude and out of phase, while the oscillation of the bridge remains small-amplitude throughout with little correlation to either end group. A Fourier transform of the charge oscillations of the constituent groups is shown in Figure 4.4(a). The prominent peak in both the D and A traces, centered about 2.4 eV, corresponds to the fast oscillation seen in the inset. The B spectrum shows a distribution of frequencies centered near 4.8 eV, twice the frequency of the main peak in both the D and A spectra. There is a strong overlap between the D and A spectra while there is very small correlation between B spectra and either D or A spectrum. This,

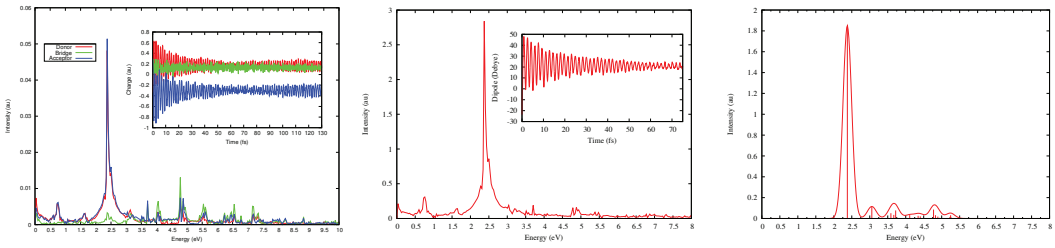

(a) Natural charge (b) Dipole (c) LR-TDDFT

Figure 4.4: NPA and Dipole spectra for DBA-2

when coupled with the phase relationship evident in the inset of Figure 4.4(a), indicate that the SX mechanism is responsible for the eventual net charge transfer from the donor to the acceptor. Additionally we can evaluate the spectrum of the dipole oscillation, seen in Figure 4.4(b). The intense peak is also centered around 2.4 eV, which is consistent with the absorption spectrum (Figure 4.4(c)) calculated using linear-response TDDFT. This peak corresponds to a transition from the HOMO in which the electron density is mainly localized in the donor region to the LUMO where the electron density is localized in the acceptor region. The absence of a peak corresponding to the bridge charge oscillation near 4.8 eV further points to the SX mechanism.

As the polyene bridge is lengthened, the energy gap between the donor and bridge state is lowered, as a consequence the charge oscillation on the B group can become more correlated with the donor group, and the phase relationship of the charge oscillations on D and A is altered. As evident in Figures 4.5(a)-4.7(a), the amplitude of charge oscillation on the bridge becomes more significant and the relative amplitude of the charge oscillations is modified so that an increase on the D (A) group is not compensated for by a commensurate decrease in charge on the A (D) group. This is a signature of bridge-mediated SQ charge transfer and becomes more pronounced with a longer conjugation length, as one would expect.

Specifically, for DBA-4 there is sizable oscillation of the bridge charge population during the course of charge transfer, as seen in the inset of Figure 4.5(a). The frequency domain spectrum for the bridge becomes more correlated with both D and A spectra, in particular, at $\sim$2.0 eV where the prominent peak in both D and A spectra is located. The Fourier

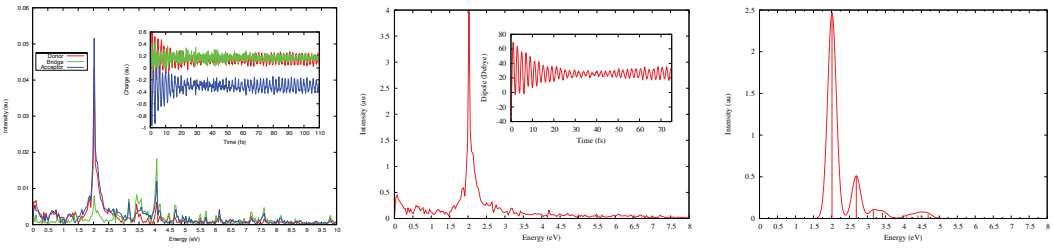

(a) Natural charge (b) Dipole (c) LR-TDDFT

Figure 4.5: NPA and Dipole spectra for DBA-4

transformed spectrum of the dipole also reveals an intense peak at ∼2.0 eV, which corresponds to a transition mainly from HOMO to LUMO as determined from the linear response TDDFT calculation. Figures 4.6(a) and 4.6(b) show the natural charge and dipole spectra for DBA-6. The main peak shows considerably more bridge intensity, indicating a more active role for the bridge in mediating charge transfer between the donor and acceptor. The D, B, and A peaks centered near 4.8 eV in the DBA-2 spectrum are red-shifted by ∼1.4 eV and noticeably broadened for DBA-6 due to the presence of multiple bridge sites. For DBA-8, Figure 4.7(a) shows that the amplitude of charge oscillation on the bridge is even more pronounced. In the NPA spectrum almost all the bridge peaks overlap with the D/A peaks and the main peak is further broadened compared to those seen in DBA-6 and DBA-4. The red shifting and broadening of all of the peaks, along with an increased bridge activity is evidence for the presence of the SQ mechanism, but is not indicative of SQ being the dominant mode of ET.

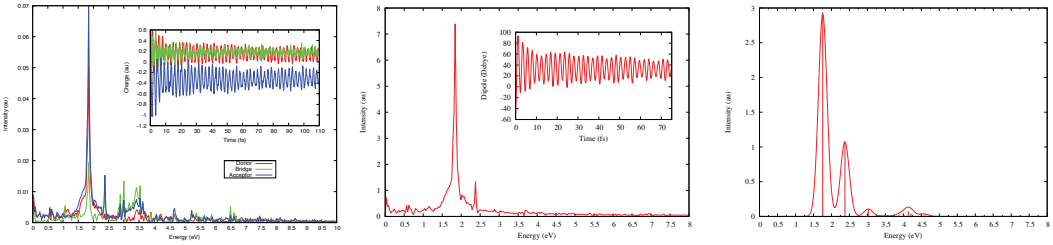

(a) Natural charge (b) Dipole (c) LR-TDDFT

Figure 4.6: NPA and Dipole spectra for DBA-6

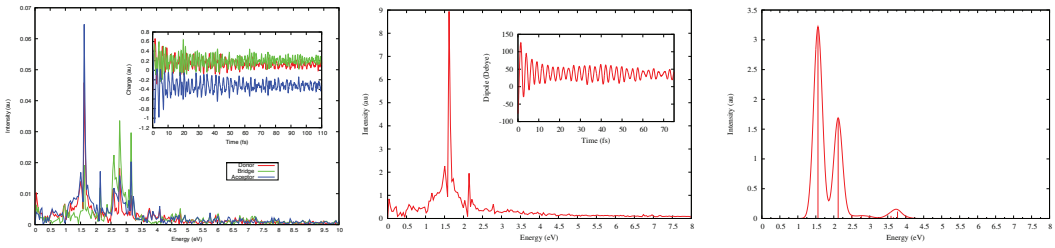

(a) Natural charge (b) Dipole (c) LR-TDDFT

Figure 4.7: NPA and Dipole spectra for DBA-8

A crossover to the SQ regime occurs when the bridge consists of around ten double bonds, DBA-10, as evident in Figure 4.8(a). The main peak in the NPA spectrum becomes drastically split and red-shifted while the overlap of the previously distinct bridge-dominated and donor or acceptor-dominated peaks increases. In addition, the amplitude of the charge oscillation on the bridge is almost comparable to that on either donor or acceptor site. This indicates the bridge states play a dominant role in the charge transfer. The dipole spectrum also reveals a collection of peaks at ∼1.4 eV where there is only one peak in the linear response TDDFT spectrum. This is a signature of active participation of multiple bridge states in mediating SQ charge transfer. This trend is further enforced with DBA-12, see Figures 4.9(a) and 4.9(b). It is worthwhile to point out that the NPA and dipole spectra presented for these SQ-dominant ET triads do not include line-broadening from the thermalization of phonons from the bridge state that is populated during the electron transfer. Since we hold all nuclei fixed during the dynamical propagation the peak widths are due solely to electronic coupling to multiple localized bridge sites.

B. Photoinduced ET

The photoinduced ET is simulated for the cations of DBA-2, 6, and 10, and is initiated by a Koopman excitation of one electron from the HOMO to some low-lying donor-localized unoccupied MO in the ground-state MO representation. We first consider the approximate situation when electronic and nuclear motions are decoupled and perform the electronic dynamics simulation with the MMUT-TDDFT algorithm. Again, the B3LYP functional

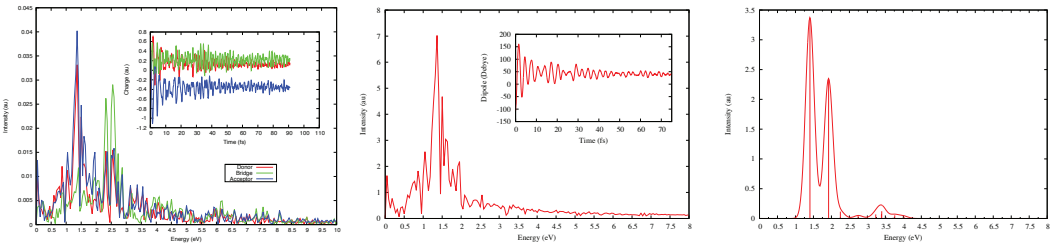

(a) Natural charge (b) Dipole (c) LR-TDDFT

Figure 4.8: NPA and Dipole spectra for DBA-10

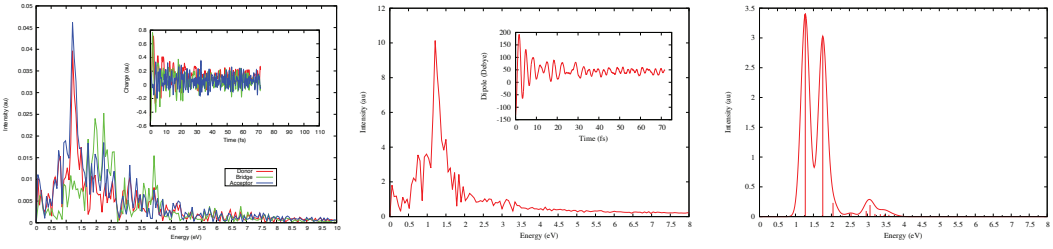

(a) Natural charge (b) Dipole (c) LR-TDDFT

Figure 4.9: NPA and Dipole spectra for DBA-12

with the 6-31G(d) basis set is used for calculations of ground-state properties and for the electronic dynamics simulations. The electronic dynamics is invetigated at the equilibrium geometries of the cations of DBA-2, 6, and 10. A step size of $\Delta t_e = 0.0012$ fs is used for the propagation of the electronic density matrix. Different from the preceding analysis, in this case we examine the time evolution of the orbital occupation numbers, which are obtained by the projection of the time-dependent electron density onto the ground-state MO space. In the one-electron orbital approximation, the time-dependent occupation numbers describe the population evolution of the corresponding donor/bridge/acceptor states.

Figure 4.10 shows the time evolution of the orbital occupation numbers for several of the relevant MO's that exhibit significant changes in their populations. For all the cations studied herein the overall dynamics is characterized by a population decay in the donor-dominant MO and a population gain in the acceptor-dominant MO. This process occurs within ∼80 fs as most of the electron density is transferred from donor to acceptor in absence of re-

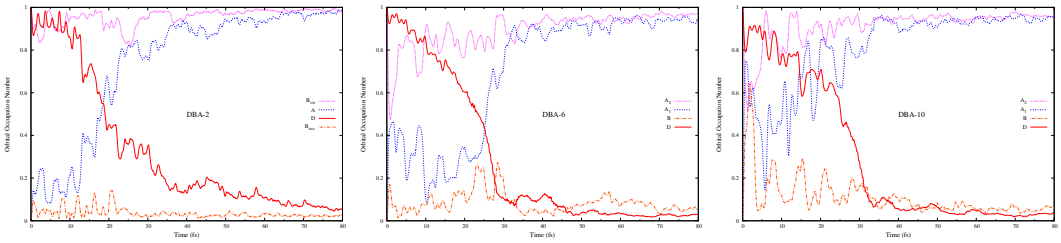

Figure 4.10: Time evolution of the populations of the projected one-electron orbitals. Characters in parenthesis indicate the localization site of the density: A = acceptor, B = bridge, D = donor.

laxation. Significant contributions from nearby MO's are also seen in the simulations. The small population oscillations are the result of the composite interaction between the MO's that are either energetically close or localized on the same site. For DBA-2, the process is dominated by the population decay(gain) in the donor(acceptor)-dominant MO and there is very small involvement of the bridge-dominant MO's during the course of simulation. This implies that the SX mechanism is responsible for the electron transfer in DBA-2. As the polyene bridge is lengthened, the bridge-dominant orbitals can become more correlated with the donor/acceptor -dominant MO's. For DBA-6, there is sizable transient population ($\sim$25%) in one bridge-dominant MO (see Figure 4.3 for MO picture). This is an indication of the presence of the SQ mechanism, though not predominant over SX. The relative importance of the SQ mechanism becomes evident when the polyene bridge is lengthened to ten double bonds. For DBA-10, more than one bridge-dominant MO actively participates in the electron transfer process. Figure 4.10 shows the orbital occupation numbers for one of the bridge-dominant MO's that exhibit significant changes in their populations, with $\sim$ 60% transient population gain in the initially unoccupied bridge orbital. This, together with the out-of-phase oscillation relation between the donor(acceptor)-dominant MO and the bridge-dominant MO's, is a signature of the SQ being the prominent mechanism for electron transfer.

C. Effect of Molecular Vibration on Charge Transfer

While the above electronic dynamics simulations may provide some insights into the understanding of the ultrafast ET in conjugated DBA systems, it is still unclear whether the nuclear motion and the nuclear-electronic coupling would have significant effects on the short-time dynamics. As a first attempt to account for these effects, we perform a short-time (100 fs) TDDFT Ehrenfest dynamics simulation of the photoinduced ET in the DBA-6 cationic radical, where both the SQ and SX mechanisms are considered to be active. In the Ehrenfest dynamics approach the nuclei are treated as classical point charges that evolve in time on the mean field TDDFT potential energy surface defined by the nonequilibrium electronic density. We use a triple-split propagator scheme where the nuclei, electronic-nuclear interaction, and the electronic density are propagated with time steps Δt_N, Δt_{Ne}, and Δt_e, respectively. For detailed implementation of the TDDFT Ehrenfest dynamics, please see references 37, 44. The initial geometry and the initial velocities of the nuclei are chosen to be the most probable according to a Boltzmann distribution at room temperature (298 K). The initial nonequilibrium electronic state is prepared by exciting one electron from the acceptor-localized HOMO to the donor-localized LUMO, in the ground-state MO representation. The nuclei and electronic density are propagated using the velocity Verlet algorithm and MMUT method with time steps of $\Delta t_N = 0.10$ fs and $\Delta t_e = 0.002$ fs, respectively. The nuclei-position dependent Kohn-Sham operator is recomputed at every 10 electronic steps ($\Delta t_{Ne} = 0.002$ fs). To reduce the computational cost while maintaining reasonable accuracy, we use a smaller Stuttgart/Dresden[268] basis for the electronic degrees of freedom. The total energy for the studied system is conserved to within 0.2 kcal/mol.

We use the natural charge population[267] on the D, B, and A groups to perform our analysis. To gauge the effect of nuclear motion on ET in our DBA-n system, we have also performed pure electronic dynamics simulation with the same initial conditions and frozen nuclei. Figure 4.11 shows the time evolution of the natural charge on each of the D, B, and A groups of the DBA-6 cation. As can be expected the dynamics at times shorter than any characteristic nuclear motion (< 10 fs), the TDDFT and Ehrenfest calculations are in agreement. At longer times the Ehrenfest results shows some effects of nuclear vibration.

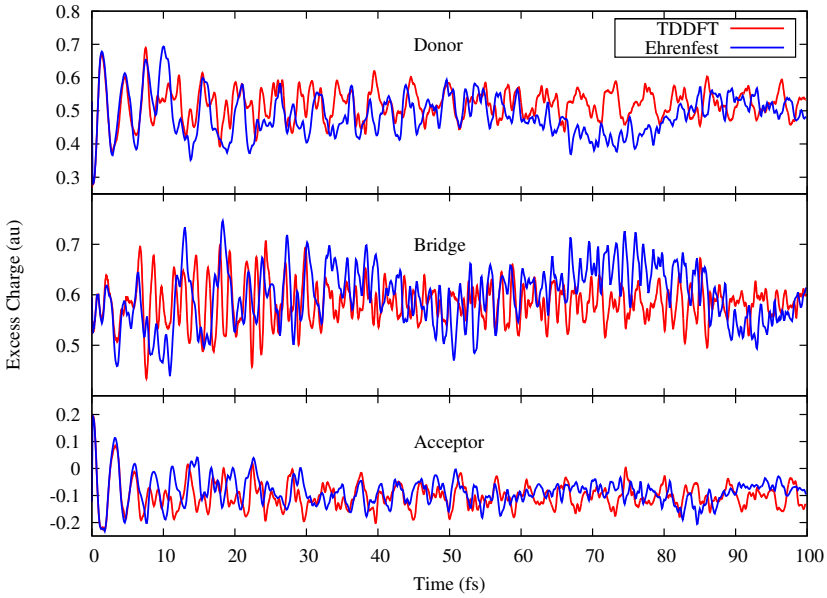

Figure 4.11: Time evolution of the natural charges on the donor, bridge, and acceptor groups of the DBA-6 cation, following a HOMO-LUMO excitation.

In the donor low-frequency modulation of the charge grows in slowly and is most apparent around 70 fs. The low frequency modulation is more pronounced in the bridge, as the electrons can more effectively couple to the polyene backbone vibrations, and the phase is altered. The nuclear effects are relatively small on the acceptor group, with only a small amplitude modulation and a decrease phase disruption. Though effects of nuclear motion can be seen on all three portions of the molecule, the general trend is largely unaffected, at least for these short times. At much longer timescales (ps to ns) the dephasing of the coherent electronic density by the nuclei can be expected to play a dominant role in determining the effectiveness of long-range ET.

Figure 4.12 shows the Fourier transform spectra for both the Ehrenfest and the pure electronic dynamics charges shown in Figure 4.11. The two approaches give similar spectra for the D, B, and A charges in the high-energy (> 1 eV) range, where both the SX and SQ transfer occurs. The major differences upon the inclusion of nuclear motion are the appearance of low-energy (< 0.5 eV) peaks and the quenching of the large peak at ~ 1 eV

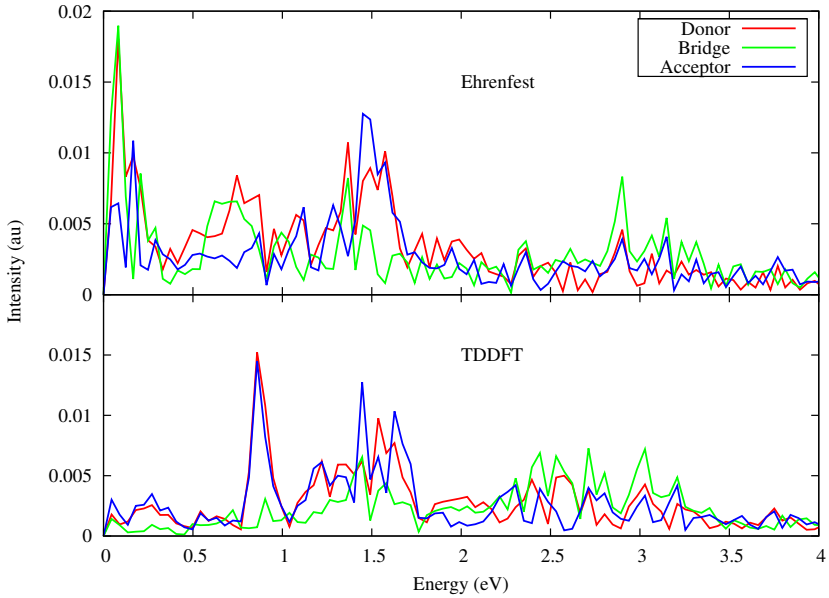

Figure 4.12: Fourier transforms of the time evolution of the natural charges of the DBA-6 cation, following a HOMO-LUMO excitation.

in the Ehrenfest dynamics. The low-energy peak can be attributed to the slow amplitude-modulation that is most apparent in the D and B groups. This peak appears near 0.1 eV, which corresponds to the 40 fs oscillation seen in Figure 4.11 due to molecular vibrations. The large peak at $\sim$ 1 eV in the pure electronic dynamics shows very strong overlap between the D and A charges and implying SX transfer, while in Ehrenfest dynamics the SX pathway has been partially quenched, leaving SQ as the dominant transfer pathway. In addition, a new bridge peak arises at $\sim$ 1 eV in Ehrenfest dynamics indicating the effect of the nuclear motion in the bridge on the ET dynamics, which is consistent with what was found in an Ehrenfest-electron-dynamics study by Pacheco and Iyengar.[269] For shorter times systems where SX plays a smaller role the dynamics of the ET will be effectively the same, while for shorter molecules that rely more heavily on SX as the transfer mechanism the effect can be more important.

4.1.5 Conclusions

In this section, we studied intramolecular charge transfer in model systems relevant to molecular junctions and photovoltaic applications. We have focused on the crossover between the two ET mechanisms, SX and SQ, on a series of DBA polyene dye systems with varying lengths of conjugated bridges. We prepared the initial states by either applying a static electric field to the molecules or inducing a single-electron photoexcitation, and carried out the electronic density matrix propagation using real-time TDDFT. In particular, we investigated the time evolution of the NPA charge and dipole moment of the molecules in both the SX and SQ regimes. It is found that the SX mechanism is dominant for the system with the shortest polyene bridge length, i.e., with two double bonds. As the polyene bridge is lengthened, the charge oscillation on the bridge becomes more correlated with the donor/acceptor and both the SX and SQ mechanisms contribute the ET event. For the polyene dyes with more than eight double bonds, the SQ charge transfer becomes predominant over the SX mechanism. The effect of nuclear motion on ET in the DBA-6 cation was studied using Ehrenfest dynamics. At very short times (<10 fs) the frozen nuclei approximation is nearly quantitatively valid, when compared to Ehrenfest dynamics. There are only minor subsequent alterations to the overall ET in the 10-100 fs time range. Most of the vibrational effects are manifested as relatively small, low-frequency modulations in the natural charge on the donor and bridge groups, with less effect on the acceptor group. We found the SQ mechanism to be less strongly affected than SX for the sub-100 fs time scale.

4.2 Non-Equilibrium QM/Continuum Embedding Theory for Studying Solvated Ultrafast Charge Transfer Dynamics

The Polarizable Continuum Models (PCMs) are some of the most inexpensive yet successful methods for including the effects of solvation in quantum-mechanical calculations of molecular systems. However, when applied to the electronic excitation process, these methods are restricted to dichotomously assuming either that the solvent has completely equilibrated with the excited solute charge density (infinite-time limit), or that it retains the configuration that was in equilibrium with the solute prior to excitation (zero-time limit.) This renders the traditional PCMs inappropriate for resolving time-dependent solvent effects on non-equilibrium solute electron dynamics like those implicated in the instants following photoexcitation of a solvated molecular species. To extend the existing methods to this non-equilibrium regime, we herein derive and apply a new formalism for a general time-dependent continuum embedding method designed to be propagated alongside the solute's electronic degrees of freedom in the time domain. Given the frequency-dependent dielectric constant of the solvent, an equation of motion for the dielectric polarization is derived within the PCM framework and numerically integrated simultaneously with the TDHF/TDDFT equations. Results for small molecular systems show the anticipated dipole quenching and electronic state dephasing/relaxation resulting from out-of-phase charge fluctuations in the dielectric and embedded quantum system.

4.2.1 Introduction

In spite of the transformative power and ubiquity of solvation effects across all branches of chemistry, a complete depiction of the solvation process from first principles is inherently intractable owing to the countless solvent degrees of freedom that contribute to the solute's electronic structure. In recognition of this insurmountable issue, generations of physical chemists have endeavored to reduce the dimensionality of the solvation problem in such a way that preserves the essential physics of this important interaction. Immense cost savings are realized upfront by sacrificing the quantum mechanical description of the solvent molecules in favor of a purely electrostatic model in which classical charges are used to

represent solvent atoms or group of atoms.[270–275] While this approach makes the inclusion of numerous solvent molecules in a given electronic structure calculation feasible, one is still faced with the challenge of ensemble-averaging these interactions over all thermally-accessible solvent/solute configurations to obtain statistically meaningful results. Often times, a large number of conformations must be sampled to achieve acceptable convergence for solvated molecular properties. Rather than explicitly sampling individual configurations only to later ensemble average them, one can circumvent the problem altogether by mapping all of the possible Coulomb interactions between solute and solvent onto the solute-solvent interface. Practically, this idea translates to a model in which the molecular system is embedded into a continuously polarizable dielectric medium with the dielectric permittivity of the solvent.[276–279] Forgoing the ability to resolve solvent molecules' positions obviously prevents any description of how the slow-moving nuclear degrees of freedom of the solvent impose limits on its polarization. This effect is unimportant for obtaining equilibrium solvated properties though, since all thermally-accessible solvent configurations contribute to the equilibrium properties. This concept forms the basis of the polarizable continuum model (PCM)[279] and its many variants[280–287] which attempt to capture solvent effects in electronic structure calculations for molecular systems with minimal additional computational effort.

Because of their low cost and satisfactory results, PCMs have become the standard methods by which the properties of solvated systems are approached in *ab initio* calculations. How, though, can these continuum embedding approaches be adapted to elucidate the influence of solvation on the time-evolution of *non*-equilibrium molecular systems, where the assumed solute-solvent equilibrium that these methods rely on is no longer satisfied? The goal of the current work is to derive and implement a time-dependent PCM formalism that can be faithfully applied to the problem of resolving ultrafast electronic dynamics of photo-excited molecular systems in solution.

In an effort to bridge the time-dependence gap between the equilibrium PCM models and the realistic (but wholly intractable) model in which the solvent degrees of freedom are treated equivalently with those of the solute, some of the authors have recently developed a real-time, naievely time-dependent equilibrium PCM (TDePCM)[15,17,288] method in which the solvent dielectric permittivity is relaxed from that of the high frequency (optical) limit to

the bulk dielectric constant according to the Debye relaxation model. The goal of the TDePCM development was to introduce the time-dependent solvent-solute interactive response and the solvent-induced electronic decoherence into first-principles electronic dynamics in a physically meaningful, but affordable fashion. The interaction between solute and solvent is modeled in TDePCM using the PCM method with the solute electron density evolution determined by integrating the time-dependent Hartree fock (TDHF) / density functional theory (TDDFT) equation.

With TDePCM we demonstrated that the relaxation of the dielectric constant brings about sufficient dephasing of the excited electronic state of the embedded system to non-trivially extend the excited state lifetime (relative to analogous calculations in vacuum) and bring it into far greater agreement with experiment. However, a critical shortcoming of the TDePCM method is that it still prescribes the self-consistent solution of the electrostatic problem at all times during the evolution of the embedded system. By solving such a problem at each step in the numerical integration of the TDHF/TDDFT equation, the dielectric response is artificially locked in-phase with the charge fluctuations of the embedded system. In this sense, the TDePCM model implicitly imposes equilibrium behavior for the dielectric's response to the non-equilibrium embedded system. The response of the dielectric medium that we recover with this treatment is that of the instantaneous polarization limit; a regime that is incapable of reproducing the dielectric medium's lagging response relative to the polarization fluctuations in a photo-excited embedded system. The TDePCM model is an acceptable and widely used approximation in quantum chemistry practice when the solvent response is in near-resonance with or much faster than the solute polarization fluctuation. However, this approximation breaks down for the dielectric response to a high-energy excitation in the embedded system which is the focus of this study. The retardation of the dielectric response must be fully accounted for in this case to accurately recreate the non-equilibrium solvation effects.

In order to escape from the instantaneous dielectric response limit, we must treat the time dependent response of the dielectric medium to the perturbation explicitly.[289–291] An embedding scheme of this type has implications reaching beyond the ability to resolve instantaneous/nonequilibrium solvent effects. Once outside of the memoryless, instantly-

polarized limit, continuum embedding represents a general framework through which the environmentally-induced dephasing of excited states can be tractably approached in real-time time-dependent electronic structure methods. Furthermore, since polarization of the dielectric medium occurs at an energetic cost to the embedded system, energy can be freely exchanged with and/or dissipated to the dielectric bath. The dephasing and dissipation afforded by propagating the bath degrees of freedom prevents revivals in excited state population that have plagued the interpretation of lifetimes calculated from real-time TDHF/TDDFT calculations, and brings them into better agreement with those observed experimentally for systems in their true chemical environments.

4.2.2 Methodology

A. Equation of Motion for Dielectric Relaxation

The standard "static" version of PCM implicitly assumes that the solute and solvent have interacted for a sufficiently long time for the solute charge distribution and solvent reaction field to reach equilibrium. When there is a sudden change in the solute charge distribution, for instance upon photo-excitation of the solute, the solvent configuration is thrust out of equilibrium with the new solute charge density and will time evolve according to charge fluctuations in the solute until equilibrium is reestablished some time later. To properly account for lag in solvent reorganization upon perturbation of the solute charge density with the polarizable continuum model, we follow the work by Ingrosso *et al.*[292] and derive a general expression for the time-dependent PCM equation. The response of the dielectric medium to a new solute charge distribution can be characterized by the time delay between the imposition of the external electric field and the resulting polarization of the medium. Under the assumption that the coupling between the external electric field and the dielectric medium is weak, the linear response approximation will suffice to describe the dielectric polarization. For a homogeneous medium, the linear response of the polarization P to a time-varying electric field E can be expressed as:

$$\mathbf{P}(\mathbf{r},t) = \int_{-\infty}^{t} \mathrm{d}t' \chi(t-t')\mathbf{E}(\mathbf{r},t') \tag{4.20}$$

where χ is the time domain response function of the dielectric medium, or the electric susceptibility. In the present case, it is assumed that the response function is local in space. Causality requires that $\chi(t) = 0$ for $t < 0$. Fourier transforming the above relationship and applying the convolution theorem, one obtains the following relation in the complex frequency domain

$$\tilde{\mathbf{P}}(\mathbf{r}, z) = \tilde{\chi}(z)\tilde{\mathbf{E}}(\mathbf{r}, z) \tag{4.21}$$

where $z = \omega - i\eta$ with ω the real component of the frequency and η being a small positive number.

Using the definition of the dielectric displacement $\mathbf{D} = \mathbf{E} + 4\pi\mathbf{P}$, we have

$$\tilde{\mathbf{D}}(\mathbf{r}, z) = \varepsilon(z)\tilde{\mathbf{E}}(\mathbf{r}, z) \tag{4.22}$$

where the frequency-dependent dielectric constant $\varepsilon(z)$ is given by

$$\varepsilon(z) = 1 + 4\pi\tilde{\chi}(z) \tag{4.23}$$

With the frequency-dependent displacement field, Gauss's law in the frequency domain reads:

$$\boldsymbol{\nabla} \cdot \tilde{\mathbf{D}}(\mathbf{r}, z) = 4\pi\tilde{\rho}(\mathbf{r}, z) \tag{4.24}$$

which leads to Poisson's equation in the frequency domain:

$$\boldsymbol{\nabla} \cdot \left[\varepsilon(\mathbf{r}, z)\boldsymbol{\nabla}\tilde{V}^{\mathrm{tot}}(\mathbf{r}, z)\right] = -4\pi\tilde{\rho}(\mathbf{r}, z) \tag{4.25}$$

where $\tilde{V}^{\text{tot}}(\mathbf{r}, z)$ is the frequency-dependent scalar potential that has contributions from both the solute and the surrounding medium. For a homogeneous medium, $\varepsilon(\mathbf{r}, z)$ is defined as

$$\varepsilon(\mathbf{r}, z) = \begin{cases} 1 & \mathbf{r} \in \text{cavity} \\ \varepsilon(z) & \mathbf{r} \notin \text{cavity} \end{cases} \tag{4.26}$$

The Fourier transform in the time-frequency domain does not affect the linearity of the boundary conditions imposed to solve the electrostatic problem. In particular, within the PCM approach, the continuity of the scalar potential and the displacement field in frequency domain may be written as:

$$\tilde{V}_{\text{in}}^{\text{tot}}(z) = \tilde{V}_{\text{out}}^{\text{tot}}(z) \tag{4.27}$$

$$\tilde{\mathbf{D}}_{\text{in}}^{\perp}(z) = \tilde{\mathbf{D}}_{\text{out}}^{\perp}(z) \tag{4.28}$$

Eqs. (4.25) - (4.28) are the same as the static equations, except that all the quantities are now frequency dependent. In the PCM approach, the polarization of the medium is represented by an apparent surface charge (ASC) density $\boldsymbol{\sigma}$ placed on the cavity surface. Practical applications of all PCM methods also require a discrete representation of the ASC density using a set of polarization charges q_i on a selected mesh of the cavity surface. Applying such a strategy, one thus obtains the frequency-dependent PCM equation:

$$\tilde{\mathbf{q}}(z) = \tilde{\mathbf{Q}}(z)\tilde{\mathbf{V}}^{s}(z) \tag{4.29}$$

where $\mathbf{q}$ is the vector containing the surface polarization charges and $\mathbf{V}^s$ is the vector containing the average solute potential over the mesh points. $\tilde{\mathbf{Q}}(z)$ is a square matrix collecting the cavity geometrical paramters and the dielectric constant of the medium that has different expressions depending on the particular models within the PCM family, but has the same form as in the static case. However, the static dielectric constant ε is now replaced with frequency-dependent $\varepsilon(z)$.

Fourier transforming Eq. (4.29) back to the time domain, one arrives at the equation of

motion for the solvent effective surface charges $\mathbf{q}(t)$:

$$\mathbf{q}(t) = \int_{-\infty}^{t} \mathrm{d}t' \mathbf{Q}(t-t') \mathbf{V}^s(t') \tag{4.30}$$

where $\mathbf{V}^s(t)$ is the time-dependent potential generated by the solute charge distribution. $\mathbf{Q}(t)$ is the inverse Fourier transform of $\tilde{\mathbf{Q}}(z)$, which is defined by the standard complex integration:

$$\mathbf{Q}(t) = \frac{1}{2\pi} \oint_C \mathrm{d}z e^{izt} \tilde{\mathbf{Q}}(z) \tag{4.31}$$

B. Coupled quantum many-electron dynamics with dielectric relaxation

Eq. (4.30) is the equation of motion for the dielectric relaxation. It describes the delayed response of the solvent effective surface charges $\mathbf{q}(t)$ to the time-varying potential $\mathbf{V}^s(t)$ generated by the time-dependent solute charge distribution, which may be obtained by integrating the corresponding equation of motion for the electronic degrees of freedom of the solute in the time domain.

In the present work, the time evolution of the solute electronic degrees of freedom is governed by the quantum Liouville equation within the TDHF/TDDFT[45,78,80,92] framework. The TDHF/TDDFT equation in an orthonormal basis is given in matrix form by[43,44,165]

$$\dot{\mathbf{P}}(t) = -i[\mathbf{K}(t), \mathbf{P}(t)] \tag{4.32}$$

where the Fock/Kohn-Sham matrix $\mathbf{K}(t)$ is a function of the time-dependent electronic density of the system, $\mathbf{P}(t)$, and the time-dependent polarization charges of the dielectric medium $\mathbf{q}(t)$.

In the atomic orbital basis and within the adiabatic DFT approximation, the time-dependent Fock/Kohn-Sham matrix $\mathbf{K}(t)$ is given by

$$\mathbf{K}'(\mathbf{P}'(t), \mathbf{q}(t)) = \mathbf{K}'^0(\mathbf{P}'(t)) + \mathbf{V}^\sigma(\mathbf{q}(t)) \tag{4.33}$$

where $\mathbf{V}^\sigma(\mathbf{q}(t))$ is the time-dependent interaction potential induced by the dielectric charge

density. $\mathbf{K}'^0(\mathbf{P}'(t))$ is the unperturbed yet implicitly time-dependent Fock/Kohn-Sham matrix of the solute in the atomic orbital basis, and is expressed as:

$$\mathbf{K}'^0(\mathbf{P}'(t)) = \mathbf{h} + \mathbf{J}[\mathbf{P}'(t)] + (1-\alpha)\mathbf{K}[\mathbf{P}'(t)] + \alpha\mathbf{V}_{xc}[\mathbf{P}'(t)] \tag{4.34}$$

where $\mathbf{h}$ is the one-electron Hamiltonian containing the electronic kinetic energy and electron-nuclear attraction potential, $\mathbf{J}$ and $\mathbf{K}$ are the two-electron Coulomb and exchange matrices respectively, and $\mathbf{V}_{xc}$ is the DFT exchange-correlation potential. α is a tuning parameter for hybrid functionals, where $\alpha = 0$ corresponds to pure Hartree-Fock exchange and $\alpha = 1$ to pure DFT functionals. An efficient method to compute $\mathbf{K}'^0(\mathbf{P}'(t))$ has been recently developed using fast integral methods and an adaptive-stepsize incremental Fock-built technique.[165]

Thus, the time evolution of the solvent and solute, governed by Eqs. (4.30) and (4.32), are coupled through the potentials $\mathbf{V}^s$ and $\mathbf{V}^\sigma$ induced by the solute and solvent, respectively. In our implementation, we have used a continuous surface charge (CSC) approach[293] within the PCM framework. Using the CSC approach, the solute and solvent potentials $\mathbf{V}^s$ and $\mathbf{V}^\sigma$ can be computed as:

$$V_i^s(t) = \sum_A \int \mathrm{d}^3\,\mathbf{r}\frac{Z_A\phi_i(\mathbf{r})}{|\mathbf{r}-\mathbf{R}_A|} - \sum_{\mu\nu} P'_{\mu\nu}(t)\iint \mathrm{d}^3\,\mathbf{r}\,\mathrm{d}^3\,\mathbf{r}'\frac{\phi_i(\mathbf{r})\chi_\mu(\mathbf{r}')\chi_\nu(\mathbf{r}')}{|\mathbf{r}-\mathbf{r}'|} \tag{4.35}$$

$$\mathrm{V}^\sigma_{\mu\nu}(t) = \sum_i \iint \mathrm{d}^3\,\mathbf{r}\,\mathrm{d}^3\,\mathbf{r}'\frac{q_i(t)\phi_i(\mathbf{r})\chi_\mu(\mathbf{r}')\chi_\nu(\mathbf{r}')}{|\mathbf{r}-\mathbf{r}'|} \tag{4.36}$$

where Z_A and R_A are nuclear charges and positions, $\{q_i\}$ are the solvent effective surface charges, ϕ_i are surface elements basis functions (spherical Gaussian functions in the current study) and $\{\chi_\mu\}$ are atomic orbital basis functions.

C. Implementation of the coupled dielectric-quantum-many-electron dynamics

To properly describe the solvated many-electron dynamics, one needs to carry out a simultaneous integration of both Eqs. (4.30) and (4.32), which can be numerically integrated using various techniques. For the solute electronic dynamics, we use a modified mid-point

and unitary transformation (MMUT) method[43,44,165] that has been successfully used in integrating the TDHF/TDDFT equation (Eq. (4.32)).

Integration of the equation of motion for the solvent, Eq. (4.30), is less straightforward, largely due to the rapid change of the solute potential $\mathbf{V}^s(t)$ which arises from fast oscillations of the solute charge distribution during the time evolution. Thus the integration step for the solvent cannot be much larger than that for the solute electronic propagation, even though the time scale of the solvent relaxation is much larger than that of the solute electronic transitions. Furthermore, direct computation of the PCM response function $\mathbf{Q}(t)$ using Eq. (4.31) may be cumbersome since one has to deal with the complex contour integration.

In the present implementation, we use a multi-step integration approach originally developed by Caricato *et al.*[294] to propagate the solvent polarization charges. In this approach, the time-dependent solute potential $\mathbf{V}^s(t)$ is expressed in terms of a series of stepwise changes, with each step synchronized with the solute electronic propagation, i.e.

$$\mathbf{V}^s(t) = \mathbf{V}^s(t_{-\infty}) + \theta(t)\Delta\mathbf{V}^s_0 + \theta(t-t_1)\Delta\mathbf{V}^s_1 + \cdots + \theta(t-t_{k-1})\Delta\mathbf{V}^s_{k-1}, \text{ for } t_{k-1} \le t < t_k \tag{4.37}$$

where $\theta(t)$ is the Heaviside step function. $\Delta\mathbf{V}^s_n$ are defined as the changes of the solute potential between each time interval and are given as

$$\Delta\mathbf{V}^s_n = \mathbf{V}^s(t_n) - \mathbf{V}^s(t_{n-1}), \text{ for } n \ge 1 \tag{4.38}$$

In deriving Eq. (4.37), we have considered the case where the solvent relaxation occurs upon instantaneous photo-excitation of the solute molecule. In this case, the solute electronic density distribution at time t_0 is changed from that of the ground-state to some excited state, which gives rise to a sudden change of the solute potential from $\mathbf{V}^s(t_{-\infty})$ to $\mathbf{V}^s(t_0)$. Namely,

$$\Delta\mathbf{V}^s_0 = \mathbf{V}^s(t_0) - \mathbf{V}^s(t_{-\infty}) \tag{4.39}$$

With the above expansion of the solute potential $\mathbf{V}^s(t)$ in time, the solvent equation of motion, Eq. (4.30), can be rewritten as:

$$\mathbf{q}(t) = \mathbf{q}(t_{-\infty}) + \left[\int_{-\infty}^{t} \mathrm{d}t' \mathbf{Q}(t-t')\theta(t')\right] \Delta\mathbf{V}_0^s + \left[\int_{-\infty}^{t} \mathrm{d}t' \mathbf{Q}(t-t')\theta(t'-t_1)\right] \Delta\mathbf{V}_1^s + \cdots + \left[\int_{-\infty}^{t} \mathrm{d}t' \mathbf{Q}(t-t')\theta(t'-t_{k-1})\right] \Delta\mathbf{V}_{k-1}^s, \text{ for } t_{k-1} \leq t < t_k \tag{4.40}$$

which can be expressed for simplicity as follows:

$$\mathbf{q}(t) = \mathbf{q}(t_{-\infty}) + \mathbf{R}(t)\Delta\mathbf{V}_0^s + \mathbf{R}(t-t_1)\Delta\mathbf{V}_1^s + \cdots + \mathbf{R}(t-t_{k-1})\Delta\mathbf{V}_{k-1}^s, \text{ for } t_{k-1} \leq t < t_k \tag{4.41}$$

where we have defined the propagation function $\mathbf{R}(t)$,

$$\mathbf{R}(t) = \int_{-\infty}^{t} \mathrm{d}t' \mathbf{Q}(t-t')\theta(t') \tag{4.42}$$

The above equation can be recast into an integration in real frequency space by taking the Fourier transform and applying the convolution theorem. Following the procedure of Hsu, Song and Marcus,[295] the propagation function $\mathbf{R}(t)$ can be computed as

$$\mathbf{R}(t) = \frac{2}{\pi} \int_0^{\infty} \mathrm{d}\omega \frac{\cos(\omega t)}{\omega} \operatorname{Im} \mathbf{Q}(\omega) + \mathbf{Q}(0) \tag{4.43}$$

where $Q(\omega)$ is the frequency-dependent PCM matrix with the frequency-dependent dielectric permittivity $\varepsilon(\omega)$, and $\mathbf{Q}(0)$ is the static PCM matrix.

Eq. (4.43) may be evaluated either analytically or numerically depending on the specific PCM method being used and the expression of the frequency-dependent dielectric permittivity $\varepsilon(\omega)$. In the current implementation, we use the conductor-like PCM model (CPCM)[296] for describing the solvent reaction field. Within the CPCM model, $\mathbf{Q}(\omega)$ and $\mathbf{Q}(0)$ are given

by

$$\mathbf{Q}(\omega) = -\frac{\varepsilon(\omega) - 1}{\varepsilon(\omega)}\mathbf{S}^{-1} \tag{4.44}$$

$$\mathbf{Q}(0) = -\frac{\varepsilon_0 - 1}{\varepsilon_0}\mathbf{S}^{-1} \tag{4.45}$$

where the matrix $\mathbf{S}$ depends on the shape of the cavity and is defined as

$$S_{ii} = 1.0694\sqrt{\frac{4\pi}{a_i}} \tag{4.46}$$

$$S_{ij} = \frac{1}{|\mathbf{r}_i - \mathbf{r}_j|} \tag{4.47}$$

with a_i denoting the area of i-th element of the surface mesh.

The frequency-dependent dielectric permittivity $\varepsilon(\omega)$ can be obtained either from some purely diffusive relaxation models or from direct experimental measurements of the absorption. In this work, we used the simple Debye relaxation model[297] for the frequency-dependent dielectric permittivity $\varepsilon(\omega)$:

$$\varepsilon(\omega) = \varepsilon_\infty + \frac{\varepsilon_0 - \varepsilon_\infty}{1 + i\omega\tau_D} \tag{4.48}$$

where ε_∞ is the infinite frequency dielectric permittivity of the medium and τ_D is the Debye relaxation time. The Debye model describes low-frequency, diffusive orientational relaxation of the solvent by a single exponential decay, characterized by the Debye relaxation time τ_D. Empirical modifications of the Debye model[298–300] and multi-exponential generalization[301] of Eq. (4.48) may also be used to give a better description of the solvent relaxation. A combined approach can also be applied, where the low-frequency part of dielectric permittivity is described by those empirical models and the high-frequency part is obtained from experimental data.

With the CPCM method and the Debye relaxation model, the propagation function $\mathbf{R}(t)$ in Eq. (4.43) can be integrated analytically and its final expression is given by

$$\mathbf{R}(t) = \left[-\frac{\varepsilon_0 - \varepsilon_\infty}{\varepsilon_0\varepsilon_\infty}e^{-t/\tau_L} + \frac{\varepsilon_0 - 1}{\varepsilon_0}\right]\mathbf{S}^{-1} \tag{4.49}$$

where τ_L is called the longitudinal relaxation time and is defined as

$$\tau_L = \frac{\varepsilon_\infty}{\varepsilon_0}\tau_D \tag{4.50}$$

The propagation function $\mathbf{R}(t)$ also exhibits a single exponential decay behavior, however, with a smaller characteristic time (τ_L) than the Debye relaxation time τ_D for highly polar solvents.

With the analytical expression for $\mathbf{R}(t)$ given in Eq. (4.49), the solvent surface charges can be calculated at every time step as:

$$\mathbf{q}(t_k) = \mathbf{q}(t_{-\infty}) + \mathbf{R}(t_k)\Delta\mathbf{V}_0^s + \mathbf{R}(t_{k-1})\Delta\mathbf{V}_1^s + \cdots + \mathbf{R}(t_1)\Delta\mathbf{V}_{k-1}^s \tag{4.51}$$

This equation, together with the MMUT-TDHF/TDDFT equation Eq. (2.55), forms the working equations for the solvated many-electron dynamics with dielectric relaxation.

4.2.3 Benchmark and Discussion

The coupled equations of PCM dielectric relaxation and the TDHF/TDDFT equation have been implemented in the development version of the GAUSSIAN suite of electronic structure programs.[302]

A. Solvent relaxation in a two-state problem: HeH^{2+}

To test our methodology, we first consider a simple two-state problem in a polar solvent. In this problem, the solute molecule is described by a two-state model, with the ground state in equilibrium with the solvent. Then the solute is suddenly promoted to its excited state, resulting in a change in the solute dipole moment. The solvent will slowly respond to this sudden change, and eventually reach equilibrium with the excited state. HeH^{2+} in the minimum STO-3G basis provides a good example for such two-state problem. In our simulation, we use water as the solvent and the Debye model for describing the dielectric relaxation. The static and optical dielectric permittivity of water are 78.36 and 1.78, respectively. We use a Debye relaxation time $\tau_D = 8.2$ ps.

Fig. 4.13(a) shows the time-evolution of the solvation energy, computed as follows:

$$\Delta E_{\text{solv}}(t) = \frac{1}{2}\left[\mathbf{V}^s(t)\right]^\dagger \mathbf{q}(t) \tag{4.52}$$

As can be seen, the solvation energy exhibits an exponential decay, which arises from the relaxation of the solvent according the Debye model. The relaxation life time is computed to be $\tau_L = 440$ fs, consistent with the analytical result. Since the excited state of HeH^{2+} is very stable, there will be no change in the solute charge density distribution and thus no change in the evolution of the solute dipole moment, which is not shown here. The relaxation of the solvent leads to reestablishment of equilibrium with the solute, during which there will be loss of the solute energy, which is depicted in Fig. 4.13(b).

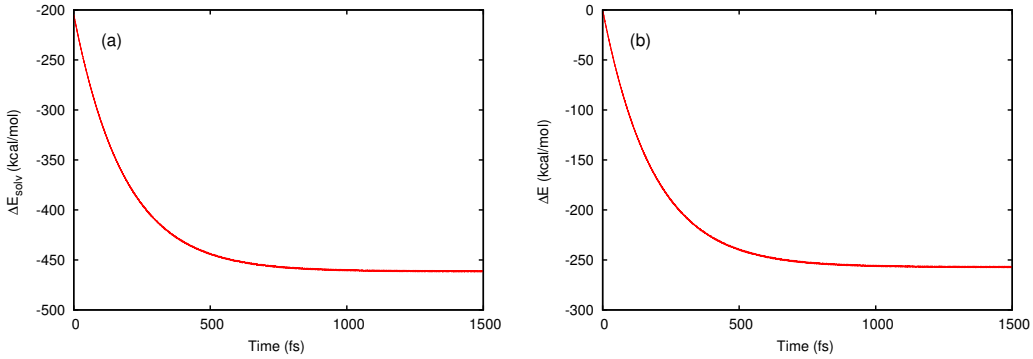

Figure 4.13: Time evolution of (a) solvation energy and (b) solute electronic energy after the photo-excitation of the solute HeH^{2+} molecule.

B. Effects of solvent relaxation on solute electronic dynamics: CO in water

Next we consider a more realistic case: the carbon monoxide molecule in water. We shall examine the effects of solvent relaxation on the electronic dynamics of the solute molecule. In our simulation, the HF/3-21G level of theory was used to describe the electronic dynamics of the CO molecule. For illustration purposes and computational convenience, we chose a pseudo relaxation time $\tau_D = 240$ fs for the water solvent and the Debye relaxation model

for the dielectric relaxation. The CO molecule was initially in its ground state and was in equilibrium with the solvent. Then it was promoted to its first excited state and the dynamical simulation of both the solute and solvent was carried out . Here we determine the nonequilibrium energy changes in terms of the solvation correlation function $S(t)$ defined as

$$S(t) = \frac{\Delta E_{\rm solv}(t) - \Delta E_{\rm solv}(\infty)}{\Delta E_{\rm solv}(0) - \Delta E_{\rm solv}(\infty)} \tag{4.53}$$

Fig. 4.14(a) shows the time-evolution of the solvation energy after the excitation of the CO molecule. As can be seen in Fig. 4.14(a), the solvation correlation energy exhibits fast oscillations due to the oscillation of the solute dipole. An overall exponential decay can still be observed, which is related to the Debye relaxation model. Fig. 4.14(b) illustrates the decay in both the solvent and solute dipole oscillation amplitudes indicative of a decoherence process. There is only smooth change in the solvent dipole due to the lagging response of the solvent to the change of the solute potential. As expected, both the solvation energy and the solute dipole will cease to oscillate as the simulation times approach infinity as the solute and solvent reach new equilibrium. This long-time behavior is further supported by the loss of the solute energy shown in Fig. 4.14(c).

C. Effects of solvent relaxation on charge transfer dynamics: pNA in acetonitrile

The study of charge transfer processes in solution has been gaining interest in recent years and presents challenges to experimentalists and theoreticians alike. Here, we examine the effects of the solvent (i.e. acetonitrile) relaxation on the charge transfer electronic dynamics of a p-nitroaniline (pNA) molecule. pNA is classic model for theoretical and experimental investigation[17,303,304] of charge transfer properties, due to the large change in the dipole moment upon photo-excitation. Using the pump-supercontinuum probe technique (PSCP), Kovalenko et al.[303] found that the ultrafast excited state relaxation of pNA in acetonitrile includes several stages with distinct time scales: the first 100 fs is characterized by solvent relaxation, followed by charge transfer and internal conversion governed by twisting of the -NO_2 group at 140 fs and 400 fs respectively. Although in a previous study[17] we reproduced

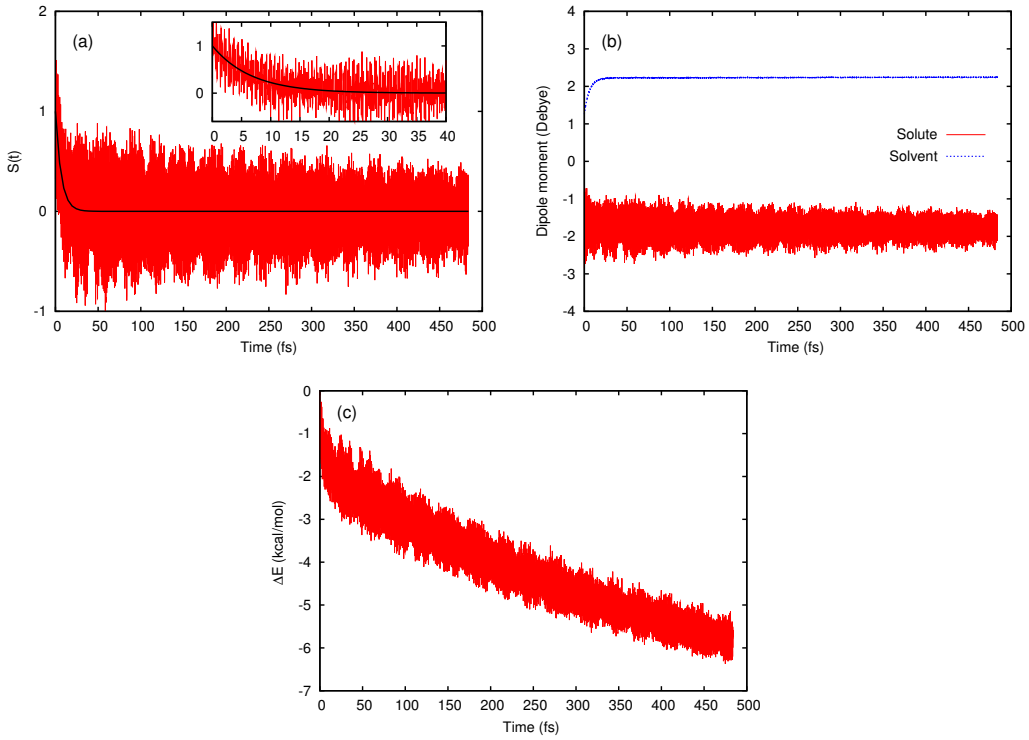

Figure 4.14: Time evolution of (a) solvation energy, (b) solute and solvent dipole moments, and (c) solute energy after the excitation of the CO molecule.

the charge transfer life time using the time-dependent equilibrium PCM (TDePCM) model, the use of a phenomenological, instantaneous dielectric response model does not take into account the retarded response of the solvent. In this study, we used the B3LYP/6-31G level of theory for the electronic dynamics of the pNA molecule. We chose the experimental relaxation time $\tau_D = 5.9$ ps[305] for the acetonitrile solvent and the Debye relaxation model for the dielectric relaxation. We used the static and optical dielectric permittivity of acetonitrile, i.e. $\varepsilon_0 = 35.69$ and $\varepsilon_\infty = 1.81$ respectively, and the CPCM model for the solvation. The pNA molecule was initially in its ground state and was in equilibrium with the solvent. The dynamical simulation was carried out after exciting the pNA molecule by promoting an electron from the HOMO to LUMO, which comprises the dominant contribution to the charge transfer excited state.

To examine the effect of the solvent relaxation on the charge transfer life time, we compute the time evolution of the occupation numbers of the HOMO and LUMO molecular orbitals, by projecting the time-dependent density onto the ground state molecular orbital space:

$$n_i(t_k) = \mathbf{C}_i(t_0)^\dagger \mathbf{P}(t_k) \mathbf{C}_i(t_0) \tag{4.54}$$

Fig. 4.15 shows the time evolution of the occupation numbers of the HOMO and LUMO molecular orbitals of pNA molecule in vacuum (top) and in acetonitrile (bottom). As seen in Fig. 4.15, in vacuum the charge transfer excited state of pNA quickly relaxes to the ground state within $\sim$ 10 fs via LUMO $\rightarrow$ HOMO transition, whereas in acetonitrile, the charge transfer excited state is stabilized by the solvent relaxation, showing a much longer lifetime ($\sim$ 70 fs). The simulated charge transfer life time is shorter than that observed experimentally ($\sim$ 140 fs) using transient absorption spectra.[303] This might be due to the lack of nuclear motion in the electronic dynamics simulation and the use of a small basis set.

Fig. 4.16 (a) shows the time evolution of the dipole moment of pNA after photo-excitation in acetonitrile. Accompanied by the LUMO $\rightarrow$ HOMO charge transfer, the dipole moment of pNA decreases from $\sim$ 17 Debye of the initial excited state to $\sim$ 11 Debye of the ground

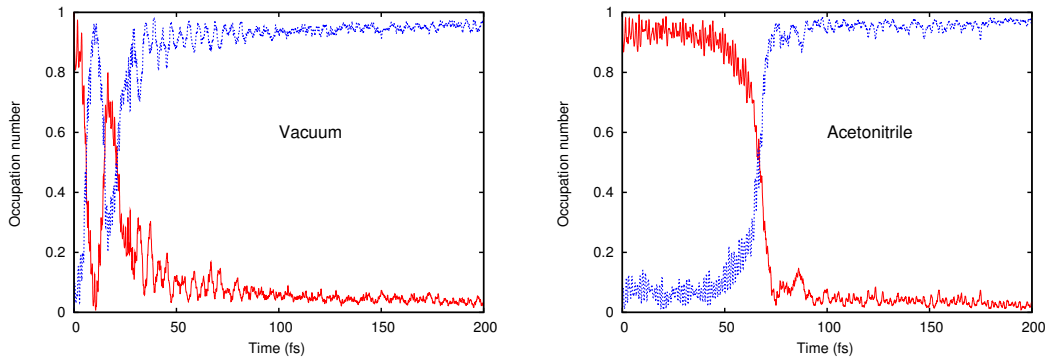

Figure 4.15: Time evolution of the HOMO (blue) and LUMO (red) occupation numbers in vacuum and in acetonitrile with TDPCM model after the photo-excitation of the pNA molecule.

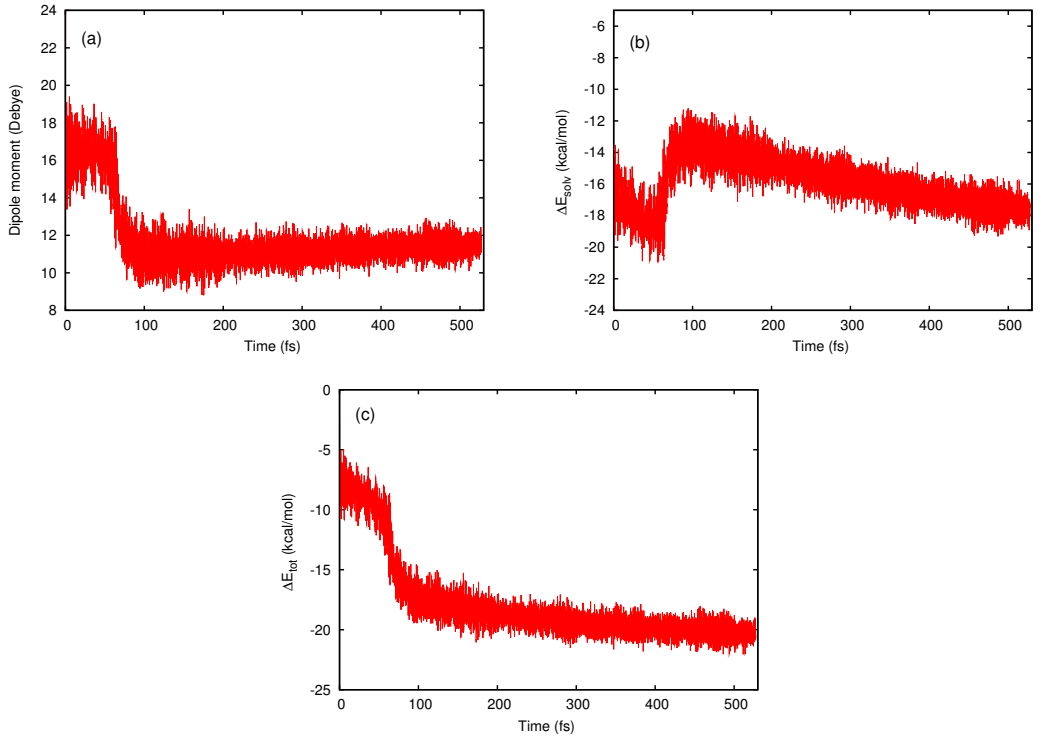

Figure 4.16: Time evolution of (a) solute dipole moment, (b) solvation energy, and (c) solute electronic energy after the excitation of the pNA molecule.

state, which proceeds at ~ 70 fs. Moreover, we observe a quenching of the dipole oscillations before and after the charge transfer, indicating the decoherence of the solute afforded by the solvent relaxation. Fig. 4.16 (b) shows the time evolution of the solvation energy. It is seen that within the first 70 fs, i.e. before the charge transfer occurs, the solvation energy exhibits an exponential decay as a result of the sovlent relaxation. This is followed by a raise in the solvation energy due to the charge transfer to the ground state. Once the charge transfer is complete, the solvent energy continues to decay until the solute and solvent reach new equilibrium. This process is in accordance with the loss of the solute energy displayed in Fig. 4.16 (c), which indicates the dissipation of the solute excitation energy to the surrounding medium.

4.2.4 Conclusions

In this section, we have derived working expressions to treat the time-dependent response of a dielectric medium to an instantaneous change in charge distribution of a molecular system embedded in this medium. These expressions were implemented in conjunction with the real-time TDHF/TDDFT methods, and used to resolve the electronic dynamics of a few small photoexcited molecules in solution. This work can be viewed as an extension of our previous efforts in this field which no longer makes the assumption that an instantaneous equilibrium is upheld throughout the electronic/dielectric time evolution. The developed formalism is centered around the use of a linear-response function to describe the retardation of the dielectric polarization, and requires only that the frequency-dependent dielectric constant for the solvent be known *a priori* and be input as a parameter. The frequency-dependent dielectric permittivity can be measured experimentally for use with the developed model, or some analytical treatment of $\varepsilon(\omega)$ can be used. For simplicity and consistency with our previous work, we have invoked the analytical Debye relaxation model for all calculations presented here. The derived equation of motion for the apparent surface charges that define the dielectric polarization were coupled to and numerically integrated alongside the electronic equation of motion in the TDHF/TDDFT formalism.

Applications of the work are not limited to the treatment of nonequilibrium solvation

effects. Rather, we have herein established a framework for the general treatment of electronic dephasing and energy dissipation in first-principles electronic dynamics calculations. For example, the dielectric medium that has been hitherto considered to represent a solvent could just as well act as a cost effective stand-in for an infinitely extended semiconductor lattice.

Chapter 5

AB INITIO SPIN DYNAMICS

5.1 *Ab Initio* Non-Relativistic Spin Dynamics Using Two-Component Spinors

Many magnetic materials do not conform to the (anti-)ferromagnetic paradigm where all electronic spins are aligned to a global magnetization axis. Unfortunately, most electronic structure methods cannot describe such materials with noncollinear electron spin on account of formally requiring spin alignment. To overcome this limitation, it is necessary to generalize electronic structure methods and allow each electron spin to rotate freely. Here we report the development of an *ab initio* time-dependent non-relativistic two-component spinor (TDN2C), which is a generalization of the time-dependent Hartree-Fock equations. Propagating the TDN2C equations in the time domain allows for the first-principles description of spin dynamics. A numerical tool based on the Hirshfeld partitioning scheme is developed to analyze the time-dependent spin magnetization. In this work, we also introduce the coupling between electron spin and a homogenous magnetic field into the TDN2C framework to simulate the response of the electronic spin degrees of freedom to an external magnetic field. This is illustrated for several model systems, including the spin-frustrated Li_3 molecule. Exact agreement is found between numerical and analytic results for Larmor precession of hydrogen and lithium atoms. The TDN2C method paves the way for the *ab initio* description of molecular spin transport and spintronics in the time domain.

5.1.1 Introduction

Spin-based technology takes on an ever-increasing role in material design as scientists and engineers seek to utilize and manipulate spins to maximize the quantum yield of solar cells, to process quantum information, and to resolve complex molecular structure. Fundamental to these scientific and technological applications are the spin-dependent many-electron dy-

namics.[306–309] To date, most theoretical investigations on molecular spintronics rely on the use of effective model Hamiltonians which depend on experimental parameterization[310–313] and focus on collinear spin systems, in which all the spin magnetizations are aligned along a single anisotropy axis. While these methods have their merits, they are limited in their description of the time-dependent nature of the spin-dependent many-electron wave function. This is especially true for phenomena driven by strong spin non-collinearity, spin-orbit coupling or by interaction with intense electromagnetic fields. A proper description of spin dynamics must come from a solution of the first-principles spin-dependent Hamiltonian in the time domain.

Most standard electronic structure methods, however, cannot treat systems involving non-collinear spins because they formally require electronic spins to be aligned (anti-)parallel with respect to each other. In both the unrestricted Hartree-Fock (UHF) and spin-density density functional theories (SDFT), the one-electron spin orbitals are required to be eigenfunctions of the spin operator $\hat{S}_z$. Practically, this means requiring the number of spin-up and spin-down electrons to be conserved in the solution of the self-consistent-field (SCF) equations. As a result, spin orbitals are a product of a spatial function with either a spin-up or spin-down component. This description is equivalent to the assumption of collinear spins, i.e. there exists a global spin quantization axis for the whole system, and the magnetization vector $\mathbf{m}(\mathbf{r})$ is of the same direction at all points in space.

In order to treat non-collinear spins, one needs to retain the full vector form of the magnetization $\mathbf{m}(\mathbf{r})$ and let each spin rotate freely. This is equivalent to writing the spin orbitals as a superposition of the spin-up and spin-down states. For Hartree-Fock, this leads to the generalized Hartree-Fock (GHF) method,[314] which is similar in structure to the wave function used in two-component relativistic models. For DFT, a generalization of the functionals to account for non-collinear spins is required.[315–320]

From the point of view of electronic dynamics, the extension of the collinear DFT and HF to the time domain gives rise to the time-dependent density functional theory (TDDFT) and time-dependent Hartree-Fock (TDHF).[45,76–82,92,157,321] In particular, the real-time formalism of TDDFT/TDHF (RT–TDDFT/RT–TDHF) has proven to be a promising method for revealing the physical underpinnings of dynamical multi-electron phenomena.[19,37,43,44,165]

However, these methods are unable to capture the spin dynamics driven by an external magnetic field, or an internal magnetic field generated by the motion of other electrons within the system. Implicit to the single Slater determinant based RT–TDDFT/RT–TDHF method are the constraints that spin state of each electron cannot change during the time-evolution and that they are collinear with respect to each other. These constraints prevent conventional RT–TDDFT/RT–TDHF from fully accounting for spin-dependent many-electron dynamics.

In order to describe non-collinear spin dynamics, we extend the generalized Hartree-Fock to the time domain, giving rise to the real-time time-dependent non-relativistic two-component spinor (RT–TDN2C) method. We present in this work the mathematical formalism and numerical implementation with case studies of non-collinear spin dynamics in response to an external magnetic field. To the best of our knowledge, this work is the first attempt to address many-body spin dynamics within the full ab initio description.

5.1.2 Methodology

A. Time-Dependent Non-Relativistic Two-Component Spinor Formalism

In the time-dependent Hartree-Fock (TDHF) theory, the N-electron wave function is represented by a single Slater determinant $\psi(t)$ composed of N time-dependent spin orbitals, $\{\psi_k(\mathbf{x},t)\}$

$$\psi(t) = \frac{1}{\sqrt{N!}} \begin{vmatrix} \psi_1(\mathbf{x}_1,t) & \psi_2(\mathbf{x}_1,t) & \dots & \psi_N(\mathbf{x}_1,t) \\ \psi_1(\mathbf{x}_2,t) & \psi_2(\mathbf{x}_2,t) & \dots & \psi_N(\mathbf{x}_2,t) \\ \vdots & \vdots & \ddots & \vdots \\ \psi_1(\mathbf{x}_N,t) & \psi_2(\mathbf{x}_N,t) & \dots & \psi_N(\mathbf{x}_N,t) \end{vmatrix} \tag{5.1}$$

where the variable $\mathbf{x}$ includes both the spatial coordinate $\mathbf{r}$ and the spin coordinate $\boldsymbol{\omega}$ for one electron.

Applying the Dirac-Frenkel time-dependent variational principle to this approximate wave function, we obtain the equations of motion for the single-particle spin orbitals,

$$i\frac{\partial}{\partial t}\psi_k(\mathbf{x},t) = \hat{f}(t)\psi_k(\mathbf{x},t) \tag{5.2}$$

where $\hat{f}$ is the Fock operator. Equivalently, Eq. (5.2) can be written in the Liouville-von Neumann form:

$$i\frac{\partial\hat{\gamma}(t)}{\partial t} = \left[\hat{f}(t), \hat{\gamma}(t)\right] \tag{5.3}$$

where $\hat{\gamma}(t)$ is the reduced single-particle density operator and is defined by

$$\hat{\gamma}(t) = \sum_{i}^{N} |\psi_k(t)\rangle\langle\psi_k(t)| \tag{5.4}$$

In order to allow for non-collinearity, we express the time-dependent spin orbitals as a time-dependent two-component spinor,

$$\psi_k(\mathbf{x}, t) = \begin{pmatrix} \phi_k^{\alpha}(\mathbf{r}, t) \\ \phi_k^{\beta}(\mathbf{r}, t) \end{pmatrix} \tag{5.5}$$

where the spatial functions $\{\phi_k^{\alpha}(\mathbf{r}, t)\}$, $\{\phi_k^{\beta}(\mathbf{r}, t)\}$ are expanded in terms of a common set of real atomic orbital (AO) basis functions $\{\chi_\mu(\mathbf{r})\}$

$$\phi_k^{\alpha}(\mathbf{r}, t) = \sum_{\mu} C_{\mu k}^{\alpha}(t)\chi_\mu(\mathbf{r}) \tag{5.6}$$

$$\phi_k^{\beta}(\mathbf{r}, t) = \sum_{\mu} C_{\mu k}^{\beta}(t)\chi_\mu(\mathbf{r}) \tag{5.7}$$

where the time-dependent expansion coefficients C's can be of complex values. With the definition of the two-component spinor, the time-dependent single-particle density operator can be formulated with the following spin-blocked structure:

$$\hat{\gamma}(t) = \begin{pmatrix} \hat{\gamma}^{\alpha\alpha}(t) & \hat{\gamma}^{\alpha\beta}(t) \\ \hat{\gamma}^{\beta\alpha}(t) & \hat{\gamma}^{\beta\beta}(t) \end{pmatrix} \tag{5.8}$$

In AO basis, its matrix form can be written as

$$\mathbf{P}'(t) = \begin{pmatrix} \mathbf{P}'^{\alpha\alpha}(t) & \mathbf{P}'^{\alpha\beta}(t) \\ \mathbf{P}'^{\beta\alpha}(t) & \mathbf{P}'^{\beta\beta}(t) \end{pmatrix} \tag{5.9}$$

where each spin block $\mathbf{P}'^{\sigma\tau}(t)$ is given by

$$P'^{\sigma\tau}_{\mu\nu}(t) = \sum_{i}^{N} C^{\sigma}_{\mu i}(t) \cdot C^{\tau *}_{\nu i}(t) \tag{5.10}$$

The Fock matrix in the AO basis also takes a spin-blocked form analogous to the density matrix:

$$\mathbf{F}'(t) = \begin{pmatrix} \mathbf{F}'^{\alpha\alpha}(t) & \mathbf{F}'^{\alpha\beta}(t) \\ \mathbf{F}'^{\beta\alpha}(t) & \mathbf{F}'^{\beta\beta}(t) \end{pmatrix} \tag{5.11}$$

where each spin block $\mathbf{F}'^{\sigma\tau}(t)$ is given by

$$\mathbf{F}'^{\sigma\tau}(t) = \mathbf{h}'^{\sigma\tau}(t) + \delta_{\sigma\tau}\left[\mathbf{J}'^{\alpha\alpha}(t) + \mathbf{J}'^{\beta\beta}(t)\right] - \mathbf{K}'^{\sigma\tau}(t) \tag{5.12}$$

where $\mathbf{h}'^{\sigma\tau}$ is the one-electron Hamiltonian matrix, whose time-dependence arises from the interaction of the spin system with external electromagnetic perturbations (to be discussed

in Sec. B.). $\mathbf{J}'$ and $\mathbf{K}'$ are Coulomb and exchange matrices, respectively,

$$\begin{aligned} J'^{\sigma\sigma}_{\mu\nu}(t) \equiv \langle\mu|\hat{J}^{\sigma\sigma}|\nu\rangle &= \sum_j^N \int dr_1 dr_2 \chi^*_\mu(1)\phi^{\sigma *}_j(2) r_{12}^{-1} \phi^\sigma_j(2)\chi_\nu(1) \\ &= \sum_j^N \sum_{\lambda\kappa} C^\sigma_{\lambda j}(t)\cdot C^{\sigma *}_{\kappa j}(t) \int dr_1 dr_2 \chi^*_\mu(1)\chi^*_\kappa(2) r_{12}^{-1}\chi_\lambda(2)\chi_\nu(1) \\ &= \sum_{\lambda\kappa} P'^{\sigma\sigma}_{\lambda\kappa}(t)\cdot\big(\mu\nu|\kappa\lambda\big) \end{aligned} \tag{5.13}$$

$$\begin{aligned} K'^{\sigma\tau}_{\mu\nu}(t) \equiv \langle\mu|\hat{K}^{\sigma\tau}|\nu\rangle &= \sum_j^N \int dr_1 dr_2 \chi^*_\mu(1)\phi^{\tau *}_j(2) r_{12}^{-1} \chi_\nu(2)\phi^\sigma_j(1) \\ &= \sum_j^N \sum_{\lambda\kappa} C^\sigma_{\lambda j}(t)\cdot C^{\tau *}_{\kappa j}(t) \int dr_1 dr_2 \chi^*_\mu(1)\chi^*_\kappa(2) r_{12}^{-1}\chi_\nu(2)\chi_\lambda(1) \\ &= \sum_{\lambda\kappa} P'^{\sigma\tau}_{\lambda\kappa}(t)\cdot\big(\mu\lambda|\kappa\nu\big) \end{aligned} \tag{5.14}$$

We use a set of atom-centered atomic orbital basis functions which form a non-orthogonal basis set. The density and Fock matrices are then transformed from the AO basis to an orthonormal basis using the following equations,

$$\begin{pmatrix} \mathbf{P}^{\alpha\alpha}(t) & \mathbf{P}^{\alpha\beta}(t) \\ \mathbf{P}^{\beta\alpha}(t) & \mathbf{P}^{\beta\beta}(t) \end{pmatrix} = \begin{pmatrix} \mathbf{V} & 0 \\ 0 & \mathbf{V} \end{pmatrix} \cdot \begin{pmatrix} \mathbf{P}'^{\alpha\alpha}(t) & \mathbf{P}'^{\alpha\beta}(t) \\ \mathbf{P}'^{\beta\alpha}(t) & \mathbf{P}'^{\beta\beta}(t) \end{pmatrix} \cdot \begin{pmatrix} \mathbf{V}^T & 0 \\ 0 & \mathbf{V}^T \end{pmatrix} \tag{5.15}$$

$$\begin{pmatrix} \mathbf{F}^{\alpha\alpha}(t) & \mathbf{F}^{\alpha\beta}(t) \\ \mathbf{F}^{\beta\alpha}(t) & \mathbf{F}^{\beta\beta}(t) \end{pmatrix} = \begin{pmatrix} \mathbf{V}^{-T} & 0 \\ 0 & \mathbf{V}^{-T} \end{pmatrix} \cdot \begin{pmatrix} \mathbf{F}'^{\alpha\alpha}(t) & \mathbf{F}'^{\alpha\beta}(t) \\ \mathbf{F}'^{\beta\alpha}(t) & \mathbf{F}'^{\beta\beta}(t) \end{pmatrix} \cdot \begin{pmatrix} \mathbf{V}^{-1} & 0 \\ 0 & \mathbf{V}^{-1} \end{pmatrix} \tag{5.16}$$

The transformation matrix $\mathbf{V} = \mathbf{S}^{1/2}$ in the Löwdin orthonormalization method, or obtained by the Cholesky decomposition $\mathbf{S} = \mathbf{V}^T\mathbf{V}$, where $\mathbf{S}$ is the overlap matrix of AO basis functions, $S_{\mu\nu} = \langle\mu|\nu\rangle$.

The final density-matrix based TDN2C Liouville-von Neumann equation in the orthonormal

basis can be written as:

$$i\frac{\partial}{\partial t}\begin{pmatrix}\mathbf{P}^{\alpha\alpha}(t) & \mathbf{P}^{\alpha\beta}(t)\\ \mathbf{P}^{\beta\alpha}(t) & \mathbf{P}^{\beta\beta}(t)\end{pmatrix} = \left[\begin{pmatrix}\mathbf{F}^{\alpha\alpha}(t) & \mathbf{F}^{\alpha\beta}(t)\\ \mathbf{F}^{\beta\alpha}(t) & \mathbf{F}^{\beta\beta}(t)\end{pmatrix}, \begin{pmatrix}\mathbf{P}^{\alpha\alpha}(t) & \mathbf{P}^{\alpha\beta}(t)\\ \mathbf{P}^{\beta\alpha}(t) & \mathbf{P}^{\beta\beta}(t)\end{pmatrix}\right] \tag{5.17}$$

Equation (5.17) is the working equation to describe the time-evolution of the non-relativistic two-component spinor. It can be considered as a time-dependent extension of the generalized Hartree-Fock equation. As with most time-dependent electronic structure theories, Eq. (5.17) can be solved in a response formalism in the frequency domain or propagated explicitly in the time-domain. In the following methodology sections we will present a time-propagation approach and perturbation terms arising from the interaction between a spin system and a static magnetic field, as well as a method designed to analyze spin magnetization in the time-domain.

To obtain a time-evolution dynamics of a spin system, the time-dependent equation for non-relativistic two-component spinors (Eq. (5.17)) is integrated with a modified midpoint and unitary transformation (MMUT) algorithm.[43,44]

B. Two-Component Spinor in the Presence of a Static Magnetic Field

The formalism of the non-relativistic two-component spinor allows realistic simulations of non-collinear spin dynamics within the ab initio framework. In this work, we consider a spin system interacting with an external uniform magnetic field $\mathbf{B}$. The effective perturbation term enters the one electron Hamiltonian as:[322,323]

$$\hat{h}(\mathbf{x}_1) = \hat{h}_0(\mathbf{r}_1) + \mu_S\boldsymbol{\sigma}\cdot\mathbf{B} + \mu_L\mathbf{L}\cdot\mathbf{B} + \frac{1}{2}\mu_L^2\left(\mathbf{B}\times\mathbf{r}_1\right)^2 \tag{5.18}$$

where $\hat{h}_0$ is the unperturbed one-electron Hamiltonian. $\mu_S = \frac{1}{2}g_s\mu_B$ is the electron magnetic dipole factor, with g_s denoting the spin g-factor and μ_B the Bohr magneton. $\boldsymbol{\sigma}$ are the Pauli matrices. $\mu_L = \mu_B$ is the orbital magnetic dipole factor. $\mathbf{L}$ is the orbital angular momentum. The last two terms represent the interaction of the orbital angular momentum with the magnetic field and the higher order term that is quadratic in the field strength.

These two terms will affect the time evolution of the spatial distribution of the electrons and thus affect the total energy of the system. For weak magnetic fields (e.g. $< 10^{-4}$ a.u.), the contributions of the last two terms are small and will be neglected here. Thus we only consider the interaction of the electron spin with the magnetic field:

$$\hat{h}(\mathbf{x}_1) = \hat{h}_0(\mathbf{r}_1) + \mu_S \boldsymbol{\sigma} \cdot \mathbf{B} \tag{5.19}$$

$\boldsymbol{\sigma}$ are the Pauli matrices, and their action on the spin eigenfunctions gives:

$$\sigma_x|\alpha\rangle = |\beta\rangle \qquad \sigma_x|\beta\rangle = |\alpha\rangle \tag{5.20a}$$

$$\sigma_y|\alpha\rangle = i|\beta\rangle \qquad \sigma_y|\beta\rangle = -i|\alpha\rangle \tag{5.20b}$$

$$\sigma_z|\alpha\rangle = |\alpha\rangle \qquad \sigma_z|\beta\rangle = -|\beta\rangle \tag{5.20c}$$

Using the above relations, we can write the one-electron Hamiltonian as follows:

$$\hat{h}^{\alpha\alpha} \equiv \langle\alpha|\hat{h}(\mathbf{x}_1)|\alpha\rangle = \hat{h}_0(\mathbf{r}_1) + \mu_S B_z \tag{5.21a}$$

$$\hat{h}^{\alpha\beta} \equiv \langle\alpha|\hat{h}(\mathbf{x}_1)|\beta\rangle = \mu_S(B_x - iB_y) \tag{5.21b}$$

$$\hat{h}^{\beta\alpha} \equiv \langle\beta|\hat{h}(\mathbf{x}_1)|\alpha\rangle = \mu_S(B_x + iB_y) \tag{5.21c}$$

$$\hat{h}^{\beta\beta} \equiv \langle\beta|\hat{h}(\mathbf{x}_1)|\beta\rangle = \hat{h}_0(\mathbf{r}_1) - \mu_S B_z \tag{5.21d}$$

The resulting one-electron Hamiltonian matrix in the spin-blocked form in the AO basis is

$$\mathbf{h}' = \begin{pmatrix} \mathbf{h}'^{\alpha\alpha} & \mathbf{h}'^{\alpha\beta} \\ \mathbf{h}'^{\beta\alpha} & \mathbf{h}'^{\beta\beta} \end{pmatrix} = \begin{pmatrix} \mathbf{h}'_0 + \mu_S B_z \mathbf{S} & \mu_S(B_x - iB_y)\mathbf{S} \\ \mu_S(B_x + iB_y)\mathbf{S} & \mathbf{h}'_0 - \mu_S B_z \mathbf{S} \end{pmatrix} \tag{5.22}$$

In the time-dependent non-relativistic two-component formalism, Eq. (5.22) enters the Fock matrix in Eq. (5.17). The effect of the interaction between the spin system and external homogeneous magnetic field will drive the spin dynamics propagated by the MMUT algorithm in Eq. (2.55).

The effective spin Hamiltonian approach can be considered as a result of taking the

non-relativistic limit of the Dirac equation for a spin in a homogeneous magnetic field. This is a simple step to test the time-dependent non-relativistic two-component formalism and algorithms presented here as the analytical solution is readily obtainable. The prospectus of including other perturbative terms will be discussed.

C. Spin Magnetization Analysis

The time evolution of the electron density $n(\mathbf{r},t)$ and the spin magnetization density vector $\mathbf{m}(\mathbf{r},t)$ are defined through the reduced density matrix $\gamma(t)$:

$$n(\mathbf{r},t) = \mathrm{Tr}[\gamma(t)] = \gamma^{\alpha\alpha}(t) + \gamma^{\beta\beta}(t) \tag{5.23}$$

$$\mathbf{m}(\mathbf{r},t) = \begin{pmatrix} m_x(\mathbf{r},t) \\ m_y(\mathbf{r},t) \\ m_z(\mathbf{r},t) \end{pmatrix} = \mathrm{Tr}[\boldsymbol{\sigma}\gamma(t)] = \begin{pmatrix} \gamma^{\alpha\beta}(t) + \gamma^{\beta\alpha}(t) \\ i\left[\gamma^{\alpha\beta}(t) - \gamma^{\beta\alpha}(t)\right] \\ \gamma^{\alpha\alpha}(t) - \gamma^{\beta\beta}(t) \end{pmatrix} \tag{5.24}$$

In the AO basis, they are expressed as

$$n(\mathbf{r},t) = \sum_{\mu\nu}\left[P'^{\alpha\alpha}_{\mu\nu}(t) + P'^{\beta\beta}_{\mu\nu}(t)\right]\chi_\mu(\mathbf{r})\chi_\nu(\mathbf{r}) \tag{5.25a}$$

$$m_x(\mathbf{r},t) = \sum_{\mu\nu}\left[P'^{\alpha\beta}_{\mu\nu}(t) + P'^{\beta\alpha}_{\mu\nu}(t)\right]\chi_\mu(\mathbf{r})\chi_\nu(\mathbf{r}) \tag{5.25b}$$

$$m_y(\mathbf{r},t) = i\sum_{\mu\nu}\left[P'^{\alpha\beta}_{\mu\nu}(t) - P'^{\beta\alpha}_{\mu\nu}(t)\right]\chi_\mu(\mathbf{r})\chi_\nu(\mathbf{r}) \tag{5.25c}$$

$$m_z(\mathbf{r},t) = \sum_{\mu\nu}\left[P'^{\alpha\alpha}_{\mu\nu}(t) - P'^{\beta\beta}_{\mu\nu}(t)\right]\chi_\mu(\mathbf{r})\chi_\nu(\mathbf{r}) \tag{5.25d}$$

To characterize the electron spin dynamics, we examine the evolution of the atomic magnetic moments computed using Hirshfeld partitioning scheme.[324] In this approach, one defines a pro-molecular or fuzzy magnetization density $\mathbf{m}^{\mathrm{mol}}(\mathbf{r})$ that is composed of spherically averaged magnetization densities of the atoms $\mathbf{m}_A^{\mathrm{pro}}(\mathbf{r})$:

$$\mathbf{m}^{\mathrm{mol}}(\mathbf{r}) = \sum_A \mathbf{m}_A^{\mathrm{pro}}(\mathbf{r}) \tag{5.26}$$

where A's are the indices of atomic centers. The atomic contribution of the total magnetization density, i.e. the atomic magnetic moments, $\mathbf{m}_A(t)$ can be calculated through the weight function $w_A(\mathbf{r})$:

$$w_A(\mathbf{r}) = \frac{\mathbf{m}_A^{\text{pro}}(\mathbf{r})}{\mathbf{m}^{\text{mol}}(\mathbf{r})} \tag{5.27}$$

$$\mathbf{m}_A(t) = \int d\mathbf{r} w_A(\mathbf{r}) \mathbf{m}(\mathbf{r}, t) \tag{5.28}$$

The resulting time-dependent atomic magnetization moment $\mathbf{m}_A(t)$ provides a convenient way for analyzing the time-evolution of spin dynamics in a many-body system.

5.1.3 Benchmark and Discussion

Evolution of a quantum mechanical spin $\frac{1}{2}$ particle in a uniform magnetic field is a well-known two-state problem in the literature and in textbooks. Particularly, in the absence of spin dephasing mechanisms, the expectation value of the spin magnetic moment rotates about the magnetic field with a constant angular velocity, behaving like a classical angular momentum of modulus $\frac{1}{2}$ (also known as Larmor precession). The angular frequency of the precession (Larmor frequency) is $\omega_0 = 2\mu_S|\mathbf{B}|$ where μ_S is the electron magnetic dipole moment, $\mu_S \approx \frac{1}{2}$ a.u.

The Hirshfeld atomic moment is analyzed on-the-fly using the time-dependent magnetization densities. In this work, we choose three test cases to illustrate the spin dynamics within the framework of ab initio time-dependent non-relativistic two-component spinor: (1) one electron with one unpaired spin, (2) many electrons with one unpaired spin, and (3) many electrons with three non-collinear spins. Integration of the time-dependent non-relativistic two-component equation with the modified mid-point and unitary transformation (MMUT) algorithm is implemented in the development version of GAUSSIAN program.[302] The integration step size of 0.05 a.u. ($\sim$1.21 attoseconds) is used for all test cases.

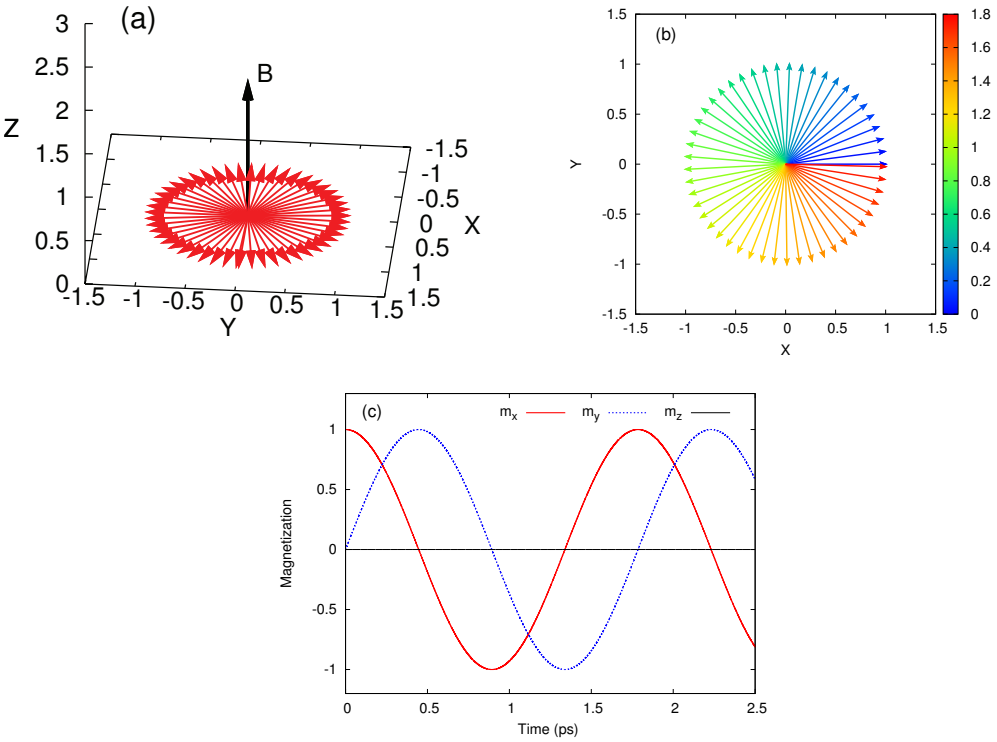

Figure 5.1: Time evolution of the electron spin magnetization (in the unit of Bohr magneton) of a hydrogen atom in a uniform magnetic field. The initial spin is polarized along the x axis. The magnetic field is positioned perpendicular to the $x-y$ plane: (a) 3D view of the precession of the overall magnetization vector about the magnetic field; (b) the xy-plane projection of the magnetization over time (the time-evolution is represented as the progression of coloration in the unit of picosecond); and (c) the evolutions of the x, y, and z components of spin magnetization.

A. Hydrogen Atom in a Uniform Magnetic Field

The hydrogen atom with a minimum STO-3G basis set provides an ideal test case for a simple two spin-state problem. In our simulation, the initial electron spin was aligned along x axis of the reference frame. A magnetic field was applied along z direction with a constant magnitude of 8.5×10^{-5} a.u., corresponding to ∼20 Tesla. Figure 5.1(a) and (b) show the time evolution of the spin magnetization. As time evolves, the electron spin gradually changes its direction and exhibits a perfect precession about the applied magnetic field. Figure 5.1(c) displays the evolution of the x, y and z components of the spin magnetization. As seen from Figure 5.1(c), time-evolutions of spin magnetization (i.e. Larmor type precession) exhibit sinusoidal behavior, with an angular frequency $\omega = 8.5 \times 10^{-5}$ a.u. This result is in excellent agreement with the analytic Larmor frequency $\omega_0 = 8.5 \times 10^{-5}$ a.u. In the absence of any spin dephasing mechanism, the Larmor type of precession of spin magnetization persists without any decay and the simulation also nicely demonstrates such a phenomenon.

B. Li Atom in a Uniform Magnetic Field

Now we use lithium atom as an example to illustrate spin dynamics of a multi-electron system. The 3-21G basis set is used in this study to test the stability of the two-component spinor dynamics with a slightly larger basis set. The initial spin magnetization is aligned along the y axis of the reference frame, with the two $1s$ spins pointing in opposite directions with respect to each other, and the single $2s$ spin pointing in the y direction. The total spin magnetization is 1/2. A homogenous magnetic field is applied with a polar angle $\theta = 45^\circ$ about z axis, and an azimuthal angle $\phi = 45^\circ$ about x axis. The field strength was again chosen to be 8.5×10^{-5} a.u. (∼20 Tesla). Figure 5.2(a) shows the time evolution of the total spin magnetization. As can be seen in Figure 5.2(a), the total spin magnetization precesses about the applied magnetic field with a constant angle and modulus, indicating the collinearity of the spins during time evolution. To have a better visualization of the precession, the total spin magnetization is projected on to the plane perpendicular to the applied magnetic field, referred to as as the $\mathcal{O}_x$-$\mathcal{O}_y$ plane. Figure 5.2(b) shows the evolution

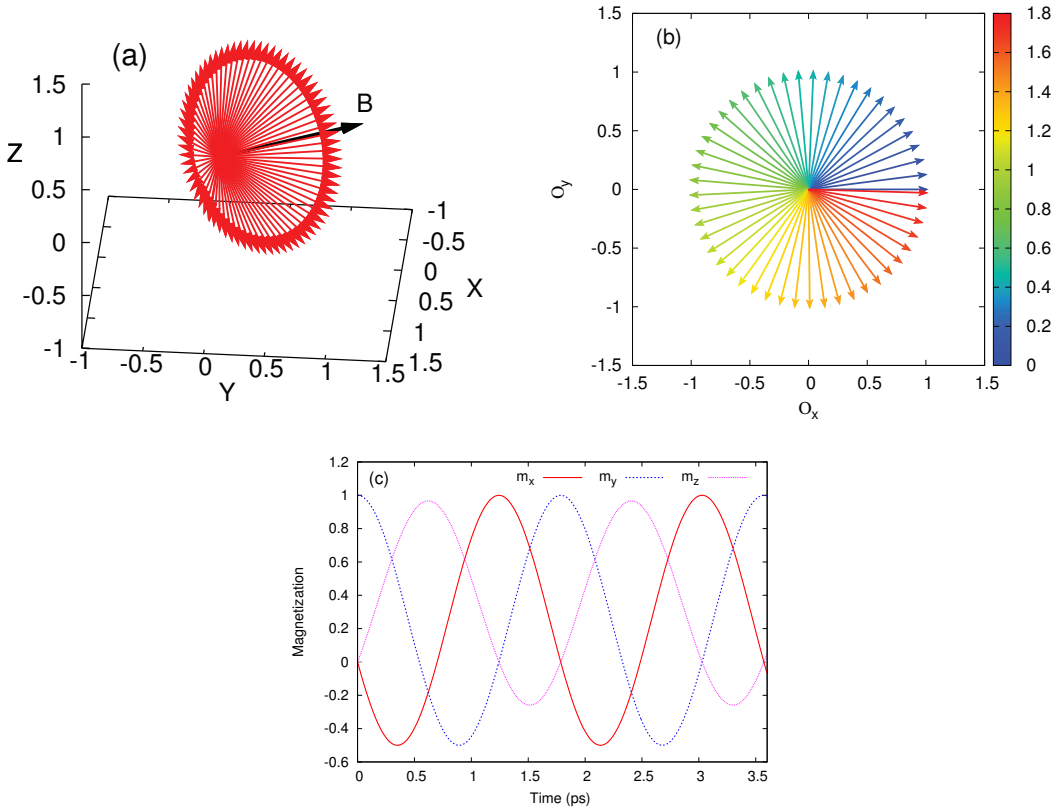

Figure 5.2: Time evolution of the electron spin magnetization (in the unit of Bohr magneton) of Li atom in a uniform magnetic field. The initial spin is polarized along the y axis. The magnetic field is positioned with a 45° angle to the initial spin polarization (see article text for details): (a) 3D view of the precession of the overall magnetization vector about the magnetic field; (b) the $\mathcal{O}_x$-$\mathcal{O}_y$ plane projection of the magnetization over time (the time-evolution is represented as the progression of coloration in picoseconds); and (c) the evolutions of the x, y, and z components of spin magnetization.

of the projected magnetization on to this plane. The projected time-evolution displays a perfect rotation about the axis of the magnetic field with a rotation period of ∼1.8 picosecond. Figure 5.2(c) plots the x, y and z components of the spin magnetization with respect to the reference frame. Sinusoidal oscillations of the spin magnetization were again observed. The computed angular frequency $\omega = 8.5 \times 10^{-5}$ a.u. is consistent with the analytic Larmor frequency.

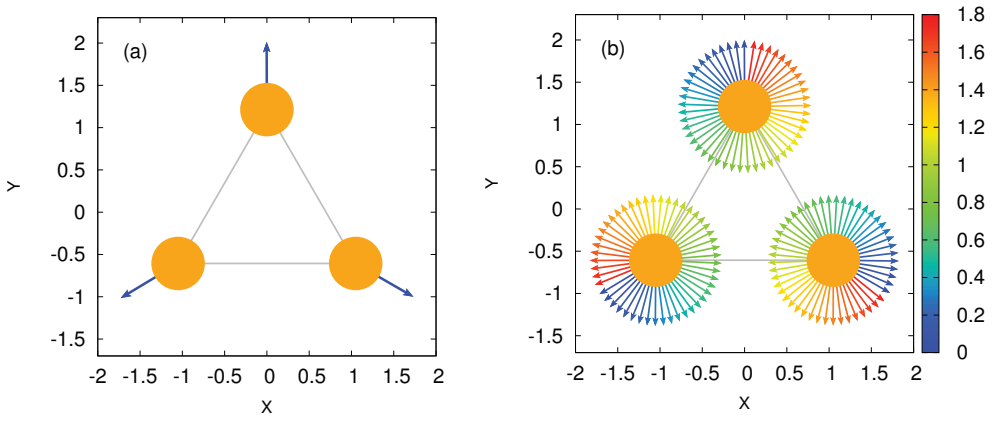

Figure 5.3: (a) the initial magnetization (in the unit of Bohr magneton) of Li_3 at $t = 0$, and (b) the time evolution of the spin magnetization (in the unit of Bohr magneton) in a uniform magnetic field applied perpendicular to the xy plane (the time-evolution is represented as the progression of coloration in the unit of picosecond).

C. Non-collinear Li_3 Trimer in a Uniform Magnetic Field

As a prototypical application of the time-dependent non-relativistic two-component spinor method, we investigate the spin dynamics of a two-dimensional spin-frustrated lattice model with three lithium atoms forming a triangular trimer. Such triangular systems are known to exhibit a non-collinear antiferromagnetic Néel state,[316,325] where the magnetization at each lattice node is oriented at angle of $\frac{2}{3}\pi$ with respect to each other point. In these spin frustrated systems, spin waves have been measured through neutron scattering experiments, as well as spin reorientation events in response to an applied external magnetic field. The spin dynamics of these systems have been studied with parameterized spin models such

as the Heisenberg Hamiltonian.[310–313] The *ab initio* time-dependent non-relativistic two-component spinor method offers a step towards the first-principles simulation of systems with non-collinear spins, and opportunities to obtain the insights of the complex nature of the spin dynamics.

The model system tested herein consists of three Li atoms with the Li–Li bond length of 2.10 Å. The initial wave function at $t = 0$ is obtained by a self-consistent-field procedure using the generalized Hartree-Fock method and the 3-21G basis set. As expected, the GHF method properly identified the non-collinearity of the spin magnetization in the Li_3 trimer, as shown in Figure 5.3(a). With this initial spin arrangement, at $t = 0$ a uniform magnetic field oriented perpendicularly to the trimer plane, with the same field strength of 8.5×10^{-5} a.u. ($\sim$20 Tesla) as used in previous simulations. Figure 5.3(b) illustrates the time evolution of the spin magnetization at each lattice point. Figure 5.3(b) shows that the magnetization of each individual Li atom precesses about the magnetic field, with the same angular frequency $\omega = 8.5 \times 10^{-5}$ a.u. Due to the effect of the external magnetic field, the atomic magnetization vector on each node switches its direction in $\sim$1.0 picosecond. But the overall non-collinearity is maintained throughout the simulation. This is not surprising since we are analyzing the atomic magnetizations in the absence of the spin-orbit and spin-spin coupling terms in our simulation.

5.1.4 Conclusions

In this section, we have formulated an *ab initio* time-dependent non-relativistic two-component spinor theory, to study the non-collinear spin dynamics of many-electron systems in response to an external magnetic field. We employed a direct integration of the time-dependent non-relativistic two-component (TDN2C) Hartree-Fock equation using atom-centered basis functions and a unitary propagation approach with a modified midpoint algorithm. An analysis tool based on the Hirshfeld partitioning scheme has been developed to analyze the time-dependent spin magnetization.

For the simple one-electron system of H atom and collinear multi-electron system of Li atom, the RT–TDN2C simulations yield the same results as the analytical Larmor preces-

sions. As an important application of our methodology, we have simulated spin dynamics of a non-collinear Li_3 trimer in response to an external magnetic field. The switching of the magnetization at each lattice node was observed during the dynamical simulation.

5.2 *Ab Initio* Ehrenfest Spin and Molecular Dynamics Using Two-Component TDDFT

In this section, we present an *ab initio* two-component Ehrenfest-based mixed quantum/classical molecular dynamics method for the description of the effect of nuclear motion on the spin dynamics in molecular systems. The two-component time-dependent non-collinear density functional theory is used for the propagation of spin-polarized electrons while the nuclei are treated classically. We use a three-time-step algorithm for the numerical integration of the coupled equations of motion, namely the velocity Verlet for nuclear motion, the nuclear-position-dependent midpoint Fock update, and the modified midpoint and unitary transformation method for electronic propagation. As a test case, the method is applied to the dissociation of H_2 and O_2 molecules. In contrast to conventional Ehrenfest dynamics, this two-component approach provides a first principles description of the dynamics of non-collinear (e.g. spin-frustrated) magnetic materials, as well as the proper description of spin-state crossover, spin-rotation and spin-flip dynamics by relaxing the constraint on spin configuration. This method also holds potential for applications to spin transport in molecular or even nanoscale magnetic devices.

5.2.1 Introduction

Studies of spin dynamics in nanoscale materials and single molecules are important for the realization of molecular spintronics[306,326] and quantum computing.[327] The major difficulties in the theoretical modeling of spin dynamics come from treating the complex interactions among electron spins and interaction between electron spin and other degrees of freedom such as electron motion (which leads to spin-orbit coupling), external magnetic field and lattice/molecular vibrations. The electron spin-spin interaction is the major cause of various spin dynamics phenomena such as non-collinear magnetism, helical spin order and spin waves, while the coupling between spin and other degrees of freedom also play an important role in many processes such as those involving spin flip transitions. As another example, the interplay between spin dynamics and lattice vibration has been suggested as an important part of the problem in high-temperature superconductivity.[328]

Over the past decade, several theoretical atomistic simulations have been attempted to study some interesting spin dynamic processes.[329–334] So far most of these studies utilize model spin Hamiltonians with parametrized local magnetic exchanges by fitting either to experimental data or static first-principles calculations. While semi-empirical model Hamiltonians have been successful in describing spin-lattice relaxation and spin-transport dynamics, molecular dynamics with first-principles description of spin dynamics that do not depend on problem-specific parameterizations will be highly appreciated.

One of the widely used approaches toward affordable computation is the mixed quantum-classical scheme in which the electronic degrees of freedom are treated quantum mechanically and nuclei move as classical particles. Within such a framework, two general approaches, namely the surface hopping[33,34] and Ehrenfest dynamics[35–38,44] have emerged. Both approaches incorporate electronic nonadiabaticity and both include quantum coherence effects. The surface hopping method describes nonadiabaticity by allowing stochastic electronic transitions subject to a time- and momentum-dependent hopping probability. The Ehrenfest dynamics, on the other hand, propagates the classical nuclei on a superposition of electronic states that follow the time-dependent quantum mechanics. Within these mixed quantum-classical frameworks, spin dynamics can be simulated given that the spin-dependent couplings can be computed or approximated. For example, the surface hopping approach with parameterized spin-couplings has been used in studying a number of spin dynamics processes.[335–341]

However, the first-principles description of spin-dynamics in the mixed quantum-classical scheme still presents several challenges. Most standard time-dependent electronic structure methods, such as time-dependent restricted/unrestricted Hartree-Fock and density functional theories, require electronic spins to be aligned (anti-)parallel with respect to each other, also known as the spin collinearity constraint.[19,37,43–45,76–82,92,157,165,321] As a result, conventional first-principles methods are unable to describe free spin rotation or the change of spin quantization axis. In principle, the time-dependent four-component Dirac equation affords the complete description of spin dynamics. For most chemical problems, where the dominant interaction that drives the spin dynamics is the exchange interaction resulting from the Pauli exclusion principle, an approximate two-component formalism is

sufficient. To approach a truly first-principles description of spin-dynamics in the mixed quantum-classical scheme, we adopt a bottom-up approach starting with the two-component non-relativistic Schrödinger equation. Spin-orbit coupling and higher order spin-spin interactions can be included with the use of two-component quasi-relativistic approaches, such as the Douglas-Kroll-Hess (DKH)[342–344] transformed Hamiltonian. Within the two-component framework, one affordable approach to approximately solving the many-electron problem is to use a single Slater determinant ansatz for the two-component wave function. Along this direction, we have developed an *ab initio* real-time time-dependent non-relativistic two-component spinor (TD-2c) method[26] to study spin dynamics of many-electron systems. The use of the two-component spinor wave function enables a proper description of non-collinear spin polarization. Another conceptually different route is the use of time-dependent density functional theory (TD-DFT). Along this direction, non-collinear (i.e. two-component) ground-state density functional theory has been established by Barth and Hedin,[345] who generalized the Hohenberg-Kohn theorem[31] and the Kohn-Sham scheme[32] to spin-polarized systems. Here we follow Barth and Hedin[345] and generalize the Runge-Gross theorem[45] for the time-dependent problem, which leads to the time-dependent two-component density functional theory (TD-2cDFT). The corresponding effective single-particle equations are solved according to the Kohn-Sham scheme. The adiabatic approximation, i.e. the use of ground-state non-collinear density functionals, is adopted.

In this paper, we introduce an *ab initio* two-component Ehrenfest (2c-Ehrenfest) molecular spin dynamics approach by propagating the electronic spin degrees of freedom using the TD-2cDFT equation. We present derivations of the analytical forces in the TD-2cDFT framework that drive classical nuclear degrees of freedom. Electronic and nuclear time-evolutions are propagated with a three-time-step integrator. The energy, forces, and magnetic/electronic properties are computed "on the fly", giving rise to the direct 2c-Ehrenfest dynamics. This approach has several advantages over the conventional Ehrenfest dynamics. First, it can be directly applied to the study of the dynamics of non-collinear (e.g. spin-frustrated) magnetic materials where the collinear approaches are not applicable. Second, it provides a proper description of spin-rotation and spin-flip dynamics by relaxing the constraint on spin symmetry, for example, it is able to recover some aspects of the correct

dissociation limit. This paper is organized as follows: In Sec. 5.2.2, we present the theoretical framework and mathematical derivations of the 2c-Ehrenfest method and numerical integration scheme. In Sec. 5.2.3, we consider two illustrative examples: the dissociation of the H_2 molecule and the O_2 molecule. In Sec. 5.2.4 we present concluding remarks.

5.2.2 Methodology

A. Two-Component Ehrenfest Dynamics

The derivation for the 2c-Ehrenfest dynamics follows closely the one for the spin-free, one-component approach,[37,346] and we only present a brief review of the Ehrenfest approach. We begin with the following molecular Hamiltonian,

$$\hat{H}_{\mathrm{mol}} = \hat{T}_{\mathrm{nuc}}(\mathbf{R}) + \hat{H}_{\mathrm{el}}(\mathbf{x}, \mathbf{R}) \tag{5.29}$$

where $\hat{T}_{\mathrm{nuc}}(\mathbf{R})$ is the kinetic energy operator for the nuclear degrees of freedom $\mathbf{R}$, and $\hat{H}_{\mathrm{el}}(\mathbf{x}, \mathbf{R})$ is the electronic Hamiltonian that depends on both the nuclear coordinates $\mathbf{R}$ and the electronic coordinates $\mathbf{x}$ of both spatial $\mathbf{r}$ and spin σ.

The starting point of the derivation of Ehrenfest dynamics is a product ansatz for the total wave function $\Psi(\mathbf{x}, \mathbf{R}; t)$,

$$\Psi(\mathbf{x}, \mathbf{R}; t) \approx \Phi(\mathbf{x}; t)\, \Theta(\mathbf{R}; t) \exp\left[\frac{i}{\hbar} \int_{t_0}^{t} E_{\mathrm{el}}(t')\mathrm{d}t'\right] \tag{5.30}$$

where $\Phi(\mathbf{x}; t)$ is the electronic wave function and $\Theta(\mathbf{R}; t)$ the nuclear wave function. $E_{\mathrm{el}}(t')$ is a phase factor that is defined by

$$E_{\mathrm{el}}(t) = \int \Phi^*(\mathbf{x}; t)\, \Theta^*(\mathbf{R}; t)\, \hat{H}_{\mathrm{el}} \Phi(\mathbf{x}; t)\, \Theta(\mathbf{R}; t)\, \mathrm{d}\mathbf{x}\mathrm{d}\mathbf{R} \tag{5.31}$$

Separating the equations of motion for the nuclear and electronic wavefunctions and making the classical approximation for the nuclei,[346] one eventually arrives at the mixed-

quantum/classical equations of motions for Ehrenfest dynamics,

$$M_I \ddot{\mathbf{R}}_I = -\nabla_I \langle \Phi | H_{\mathrm{el}} | \Phi \rangle \tag{5.32}$$

$$i\hbar \frac{\partial \Phi}{\partial t} = H_{\mathrm{el}} \Phi \tag{5.33}$$

where the nuclei move classically according to a mean-field potential generated by the electronic wave function, and the electrons are treated quantum mechanically and depends parametrically on the classical nuclear positions.

Here we have not specified the form of the electronic Hamiltonian $\hat{H}_{\mathrm{el}}(\mathbf{x}, \mathbf{R})$. It can be of a non-relativistic, spin-free form, or of a non-relativistic, two-component form such as the Pauli-Schrödinger Hamiltonian, or of a two-component, quasi-relativistic form such as a DKH transformed Hamiltonian. However, in order to describe the spin dynamics of a molecular system, a two-component formalism of Eq. (5.33) is necessary.

B. Time-Dependent Non-Collinear Density Functional Theory

Recently, we developed an *ab initio* real-time time-dependent non-relativistic two-component spinor (TD-2c) formalism to study spin dynamics.[26] This formalism in the zero-field case is identical to the generalized Hartree-Fock method for the electronic wave function. As inherited from Hartree-Fock, the TD-2cHF lacks electron correlation. In this work, we extend the two-component spinor formalism to the TD-DFT framework to include electron correlation in spin dynamics. This leads to the time-dependent two-component density functional theory (TD-2cDFT).

In TD-2cDFT, the Kohn-Sham orbitals are expressed as complex two-component spinors,

$$\psi_k(\mathbf{x}, t) = \begin{pmatrix} \phi_k^{\alpha}(\mathbf{r}, t) \\ \phi_k^{\beta}(\mathbf{r}, t) \end{pmatrix} \tag{5.34}$$

where k spans the number of basis functions, which gives rise to a complex two-component

density matrix,

$$\rho_{\sigma\tau}(\mathbf{r},t) = \sum_{i}^{N} \psi_k^{\sigma}(\mathbf{r},t)\psi_k^{\tau *}(\mathbf{r},t). \tag{5.35}$$

Following Barth and Hedin[345] for the ground-state problem, we can generalize the Runge-Gross theorem[45] to the time-dependent spin-polarized systems. It can be shown that the spin-dependent scalar external potential $v_{\mathrm{ext},\sigma\tau}$ uniquely determines the time-dependent density $\rho_{\sigma\tau}(\mathbf{r},t)$, and this map is invertible up to an additive time-dependent function and a universal spin rotation. Based on the stationary action principle, a set of time-dependent effective single-particle Kohn-Sham equations can be derived,

$$i\frac{\partial}{\partial t}\psi_k^{\sigma}(\mathbf{r},t) = \sum_{\tau=\alpha,\beta}\left[\left(-\frac{1}{2}\nabla^2 + \int \mathrm{d}\mathbf{r}'\frac{n(\mathbf{r}',t)}{|\mathbf{r}-\mathbf{r}'|}\right)\delta_{\sigma\tau} + v_{\mathrm{ext},\sigma\tau} + v_{\mathrm{xc},\sigma\tau}\right]\psi_k^{\tau}(\mathbf{r},t) \tag{5.36}$$

where we have used the atomic units. $n = \rho_{\alpha\alpha} + \rho_{\beta\beta}$ is the particle density, v_{ext} is the external one-electron potential which also includes the nuclei-nuclei repulsion, $v_{\mathrm{xc},\sigma\tau}$ is the non-collinear exchange-correlation (xc) potential and is obtained from functional derivative of the xc energy $E_{\mathrm{xc}}[\rho](t)$,

$$v_{\mathrm{xc},\sigma\tau}(t) = \frac{\delta E_{\mathrm{xc}}[\rho](t)}{\delta\rho_{\sigma\tau}}. \tag{5.37}$$

Now, the time-dependent xc potential $v_{\mathrm{xc}}[\rho](t)$ is not known in general. Here we use the so-called adiabatic approximation where the time-non-local $v_{\mathrm{xc}}[\rho](t)$ is replaced by some ground-state xc functional $\tilde{v}_{\mathrm{xc}}[\rho]$ which is local in time. Within the adiabatic approximation, we are still facing the problem of finding a proper two-component (i.e. non-collinear) ground-state xc functional. Recently, efforts have been made to the development of non-collinear density functional theory (nc-DFT).[315–317,319,347] One of the common approaches is to approximate the two-component xc functional using any one of the known density functional approximations, assuming a local quantization axis. In this paper, we use the non-collinear generalization to the generalized gradient approximation (GGA) functionals.[319]

In this work, we use a set of real atom-centered atomic orbital (AO) basis functions $\{\mu\}$ to span the Kohn-Sham complex two-component spinor space. In the AO basis, the density matrix can be written as

$$\mathbf{P}'(t) = \begin{pmatrix} \mathbf{P}'^{\alpha\alpha}(t) & \mathbf{P}'^{\alpha\beta}(t) \\ \mathbf{P}'^{\beta\alpha}(t) & \mathbf{P}'^{\beta\beta}(t) \end{pmatrix} \tag{5.38}$$

where each spin block $\mathbf{P}'^{\sigma\tau}(t)$ is given by

$$P'^{\sigma\tau}_{\mu\nu}(t) = \sum_{i}^{N} C^{\sigma}_{\mu i}(t) \cdot C^{\tau *}_{\nu i}(t) \tag{5.39}$$

where $\mathbf{C}^{\sigma}$ are the MO coefficient matrices.

The two-component Kohn-Sham matrix in the AO basis also takes a spin-blocked form analogous to the density matrix,

$$\mathbf{F}'(t) = \begin{pmatrix} \mathbf{F}'^{\alpha\alpha}(t) & \mathbf{F}'^{\alpha\beta}(t) \\ \mathbf{F}'^{\beta\alpha}(t) & \mathbf{F}'^{\beta\beta}(t) \end{pmatrix} \tag{5.40}$$

where each spin block $\mathbf{F}'^{\sigma\tau}(t)$ is given by

$$\mathbf{F}'^{\sigma\tau}(t) = \mathbf{h}'^{\sigma\tau}(t) + \mathbf{G}'^{\sigma\tau}(t) \tag{5.41}$$

where $\mathbf{h}'$ is the one-electron Hamiltonian matrix and $\mathbf{G}'$ is the two-electron matrix. For a hybrid density functional, $\mathbf{G}'$ is given by

$$\mathbf{G}'^{\sigma\tau}(t) = \delta_{\sigma\tau}\left[\mathbf{J}'^{\alpha\alpha}(t) + \mathbf{J}'^{\beta\beta}(t)\right] - c_{\mathrm{HF}}\mathbf{K}'^{\sigma\tau}(t) + (1 - c_{\mathrm{HF}})\mathbf{V}^{\sigma\tau}_{xc}(t) \tag{5.42}$$

where $\mathbf{J}'$ and $\mathbf{K}'$ are the two-electron Coulomb and exchange matrices, and $\mathbf{V}_{xc}$ is the DFT exchange-correlation potential matrix. c_{HF} is the tuning parameter for hybrid functionals with $c_{\mathrm{HF}} = 1$ corresponding to pure Hartree-Fock exchange and $c_{\mathrm{HF}} = 0$ to pure DFT functionals.

The AO density and Kohn-Sham matrices are then transformed to an orthonormal basis

by the following transformation,

$$\begin{pmatrix} \mathbf{P}^{\alpha\alpha}(t) & \mathbf{P}^{\alpha\beta}(t) \\ \mathbf{P}^{\beta\alpha}(t) & \mathbf{P}^{\beta\beta}(t) \end{pmatrix} = \begin{pmatrix} \mathbf{V} & 0 \\ 0 & \mathbf{V} \end{pmatrix} \cdot \begin{pmatrix} \mathbf{P}'^{\alpha\alpha}(t) & \mathbf{P}'^{\alpha\beta}(t) \\ \mathbf{P}'^{\beta\alpha}(t) & \mathbf{P}'^{\beta\beta}(t) \end{pmatrix} \cdot \begin{pmatrix} \mathbf{V}^T & 0 \\ 0 & \mathbf{V}^T \end{pmatrix} \tag{5.43}$$

$$\begin{pmatrix} \mathbf{F}^{\alpha\alpha}(t) & \mathbf{F}^{\alpha\beta}(t) \\ \mathbf{F}^{\beta\alpha}(t) & \mathbf{F}^{\beta\beta}(t) \end{pmatrix} = \begin{pmatrix} \mathbf{V}^{-T} & 0 \\ 0 & \mathbf{V}^{-T} \end{pmatrix} \cdot \begin{pmatrix} \mathbf{F}'^{\alpha\alpha}(t) & \mathbf{F}'^{\alpha\beta}(t) \\ \mathbf{F}'^{\beta\alpha}(t) & \mathbf{F}'^{\beta\beta}(t) \end{pmatrix} \cdot \begin{pmatrix} \mathbf{V}^{-1} & 0 \\ 0 & \mathbf{V}^{-1} \end{pmatrix} \tag{5.44}$$

The transformation matrix $\mathbf{V} = \mathbf{S}^{1/2}$ in the Löwdin orthonormalization method, or obtained by the Cholesky decomposition $\mathbf{S} = \mathbf{V}^T\mathbf{V}$, where $\mathbf{S}$ is the overlap matrix of AO basis functions, $S_{\mu\nu} = \langle\mu|\nu\rangle$.

Expressing Eq. (5.36) in terms of orthonormal basis, we obtain the two-component TDDFT equation (TD-2cDFT) in the density matrix formalism,

$$i\frac{\partial}{\partial t}\begin{pmatrix} \mathbf{P}^{\alpha\alpha}(t) & \mathbf{P}^{\alpha\beta}(t) \\ \mathbf{P}^{\beta\alpha}(t) & \mathbf{P}^{\beta\beta}(t) \end{pmatrix} = \left[\begin{pmatrix} \mathbf{F}^{\alpha\alpha}(t) & \mathbf{F}^{\alpha\beta}(t) \\ \mathbf{F}^{\beta\alpha}(t) & \mathbf{F}^{\beta\beta}(t) \end{pmatrix}, \begin{pmatrix} \mathbf{P}^{\alpha\alpha}(t) & \mathbf{P}^{\alpha\beta}(t) \\ \mathbf{P}^{\beta\alpha}(t) & \mathbf{P}^{\beta\beta}(t) \end{pmatrix}\right] \tag{5.45}$$

C. The Nuclear Force

Solution of the classical Newtonian equation of motion for nucleus I requires the evaluation of the mean-field force as the energy gradient,

$$\mathbf{f}_I = -\frac{\partial E}{\partial \mathbf{R}_I} = -\nabla_I \langle\Phi|H_{\text{el}}|\Phi\rangle \tag{5.46}$$

where E denotes the electronic energy.

For a spin-dependent process described by the TD-2cDFT equation, the nuclear force $\mathbf{f}_I$ is composed of two parts, which we label as spin-collinear part $\mathbf{f}_I^{\text{c}}$ and spin-non-collinear part $\mathbf{f}_I^{\text{nc}}$, respectively,

$$\mathbf{f}_I = \mathbf{f}_I^{\text{c}} + \mathbf{f}_I^{\text{nc}} \tag{5.47}$$

where $\mathbf{f}_I^{\text{c}}$ and $\mathbf{f}_I^{\text{nc}}$ are given by

$$\mathbf{f}_I^{\mathrm{c}} = -\mathrm{Tr}\left\{\sum_{\sigma}\left[\frac{d\mathbf{h}'^{\sigma\sigma}}{d\mathbf{R}_I}\mathbf{P}'^{\sigma\sigma} + \frac{1}{2}\frac{\partial\mathbf{G}'^{\sigma\sigma}}{\partial\mathbf{R}_I}\mathbf{P}'^{\sigma\sigma}\right]\right\} + \mathrm{Tr}\left\{\sum_{\sigma}\left[\mathbf{F}'^{\sigma\sigma}\mathbf{V}^{-1}\frac{d\mathbf{V}}{d\mathbf{R}_I}\mathbf{P}'^{\sigma\sigma} + \mathbf{P}'^{\sigma\sigma}\frac{d\mathbf{V}^T}{d\mathbf{R}_I}\mathbf{V}^{-T}\mathbf{F}'^{\sigma\sigma}\right]\right\} - \frac{\partial V_{nn}}{\partial\mathbf{R}_I} \tag{5.48}$$

$$\mathbf{f}_I^{\mathrm{nc}} = -\mathrm{Tr}\left\{\sum_{\sigma\neq\tau}\left[\frac{d\mathbf{h}'^{\sigma\tau}}{d\mathbf{R}_I}\mathbf{P}'^{\tau\sigma} + \frac{1}{2}\frac{\partial\mathbf{G}'^{\sigma\tau}}{\partial\mathbf{R}_I}\mathbf{P}'^{\tau\sigma}\right]\right\} + \mathrm{Tr}\left\{\sum_{\sigma\neq\tau}\left[\mathbf{F}'^{\sigma\tau}\mathbf{V}^{-1}\frac{d\mathbf{V}}{d\mathbf{R}_I}\mathbf{P}'^{\tau\sigma} + \mathbf{P}'^{\sigma\tau}\frac{d\mathbf{V}^T}{d\mathbf{R}_I}\mathbf{V}^{-T}\mathbf{F}'^{\tau\sigma}\right]\right\} \tag{5.49}$$

where the trace is taken over different spin blocks. Note that Pulay terms that arise from non-orthogonal AO basis split into two contributions in Eq. (5.48) and Eq. (5.49), respectively, because $[\mathbf{F}, \mathbf{P}] \neq 0$ as the many-electron system deviates from eigenstates.[37]

The expression for the derivative of the transformation matrix $\mathbf{V}$ depends on the type of orthonormalization. In the case of Löwdin orthonormalization, i.e. $\mathbf{V} = \mathbf{S}^{1/2}$, and $\partial\mathbf{V}/\partial\mathbf{R}$ may be expressed in the eigenvector basis of the overlap matrix $\mathbf{S}$,

$$\left(\frac{\partial\mathbf{V}}{\partial\mathbf{R}_I}\right)_{ij} \equiv \left(\frac{\partial\mathbf{S}^{1/2}}{\partial\mathbf{R}_I}\right)_{ij} = \frac{1}{\sigma_i^{1/2} + \sigma_j^{1/2}}\left(\frac{\partial\mathbf{S}}{\partial\mathbf{R}_I}\right)_{ij} \tag{5.50}$$

where σ_i are the eigenvalues of the overlap matrix $\mathbf{S}$. In the case of Cholesky orthonormalization,

$$\begin{aligned}\left(\frac{d\mathbf{V}}{d\mathbf{R}_I}\mathbf{V}^{-1}\right)_{\mu\nu} &= \left(\mathbf{V}^{-T}\frac{d\mathbf{V}^T}{d\mathbf{R}_I}\right)_{\nu\mu} \\ &= \left(\mathbf{V}^{-T}\frac{\partial\mathbf{S}}{\partial\mathbf{R}_I}\mathbf{V}^{-1}\right)_{\mu\nu}, \qquad \mu < \nu \\ &= \frac{1}{2}\left(\mathbf{V}^{-T}\frac{\partial\mathbf{S}}{\partial\mathbf{R}_I}\mathbf{V}^{-1}\right)_{\mu\nu}, \qquad \mu = \nu \\ &= 0, \qquad \mu > \nu\end{aligned} \tag{5.51}$$

The spin-collinear part $\mathbf{f}_I^{\mathrm{c}}$ resembles what can be found in a collinear (spin-unrestricted)

DFT calculation, as shown in Eq. (5.48). The spin-noncollinear part $\mathbf{f}_I^{\mathrm{nc}}$ in Eq. (5.49) corresponds to the contribution from the non-collinearity of the spin configuration during the dynamics, which is important in accounting for the coupling between nuclear motion and spin dynamics.

D. Numerical Integration

Because of the large mass ratio between the nuclei and electrons, propagation of the nuclear and electronic motions is often carried out with two distinct time steps, namely Δt_N and Δt_e, respectively, with Δt_N usually two- or three-orders of magnitude greater than Δt_e. Such a two-time-step propagation scheme is only of first-order accuracy and thus very small time steps of Δt_N and Δt_e must be used in order to avoid significant integration errors. We use a three-time-step algorithm[37] in this work for efficient and accurate solution of mixed quantum-classical dynamics. The three different time steps are associated with the velocity Verlet method for nuclear propagation, the nuclear-position-dependent midpoint Fock update, and modified midpoint and unitary transformation method for integrating electronic Schrödinger equation.

Velocity Verlet method for nuclear motion The Newtonian equation of motion for nuclei, Eq. (5.32), can be solved numerically using a number of standard methods. One of the widely used methods is the velocity Verlet method:

$$\mathbf{p}_I(t+\frac{1}{2}\Delta t_N) = \mathbf{p}_I(t) + \frac{1}{2M_I}\mathbf{f}_I(t)\Delta t_N \tag{5.52}$$

$$\mathbf{R}_I(t+\Delta t_N) = \mathbf{R}_I(t) + \frac{1}{M_I}\mathbf{p}_I(t+\frac{1}{2}\Delta t_N)\Delta t_N \tag{5.53}$$

$$\mathbf{p}_I(t+\Delta t_N) = \mathbf{p}_I(t+\frac{1}{2}\Delta t_N) + \frac{1}{2M_I}\mathbf{f}_I(t+\Delta t_N)\Delta t_N \tag{5.54}$$

where $\mathbf{p}_I$ and $\mathbf{f}_I$ are the momentum and force of I-th nucleus, respectively.

Modified mid-point method for the two-component TDDFT equation The integration of the TD-2cDFT equation, Eq. (5.45), can be achieved using a number of unitary propagation methods such as the Crank-Nicolson method,[41] the Magnus method,[42] and the exponential midpoint method. These methods are all second-order methods. The efficiency of these

methods are comparable since the most expensive step is the formation of the Fock matrix. In the present work, we use a modified version of the exponential midpoint method which is called the modified midpoint and unitary transformation (MMUT) algorithm.[43,44] In the MMUT method, the time-evolution operator is a unitary transformation matrix $\mathbf{U}(t)$ that is constructed from the eigenvectors $\mathbf{C}(t)$ and eigenvalues $\boldsymbol{\epsilon}(t)$ of the two-component Kohn-Sham matrix at time t:

$$\mathbf{C}^{\dagger}(t) \cdot \mathbf{F}(t) \cdot \mathbf{C}(t) = \boldsymbol{\epsilon}(t) \tag{5.55}$$

$$\begin{aligned} \mathbf{U}(t) &= \exp\bigl[-i \cdot 2\Delta t_e \cdot \mathbf{F}(t)\bigr] \\ &= \mathbf{C}(t) \cdot \exp\bigl[-i \cdot 2\Delta t_e \cdot \boldsymbol{\epsilon}(t)\bigr] \cdot \mathbf{C}^{\dagger}(t) \end{aligned} \tag{5.56}$$

where Δt_e is the time step. The density matrix is then propagated from time $t - \Delta t_e$ to $t + \Delta t_e$ using the time-evolution operator $\mathbf{U}(t)$:

$$\mathbf{P}(t + \Delta t_e) = \mathbf{U}(t) \cdot \mathbf{P}(t - \Delta t_e) \cdot \mathbf{U}^{\dagger}(t) \tag{5.57}$$

Note that the Kohn-Sham and density matrices in Eqs. (5.55)–(5.57) are assumed to have a spin-blocked structure. By computing the Kohn-Sham matrix at the midpoint of the step, the MMUT method accounts for linear changes in the density matrix during the time step. The MMUT algorithm can be used with a large step size, while still maintaining very good control of numerical noise and integration errors.[43]

Nuclear-position-dependent midpoint Fock update Because the Kohn-Sham matrix is a function of the nuclear positions, which is implicitly time-dependent, in order to achieve high accuracy, the Kohn-Sham matrix $\mathbf{F}$ needs to be updated within the nuclear step Δt_N. Since the change in the nuclear positions is much slower than the change in the electron density, it is reasonable to assume stationary nuclei for several TDDFT iterations. Thus we introduce a third time step, $\Delta t_{Ne} = m\Delta t_e$, the time step within which the nuclear positions are fixed. The integrals required to build the Kohn-Sham matrix $\mathbf{F}$ are updated once every

Δt_{Ne} step at the midpoint of the time interval $[t', t' + \Delta t_{Ne}]$:

$$\mathbf{F}'(t) = \mathbf{h}' \left[\mathbf{R}(t' + \frac{1}{2}\Delta t_{Ne}) \right] + \mathbf{G}' \left[\mathbf{R}(t' + \frac{1}{2}\Delta t_{Ne}), \mathbf{P}'(t) \right] \tag{5.58}$$

where the instantaneous electron density matrix $\mathbf{P}'(t)$ is used. Since the computation of the energy gradient is the most time-consuming step, it will be efficient to make several nuclear-position-dependent midpoint Fock updates before one calculates the next energy gradient. This amounts to setting $\Delta t_N = n\Delta t_{Ne}$.

This nuclear-position-dependent midpoint Fock update is equivalent to the widely used triple-split-operator method, where the Fock operator is split into nuclear-position-dependent and nuclear-position-independent parts. Such decomposition is second order for a single step and has been shown to approach a third-order accuracy with increasing number of splitting or iterations, i.e. $n \to \infty$ in $\Delta t_N = n\Delta t_{Ne}$.

5.2.3 Benchmark and Discussion

The 2c-Ehrenfest molecular and spin dynamics with the TD-2cDFT method described above is implemented within the development version of the GAUSSIAN series of programs.[348] In this section, we present two pedagogical examples including the dissociation of H_2 molecule, and O_2 molecule, to illustrate the characteristics of the method. To characterize the spin dynamics, we examine the evolution of the atomic magnetic moments computed using the Hirshfeld partitioning scheme[324] with time-dependent magnetic densities.[26]

A. Dissociation of H_2

H_2 dissociation is one of the most widely used benchmark problems because characteristics of electronic structure methods can easily be probed, although the spin dynamics of the H_2 dissociation, to the best our knowledge, has not been studied previously. In this work, we apply the 2c-Ehrenfest method presented above to illustrate the spin evolution during the H_2 dissociation. In the following simulations, the non-collinear density functional theory with the B3LYP hybrid functional and the 6-31G basis set were used. The initial H-H distance was 0.75 Å. The initial vibrational kinetic energy of the molecule was set to 0.2666 a.u.,

and nuclei were moving apart from each other along the molecular axis. Simulations with the same initial condition but different time-step sizes were carried out for testing purposes. The three step sizes used in Ehrenfest dynamics presented below are $\Delta t_N = 0.02fs$, $\Delta t_{Ne} = 0.004fs$, $\Delta t_e = 0.001fs$. BOMD trajectories are integrated using velocity-Verlet algorithm with a step size of 0.02 fs.

Figure 5.4 compares the errors in the total energy for different time-step sizes: Ehrenfest dynamics with (1) $\Delta t_N = 0.01fs$, $\Delta t_{Ne} = 0.002fs$, $\Delta t_e = 0.001fs$; (2) $\Delta t_N = 0.02fs$, $\Delta t_{Ne} = 0.004fs$, $\Delta t_e = 0.001fs$; (3) $\Delta t_N = 0.05fs$, $\Delta t_{Ne} = 0.005fs$, $\Delta t_e = 0.001fs$; (4) $\Delta t_N = 0.1fs$, $\Delta t_{Ne} = 0.01fs$, $\Delta t_e = 0.001fs$; (5) restricted B3LYP with $\Delta t_N = 0.02fs$, $\Delta t_{Ne} = 0.004fs$, $\Delta t_e = 0.001fs$; (6) unrestricted B3LYP with $\Delta t_N = 0.02fs$, $\Delta t_{Ne} = 0.004fs$, $\Delta t_e = 0.001fs$; and (7) BOMD with $\Delta t_N = 0.02fs$. For all cases, there is a positive shift in the total energy, which decreases as the nuclear step becomes smaller. For Ehrenfest dynamics with nuclear step $\Delta t_N = 0.02fs$, the total energy is conserved to within 0.02 kcal/mol, which is comparable to that obtained by BOMD with the same step size.

All dynamics results are converged by comparing to those using smaller step sizes. The total energy for all trajectories presented below is conserved to be less than 0.04 kcal/mol. The Ehrenfest dynamics[37] with conventional one-component electronic structure methods and Born-Oppenheimer molecular dynamics (BOMD)[349] simulations with the same initial condition are also compared in this work.

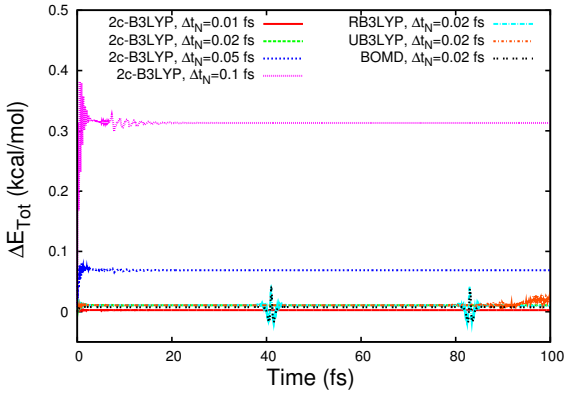

Figure 5.4: Energy conservation for different time-step sizes

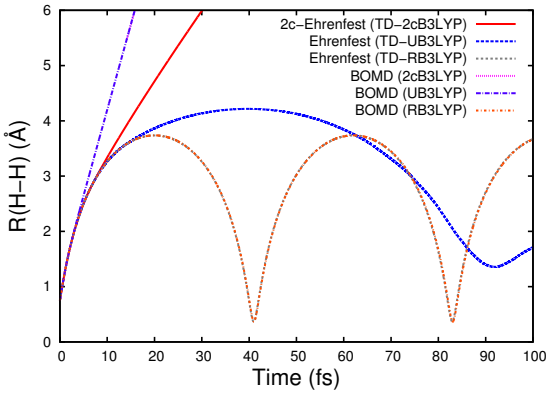

Figure 5.5: Time evolution of the H-H distance computed with different methods.

Figure 5.5 shows the time-evolution of the H-H distance computed using the 2c-Ehrenfest, conventional Ehrenfest and BOMD approaches. The BOMD and conventional Ehrenfest trajectories with the spin-restrict closed-shell (RB3LYP and TD-RB3LYP) formalism produce nearly identical results, suggesting an insignificant nonadibatic mixing of higher-energy spin-restrict closed-shell solutions. At the asymptotic dissociation limit, conventional spin-restricted closed-shell (RB3LYP) formalism of HF/KS follows the spin-diabatic potential to the ionic $H^- + H^+$, which is of a much higher dissociation potential than the homogenous dissociation pathway (see Fig. 5.6). As a result, H_2 is unable to dissociate under the given condition and vibrational phenomenon appears in the BOMD and conventional Ehrenfest simulations.

The result of the conventional Ehrenfest dynamics with the open-shell (TD-UB3LYP) formalism deviates from the open-shell (UB3LYP) BOMD trajectory, and both open-shell dynamics deviate from the closed-shell results. The open-shell BOMD dynamics is dissociative, whereas the Ehrenfest dynamics with TD-UB3LYP is not. The TD-UB3LYP potential from the Ehrenfest dynamics under the chosen initial condition is plotted in Fig. 5.6. Note that the potential energy arising from the real-time integration of TD-UB3LYP depends on the initial condition of the molecular dynamics. The TD-UB3LYP potential is higher than that of UB3LYP (SCF-converged and stable in the unrestricted space), but lower than that of RB3LYP potential. This is an outcome of the intrinsic mean-field approximation in

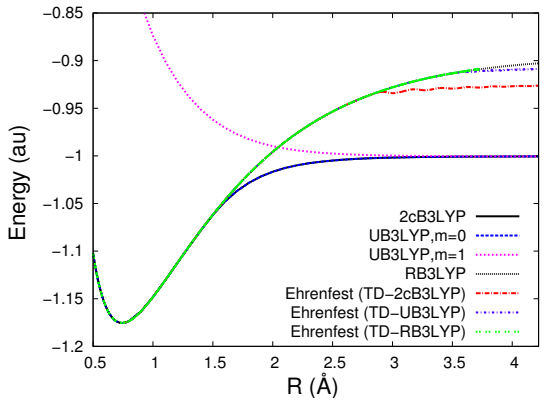

Figure 5.6: Potential energy surfaces of H_2 at different levels of theory, including energies from SCF converged solutions at the RB3LYP, UB3LYP (stability-tested), 2cB3LYP levels, and energies from TD-propagated electron density in the Ehrenfest dynamics with the given initial condition.

the Ehrenfest approach, which leads to a mean potential that resides between the RB3LYP and UB3LYP results and the observed dynamical behavior of Ehrenfest dynamics with TD-UB3LYP. Since the ground state electronic structure does not have non-collinear instability, the result from BOMD dynamics with 2cB3LYP (SCF-converged and stable) is identical to that of BOMD with UB3LYP (also SCF-converged and stable).

In contrast, the first 8 fs of the 2c-Ehrenfest with TD-2cB3LYP trajectory follows the BOMD with UB3LYP trajectory, but they deviate from each other at the H-H distance of ∼3 Å. The mean-field approach exhibits a different mixing and reaction dynamics with TD-2cDFT compared to that in TD-UDFT or TD-RDFT. The 2c-Ehrenfest dynamics with TD-2cB3LYP is dissociative under the given initial condition. The ground state adiabatic potential is a result of avoided crossing of the singlet and triplet states. Therefore, there is a change of spin configuration at the avoided crossing region (∼1.5 – ∼2.5 Å). The two-component formalism using TD-2cDFT relaxes the constraint on the spin-configuration. As a result, the 2c-Ehrenfest is better able to handle avoided crossing arising from two different spin states, giving rise to a TD-2cB3LYP potential below that of TD-UB3LYP.

Figure 5.7(a) shows the time evolution of the localized spin magnetization (i.e. atomic

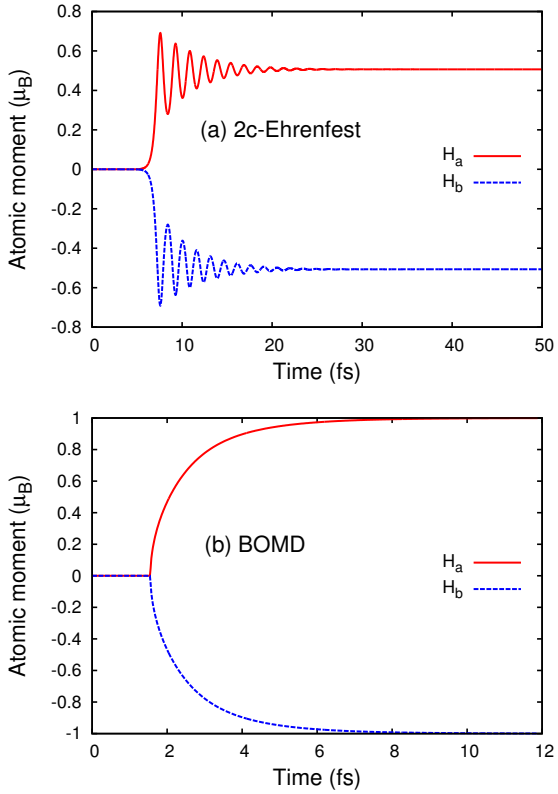

Figure 5.7: Time evolution of the atomic magnetic moments of the two hydrogen atoms computed with (a) 2c-Ehrenfest dynamics with TD-2cB3LYP and (b) BOMD dynamics with UB3LYP and 2cB3LYP. Note that BOMD results using UB3LYP and 2cB3LYP are indistinguishable.

moments) during the H_2 dissociation, computed using the 2c-Ehrenfest method. Within the first 8 fs where the Ehrenfest dynamics is still following the closed-shell singlet potential surface, there are no net magnetic moments on either of the hydrogen atoms. At the asymptotic dissociative limit (i.e. $R_{H-H} \rightarrow \infty$), fractional atomic moments are built up with opposite signs on separated atoms. However, the magnetic moment on each dissociated H atom does not reach unit Bohr magneton, compared to the correct dissociation limit obtained using BOMD dynamics with SCF-converged and stability-tested UB3LYP or 2cB3LYP (Fig. 5.7(b)). This observation suggests that even though the 2c-Ehrenfest formalism improves the description of the crossover of different spin-state, it is still a mean-

field description. An interesting oscillatory phenomenon is observed in the time-evolution of atomic moment in the avoided crossing region. As the molecule starts to dissociate into two hydrogen atoms, there is mixing-in of triplet spin state and the trajectory no longer follows one single spin-configurational potential surface. The coherent oscillation of the atomic moments between 8 fs – 20 fs indicates such mixing between singlet and triplet states. Such a spin coherence is absent in the BOMD dynamics and can only be observed by solving the time-dependent many-body equations. In other words, the 2c-Ehrenfest formalism can be used to investigate spin coherence in reaction dynamics.

B. Dissociation of O_2

Our next example corresponds to the O_2 dissociation dynamics, which plays a prominent role in the circle of life as well as in catalysis. At equilibrium geometry, the ground state of the O_2 molecule is a triplet ($^3\Sigma_g^-$), which behaves rather inert in the gas-phase where other reactant and product molecules are in the spin singlet state. This is due to Wigner's spin conservation rule by which the spin triplet-to-singlet transition is strongly suppressed. In order to facilitate the reaction, O_2 must go through a spin-state transition which can be initiated either by spin-orbit coupling or by interaction with nuclear motion. Depending on different initial conditions, O_2 may go through three different dissociation pathways:

$$
\begin{aligned}
(a) \qquad & O_2(^3\Sigma_g^-) \rightarrow O(^3P) + O(^3P) \\
(b) \qquad & O_2(^3\Sigma_g^-) \rightarrow O(^3P) + O(^1D) \\
(c) \qquad & O_2(^3\Sigma_g^-) \rightarrow O(^3P) + O(^1S) ins
\end{aligned}
$$

where Reaction (a) is the lowest-energy dissociation path with a possible change in the overall spin state, i.e. from triplet to the degenerate singlet or quintet. Reactions (b) and (c) are higher-energy dissociation pathways where the overall spin is conserved. These two pathways are more desirable in catalysis, since the singlet oxygen atoms are generated.

In the following dynamical simulations, the 2cB3LYP hybrid functional and the cc-pVDZ basis set were used. At the B3LYP/cc-pVDZ level, the dissociation limit (c) is $\sim$ 8.2 eV above the equilibrium $^3\Sigma_g^-$ energy, as indicated in Figure 5.8. Note that the dissociation

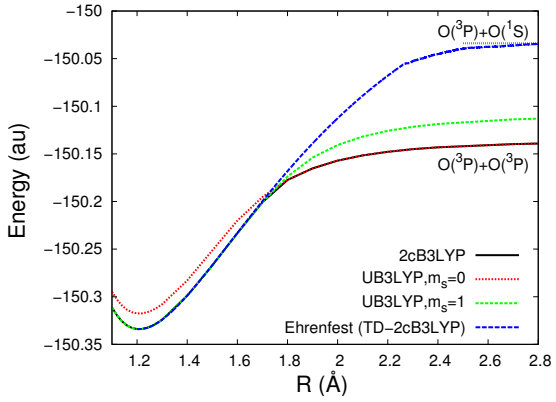

Figure 5.8: Potential energy surfaces of O_2 at different levels of theory, including energies from SCF converged solutions at the UB3LYP (stability-tested), 2cB3LYP levels, and energies from TD-propagated electron density in the Ehrenfest dynamics with the given initial condition. The dissociation limit of $O(^3P) + O(^1S)$ is also shown.

limit (b) with $O(^1D)$ cannot be obtained within the single-configuration approach, however the energy should be slightly lower than that of dissociation limit (c). Since the 2c-Ehrenfest dynamics preserves the projected spin, i.e. the $m_s = 1$ value. Therefore, the lowest-energy dissociation path is not accessible within the single-configuration approach since the m_s value changes from 1 to 0. That leaves the Reactions (b) and (c) the lowest accessible states in the Ehrenfest mean-potential calculations. In this work, we only showcase the characteristics of a single dynamics that follows closely the Reaction pathways (b) and (c). The 2c-Ehrenfest dynamics simulation was carried out with the following initial condition: the initial geometry was at the ground state equilibrium with the O-O distance of 1.2 Å, and the initial kinetic energy was set to $\sim$ 8.1 eV, with the directions of the nuclear momenta pointing away from each other along the molecular axis. A step size of $\Delta t_N = 0.01 fs$, $\Delta t_{Ne} = 0.002 fs$, $\Delta t_e = 0.001 fs$ was used for the simulation.

Figure 5.9 shows the time evolution of the atomic magnetic moments of the two oxygen atoms. At $t = 0$, the magnetic moment is equally distributed among two oxygen atoms (one μ_B on each atom) in the triplet O_2 configuration. Within the first 12 fs the O_2 molecule remains in the collinear, triplet state. Starting from $\sim$ 12 fs, spin coherence starts to appear

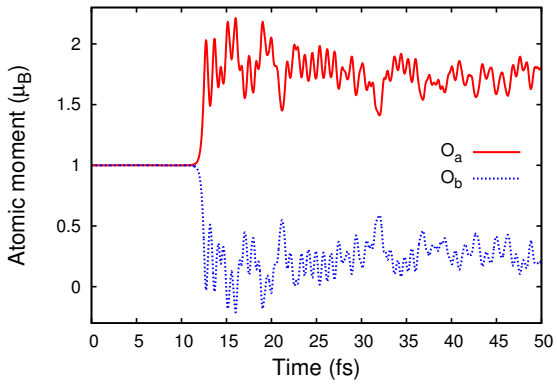

Figure 5.9: Time evolution of the atomic magnetic moments of the two oxygen atoms for the dissociative trajectory.

arising from breaking paired electrons. This spin coherence persists until the two oxygen atoms are far enough away from the spin-state crossing region. At the asymptotic dissociation limit, two atomic oxygens with atomic moments of $\sim 2\ \mu_B$ and $\sim 0\ \mu_B$, respectively, are observed. As the final total TD-2cB3LYP potential energy is close to the dissociation limit (b) and (c), it is likely that the nonadiabatic 2c-Ehrenfest dynamics under the given initial condition is able to dissociate the $O_2(^3\Sigma_g^-)$ into atomic species dominated by $O(^3P)$ + $O(^1D)/O(^1S)$, a highly desirable pathway from electro-catalytic point of view.

5.2.4 Conclusions

In this section, an *ab initio* two-component Ehrenfest molecular and spin dynamics approach is developed to study the effects of nuclear motion on the spin evolution of molecular systems. In this formulation, nuclei move classically in a mean-field potential generated by the electrons, and the electronic and spin degrees of freedom are propagated using the time-dependent two-component density functional theory (TD-2cDFT). Integration of the Ehrenfest dynamics equations of motion was achieved using three-time-step algorithm with the velocity-Verlet for nuclear motion, the nuclear-position-dependent midpoint Fock update, and the modified midpoint and unitary transformation method for electronic propagation.

Compared to conventional TDDFT Ehrenfest dynamics, the TD-2cDFT Ehrenfest dy-

namics method provides several improvements. In addition to enabling the study of the dynamics of non-collinear and spin frustrated magnetic materials, it also provides a proper description of spin-rotation and spin-flip dynamics by relaxing spin symmetry constraints. The method also accounts for electronic nonadiabaticity within a mean-field framework. The method is applied to study the spin evolution during the H_2 and O_2 dissociation. The results suggest that TD-2cDFT Ehrenfest can recover some aspects of the correct dissociation limit, particularly in situations where there are crossovers of different spin states. Because we have not accounted for spin-orbit coupling, the transitions in spin state arise wholly from the coupled electronic and nuclear dynamics. Incorporating spin-orbit coupling into the 2c-Ehrenfest dynamics remains to be seen. Comparison of (2c)Ehrenfest dynamics with TD-RB3LYP, TD-UB3LYP and TD-2cB3LYP suggests that as the constraint on spin configuration is relaxed in electronic structure theory, the Ehrenfest method is better able to handle diabatic surface crossing of different spin configurations.

A unique feature of the 2c-Ehrenfest dynamics is that spin coherence arising from mixings of spin states can be resolved as seen in the test cases. In addition, an important potential application of the TD-2cDFT Ehrenfest dynamics is the study of spin transport processes in molecular or nanoscale magnetic devices. Since the spacings between adiabatic energy surfaces are smaller than the thermal energy at room temperature, the nonadiabatic effects become more prominent and the following of specific adiabatic surfaces is no longer important. Spin fluctuations will be accounted for by statistical averaging of Ehrenfest trajectories.

Chapter 6

EFFICIENT MCSCF METHOD

6.1 Overview of the CASSCF Optimization

In the CASSCF method, the initial wavefunction $|0\rangle$ is described as a linear combination of some configuration state functions (CSFs) or Slater determinants $|K\rangle$, generated by excitations within the active space,

$$|0\rangle = \sum_{K=1}^{M} c_K |K\rangle \tag{6.1}$$

where M is the dimension of the expansion.

Optimization of the CASSCF wavefunction consists of two parts: (1) variation of the CI expansion coefficients, and (2) variation of the molecular orbitals.

6.1.1 Variation of the CI Expansion Coefficients

There are several ways to parameterize the CI problem. The simplest way is to use the linear expansion coefficients $\{c_K\}$ as the variational parameters. However, this parameterization contains a redundancy because of the normalization constraint

$$\sum_{K=1}^{M} c_K = 1 \tag{6.2}$$

Another way is to use an exponential unitary parameterization of the CI space, where the variation of the CI wavefunction $\{c_K\}$ is achieved by

$$|\tilde{0}\rangle = \exp(\hat{S})|0\rangle$$

where the operator $\hat{S}$ is defined as

$$\hat{S} = \sum_{n \neq 0}^{M} s_n |n\rangle\langle 0| - |0\rangle\langle n| \tag{6.3}$$

and $\{|n\rangle\}$ are orthogonal complement to the reference state $|0\rangle$.

The advantege of using this exponential parameterization is that it includes the normalization constraint through the exponential unitary operator and the optimization can be easily controlled.

6.1.2 Variation of the Orbitals

The variation of the orbitals $\{\phi_p\}$ can be achieved by orbital rotation through the real unitary matrix $\mathbf{U}$:

$$\tilde{\phi}_p = \sum_q U_{pq} \phi_q \tag{6.4}$$

where the $\mathbf{U}$ matrix may be written in terms of an anti-symmetrix matrix $\mathbf{x}$:

$$\mathbf{U} = \exp(\mathbf{x}) \tag{6.5}$$

It can be shown that the unitary transformation on the orbitals is equivalent to the following transformation on the CASSCF wavefunction:[350]

$$|\tilde{0}\rangle = \exp(\hat{T})|0\rangle$$

where the operator $\hat{X}$ is defined in the formulism of second quantization:

$$\hat{T} = \sum_{pq} x_{pq} \hat{E}_{pq} \tag{6.6}$$

where $\hat{E}_{pq}$ is the single-excitation operator and are defined as

$$\hat{E}_{pq} = \hat{E}^{\alpha}_{pq} + \hat{E}^{\beta}_{pq} = a^{\dagger}_{p\alpha} a_{q\alpha} + a^{\dagger}_{p\beta} q_{l\beta} \tag{6.7}$$

where $a^{\dagger}_{p}$ and a_q are creation and annihilation operators in second quantized formalism.

6.1.3 The CASSCF Energy Expression

With the above mentioned exponential parameterization for the CI coefficients and orbital rotations, the CASSCF wavefunction can be written as

$$|\tilde{0}\rangle = \exp(\hat{T}) \exp(\hat{S}) |0\rangle \tag{6.8}$$

The total CASSCF energy is then

$$E = \langle \tilde{0} | \hat{H} | \tilde{0} \rangle = \langle 0 | \exp(-\hat{S}) \exp(-\hat{T}) \hat{H} \exp(\hat{T}) \exp(\hat{S}) | 0 \rangle \tag{6.9}$$

Expanding the above expression using the Baker-Campbell-Hausdorff formula, we have

$$\begin{aligned} E &= \langle \tilde{0} | \exp(-\hat{S}) (\hat{H} + [\hat{H}, \hat{T}] + \frac{1}{2}[[\hat{H}, \hat{T}], \hat{T}] + \cdots) \exp(\hat{S}) | 0 \rangle + [[\hat{H}, \hat{T}], \hat{S}] + \cdots | 0 \rangle \\ &= E^{(0)} + \mathbf{s}^T \mathbf{g}^c + \mathbf{x}^T \mathbf{g}^o + \frac{1}{2} \mathbf{s}^T \mathbf{H}^{cc} \mathbf{s} + \frac{1}{2} \mathbf{x}^T \mathbf{H}^{oo} \mathbf{x} + \mathbf{x}^T \mathbf{H}^{oc} \mathbf{s} + \cdots \end{aligned} \tag{6.10}$$

where $\mathbf{g}^c$ is called the state gradient, $\mathbf{g}^o$ the orbital gradient, $\mathbf{H}^{cc}$ the state Hessian, $\mathbf{H}^{oo}$ the orbital Hessian, and $\mathbf{H}^{oc}$ the state-orbital coupling Hessian.

Optimization of the CASSCF wavefunction is equivalent to finding the stationary solution of the energy with respect to the CI variation $\mathbf{s}$ and the orbital rotation $\mathbf{x}$:

$$\frac{\partial E}{\partial \mathbf{s}} = \mathbf{g}^c = 0 \tag{6.11}$$

$$\frac{\partial E}{\partial \mathbf{x}} = \mathbf{g}^o = 0 \tag{6.12}$$

If we truncate terms up to second order in $\mathbf{s}$ and $\mathbf{x}$, we obtain the second-order energy

expression:

$$E^{(2)} \approx E^{(0)} + \begin{pmatrix} \mathbf{s}^T & \mathbf{x}^T \end{pmatrix} \begin{pmatrix} \mathbf{g}^c \\ \mathbf{g}^o \end{pmatrix} + \frac{1}{2} \begin{pmatrix} \mathbf{s}^T & \mathbf{x}^T \end{pmatrix} \begin{pmatrix} \mathbf{H}^{cc} & \mathbf{H}^{co} \\ \mathbf{H}^{oc} & \mathbf{H}^{oo} \end{pmatrix} \begin{pmatrix} \mathbf{s} \\ \mathbf{x} \end{pmatrix} \tag{6.13}$$

Optimization of this truncated energy expression leads to the Newton-Raphson equation:

$$\begin{pmatrix} \mathbf{H}^{cc} & \mathbf{H}^{co} \\ \mathbf{H}^{oc} & \mathbf{H}^{oo} \end{pmatrix} \begin{pmatrix} \mathbf{s} \\ \mathbf{x} \end{pmatrix} = - \begin{pmatrix} \mathbf{g}^c \\ \mathbf{g}^o \end{pmatrix} \tag{6.14}$$

6.1.4 The Two-Step Optimization Approach

Eq. (6.14) can be either solved simultaneously for both CI variation $\mathbf{s}$ and orbital rotation $\mathbf{x}$, or solved in a two-step manner where the CI coefficients are optimized for the current set of orbitals and the Newton-Raphson step is taken only for the orbital rotations. Both simultaneous method and two-step approach possess the same local convergence properties, however, the two-step procedure is expected to be more stable since the CI coefficients are optimized more fully at each iteration.

In the two-step procedure, the CI coefficients are optimized first. This amounts to solving $\mathbf{g}^c = 0$, and the Newton-Raphson equation, Eq. (6.14) becomes

$$\mathbf{H}^{cc}\mathbf{s} + \mathbf{H}^{co}\mathbf{x} = 0 \tag{6.15}$$

$$\mathbf{H}^{oc}\mathbf{s} + \mathbf{H}^{oo}\mathbf{x} = -\mathbf{g}^o \tag{6.16}$$

which can be written as a partitioned Newton-Raphson equation for orbital rotations only:

$$\left(\mathbf{H}^{oo} - \mathbf{H}^{oc}\mathbf{H}^{\mathbf{cc}\,-1}\mathbf{H}^{co}\right)\mathbf{x} = -\mathbf{g}^o \tag{6.17}$$

The flow chart for the two-step CASSCF wavefunction optimization is given in Figure 6.1. The matrix elements for orbital rotation gradient $\mathbf{g}^o$, the orbital-orbital Hessian $\mathbf{H}^{oo}$, and the state-state Hessian $\mathbf{H}^{cc}$, and the state-orbital coupling Hessians $\mathbf{H}^{oc}$ and $\mathbf{H}^{co}$ will be given in Appendix I.

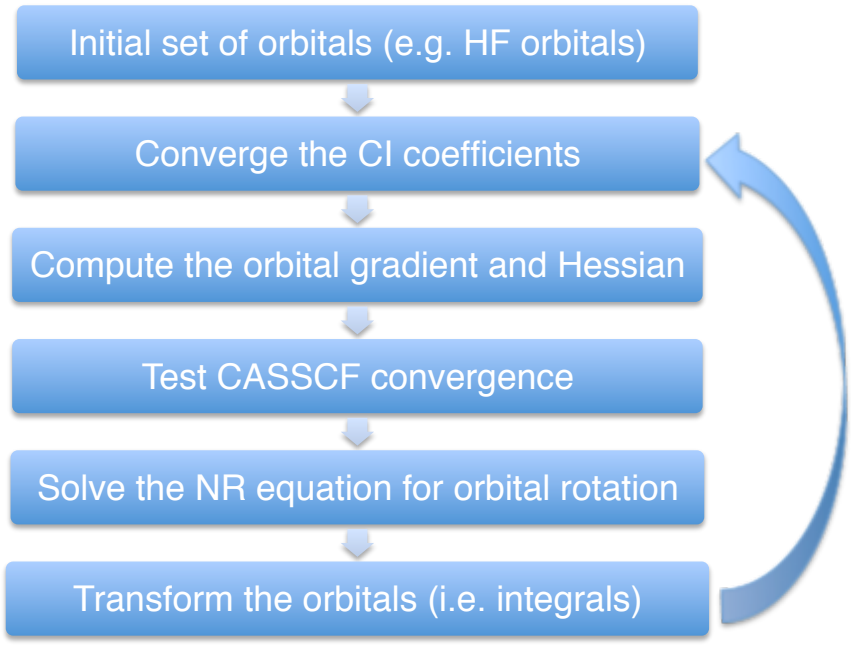

Figure 6.1: Flow chart for the two-step CASSCF wavefunction optimization.

6.1.5 The CI Coefficient Optimization

As discussed above, the first step in the two-step CASSCF optimziation is to solve for the stationary point of the energy with respect to the CI variation, i.e.

$$g_n^c = 2\langle 0|\hat{H}|n\rangle = 0 \tag{6.18}$$

where $|n\rangle$ is an orthogonal complement to $|0\rangle$. Note that the dimension of the state gradient $\mathbf{g}^c$ is $M-1$.

The choice of the orthogonal complement basis $\{|n\rangle\}$ is arbitrary. For computational convenience, two bases have been used for constructing the orthogonal complement basis: the CI eigenvector basis and the projected basis. The CI eigenvector basis is linearly independent and orthonormal. However, it is not a practical choice when the CI expansion becomes large where full diagonalization of the CI Hamiltonian is impossible.

The projected basis is defined as a projection on to the configurational space:

$$|n\rangle = (1 - |0\rangle\langle 0|)|\tilde{n}\rangle \tag{6.19}$$

where $|\tilde{n}\rangle$ are the configurational state functions (CSFs) or Slater determinants, and they are orthonormal:

$$\langle\tilde{m}|\tilde{n}\rangle = \delta_{mn} \tag{6.20}$$

Note that the dimension of the projected basis is M. Therefore it is overcomplete.

The advantage of using the projected basis is that it can be readily constructed and requires no additional computational cost.

In the projected basis, the state gradient becomes

$$g_n^c = 2\langle 0|\hat{H}(1 - |0\rangle\langle 0|)|\tilde{n}\rangle = 2\sum_m \langle\tilde{m}|\hat{H} - E_0|\tilde{n}\rangle c_m \tag{6.21}$$

and in matrix notation,

$$\mathbf{g}^c = (\mathbf{H} - E_0)\mathbf{c} \tag{6.22}$$

Therefore, the optimization of the CI coefficients in the project basis is equivalent to solving the eigenvalue problem:

$$\mathbf{g}^c = 0 \quad \Leftrightarrow \quad \mathbf{Hc} = E_0\mathbf{c} \tag{6.23}$$

6.1.6 The CAS-CI Eigenvalue Problem

For a CASSCF wavefunction, the CI expansion is limited to excitations within the active space. In this case, the Hamiltonian operator $\hat{H}$ can be written as

$$\hat{H} = \varepsilon^c + \hat{H}^{\mathrm{CAS}} \tag{6.24}$$

where ε^c is the Hartree-Fock energy of the closed shell inactive orbitals and is defined as

$$\varepsilon^c = 2\sum_i h_{ii} + \sum_{ij}\Big[2\,(ii|jj) - (ij|ji)\Big] \tag{6.25}$$

and $\hat{H}^{\mathrm{CAS}}$ is the active space Hamiltonian and is defined as

$$\begin{aligned}\hat{H}^{\mathrm{CAS}} &= \sum_{tu} h^c_{tu}\hat{E}_{tu} + \frac{1}{2}\sum_{tuvw}(tu|vw)\,(\hat{E}_{tu}\hat{E}_{vw} - \delta_{uv}\hat{E}_{tw}) \\ &= \sum_{tu} h^{c\prime}_{tu}\hat{E}_{tu} + \frac{1}{2}\sum_{tuvw}(tu|vw)\,\hat{E}_{tu}\hat{E}_{vw}\end{aligned} \tag{6.26}$$

where $\mathbf{h}^c$ is the closed shell inactive orbital Fock matrix, and is given by

$$h^c_{tu} = h_{tu} + \sum_i\Big[2\,(tu|ii) - (ti|ui)\Big] \tag{6.27}$$

and $\mathbf{h}^{c\prime}$ is

$$h^{c\prime}_{tu} = h^c_{tu} - \frac{1}{2}\sum_v (tv|uv) \tag{6.28}$$

Therefore, the CAS-CI eigenvalue problem can be written as

$$\mathbf{H}^{\mathrm{CAS}}\mathbf{c} = E^{\mathrm{CAS}}\mathbf{c} \tag{6.29}$$

where E^{CAS} is defined as

$$E^{\mathrm{CAS}} = E_0 - \varepsilon^c \tag{6.30}$$

Since the CI expansion is complete within the active space, by writting the CAS-CI eigenvalue problem in the form given in Eq. (6.29), we can directly apply efficient diagonalization algorithms developed for the full-CI problem.

6.2 A New Integral-Driven Determinant-Based CI Algorithm

6.2.1 The Determinant CI Approach

Large-scale CI/CAS calculations usually require the computation of only a few eigenvalues and eigenvectors of a large, real-symmetric CI matrix. Iterative eigensolvers, such as the Cooper-Nesbet method,[351] Lanczos method,[352] and Davidson algorithm[353] are widely used. In these iterative procedures, the most time-consuming step is the calculation of the following matrix-vector product:

$$\sigma_I = \sum_J \langle I|\hat{H}|J\rangle c_J \tag{6.31}$$

where I, J stand for the CI basis functions (either configurational state functions or determinants) and $\mathbf{c}$ is an approximate eigenvector from previous iteration. $\hat{H}$ is the Hamiltonian operator and is expressed in a second-quantized form:

$$\hat{H} = \sum_{kl} h'_{kl}\hat{E}_{kl} + \frac{1}{2}\sum_{ijkl} \big(ij|kl\big)\, \hat{E}_{ij}\hat{E}_{kl} \tag{6.32}$$

where $i, j, k.l$ are indices for spatial orbitals, and the summations run through all the spatial orbitals. $\hat{E}_{kl}$ are the single-exciation operators and are defined as

$$\hat{E}_{kl} = \hat{E}^{\alpha}_{kl} + \hat{E}^{\beta}_{kl} = a^{\dagger}_{k\alpha}a_{l\alpha} + a^{\dagger}_{k\beta}a_{l\beta} \tag{6.33}$$

$\big(ij|kl\big)$ are two-electron integrals in chemist's notation and are defined as

$$\big(ij|kl\big) = \int \phi^*_i(\mathbf{r}_1)\phi_j(\mathbf{r}_1)\frac{1}{\mathbf{r}_{12}}\phi^*_k(\mathbf{r}_2)\phi_l(\mathbf{r}_2)dr_1dr_2 \tag{6.34}$$

h_{kl} and h'_{kl} are one-electron integrals and are defined as

$$h'_{kl} = h_{kl} - \frac{1}{2}\sum_j \big(kj|jl\big) \tag{6.35}$$

6.2.2 String/Graphical Representation of Slater Determinants

As pointed out in the previous section, the most time-consuming step in a large-scale CI calculation is to construct the matrix-vector product for iterative solutions. Although the use of the configurational state functions (CSF's) can greatly reduce the size of the CI space, it is not easily vectorized for highly efficient implementations. Determinant based CI, on the other hand, can be easily vectorized when the determinants are expressed as alpha strings and beta strings:

$$|I\rangle = |S(I_\alpha)S(I_\beta)\rangle = S(I_\alpha)S(I_\beta)|\text{vac}\rangle \tag{6.36}$$

where $S(I_\alpha)$ and $S(I_\beta)$ are the alpha and beta strings, respectively, and they are ordered products of n_α and n_β creation operators. For example, for a Slater determinant

$$\begin{aligned} |I\rangle &= |\phi_{1\alpha}\phi_{2\alpha}\phi_{3\alpha}\phi_{1\beta}\phi_{3\beta}\phi_{5\beta}\rangle \\ &= a^\dagger_{1\alpha}a^\dagger_{2\alpha}a^\dagger_{3\alpha}a^\dagger_{1\beta}a^\dagger_{3\beta}a^\dagger_{5\beta}|\text{vac}\rangle \end{aligned} \tag{6.37}$$

the alpha and beta strings are given by

$$S(I_\alpha) = a^\dagger_{1\alpha}a^\dagger_{2\alpha}a^\dagger_{3\alpha} \tag{6.38}$$

$$S(I_\beta) = a^\dagger_{1\beta}a^\dagger_{3\beta}a^\dagger_{5\beta} \tag{6.39}$$

Having separated the alpha and beta strings, the next step is the construction and ordering of these strings. This can be done using the graphical representation.

The whole alpha/beta string space is defined by the number of alpha/beta electrons n_α/n_β, and the total number of spacial orbitals N. This can be uniquely mapped to the two-slope directed graphs $G_2(N, n_\alpha)$ and $G_2(N, n_\beta)$.

Figure 6.2 shows such a graph representing the alpha string space for $n_\alpha = 3, N = 5$. Each string is represented by a path on the graph, from the head ($N_{\text{el}} = 0, N_{\text{orb}} = 0$) to the tail ($N_{\text{el}} = n_\alpha, N_{\text{orb}} = N$). Moving down vertically from vertex $(N_{\text{el}}, N_{\text{orb}})$ to vertex $(N_{\text{el}}, N_{\text{orb}} + 1)$ indicates that orbital $N_{\text{orb}} + 1$ is unoccupied in the current string (or path),

while moving down diagonally from vertex $(N_{\rm el}, N_{\rm orb})$ to vertex $(N_{\rm el}+1, N_{\rm orb}+1)$ means that orbital $N_{\rm orb}+1$ is occupied. For example, in Figure 6.2 the alpha string $a^\dagger_{1\alpha}a^\dagger_{3\alpha}a^\dagger_{4\alpha}$ is represented by the following path:

$$a^\dagger_{1\alpha}a^\dagger_{3\alpha}a^\dagger_{4\alpha} : (0,0) \rightarrow (1,1) \rightarrow (1,2) \rightarrow (2,3) \rightarrow (3,4) \rightarrow (3,5) \tag{6.40}$$

Now we need a proper labeling and ordering of all the paths. We adopt the conven-

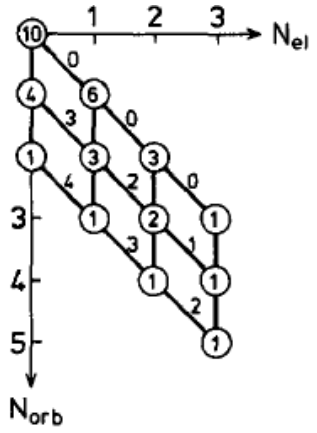

Figure 6.2: Graph of the alpha string space for $n_\alpha = 3, N = 5$. The numbers inside the circles are the vertex weights and the numbers on the sloped lines are the arc weights for lexical ordering.

tion of "lexical ordering" by Duch.[354] In this convention, each vertex is assigned a weight $W(N_{\rm el}, N_{\rm orb})$, and each arc ending at vertex $(N_{\rm el}, N_{\rm orb})$ is assigned an arc weight $Y(N_{\rm el}, N_{\rm orb})$. We label the vetical arc weights as $Y_0(N_{\rm el}, N_{\rm orb})$, and the diagonal arc weights as $Y_1(N_{\rm el}, N_{\rm orb})$.

The address of any given path or alpha string can be computed by adding all the diagonal arc weights along the path:

$$I_\alpha(L^\alpha) = 1 + \sum_{i=1}^{N} Y_{L_i}(N_i, i) \tag{6.41}$$

where L_i is the occupation of the i-th arc (0 or 1) and (N_i, i) are the coordinates of vertices in the path.

The arc weights $Y_1(N_i, i)$ can be calculated either recursively using the scheme of Duch,[354] or directly using the addressing scheme defined by Knowles and Handy:[355]

$$Y_1(N_{\rm el}, N_{\rm orb}) = \sum_{m=N-N_{\rm orb}+N_{\rm el}}^{N-N_{\rm el}} \left[\begin{pmatrix} m \\ n_\alpha - N_{\rm el} \end{pmatrix} - \begin{pmatrix} m-1 \\ n_\alpha - N_{\rm el} - 1 \end{pmatrix} \right]$$
$$(N - n_\alpha + N_{\rm el} \geq N_{\rm orb} \geq N_{\rm el}; \quad N_{\rm el} < n_\alpha) \tag{6.42}$$
$$Y_1(n_\alpha, N_{\rm orb}) = N_{\rm orb} - n_\alpha, \quad (N \geq N_{\rm orb} \geq n_\alpha)$$

Now we come to the question of how to generate all the paths of a given graph on a computer. There are two common algorithms for path searching: the depth-first search and the breadth-first search. In our implementation, we use the depth-first search algorithm to search the paths. During the search for each path, we generate and store the occupied orbital string O^α, unoccupied orbital string U^α, and the occupation string L^α. Table 1 shows an example of $n_\alpha = 3, N = 5$.

Table 6.1: List of the occupied orbital strings O^α, unoccupied orbital strings U^α, and the occupation strings L^α for $n_\alpha = 3, N = 5$.

I_α	O^α	U^α	L^α
1	123	45	11100
2	124	35	11010
3	125	34	11001
4	134	25	10110
5	135	24	10101
6	145	23	10011
7	234	15	01110
8	235	14	01101
9	245	13	01011
10	345	12	00111

6.2.3 Calculating the $\boldsymbol{\sigma}$ Vector Ssing the String Representation

Given the addresses of the alpha string I_α and beta string I_β, the associated Slater determinant I can be addressed simply as the element of a rectangular array (I_α, I_β). In this way, operations on the alpha string alone can be performed for all beta strings in a vector loop, and vice versa.

Now the $\boldsymbol{\sigma}$ vector in Eq.(6.31) can be written as

$$\sigma(I_\alpha, I_\beta) = \sum_{J_\alpha, J_\beta} \langle J_\beta J_\alpha | \sum_{kl} h'_{kl} \hat{E}_{kl} + \frac{1}{2} \sum_{ijkl} \big(ij|kl\big)\, \hat{E}_{ij}\hat{E}_{kl} | I_\alpha I_\beta \rangle c(J_\alpha, J_\beta) \tag{6.43}$$

where we have substituted the expression for $\hat{H}$ from Eq.(6.32). Further, from the relation (6.33), the above equation can be splitted into three terms:

$$\sigma(I_\alpha, I_\beta) = \sigma^\beta(I_\alpha, I_\beta) + \sigma^\alpha(I_\alpha, I_\beta) + \sigma^{\alpha\beta}(I_\alpha, I_\beta) \tag{6.44}$$

where $\boldsymbol{\sigma}^\beta$ involves only the β-component of excitation operators $\hat{E}^\beta_{kl}$:

$$\begin{aligned}
\sigma^\beta(I_\alpha, I_\beta) &= \sum_{J_\alpha, J_\beta} \langle J_\beta J_\alpha | \sum_{kl} h'_{kl} \hat{E}^\beta_{kl} + \frac{1}{2} \sum_{ijkl} \big(ij|kl\big)\, \hat{E}^\beta_{ij}\hat{E}^\beta_{kl} | I_\alpha I_\beta \rangle c(J_\alpha, J_\beta) \\
&\qquad \text{(using the resolution of identity:} \hat{1} = \sum_{K_\beta} |K_\beta\rangle\langle K_\beta|) \\
&= \sum_{J_\beta} \sum_{kl} \left[h'_{kl} \langle J_\beta | \hat{E}^\beta_{kl} | I_\beta \rangle + \frac{1}{2} \sum_{K_\beta} \sum_{ij} \big(ij|kl\big)\, \langle J_\beta | \hat{E}^\beta_{ij} | K_\beta \rangle \langle K_\beta | \hat{E}^\beta_{kl} | I_\beta \rangle \right] c(I_\alpha, J_\beta)
\end{aligned} \tag{6.45}$$

Similarly, we can be obtain the expression for $\boldsymbol{\sigma}^\alpha$, which only has the α-component of excitation operators $\hat{E}^\alpha_{kl}$:

$$\sigma^\alpha(I_\alpha, I_\beta) = \sum_{J_\alpha} \sum_{kl} \left[h'_{kl} \langle J_\alpha | \hat{E}^\alpha_{kl} | I_\alpha \rangle + \frac{1}{2} \sum_{K_\alpha} \sum_{ij} \big(ij|kl\big)\, \langle J_\alpha | \hat{E}^\alpha_{ij} | K_\alpha \rangle \langle K_\alpha | \hat{E}^\alpha_{kl} | I_\alpha \rangle \right] c(J_\alpha, I_\beta) \tag{6.46}$$

$\boldsymbol{\sigma}^{\alpha\beta}$ contains the mixing of α- and β-components of excitation operators, and is expressed as

$$\sigma^{\alpha\beta}(I_\alpha, I_\beta) = \sum_{J_\alpha, J_\beta} \sum_{ijkl} \big(ij|kl\big) \langle J_\beta|\hat{E}^{\beta}_{ij}|I_\beta\rangle \langle J_\alpha|\hat{E}^{\alpha}_{ij}|I_\alpha\rangle c(J_\alpha, J_\beta) \tag{6.47}$$

where the second equality was obtained by permuting i, j with k, l in the summation.

6.2.4 Generating the Excitation List

The computation of the $\boldsymbol{\sigma}$ vector involves the calculation of the coupling matrix elements, i.e. the matrix elements of the single-excitation operators $\langle K_\alpha|\hat{E}^{\alpha}_{kl}|L_\alpha\rangle$. There are two ways to generate these coupling matrix elements: the Configuration-Driven Excitation List and the Integral-Driven Excitation List.

In the Configuration-Driven Excitation List $\mathcal{L}1\{3, N_{kl}, L_\alpha\}$, for each alpha string L_α, all non-zero excitations kl, the addresses K_α of the corresponding excited strings and the values of the coupling $\mathrm{Sgn}(kl)$ are stored.

In the Integral-Driven Excitation List $\mathcal{L}2\{3, I, kl\}$, for each excitation index pair kl, all corresponding left string K_α and right string L_α, and the values of the coupling $\mathrm{Sgn}(kl)$ are stored.

6.2.5 A New Integral-Driven Algorithm for Computing the $\boldsymbol{\sigma}$ Vector

Having the excitation list and all the necessary one- and two-electron integrals (they are pre-calculated and stored in main memory) ready, now we can calculate the $\boldsymbol{\sigma}$ vector according to Eqs.(6.45-6.47). Here we present a new highly vectorized integral-driven CI algorithm, which is an improved version based on Olsen's algorithm[356] and Knowles and Handy's algorithm.[355]

In the integral-driven algorithm, the $\sigma^{\alpha\alpha}$ is rearranged as:

$$\sigma^{\alpha\alpha}_{I_\alpha, I_\beta} = \sum_{kl} h'_{kl} \sum_{J_\alpha} \langle I_\alpha|\hat{E}^{\alpha}_{kl}|J_\alpha\rangle C_{J_\alpha, I_\beta} + \frac{1}{2} \sum_{kl} \sum_{K_\alpha} \langle K_\alpha|\hat{E}^{\alpha}_{kl}|J_\alpha\rangle \sum_{ij} \langle I_\alpha|\hat{E}^{\alpha}_{ij}|K_\alpha\rangle \big(ij|kl\big) \sum_{J_\alpha} C_{J_\alpha, I_\beta} \tag{6.48}$$

A vectorized algorithm for $\sigma^{\alpha\alpha}$ is given by:

Loop over kl

Loop over integral-driven list: $\mathcal{L}2\{K_\alpha(I), J_\alpha(I), \mathrm{sgn}(I), I, kl\}$

$|K_\alpha(I)\rangle = \hat{E}^\alpha_{kl}|J_\alpha(I)\rangle \mathrm{sgn}(I)$

$F(K_\alpha) = F(K_\alpha) + \mathrm{sgn}(I) h'_{kl}$; vectorized over I_β

Loop over configuration-driven list: $\mathcal{L}1\{ij, I_\alpha, \mathrm{sgn}(ij), N_{ij}, K_\alpha\}$

$|I_\alpha\rangle = \hat{E}^\alpha_{ij}|K_\alpha\rangle \mathrm{sgn}(ij)$

$F(I_\alpha) = F(I_\alpha) + \frac{1}{2}\mathrm{sgn}(ij)\mathrm{sgn}(I)\,\big(ij|kl\big)$

end of loop over $\mathcal{L}1$

$\sigma^{\alpha\alpha}(I_\alpha, I_\beta) = \sigma^{\alpha\alpha}(I_\alpha, I_\beta) + F(I_\alpha) C_{J_\alpha, I_\beta}$; vectorized over I_β

end of loop over $\mathcal{L}2$

end of loop over kl

$\sigma^{\beta\beta}$ can be evaluated in a similar way.

The third term, $\sigma^{\alpha\beta}$ can be computed in the same way as in Olsen's algorithm. The pseudo-code is given by

Loop over kl

Loop over the integral-driven excitation list: $\mathcal{L}2\{I_\alpha(I), J_\alpha(I), \mathrm{sgn}(I), I, kl\}$

$|I_\alpha(I)\rangle = \hat{E}^\alpha_{kl}|J_\alpha(I)\rangle \mathrm{sgn}(I)$

$D(I, J_\beta) = \mathrm{sgn}(I) C_{J_\alpha, J_\beta}$; vectorized over J_β

end of loop over $\mathcal{L}2$

Loop over I_β

Loop over configuration-driven excitation list: $\mathcal{L}1\{ij, J_\beta, \mathrm{sgn}(ij), N_{ij}, I_\beta\}$

$|J_\beta\rangle = \hat{E}^\beta_{ij}|I_\beta\rangle \mathrm{sgn}(ij)$

$F(J_\beta) = F(J_\beta) + \mathrm{sgn}(ij)\,\big(ij|kl\big)$

end of loop over $\mathcal{L}1$

$V(I) = \sum_{J_\beta} F(J_\beta) D(I, J_\beta)$; vectorized over I

$\sigma^{\alpha\beta}(I_\alpha, I_\beta) = \sigma^{\alpha\beta}(I_\alpha, I_\beta) + V(I)$; vectorized over I

end of loop over I_β

end of loop over kl

A. Results and Discussion

Table 6.2: CPU time (in seconds) per Davidson iteration for benzene molecule in the 6-31G basis

CAS-CI	N_{det}	CPU time (seconds)		
		MOC	N-Resolution	Our algorithm
CAS(10,10)	63,504	0.16	0.44	0.23
CAS(10,11)	213,444	0.78	2.77	1.00
CAS(10,12)	627,264	2.63	10.08	3.75
CAS(12,12)	853,776	4.41	15.06	5.48
CAS(10,13)	1,656,369	10.81	35.32	13.54
CAS(12,13)	2,944,656	25.46	63.93	28.37
CAS(10,14)	4,008,004	32.46	118.66	45.89
CAS(12,14)	9,018,009	125.05	-	132.90

Appendix I: Matrix elements for $\mathbf{g}^o$, $\mathbf{H}^{oo}$, $\mathbf{H}^{oc}$, and $\mathbf{H}^{cc}$

A. The Active Space One- and Two-Particle Density Matrices

Once the converged CI coefficients have been obtained, i.e. once the CAS-CI eigenvalue problem Eq. (6.29) has been solved, the active space one-particle density matrix (1PDM) $\boldsymbol{\gamma}$ and two-particle density matrix (2PDM) $\boldsymbol{\Gamma}$ should be constructed. The 1PDM and 2PDM are needed for the calculation of the orbtial gradient $\mathbf{g}^o$ and the orbital Hessian $\mathbf{H}^{oo}$. They are defined as

$$\text{1PDM:} \quad \gamma_{tu} = \langle 0|\hat{E}_{tu}|0\rangle = \sum_{KL} c_K c_L \langle K|\hat{E}_{tu}|L\rangle \tag{6.49}$$

$$\text{2PDM:} \quad \Gamma_{tuvw} = \langle 0|\hat{e}_{tuvw}|0\rangle = \sum_{KL} c_K c_L \langle K|\hat{E}_{tu}\hat{E}_{vw} - \delta_{uv}\hat{E}_{tw}|L\rangle \tag{6.50}$$

B. Orbital Gradient $\mathbf{g}^o$

The orbital gradient $\mathbf{g}^o$ is given by

$$\begin{aligned} g^o_{pq} &= -(1-\hat{P}_{pq})\langle 0|[\hat{T}_{pq},\hat{H}]|0\rangle \\ &= -2(1-\hat{P}_{pq})\left[\sum_r \langle 0|\hat{E}_{pr}|0\rangle h_{qr} + \sum_{rs\tau}\langle 0|\hat{e}_{prs\tau}|0\rangle \left(qr|s\tau\right)\right] \\ &= -2(1-\hat{P}_{pq})\left[\sum_r \gamma_{pr} h_{qr} + \sum_{rs\tau}\Gamma_{prs\tau}\left(qr|s\tau\right)\right] \\ &= -2(F_{pq}-F_{qp}) \end{aligned} \tag{6.51}$$

where $\hat{P}_{pq}$ is the permutation operator that switches the indices p and q, and $\mathbf{F}$ is the generalized Fock matrix and its elements are given by

$$F_{pq} = \sum_r \gamma_{pr} h_{qr} + \sum_{rs\tau}\Gamma_{prs\tau}\left(qr|s\tau\right) \tag{6.52}$$

It is found that the generalized Fock matrix can be evaluated by blocks, due to the properties of the 1PDM and 2PDM:

$$F_{iq} = F^1_{iq} \tag{6.53}$$

$$F_{tq} = F^2_{tq} \tag{6.54}$$

$$F_{aq} = 0 \tag{6.55}$$

where $\mathbf{F}^1$ and $\mathbf{F}^2$ are defined as

$$F^1_{pq} = 2\left(h^c_{pq} + \sum_{tu}\gamma_{tu}[\left(pq|tu\right) - \frac{1}{2}\left(pt|qu\right)]\right) \tag{6.56}$$

$$F^2_{tq} = \sum_u \gamma_{tu} h^c_{qu} + \sum_{uvw}\Gamma_{tuvw}\left(qu|vw\right) \tag{6.57}$$

Since orbital rotations within each of the inactive, active and virtual spaces are zero, the nonzero blocks of the orbital gradient are: the inactive-active, the inactive-virtual, and

the active-virtual. The upper triangular part of the orbital gradient matrix is:

$$g^o_{it} = -2(F^1_{it} - F^2_{ti}) \tag{6.58}$$

$$g^o_{ia} = -2F^1_{ia} \tag{6.59}$$

$$g^o_{ta} = -2F^2_{ta} \tag{6.60}$$

Since the orbital gradient matrix is anti-symmetric, the lower triangular part can be readily obtained.

C. Orbital Hessian $\mathbf{H}^{oo}$

Elements of the orbital Hessian $\mathbf{H}^{oo}$ are given by:

$$\begin{aligned}\frac{1}{2}H^{oo}_{it,ju} &= \gamma_{tu}h^c_{ij} + \delta_{ij}(F^1_{tu} - F^2_{tu}) - \delta_{tu}F^1_{ij} + 2[4\left(ti|uj\right) - \left(tj|ui\right) - \left(tu|ij\right)] \\ &\quad - \sum_v \gamma_{tv}[4\left(vi|uj\right) - \left(vj|ui\right) - \left(vu|ij\right)] - \sum_v \gamma_{uv}[4\left(ti|vj\right) - \left(tj|vi\right) - \left(tv|ij\right)] \\ &\quad + \sum_{vw}\Big[\left(ij|vw\right)\Gamma_{tuvw} + \left(iv|jw\right)\left(\Gamma_{tvuw} + \Gamma_{tvwu}\right)\Big] \end{aligned} \tag{6.61}$$

$$\frac{1}{2}H^{oo}_{ia,jb} = 2[4\left(ai|bj\right) - \left(ab|ij\right) - \left(aj|bi\right)] + \delta_{ij}F^1_{ab} - \delta_{ab}F^1_{ij} \tag{6.62}$$

$$\frac{1}{2}H^{oo}_{ta,ub} = \gamma_{tu}h^c_{ab} - \delta_{ab}F^2_{tu} + \sum_{vw}\Big[\left(ab|vw\right)\Gamma_{tuvw} + \left(av|bw\right)\left(\Gamma_{tvuw} + \Gamma_{tvwu}\right)\Big] \tag{6.63}$$

$$\begin{aligned}\frac{1}{2}H^{oo}_{it,ja} &= \delta_{ij}(F^1_{at} - \frac{1}{2}F^2_{ta}) + 2[4\left(ti|aj\right) - \left(tj|ai\right) - \left(ta|ij\right)] \\ &\quad - \sum_v \gamma_{tv}[4\left(vi|aj\right) - \left(vj|ai\right) - \left(va|ij\right)] \end{aligned} \tag{6.64}$$

$$\begin{aligned}\frac{1}{2}H^{oo}_{it,ua} &= -\gamma_{tu}h^c_{ai} + \frac{1}{2}F^1_{ai} + \sum_v \gamma_{uv}[4\left(ti|av\right) - \left(tv|ai\right) - \left(ta|vi\right)] \\ &\quad - \sum_{vw}\Big[\left(ia|vw\right)\Gamma_{tuvw} + \left(iv|aw\right)\left(\Gamma_{tvuw} + \Gamma_{tvwu}\right)\Big] \end{aligned} \tag{6.65}$$

$$\frac{1}{2}H^{oo}_{ia,tb} = -\frac{1}{2}\delta_{ab}(F^1_{ti} + F^2_{ti}) + \sum_v \gamma_{tv}[4\left(ai|bv\right) - \left(ab|vi\right) - \left(av|bi\right)] \tag{6.66}$$

D. State-Orbital Coupling Hessian $\mathbf{H}^{oc}$

The state-orbital coupling Hessian $\mathbf{H}^{oc}$ is given by

$$\begin{aligned} H^{oc}_{pq,n} &= 2(1-\hat{P}_{pq})\left[\sum_r h_{pr}\langle 0|\hat{E}_{rq}+\hat{E}_{qr}|n\rangle + \sum_{rs\tau}\left(pr|s\tau\right)\langle 0|\hat{e}_{qrs\tau}+\hat{e}_{rqs\tau}|n\rangle\right] \\ &= 2(1-\hat{P}_{pq})\left[\sum_r h_{pr}\langle 0|\hat{E}_{qr}|n\rangle + \langle n|\hat{E}_{qr}|0\rangle + \sum_{rs\tau}\left(pr|s\tau\right)\langle 0|\hat{e}_{qrs\tau}|n\rangle + \langle n|\hat{e}_{qrs\tau}|0\rangle\right] \\ &= 4(1-\hat{P}_{pq})\left[\sum_r h_{pr}\gamma^{(n)}_{qr} + \sum_{rs\tau}\left(pr|s\tau\right)\Gamma^{(n)}_{qrs\tau}\right] \end{aligned} \tag{6.67}$$

where $\hat{P}_{pq}$ is the permutation operator that switches the indices p and q, and we have defined the transition 1PDMs and 2PDMs:

$$\gamma^{(n)}_{qr} = \frac{1}{2}\left[\langle 0|\hat{E}_{qr}|n\rangle + \langle n|\hat{E}_{qr}|0\rangle\right] \tag{6.68}$$

$$\Gamma^{(n)}_{qrs\tau} = \frac{1}{2}\left[\langle 0|\hat{e}_{qrs\tau}|n\rangle + \langle n|\hat{e}_{qrs\tau}|0\rangle\right] \tag{6.69}$$

Define the transition Fock matrix $\mathbf{F}^{(n)}$:

$$F^{(n)}_{pq} = \sum_r \gamma^{(n)}_{pr} h_{qr} + \sum_{rs\tau}\left(pr|s\tau\right)\Gamma^{(n)}_{qrs\tau} \tag{6.70}$$

Now the state-orbital coupling Hessian can be written as

$$H^{oc}_{pq,n} = -4(F^{(n)}_{pq} - F^{(n)}_{qp}) \tag{6.71}$$

Similar to the generalized Fock matrix in Eq. (6.52), the transition Fock matrix can also be split into three blocks:

$$F^{(n)}_{iq} = F^{(n)1}_{iq} = 2\sum_{tu}\gamma^{(n)}_{tu}[\left(iq|tu\right) - \frac{1}{2}\left(it|qu\right)] \tag{6.72}$$

$$F^{(n)}_{tq} = F^{(n)2}_{tq} = \sum_u \gamma^{(n)}_{tu} h^c_{qu} + \sum_{uvw}\Gamma^{(n)}_{tuvw}\left(qu|vw\right) \tag{6.73}$$

$$F^{(n)}_{aq} = 0 \tag{6.74}$$

As can be seen, $\mathbf{F}^{(n)1}$ and $\mathbf{F}^{(n)2}$ have the same formulas as the matrices $\mathbf{F}^1$ and $\mathbf{F}^2$, except that the transition density matrices are used and $\mathbf{F}^{(n)1}$ does not contain the inactive Hamiltonian $\mathbf{h}^c$.

According to Eq. (6.71), the state-orbital coupling Hessian can be constructed in the same way as the orbital gradient Eq. (6.51):

$$H^{oc}_{pq,n} = 2G^{(n)}_{pq} \tag{6.75}$$

The only difference is that in Eq. (6.75) the transition Fock matrices $\mathbf{F}^{(n)1}$ and $\mathbf{F}^{(n)2}$ are used.

E. The State Hessian $\mathbf{H}^{cc}$

Elements of the state Hessian $\mathbf{H}^{cc}$ are given by

$$H^{cc}_{nn'} = 2\langle n|\hat{H} - E_0|n'\rangle \tag{6.76}$$

where n, n' are the orthogonal complement to $|0\rangle$.

If the CI diagonalization is performed before the orbital rotation, that is, $|0\rangle$ and $|n\rangle$ represent the eigenvectors of the CI Hamiltontian:

$$\hat{H}|0\rangle = E_0|0\rangle \tag{6.77}$$

$$\hat{H}|n\rangle = E_n|n\rangle, \qquad n \neq 0 \tag{6.78}$$

then the state Hessian $\mathbf{H}^{cc}$ becomes diagonal:

$$H^{cc}_{nn'} = 2(E_n - E_0)\delta_{nn'} \tag{6.79}$$

F. The State-Orbital Coupling Contribution to the Orbital Hessian

We now evaluate the state-orbital coupling contribution to the orbital Hessian, i.e. the second term in the partitioned orbital Hessian in Eq. (6.17):

$$\Delta \mathbf{H}^{oo} = -\mathbf{H}^{oc}\mathbf{H}^{\mathbf{cc}\,-1}\mathbf{H}^{co} \tag{6.80}$$

We assume that the CI diagonalization is performed before the orbital rotation and thus $|0\rangle$ and $|n\rangle$ represent the eigenvectors of the CI Hamiltontian. The coupling correction to the orbital Hessian can be expressed as

$$\begin{aligned}
\Delta H^{oo}_{pq,rs} &= -\left(\mathbf{H}^{oc}\mathbf{H}^{\mathbf{cc}\,-1}\mathbf{H}^{co}\right)_{pq,rs} \\
&= -\sum_{n\neq 0}\frac{H^{oc}_{pq,n}H^{co}_{n,rs}}{2(E_n - E_0)} \\
&= -\sum_{n\neq 0}\frac{H^{oc}_{pq,n}H^{oc}_{sr,n}}{2(E_n - E_0)} \\
&= -\sum_{n\neq 0}\frac{2G^{(n)}_{pq}\cdot 2G^{(n)}_{sr}}{2(E_n - E_0)} \\
&= 2\sum_{n\neq 0}\frac{G^{(n)}_{pq}G^{(n)}_{rs}}{E_n - E_0}
\end{aligned} \tag{6.81}$$

Appendix II: The CASSCF Program

CASSCF is an in-house program, which calls the following important subroutines:

- Prepare the excitation lists: **StrLst** generates the alpha/beta strings and the excitation lists, which will be used repeatedly for solving the CI eigenvalue problem and the construction of the density matrices.

- Prepare the initial MO integrals: **LoAOIn** read the AO one- and two-electron integrals from the disk. **InCTrn** transforms AO integrals into MO integrals. Alternatively, the initial MO integrals can be read directly from the disk by calling subroutine **GetMOX**.

- **RHFCor** computes the inactive orbital HF energy ε^c, the inactive orbital Fock matrix $\mathbf{h}^c$, and the contracted inactive orbital Fock matrix $\mathbf{h}^{c\prime}$, in order to solve the CAS-CI eigenvalue problem.

- Optimization of the CI coefficients: There are three diagonalization methods implemented: (1) subroutine **Nesbet** uses the Cooper-Nesber iterative method to find the lowest eigenvalue (i.e. ground state only); (2) subroutine **DavIni** calls the Davidson diagonalization routine **DavDag**; (3) subroutine **DDagCI** directly diagonalizes the CI matrix (expensive, and only works when the CI expansion is smaller than a few thousands).

- Subroutine **ASDMat** forms the one- and two-particle density matrices, and subroutine **GenFck** forms the generalized Fock matrices. The density matrices and generalized Fock matrices will be used for constructing the orbital gradient and Hessian.

- Orbital rotation. There are 4 approaches: (1) do a quasi-Newton step using an approximate, diagonal orbital Hessian, where **OGradS** computes the orbital gradient in square matrix form (sparse!) and **OHessD** computes the diagonal elements of the orbital Hessian; (2) do a Newton-Raphson (NR) step using the full orbital Hessian, where **OGradL** computes the orbital gradient in the compact linearized form and **OHessF** computes the full orbital Hessian (indexing is consistent with **OGradL**); (3) Same as (2), except that the state-orbital coupling contributions are added to the orbital Hessian; (4) do a DIIS extrapolation of the orbital rotation matrix from previous steps.

- Subroutine **MatExp** forms the unitary matrix for orbtial transformation.

- Transform the one-electron and two-electron integrals. This is done in subroutine **InCTrn**

BIBLIOGRAPHY

[1] I. Vaya, T. Gustavsson, T. Douki, Y. Berlin and D. Markovitsi, "Electronic Excitation Energy Transfer Between Nucleobases of Natural DNA", *J. Am. Chem. Soc.*, **2012**, *19*, 11366–11368.

[2] B. G. Sumpter and V. Meunier, "Can Computational Approaches Aid in Untangling the Inherent Complexity of Practical Organic Photovoltaic Systems?", *J. Polym. Sci. Part B: Polym. Phys.*, **2012**, *50*, 1071–1089.

[3] D. M. Adams, L. Brus, C. E. D. Chidsey, S. Creager, C. Creutz, C. R. Kagan, P. V. Kamat, M. Lieberman, S. Lindsay, R. A. Marcus, R. M. Metzger, M. E. Michel-Beyerle, J. R. Miller, M. D. Newton, D. R. Rolison, O. Sankey, K. S. Schanze, J. Yardley and X. Zhu, "Charge Transfer on the Nanoscale: Current Status", *J. Phys. Chem. B*, **2003**, *107*, 6668–6697.

[4] P. F. Barbara, T. J. Meyer and M. A. Ratner, "Contemporary Issues in Electron Transfer Research", *J. Phys. Chem.*, **1996**, *100*, 13148–13168.

[5] A. T. Yeh, C. V. Shank and J. K. McCusker, "Electron Localization Dynamics Following Photo-Induced Charge Transfer", *Science*, **2000**, *289*, 935–938.

[6] I. Martini, B. Ma, T. Da Ros, R. Helgeson, F. Wudl and B. Schwartz, "Ultrafast Competition Between Energy and Charge Transfer in a Functionalized Electron Donor/Fullerene Derivative", *Chem. Phys. Lett.*, **2000**, *327*, 253–262.

[7] D. Mühlbacher, M. Scharber, M. Morana, Z. Zhu, D. Waller, R. Gaudiana and C. Brabec, "High Photovoltaic Performance of a Low-Bandgap Polymer", *Analyst*, **2006**, *18*, 2884–2889.

[8] J. M. Rehm, G. L. McLendon, Y. Nagasawa, K. Yoshihara, J. Moser and G. Michael, "Femtosecond Electron-Transfer Dynamics at a Sensitizing Dye-Semiconductor (TiO_2) Interface", *J. Phys. Chem.*, **1996**, *100*, 9577–9578.

[9] G. Yu and A. J. Heeger, "Charge Separation and Photovoltaic Conversion in Polymer Composites With Internal Donor/Acceptor Heterojunctions", *J. Appl. Phys.*, **1995**, *78*, 4510–4515.

[10] O. Carp, C. L. Huisman and A. Reller, "Photoinduced Reactivity of Titanium Dioxide", *Prog. Solid State Chem.*, **2004**, *32*, 33–177.

[11] A. L. Linsebigler, G. Lu and J. John T. Yates, "Photocatalysis on TiO_2 Surfaces: Principles, Mechanisms, and Selected Results", *Chem. Rev.*, **1995**, *95*, 735–758.

[12] D. W. Bahnemann, M. Hilgendorff and R. Memming, "Charge Carrier Dynamics at TiO_2 Particles: Reactivity of Free and Trapped Holes", *J. Phys. Chem. B*, **1997**, *101*, 4265–4275.

[13] K. Wu, H. Zhu, Z. Liu, W. Rodriguez-Cordoba and T. Lian, "Ultrafast Charge Separation and Long-Lived Charge Separated State in Photocatalytic CdS–Pt Nanorod Heterostructures", *J. Am. Chem. Soc.*, **2012**, *134*, 10337–10340.

[14] F. Ding, W. Liang, C. T. Chapman, C. M. Isborn and X. Li, "On the gauge invariance of nonperturbative electronic dynamics using the time-dependent Hartree-Fock and time-dependent Kohn-Sham", *J. Chem. Phys.*, **2011**, *135*, 164101.

[15] W. Liang, C. T. Chapman, F. Ding and X. Li, "Modeling Ultrafast Solvated Electronic Dynamics Using Time-Dependent Density Functional Theory and Polarizable Continuum Model", *J. Phys. Chem. A*, **2012**, *116*, 1884–1890.

[16] F. Ding, C. T. Chapman, W. Liang and X. Li, "Mechanisms of Bridge-mediated Electron Transfer: A TDDFT Electronic Dynamics Study", *J. Chem. Phys.*, **2012**, *137*, 22A512.

[17] P. Nguyen, F. Ding, S. A. Fischer, W. Liang and X. Li, "Solvated First-principles Excited State Charge Transfer Dynamics with Time-Dependent Polarizable Continuum Model and Solvent Dielectric Relaxation", *J. Phys. Chem. Lett.*, **2012**, *3*, 2898–2904.

[18] C. W. Schlenker, K.-S. Chen, H.-L. Yip, C.-Z. Li, L. R. Bradshaw, S. T. Ochsenbein, F. Ding, X. S. Li, D. R. Gamelin, A. K.-Y. Jen and D. S. Ginger, "Polymer Triplet Energy Levels Need Not Limit Photocurrent Collection in Organic Solar Cells", *J. Am. Chem. Soc.*, **2012**, *134*, 19661–19668.

[19] F. Ding, B. E. V. Kuiken, B. E. Eichinger and X. Li, "An Efficient Method for Calculating Dynamical Hyperpolarizabilities using Real-Time Time-Dependent Density Functional Theory", *J. Chem. Phys.*, **2013**, *138*, 064104.

[20] C.-Z. Li, C.-C. Chueh, H.-L. Yip, F. Ding, X. Li and A. K.-Y. Jen, "Solution-Processable Highly Conducting Fullerenes", *Analyst*, **2013**, *25*, 2457–2461.

[21] C.-Z. Li, C.-C. Chueh, F. Ding, H.-L. Yip, P.-W. Liang, X. Li and A. K.-Y. Jen, "Doping of Fullerenes via Anion-Induced Electron Transfer and Its Implication for Surfactant Facilitated High Performance Polymer Solar Cells", *Analyst*, **2013**, *25*, 4425–4430.

[22] B. Peng, B. E. V. Kuiken, F. Ding and X. Li, "A Guided Self-Consistent-Field Method for Excited State Wave Function Optimization: Applications to Ligand Field Transitions in Transition Metal Complexes", *J. Chem. Theor. Comput.*, **2013**, *9*, 3933–3938.

[23] J. J. Goings, F. Ding and X. Li, "Self-Consistent Field using Direct Inversion in Iterative Subspace Method and Quasi-Newton Vectors", *Adv. Quantum Chem.*, **2014**, *68*, 77–86.

[24] P. J. Lestrange, B. Peng, F. Ding, G. W. Trucks, M. J. Frisch and X. Li, "Density of States Guided Møller-Plesset Perturbation Theory", *J. Chem. Theor. Comput.*, **2014**, *10*, 1910–1914.

[25] F. Ding, E. B. Guidez, C. M. Aikens and X. Li, "Quantum Coherent Plasmon in Silver Nanowires: A Real-Time TDDFT Study", *J. Chem. Phys.*, **2014**, *140*, 244705.

[26] F. Ding, J. J. Goings, M. J. Frisch and X. Li, "Ab initio Non-relativistic Spin Dynamics", *J. Chem. Phys.*, **2014**, *141*, 214111.

[27] F. Ding, D. B. Lingerfelt, B. Mennucci and X. Li, "Time-Dependent Non-Equilibrium Dielectric Response in QM/Continuum Approaches", *J. Chem. Phys.*, **2015**, *142*, 034120.

[28] B. Peng, D. B. Lingerfelt, F. Ding, C. M. Aikens and X. Li, "Real-Time TDDFT Studies of Exciton Decay and Transfer in Silver Nanowire Arrays", *J. Phys. Chem. C*, **2015**, *119*, 6421–6427.

[29] J. J. Goings, F. Ding, M. J. Frisch and X. Li, "Stability of the Complex Generalized Hartree-Fock Equations", *J. Chem. Phys.*, **2015**, *142*, 154109.

[30] C. C. J. Roothaan, "New Developments in Molecular Orbital Theory", *Rev. Mod. Phys.*, **1951**, *23*, 69.

[31] P. Hohenberg and W. Kohn, "Inhomogeneous Electron Gas", *Phys. Rev.*, **1964**, *136*, B864.

[32] W. Kohn and L. J. Sham, "Self-Consistent Equations Including Exchange and Correlation Effects", *Phys. Rev.*, **1965**, *140*, A1133.

[33] J. C. Tully and R. K. Preston, "Trajectory Surface Hopping Approach to Nonadiabatic Molecular Collisions - Reaction of H^+ With D_2", *J. Chem. Phys.*, **1971**, *55*, 562.

[34] J. C. Tully, "Molecular-Dynamics With Electronic-Transitions", *J. Chem. Phys.*, **1990**, *93*, 1061–1071.

[35] D. A. Micha, "A Self-Consistent Eikonal Treatment of Electronic-Transitions in Molecular Collisions", *J. Chem. Phys.*, **1983**, *78*, 7138–7145.

[36] S. I. Sawada, A. Nitzan and H. Metiu, "Mean-Trajectory Approximation for Charge-Transfer and Energy-Transfer Processes at Surfaces", *Phys. Rev. B*, **1985**, *32*, 851.

[37] X. Li, J. C. Tully, H. B. Schlegel and M. J. Frisch, "Ab initio Ehrenfest dynamics", *J. Chem. Phys.*, **2005**, *123*, 084106.

[38] F. Wang, C. Y. Yam, L. H. Hu and G. H. Chen, "Time-dependent density functional theory based Ehrenfest dynamics", *J. Chem. Phys.*, **2011**, *135*, 044126.

[39] P. A. M. Dirac, "Note on Exchange Phenomena in the Thomas Atom", *Proc. Cambridge Philos. Soc.*, **1930**, *26*, 376.

[40] J. Frenkel, *Wave Mechanics, Advanced General Theory*; Clarendon Press: Oxford, U.K., 1934.

[41] J. Crank and P. Nicholson, "A Practical Method for Numerical Evaluation of Solutions of Partial Differential Equations of the Heat Conduction Type", *Proc. Camb. Philos. Soc.*, **1947**, *43*, 50.

[42] W. Magnus, "On the Exponential Solution of Differential Equations for a Linear Operator", *Pure Appl. Math.*, **1954**, *7*, 649.

[43] X. Li, S. M. Smith, A. N. Markevitch, D. A. Romanov, R. J. Levis and H. B. Schlegel, "A time-dependent Hartree-Fock approach for studying the electronic optical response of molecules in intense fields", *Phys. Chem. Chem. Phys.*, **2005**, *7*, 233–239.

[44] C. M. Isborn, X. Li and J. C. Tully, "TDDFT Ehrenfest Dynamics: Collisions Between Atomic Oxygen and Graphite Clusters", *J. Chem. Phys.*, **2007**, *126*, 134307.

[45] E. Runge and E. K. U. Gross, "Density-Functional Theory for Time-Dependent Systems", *Phys. Rev. Lett.*, **1984**, *52*, 9971–1000.

[46] C. Møller and M. S. Plesset, "Note on an approximation treatment for many-electron systems", *Phys. Rev.*, **1934**, *46*, 618–622.

[47] W. A. G. III, T. H. D. Jr., W. J. Hunt and P. J. Hay, "Generalized valence bond description of bonding in low-lying states of molecules", *Acc. Chem. Res.*, **1973**, *6*, 368–376.

[48] G. K.-L. Chan and S. Sharma, "The Density Matrix Renormalization Group in Quantum Chemistry", *Annu. Rev. Phys. Chem.*, **2011**, *62*, 465–481.

[49] B. O. Roos, "The Complete Active Space Self-Consistent Field Method and its Applications in Electronic Structure Calculations", *Adv. Chem. Phys.*, **1987**, *69*, 399–445.

[50] P. I. Richards, "On the Hamiltonian for a Particle in an Electromagnetic Field", *Phys. Rev.*, **1948**, *73*, 254.

[51] R. G. Woolley, "Molecular Quantum Electrodynamics", *Proc. R. Soc. London, Ser. A*, **1971**, *321*, 557.

[52] R. G. Woolley, "On the Hamiltonian Theory of the Molecule-Electromagnetic Field System", *Mol. Phys.*, **1971**, *22*, 1013.

[53] E. A. Power, *Introductory Quantum Electrodynamics*; Longmans and Green: New York, 1964.

[54] M. Sargent, M. O. Scully and W. E. Lamb, *Laser Physics*; Addison-Wesley: Reading, MA, 1974.

[55] H. R. Reiss, "Velocity-Gauge theory for the treatment of strong-field photodetachment", *Phys. Rev. A*, **2007**, *76*, 033404.

[56] W. E. Lamb, "Fine Structure of the Hydrogen Atom. III", *Phys. Rev.*, **1952**, *85*, 259.

[57] D. H. Kobe and A. L. Smirl, "Gauge Invariant Formulation of the Interaction of Electromagnetic Radiation and Matter", *Am. J. Phys.*, **1978**, *46*, 624.

[58] D. H. Kobe, "Gauge-invariant resolution of the controversy over length versus velocity forms of the interaction with electric dipole radiation", *Phys. Rev. A*, **1979**, *19*, 205.

[59] R. R. Schlicher, W. Becker, J. Bergou and M. O. Scully, *Quantum Electrodynamics and Quantum Optics*; Plenum: New York, 1984.

[60] D. L. Lin, "Velocity and length forms of oscillator strengths and unitary transformations of quantum electrodynamics", *Phys. Rev. A*, **1978**, *17*, 1939.

[61] D. L. Lin, "Gauge properties of the Hartree-Fock and random-phase approximations", *Phys. Rev. A*, **1977**, *16*, 600.

[62] E. A. Power and S. Zienau, "Coulomb Gauge in Non-Relativistic Quantum Electro-Dynamics and the Shape of Spectral Lines", *Philos. Trans. R. Soc. London, Ser. A*, **1959**, *251*, 427.

[63] K.-H. Yang, "Gauge Transformations and Quantum Mechanics I. Gauge Invariant Interpretation of Quantum Mechanics", *Ann. Phys.*, **1976**, *101*, 62.

[64] V. Fock, "Über die invariante Form der Wellen- und der Bewegungsgleichungen für einen geladenen Massenpunkt", *Z. Phys.*, **1927**, *39*, 226.

[65] R. McWeeny and B. T. Sutcliffe, *Methods of Molecular Quantum Mechanics*; Academic Press: London, 1969.

[66] Y.-C. Han and B. MadsenL, "Comparison between length and velocity gauges in quantum simulations of high-order harmonic generation", *Phys. Rev. A*, **2010**, *81*, 063430.

[67] H. G. Muller, "Tunneling Excitation to Resonant States in Helium as Main Source of Superponderomotive Photoelectrons in the Tunneling Regime", *Phys. Rev. Lett.*, **1999**, *83*, 3158.

[68] M. Thachuk, M. Y. Ivanov and D. M. Wardlaw, "A semiclassical approach to intense-field above-threshold dissociation in the long wavelength limit. II. Conservation principles and coherence in surface hopping", *J. Chem. Phys.*, **1998**, *109*, 5747.

[69] K. Harumiya, H. Kono, Y. Fujimura, I. Kawata and A. D. Bandrauk, "Intense laser-field ionization of H2 enhanced by two-electron dynamics", *Phys. Rev. A*, **2002**, *66*, 43403.

[70] M. Lein, T. Kreibich, E. K. U. Gross and V. Engel, "Strong-Field Ionization Dynamics of a Model H2 Molecule", *Phys. Rev. A*, **2002**, *65*, 033403.

[71] A. D. Bandrauk and S. Chelkowski, "Asymmetric Electron-Nuclear Dynamics in Two-Color Laser Fields: Laser Phase Directional Control of Photofragments in H2+", *Phys. Rev. Lett.*, **2000**, *84*, 3562.

[72] A. D. Bandrauk and H. Z. Lu, "Enhanced ionization of the molecular ion H2+ in intense laser and static magnetic fields", *Phys. Rev. A*, **2000**, *62*, 53406.

[73] L. I. Schiff, *Quantum Mechanics*; McGraw-Hill: New York, 1968.

[74] E. Merzbacher, *Quantum Mechanics*; Wiley: New York, 1970.

[75] M. Mizushima, *Quantum Mechanics of Atomic Spectra and Atomic Structure*; Benjamin: New York, 1970.

[76] K. C. Kulander, "Time-dependent Hartree-Fock Theory of Multiphoton Ionization: Helium", *Phys. Rev. A*, **1987**, *36*, 2726–2638.

[77] K. C. Kulander, "Multiphoton Ionization of Hydrogen: A Time-dependent Theory", *Phys. Rev. A*, **1987**, *35*, 445–447.

[78] G. H. Chen and S. Mukamel, "Reduced Electronic Density Matrices, Effective Hamiltonians, and Nonlinear Susceptibilities of Conjugated Polyenes", *J. Chem. Phys.*, **1995**, *103*, 9355–9362.

[79] B. X. Xu and A. K. Rajagopal, "Current-Density-Functional Theory for Time-Dependent Systems", *Phys. Rev. A*, **1985**, *31*, 2682–2684.

[80] A. K. Dhara and S. K. Ghosh, "Density-Functional Theory for Time-Dependent Systems", *Phys. Rev. A*, **1987**, *35*, 442–444.

[81] M. A. L. Marques and E. K. U. Gross, "Time-dependent Density Functional Theory", *Annu. Rev. Phys. Chem.*, **2004**, *55*, 427–455.

[82] K. Burke, J. Werschnik and E. K. U. Gross, "Time-dependent Density Functional Theory: Past, Present, and Future", *J. Chem. Phys.*, **2005**, *123*, 062206.

[83] E. K. U. Gross, J. F. Dobson and M. Petersilka, "Density functional theory of time-dependent phenomena", *Top. Curr. Chem.*, **1996**, *181*, 81.

[84] S. K. Ghosh and A. Dhara, "Density-functional theory of many-electron systems subjected to time-dependent electric and magnetic fields", *Phys. Rev. A*, **1988**, *38*, 1149.

[85] V. Chernyak and S. Mukamel, "Time-dependent density-matrix functional in Liouville space and the optical response of many-electron systems", *Phys. Rev. A*, **1995**, *52*, 3601.

[86] V. Chernyak and S. Mukamel, "Density-matrix representation of nonadiabatic couplings in time-dependent density functional TDDFT... theories", *J. Chem. Phys.*, **2000**, *112*, 3572.

[87] W. Liang, C. M. Isborn and X. Li, "Laser-Controlled Dissociation of $C_2H_2^{2+}$: Ehrenfest Dynamics Using Time-Dependent Density Functional Theory", *J. Phys. Chem. A*, **2009**, *113*, 3463–3469.

[88] W. Liang, C. M. Isborn, A. Lindsay, X. Li, S. M. Smith and R. J. Levis, "Time-Dependent Density Functional Theory Calculations of Ehrenfest Dynamics of Laser Controlled Dissociation of NO^+: Pulse Length and Sequential Multiple Single-Photon Processes", *J. Phys. Chem. A*, **2010**, *114*, 6201–6206.

[89] A. L. Fetter and J. D. Walecka, *Quantum Theory of Many-Particle Systems*; McGraw-Hill: New York, 1971.

[90] D. J. Thouless, *The Quantum Mechanics of Many Body Systems*; Academic Press: New York, 1972.

[91] E. K. U. Gross and W. Kohn, "Time-Dependent Density-Functional Theory", *Adv. Quantum Chem.*, **1990**, *21*, 255.

[92] M. E. Casida, *Recent Developments and Applications in Density Functional Theory*; Elsevier: Amsterdam, 1996.

[93] R. vanLeeuwen, "KEY CONCEPTS IN TIME-DEPENDENT DENSITY-FUNCTIONAL THEORY", *Int. J. Mod. Phys. B*, **2001**, *15*, 1969.

[94] A. D. Bandrauk, S. Barmaki, S. Chelkowski and G. L. Kamta, *Progress in Ultrafast Intense Laser Science*; Springer: Tokyo, 2008.

[95] A. D. Bandrauk, S. Chelkowski, D. J. Diestler, J. Manz and K.-J. Yuan, "Quantum Simulation of High-order Harmonic Spectra of the Hydrogen Atom", *Phys. Rev. A*, **2009**, *79*, 023403.

[96] C. A. Ullrich, S. Erhard and E. K. U. Gross, *Super Intense Laser Atom Physics*; Kluwer: Amsterdam, 1996.

[97] S. Erhard and E. K. U. Gross, *Multiphoton Processes*; IOP: Bristol, 1997.

[98] D. A. Telnov, J. Wang and S. Chu, "Two-color phase control of high-order harmonic generation in intense laser fields", *Phys. Rev. A*, **1995**, *52*, 3988.

[99] B. Walker, B. Sheehy, L. F. Di Mauro, P. Agostini, K. J. Schaefer and K. C. Kulander, "Precision Measurement of Strong Field Double Ionization of Helium", *Phys. Rev. Lett.*, **1994**, *73*, 1227.

[100] R. A. Harris, "Oscillator Strengths and Rotational Strengths in Hartree-Fock Theory", *J. Chem. Phys.*, **1969**, *50*, 3947.

[101] P. Jorgensen, "Molecular and Atomic Applications of Time-Dependent Hartree-Fock Theory", *Annu. Rev. Phys. Chem.*, **1975**, *26*, 359.

[102] C. Cohen-Tannoudji, B. Diu and Laloë, *Quantum Mechanics*; Wiley: New York, 1977.

[103] W. Bieger, G. Seifert, H. Eschrig and G. Grossman, "LCAO X calculations of nuclear magnetic shielding in molecules", *Chem. Phys. Lett.*, **1985**, *115*, 275.

[104] A. D. Becke, "Density-functional Exchange-energy Approximation With Correct Asymptotic Behavior", *Phys. Rev. A*, **1988**, *38*, 3098.

[105] C. Lee, W. Yang and R. G. Parr, "Development of the Colle-Salvetti Correlation-energy Formula Into a Functional of the Electron Density", *Phys. Rev. B*, **1988**, *37*, 785.

[106] B. Miehlich, A. Savin, H. Stoll and H. Preuss, "Results obtained with the correlation energy density functionals of becke and Lee, Yang and Parr", *Chem. Phys. Lett.*, **1989**, *157*, 200.

[107] A. D. Becke, "Density Functional Thermochemistry. III. The Role of Exact Exchange", *J. Chem. Phys.*, **1993**, *98*, 5648.

[108] S. H. Vosko, L. Wilk and M. Nusair, "Accurate spin-dependent electron liquid correlation energies for a local spin density calculations: a critical analysis", *Can. J. Phys.*, **1980**, *58*, 1200.

[109] P. J. Stephens, F. J. Devlin, C. F. Chabalowski and M. J. Frisch, "Ab Initio Calculation of Vibrational Absorption and Circular Dichroism Spectra Using Density Functional Force Fields", *J. Phys. Chem.*, **1994**, *98*, 11623–11627.

[110] R. Ditchfield, "Self-consistent perturbation theory of diamagnetism I. A gauge-invariant LCAO method for N.M.R. chemical shifts", *Mol. Phys.*, **1974**, *27*, 789.

[111] P. Pulay, J. F. Hinton and K. Wolinski, *Nuclear Magnetic Shieldings and Molecular Structure*; Kluwer: Dordrecht, 1993.

[112] J. Gauss and J. F. Stanton, "Electron-Correlated Approaches for the Calculation of NMR Chemical Shifts", *Adv. Chem. Phys.*, **2002**, *123*, 355.

[113] J. Juselius, D. Sundholm and J. Gauss, "Calculation of current densities using gauge-including atomic orbitals", *J. Chem. Phys.*, **2004**, *121*, 3952.

[114] S. T. Epstein, "Gauge invariance, current conservation, and GIAO's", *J. Chem. Phys.*, **1973**, *58*, 1592.

[115] F. Bloch and A. Nordsieck, "Note on the Radiation Field of the Electron", *Phys. Rev.*, **1937**, *52*, 54.

[116] M. H. Mittleman, *Introduction to the Theory of Laser-Atom Interactions*; Plenum: New York, 1982.

[117] F. H. M. Faisal, *Theory of Multiphoton Processes*; Plenum: New York, 1987.

[118] J. van deRee, J. Z. Kaminski and M. Gavrila, "Modified Coulomb scattering in intense, high-frequency laser fields", *Phys. Rev. A*, **1988**, *37*, 4536(R).

[119] T. T. Nguyen-Dang and A. D. Bandrauk, "Molecular dynamics in intense laser fields. I. One?dimensional systems in infrared radiation", *J. Chem. Phys.*, **1983**, *79*, 3256.

[120] A. D. Bandrauk, *Molecules in Laser Fields*; Marcel Dekker: New York, 1994.

[121] C. L. Moss, C. M. Isborn and X. Li, "Ehrenfest dynamics with a time-dependent density-functional-theory calculation of lifetimes and resonant widths of charge-transfer states of Li^+ near an aluminum cluster surface", *Phys. Rev. A*, **2009**, *80*, 024503.

[122] M. J. Frisch, G. W. Trucks, H. B. Schlegel, G. E. Scuseria, M. A. Robb, J. R. Cheeseman, G. Scalmani, V. Barone, B. Mennucci, G. A. Petersson, H. Nakatsuji, M. Caricato, X. Li, H. P. Hratchian, A. F. Izmaylov, J. Bloino, G. Zheng, J. L. Sonnenberg, M. Hada, M. Ehara, K. Toyota, R. Fukuda, J. Hasegawa, M. Ishida, T. Nakajima, Y. Honda, O. Kitao, H. Nakai, T. Vreven, J. A. M. Jr., J. E. Peralta, F. Ogliaro, M. Bearpark, J. J. Heyd, E. Brothers, K. N. Kudin, V. N. Staroverov, T. Keith, R. Kobayashi, J. Normand, K. Raghavachari, A. Rendell, J. C. Burant, S. S. Iyengar, J. Tomasi, M. Cossi, N. Rega, J. M. Millam, M. Klene, J. E. Knox, J. B. Cross, V. Bakken, C. Adamo, J. Jaramillo, R. Gomperts, R. E. Stratmann, O. Yazyev, A. J. Austin, R. Cammi, C. Pomelli, J. W. Ochterski, R. L. Martin, K. Morokuma, V. G. Zakrzewski, G. A. Voth, P. Salvador, J. J. Dannenberg, S. Dapprich, P. V. Parandekar, N. J. Mayhall, A. D. Daniels, O. Farkas, J. B. Foresman, J. V. Ortiz, J. Cioslowski and D. J. Fox, *Gaussian Development Version Revision H.09+*, Gaussian Inc., Wallingford CT 2011.

[123] *Nonlinear Optical Properties of Organic Molecules and Crystals*; edited by D. S. Chemla and J. Zyss: Academic, San Diego, 1987.

[124] P. N. Prasad and D. J. Williams, *Introduction to Nonlinear Optical Effects in Molecules and Polymers*; Wiley, New York, 1991.

[125] D. P. Shelton and J. E. Rice, "Measurements and Calculations of the Hyperpolarkabilities of Atoms and Small Molecules in the Gas Phase", *Chem. Rev.*, **1994**, *94*, 3–29.

[126] D. R. Kanis, M. A. Ratner and T. J. Marks, "Design Synthesis and Properties of Molecule Based Assemblies with Large Second Order Optical Nonlinearities", *Chem. Rev.*, **1994**, *94*, 195–242.

[127] F. Terenziani, C. Katan, E. Badaeva, S. Tretiak and M. Blanchard-Desce, "Enhanced Two-Photon Absorption of Organic Chromophores: Theoretical and Experimental Assessments", *Analyst*, **2008**, *20*, 4641–4678.

[128] Y. R. Shen, *The Principles of Nonlinear Optics*; Wiley, New York, 1984.

[129] H. D. Cohen and C. C. J. Roothaan, "Electric Dipole Polarizability of Atoms by the Hartree—Fock Method. I. Theory for ClosedShell Systems", *J. Chem. Phys.*, **1965**, *43*, S34.

[130] J. A. Pople, J. W. McIver and N. S. Ostlund, "SelfConsistent Perturbation Theory. I. Finite Perturbation Methods", *J. Chem. Phys.*, **1968**, *49*, 2960.

[131] J. E. Gready, G. B. Backsay and N. S. Hush, "Finite-field method calculations of molecular polarisabilities. I. Theoretical basis and limitations of SCF and Galerkin treatments", *Chem. Phys.*, **1977**, *22*, 141.

[132] R. J. Bartlett and G. D. Purvis, "Molecular hyperpolarizabilities. I. Theoretical calculations including correlation", *Phys. Rev. A*, **1979**, *20*, 1313.

[133] H. A. Kurtz, J. J. P. Stewart and K. M. Dieter, "Calculation of the nonlinear optical properties of molecules", *J. Comput. Chem.*, **1990**, *11*, 82.

[134] F. Sim, S. Chin, M. Dupuis and J. E. Rice, "Electron correlation effects in hyperpolarizabilities of p-nitroaniline", *J. Phys. Chem.*, **1993**, *97*, 1158.

[135] R. McWeeny, "Some Remarks on Multiconfiguration Time-dependent Hartree–Fock Theory", *Int. J. Quant. Chem.*, **1983**, *23*, 405.

[136] P. Pulay, "Second and Third Derivatives of Variational Energy Expressions: Application to Multiconfigurational Selfconsistent Field Wave Functions", *J. Chem. Phys.*, **1983**, *78*, 5043.

[137] C. E. Dykstra and P. G. Jasien, "Derivative Hartree-Fock Theory to All Orders", *Chem. Phys. Lett.*, **1984**, *109*, 388.

[138] R. D. Amos, "Calculation of Polarizability Derivatives Using Analytic Gradient Methods", *Chem. Phys. Lett.*, **1986**, *124*, 376.

[139] P. Lizeretti and R. Zanasi, "On the theoretical determination of molecular first hyperpolarizability", *J. Chem. Phys.*, **1981**, *74*, 5216.

[140] B. J. Orr and J. F. Ward, "Perturbation theory of the non-linear optical polarization of an isolated system", *Mol. Phys.*, **1971**, *20*, 513.

[141] D. Maurice and M. Head-Gordon, "Analytical second derivatives for excited electronic states using the single excitation configuration interaction method: theory and application to benzo[a]pyrene and chalcone", *Mol. Phys.*, **1999**, *96*, 1533.

[142] G. D. Purvis and R. J. Bartlett, "A full coupledcluster singles and doubles model: The inclusion of disconnected triples", *J. Chem. Phys.*, **1982**, *76*, 1910.

[143] H. Sekino and R. J. Bartlett, "Frequency Dependent Nonlinear Optical Properties of Molecules", *J. Chem. Phys.*, **1986**, *85*, 976.

[144] S. P. Karna and M. Dupuis, "Frequency dependent nonlinear optical properties of molecules: Formulation and implementation in the HONDO program", *J. Comput. Chem.*, **1991**, *12*, 487.

[145] J. E. Rice, R. D. Amos, S. M. Colwell, N. C. Handy and J. Sanz, "Frequency dependent hyperpolarizabilities with application to formaldehyde and methyl fluoride", *J. Chem. Phys.*, **1990**, *93*, 8828.

[146] J. A. vanGisbergen, J. G. Snijders and E. J. Baerends, "Calculating frequency-dependent hyperpolarizabilities using time-dependent density functional theory", *J. Chem. Phys.*, **1998**, *109*, 10644.

[147] F. Furche, "On the density matrix based approach to time-dependent density functional response theory", *J. Chem. Phys.*, **2001**, *114*, 5982.

[148] S. Tretiak and V. Chernyak, "Resonant nonlinear polarizabilities in the time-dependent density functional theory", *J. Chem. Phys.*, **2003**, *119*, 8809.

[149] X. Andrade, S. Botti, M. A. L. Marques and A. Rubio, "Time-Dependent Density Functional Theory Scheme for Efficient Calculations of Dynamic (Hyper)polarizabilities", *J. Chem. Phys.*, **2007**, *126*, 184106.

[150] H. Larsen, P. Joørgensen, J. Olsen and T. Helgaker, "Hartree–Fock and Kohn–Sham Atomic-orbital Based Time-dependent response theory", *J. Chem. Phys.*, **2000**, *113*, 8908.

[151] J.-I. Iwata, K. Yabana and G. F. Bertsch, "Real-space Computation of Dynamic Hyperpolarizabilities", *J. Chem. Phys.*, **2001**, *115*, 8773.

[152] H. H. Heinze, F. D. Sala and A. Görling, "Efficient Methods to Calculate Dynamic Hyperpolarizability Tensors by Timedependent Density-functional Theory", *J. Chem. Phys.*, **2002**, *116*, 9624.

[153] P. Sałek, O. Vahtras, T. Helgaker and H. Ågren, "Density-functional Theory of Linear and Nonlinear Time-dependent Molecular Properties", *J. Chem. Phys.*, **2002**, *117*, 9630.

[154] A. Ye and J. Autschbach, "Study of Static and Dynamic First Hyperpolarizabilities Using Time-dependent Density Functional Quadratic Response Theory With Local Contribution and Natural Bond Orbital Analysis", *J. Chem. Phys.*, **2006**, *125*, 234101.

[155] A. Ye, S. Patchkovskii and J. Autschbach, "Static and Dynamic Second Hyperpolarizability Calculated by Timedependent Density Functional Cubic Response Theory With Local Contribution and Natural Bond Orbital Analysis", *J. Chem. Phys.*, **2007**, *127*, 074104.

[156] F. Wang, C. Y. Yam and G. Chen, "Time-dependent density-functional theory/localized density matrix method for dynamic hyperpolarizability", *J. Chem. Phys.*, **2007**, *126*, 244102.

[157] K. Yabana and G. F. Bertsch, "Time-dependent Local-density Approximation in Real Time", *Phys. Rev. B*, **1996**, *54*, 4484–4487.

[158] K. Yabana and G. F. Bertsch, "Time-dependent local-density approximation in real time: Application to conjugated molecules", *Int. J. Quant. Chem.*, **1999**, *75*, 55.

[159] K. Yabana, T. Nakatsukasa, J.-I. Iwata and G. F. Bertsch, "Real-time, Real-space Implementation of the Linear Response Time-dependent Density-functional Theory", *Phys. Status Solidi B*, **2006**, *243*, 1121.

[160] A. Tsolakidis, D. Sánchez-Portal and R. M. Martin, "Calculation of the Optical Response of Atomic Clusters Using Time-dependent Density Functional Theory and Local Orbitals", *Phys. Rev. B*, **2002**, *66*, 235416.

[161] F. Wang, C. Y. Yam, G. Chen and K. Fan, "Density Matrix Based Time-dependent Density Functional Theory and the Solution of Its Linear Response in Real Time Domain", *J. Chem. Phys.*, **2007**, *126*, 134104.

[162] Y. Takimoto, F. D. Vila and J. J. Rehr, "Real-time time-dependent density functional theory approach for frequency-dependent nonlinear optical response in photonic molecules", *J. Chem. Phys.*, **2007**, *127*, 154114.

[163] M. R. Wall and D. Neuhauser, "Extraction, through filterdiagonalization, of general quantum eigenvalues or classical normal mode frequenciesfromasmallnumberofresidues or a shorttime segment of a signal. I. Theory and application to a quantumdynamics model", *J. Chem. Phys.*, **1995**, *102*, 8011.

[164] P. N. Butcher and D. Cotter, *The Elements of Nonlinear Optics*; Cambridge University Press, Cambridge, 1990.

[165] W. Liang, C. T. Chapman and X. Li, "Efficient first-principles electronic dynamics", *J. Chem. Phys.*, **2011**, *134*, 184102.

[166] W. Liang, S. A. Fischer, M. J. Frisch and X. Li, "Energy-Specific Linear Response TDHF/TDDFT for Calculating High-Energy Excited States", *J. Chem. Theor. Comput.*, **2011**, *7*, 3540–3547.

[167] J. K. P. J. P. Norman, "On the Efficiency of Algorithms for Solving Hartree–Fock and Kohn–Sham Response Equations", *J. Chem. Theor. Comput.*, **2011**, *7*, 1610.

[168] B. Champagne, E. A. Perpete, D. Jacquemin, S. J. A. Gisbergen, E. J. Baerends, C. Soubra-Ghaoui, K. A. Robins and B. Kirtman, "Assessment of Conventional Density Functional Schemes for Computing the Dipole Moment and (Hyper)polarizabilities of Push–Pull Π-Conjugated Systems", *J. Phys. Chem. A*, **2000**, *104*, 4755–4763.

[169] D. Jacquemin, J. M. Andre and E. A. Perpete, "Geometry, Dipole Moment, Polarizability and First Hyperpolarizability of Polymethineimine: An Assessment of Electron Correlation Contributions", *J. Chem. Phys.*, **2004**, *121*, 4396.

[170] E. R. Davidson, B. E. Eichinger and B. H. Robinson, "Hyperpolarizability: Calibration of Theoretical Methods for Chloroform, Water, Acetonitrile, and p-Nitroaniline", *Opt. Mater.*, **2006**, *29*, 360–364.

[171] A. P. Chafin and G. A. Lindsay, "A Pattern for Increasing the First Hyperpolarizability of a Push?Pull Polyene Dye as Indicated From DFT Calculations", *J. Phys. Chem. C*, **2008**, *112*, 7829–7835.

[172] J. Hung, W. Liang, J. Luo, Z. Shi, A. K.-Y. Jen and X. Li, "Rational Design Using Dewar's Rules for Enhancing the First Hyperpolarizability of Nonlinear Optical Chromophores", *J. Phys. Chem. C*, **2010**, *114*, 22284–22288.

[173] J. Heyd and G. Scuseria, "Efficient Hybrid Density Functional Calculations in Solids: The HS-Ernzerhof Screened Coulomb Hybrid Functional", *J. Chem. Phys.*, **2004**, *121*, 1187–1192.

[174] G. E. S. J. Heyd and M. Ernzerhof, "Hybrid Functionals Based on a Screened Coulomb Potential", *J. Chem. Phys.*, **2006**, *124*, 219906.

[175] J. R. Hammond, K. Kowalski and W. A. deJong, "Dynamic polarizabilities of polyaromatic hydrocarbons using coupled-cluster linear response theory", *J. Chem. Phys.*, **2007**, *127*, 144105.

[176] T. Kato, "On the Convergence of the Perturbation Method. I.", *Prog. Theor. Phys.*, **1949**, *4*, 514.

[177] F. Rellich, "Störungstheorie der Spektralzerlegung", *Microchim. Acta*, **1937**, *113*, 600.

[178] P. A. Sullivan, H. Rommel, Y. Liao, B. C. Olbricht, A. J. P. Akelaitis, K. A. Firestone, J.-W. Kang, J. Luo, J. A. Davies, D. H. Choi, B. E. Eichinger, P. J. Reid, A. Chen, A. K.-Y. Jen, B. H. Robinson and L. R. Dalton, "Theory-Guided Design and Synthesis of Multichromophore Dendrimers: An Analysis of the Electro-optic Effect", *J. Am. Chem. Soc.*, **2007**, *129*, 7523.

[179] J. A. Davies, A. Elangovan, P. A. Sullivan, B. C. Olbricht, D. H. Bale, T. R. Ewy, C. M. Isborn, B. E. Eichinger, B. H. Robinson, P. J. Reid, X. Li and L. R. Dalton, "Rational Enhancement of Second-Order Nonlinearity: Bis-(4-methoxyphenyl)heteroaryl-amino Donor-Based Chromophores: Design, Synthesis, and Electrooptic Activity", *J. Am. Chem. Soc.*, **2008**, *130*, 10565–10575.

[180] J. R. G. Navarro and M. H. V. Werts, "Resonant light scattering spectroscopy of gold, silver and gold-silver alloy nanoparticles and optical detection in microfluidic channels", *Adv. Mater.*, **2013**, *138*, 583–592.

[181] G. K. Joshi, P. J. McClory, B. B. Muhoberac, A. Kumbhar, K. A. Smith and R. Sardar, "Designing Efficient Localized Surface Plasmon Resonance-Based Sensing Platforms: Optimization of Sensor Response by Controlling the Edge Length of Gold Nanoprisms", *J. Phys. Chem. C*, **2012**, *116*, 20990–21000.

[182] J. K. Lim, K. Imura, T. Nagahara, S. K. Kim and H. Okamoto, "Imaging and dispersion relations of surface plasmon modes in silver nanorods by near-field spectroscopy", *Chem. Phys. Lett.*, **2005**, *412*, 41–45.

[183] B. S. Guiton, V. Iberi, S. Li, C. M. LeonardD. N.; Parish, P. G. Kotula, M. Varela, G. C. Schatz, S. J. Pennycook and J. P. Camden, "Correlated Optical Measurements and Plasmon Mapping of Silver Nanorods", *Nano Lett.*, **2011**, *11*, 3482–3488.

[184] E. Ringe, B. Sharma, A.-I. Henry, L. D. Marks and R. P. Van Duyne, "Single nanoparticle plasmonics", *Phys. Chem. Chem. Phys.*, **2013**, *15*, 4110–4129.

[185] U. Kreibig and M. Vollmer, *Optical Properties of Metal Clusters*; Springer: Berlin, 1995.

[186] M. A. Mahmoud and M. A. El-Sayed, "Different Plasmon Sensing Behavior of Silver and Gold Nanorods", *J. Phys. Chem. Lett.*, **2013**, *4*, 1541–1545.

[187] H. Okamoto and K. Imura, "Visualizing the Optical Field Structures in Metal Nanostructures", *J. Phys. Chem. Lett.*, **2013**, *4*, 2230–2241.

[188] H. Chen, L. Shao, Q. Li and J. Wang, "Gold nanorods and their plasmonic properties", *Chem. Soc. Rev.*, **2013**, *42*, 2679–2724.

[189] L. Polavarapu and L. M. Liz-Marzan, "Towards low-cost flexible substrates for nanoplasmonic sensing", *Phys. Chem. Chem. Phys.*, **2013**, *15*, 5288–5300.

[190] K. L. Kelly, E. Coronado, L. L. Zhao and G. C. Schatz, "The Optical Properties of Metal Nanoparticles: The Influence of Size, Shape, and Dielectric Environment", *J. Phys. Chem. B*, **2003**, *107*, 668–677.

[191] C. M. Aikens, "Electronic Structure of Ligand-Passivated Gold and Silver Nanoclusters", *J. Phys. Chem. Lett.*, **2010**, *2*, 99–104.

[192] S. M. Morton, D. W. Silverstein and L. Jensen, "Theoretical Studies of Plasmonics using Electronic Structure Methods", *Chem. Rev.*, **2011**, *111*, 3962–3994.

[193] P. Nordlander and E. Prodan, "Plasmon Hybridization in Nanoparticles near Metallic Surfaces", *Nano Lett.*, **2004**, *4*, 2209–2213.

[194] P. Nordlander, C. Oubre, E. Prodan, K. Li and M. I. Stockman, "Plasmon Hybridization in Nanoparticle Dimers", *Nano Lett.*, **2004**, *4*, 899–903.

[195] P. K. Jain and M. A. El-Sayed, "Surface Plasmon Resonance Sensitivity of Metal Nanostructures: Physical Basis and Universal Scaling in Metal Nanoshells", *J. Phys. Chem. C*, **2007**, *111*, 17451–17454.

[196] A. J. Haes, C. L. Haynes, A. D. McFarland, G. C. Schatz, R. P. Van Duyne and S. Zou, "Plasmonic Materials for Surface-Enhanced Sensing and Spectroscopy", *MRS Bull.*, **2005**, *30*, 368.

[197] K. Kneipp, Y. Wang, H. Kneipp, L. T. Perelman, I. Itzkan, R. R. Dasari and M. S. Feld, "Single molecule detection using surface-enhanced Raman scattering (SERS)", *Phys. Rev. Lett.*, **1997**, *78*, 1667.

[198] S. Nie and S. R. Emory, "Probing single molecules and single nanoparticles by surface-enhanced Raman scattering", *Science*, **1997**, *275*, 1102.

[199] A. M. Michaels, M. Nirmal and L. E. Brus, "Surface enhanced Raman spectroscopy of individual rhodamine 6G molecules on large Ag nanocrystals", *J. Am. Chem. Soc.*, **1999**, *121*, 9932.

[200] E. Hutter and J. H. Fendler, "Exploitation of Localized Surface Plasmon Resonance", *Analyst*, **2004**, *16*, 1685–1706.

[201] J. Mullin, N. Valley, M. G. Blaber and G. C. Schatz, "Combined Quantum Mechanics (TDDFT) and Classical Electrodynamics (Mie Theory) Methods for Calculating Surface Enhanced Raman and Hyper-Raman Spectra", *J. Phys. Chem. A*, **2012**, *116*, 9574–9581.

[202] K. Saha, S. S. Agasti, C. Kim, X. Li and V. M. Rotello, "Gold Nanoparticles in Chemical and Biological Sensing", *Chem. Rev.*, **2012**, *112*, 2739–2779.

[203] Z. A. Tagar, Sirajuddin, N. Memon, M. H. Agheem, Y. Junejo, S. S. Hassan, N. H. Kalwar and M. I. Khattak, "Selective, simple and economical lead sensor based on ibuprofen derived silver nanoparticles", *Sens. Act. B Chem.*, **2011**, *157*, 430–437.

[204] S. Jiang, K. Y. Win, S. Liu, C. P. Teng, Y. Zheng and M.-Y. Han, "Surface-functionalized nanoparticles for biosensing and imaging-guided therapeutics", *Nanoscale*, **2013**, *5*, 3127–3148.

[205] T. Hirakawa and P. V. Kamat, "Photoinduced Electron Storage and Surface Plasmon Modulation in Ag@TiO2 Clusters", *Langmuir*, **2004**, *20*, 5645–5647.

[206] I. H. El-Sayed, X. Huang and M. A. El-Sayed, "Surface Plasmon Resonance Scattering and Absorption of anti-EGFR Antibody Conjugated Gold Nanoparticles in Cancer Diagnostics: Applications in Oral Cancer", *Nano Lett.*, **2005**, *5*, 829.

[207] X. Huang, I. H. El-Sayed, W. Qian and M. A. El-Sayed, "Cancer Cell Imaging and Photothermal Therapy in the Near-Infrared Region by Using Gold Nanorods", *J. Am. Chem. Soc.*, **2006**, *128*, 2115.

[208] Y.-Y. Yu, S.-S. Chang, C.-L. Lee and C. R. C. Wang, "Gold Nanorods: Electrochemical Synthesis and Optical Properties", *J. Phys. Chem. B*, **1997**, *101*, 6661.

[209] S. Link, M. B. Mohamed and M. A. El-Sayed, "Simulation of the Optical Absorption Spectra of Gold Nanorods as a Function of Their Aspect Ratio and the Effect of the Medium Dielectric Constant", *J. Phys. Chem. B*, **1999**, *103*, 3073–3077.

[210] B. Pietrobon, M. McEachran and V. Kitaev, "Synthesis of Size-Controlled Faceted Pentagonal Silver Nanorods with Tunable Plasmonic Properties and Self-Assembly of These Nanorods", *ACS Nano*, **2008**, *3*, 21–26.

[211] M.-S. Liao, P. Bonifassi, J. Leszczynski, P. C. Ray, M.-J. Huang and J. D. Watts, "Structure, Bonding, and Linear Optical Properties of a Series of Silver and Gold Nanorod Clusters: DFT/TDDFT Studies", *J. Phys. Chem. A*, **2010**, *114*, 12701–12708.

[212] H. E. Johnson and C. M. Aikens, "Electronic Structure and TDDFT Optical Absorption Spectra of Silver Nanorods", *J. Phys. Chem. A*, **2009**, *113*, 4445–4450.

[213] S. Kümmel, K. Andrae and P. G. Reinhard, "Collectivity in the optical response. of small metal clusters", *Appl. Phys. B*, **2001**, *73*, 293–297.

[214] C. M. Aikens, S. Li and G. C. Schatz, "From Discrete Electronic States to Plasmons: TDDFT Optical Absorption Properties of Agn (n = 10, 20, 35, 56, 84, 120) Tetrahedral Clusters", *J. Phys. Chem. C*, **2008**, *112*, 11272.

[215] E. B. Guidez and C. M. Aikens, "Theoretical analysis of the optical excitation spectra of silver and gold nanowires", *Nanoscale*, **2012**, *4*, 4190–4198.

[216] G.-T. Bae and C. M. Aikens, "Time-Dependent Density Functional Theory Studies of Optical Properties of Ag Nanoparticles: Octahedra, Truncated Octahedra, and Icosahedra", *J. Phys. Chem. C*, **2012**, *116*, 10356–10367.

[217] S. Bernadotte, F. Evers and C. R. Jacob, "Plasmons in Molecules", *J. Phys. Chem. C*, **2013**, *117*, 1863–1878.

[218] E. B. Guidez and C. M. Aikens, "Diameter Dependence of the Excitation Spectra of Silver and Gold Nanorods", *J. Phys. Chem. C*, **2013**, *117*, 12325–12336.

[219] M. Walter, J. Akola, O. Lopez-Acevedo, P. D. Jadzinsky, G. Calero, C. J. Ackerson, R. L. Whetten, H. Grönbeck and H. Häkkinen, "A Unified View of Ligand-Protected Gold Clusters as Superatom Complexes", *Proc. Natl. Acad. Sci. U.S.A.*, **2008**, *105*, 9157–9162.

[220] K.-Y. Lian, P. Salek, M. Jin and D. Ding, "Density-functional studies of plasmons in small metal clusters", *J. Chem. Phys.*, **2009**, *130*, 174701.

[221] J. Yan, Z. Yuan and S. Gao, "End and Central Plasmon Resonances in Linear Atomic Chains", *Phys. Rev. Lett.*, **2007**, *98*, 216602–216605.

[222] J. Yan and S. Gao, "Plasmon resonances in linear atomic chains: Free-electron behavior and anisotropic screening of d electrons", *Phys. Rev. B*, **2008**, *78*, 235413–235422.

[223] B. Gao, K. Ruud and Y. Luo, "Plasmon resonances in linear noble-metal chains", *J. Chem. Phys.*, **2012**, *137*, 194307.

[224] C. M. Isborn and X. Li, "Singlet-triplet Transitions in Real-time Time-dependent Hartree-Fock/Density Functional Theory", *J. Chem. Theor. Comput.*, **2009**, *5*, 2415–2419.

[225] P. J. Hay and W. R. Wadt, "Ab initio effective core potentials for molecular calculations. Potentials for the transition metal atoms Sc to Hg", *J. Chem. Phys.*, **1985**, *82*, 270.

[226] P. J. Hay and W. R. Wadt, "Ab initio effective core potentials for molecular calculations. Potentials for K to Au including the outermost core orbitals", *J. Chem. Phys.*, **1985**, *82*, 299.

[227] W. R. Wadt and P. J. Hay, "Ab initio effective core potentials for molecular calculations. Potentials for main group elements Na to Bi", *J. Chem. Phys.*, **1985**, *82*, 284.

[228] A. E. DePrince III, M. Pelton, J. R. Guest and S. K. Gray, "Emergence of Excited-State Plasmon Modes in Linear Hydrogen Chains from Time-Dependent Quantum Mechanical Methods", *Phys. Rev. Lett.*, **2011**, *107*, 196806.

[229] R. A. Marcus and N. Sutin, "Electron Transfers in Chemistry and Biology", *Biochimica et Biophysica Acta*, **1985**, *811*, 265.

[230] K. Mikkelsen and M. A. Ratner, "Electron Tunneling in Solid-state Electron-transfer Reactions", *Chem. Rev.*, **1987**, *87*, 113–153.

[231] M. D. Newton and N. Sutin, "Electron Transfer Reactions in Condensed Phases", *Annu. Rev. Phys. Chem.*, **1984**, *35*, 437.

[232] M. D. Newton, "Quantum chemical probes of electron-transfer kinetics: the nature of donor-acceptor interactions", *Chem. Rev.*, **1991**, *91*, 767.

[233] M. R. Wasielewski, "Photoinduced electron transfer in supramolecular systems for artificial photosynthesis", *Chem. Rev.*, **1992**, *92*, 435.

[234] J. D. Henrich, H. Zhang, P. K. Dutta and B. Kohler, "Ultrafast Electron Transfer Dynamics in Ruthenium Polypyridyl Complexes with a π-Conjugated Ligand", *J. Phys. Chem. B*, **2010**, *114*, 14679.

[235] C. T. Chapman, W. Liang and X. Li, "Ultrafast Coherent Electron-Hole Separation Dynamics in a Fullerene Derivative", *J. Phys. Chem. Lett.*, **2011**, *2*, 1189–1192.

[236] J. Breton and A. Vermeglio, Plenum Press: New York, 1992.

[237] G. R. Fleming, J. L. Martin and J. Breton, "Rates of primary electron transfer in photosynthetic reaction centres and their mechanistic implications", *Nature*, **1988**, *333*, 190.

[238] S. R. Marder, B. Kippelen, A. K.-Y. Jen and N. Peyghambarian, "Design and synthesis of chromophores and polymers for electro-optic and photorefractive applications", *Nature*, **1997**, *388*, 845.

[239] H. Ma, A. K.-Y. Jen and L. R. Dalton, "Polymer-Based Optical Waveguides: Materials, Processing, and Devices", *Analyst*, **2002**, *14*, 1339.

[240] Y. Shi, C. Zhang, H. Zhang, J. H. Bechtel, L. R. Dalton, B. H. Robinson and W. H. Steier, "Low (Sub-1-Volt) Halfwave Voltage Polymeric Electro-optic Modulators Achieved by Controlling Chromophore Shape", *Science*, **2000**, *288*, 119.

[241] C. M. Isborn, A. Leclercq, F. D. Vila, L. R. Dalton, J. L. Bredas, B. E. Eichinger and B. H. Robinson, "Comparison of Static First Hyperpolarizabilities Calculated With Various Quantum Mechanical Methods", *J. Phys. Chem. A*, **2007**, *111*, 1319–1327.

[242] H. M. McConnell, "Intramolecular Charge Transfer in Aromatic Free Radicals", *J. Chem. Phys.*, **1961**, *35*, 508.

[243] K. Saito, T. Kikuchi, K. Mukai and H. Sumi, "Sequential or superexchange mechanism in bridged electron transfer distinguished by dynamics at a bridging molecule", *Phys. Chem. Chem. Phys.*, **2009**, *11*, 5290.

[244] M. Bixon and J. Jortner, John Wiley and Sons: New York, 1999.

[245] B. P. Paulson, J. R. Miller, W.-X. Gan and G. Closs, "Superexchange and Sequential Mechanisms in Charge Transfer with a Mediating State between the Donor and Acceptor", *J. Am. Chem. Soc.*, **2005**, *127*, 4860.

[246] C. Lambert, G. Nöll and J. Schelter, "Bridge-mediated hopping or superexchange electron-transfer processes in bis(triarylamine) systems", *Nat. Mater.*, **2002**, *1*, 69.

[247] W. Davis, W. A. Svec, M. A. Ratner and M. R. Wasielewski, "Observation of 'third sound' in superfluid 3He", *Nature*, **1998**, *396*, 60.

[248] M. Bixon, J. Jortner and M. E. Michel-Beyerle, "On the mechanism of the primary charge separation in bacterial photosynthesis", *Biochimica et Biophysica Acta*, **1991**, *1056*, 301.

[249] M. Bixon and J. Jortner, "Electron transfer via bridges", *J. Chem. Phys.*, **1997**, *107*, 5154.

[250] J. Jortner, M. Bixon, T. Langenbacher and M. E. Michel-Beyerle, "Charge transfer and transport in DNA", *Proc. Natl. Acad. Sci. U.S.A.*, **1998**, *95*, 12759.

[251] H. Sumi and R. A. Marcus, "Dynamical effects in electron transfer reactions", *J. Chem. Phys.*, **1986**, *84*, 4894.

[252] H. Sumi and T. Kakitani, "Electron transfer via a midway molecule as seen in primary processes in photosynthesis; a new process describable as superexchange or sequential in mutually opposite limits", *Chem. Phys. Lett.*, **1996**, *252*, 85.

[253] H. Sumi and T. Kakitani, "Unified Theory on Rates for Electron Transfer Mediated by a Midway Molecule, Bridging between Superexchange and Sequential Processes", *J. Phys. Chem. B*, **2001**, *105*, 9603.

[254] Y. Hu and S. Mukamel, "Tunneling versus sequential longrange electron transfer: Analogy with pump–probe spectroscopy", *J. Chem. Phys.*, **1989**, *91*, 6973.

[255] S. S. Skourtis, G. Archontis and Q. Xie, "Electron transfer through fluctuating bridges: On the validity of the superexchange mechanism and time-dependent tunneling matrix elements", *J. Chem. Phys.*, **2001**, *115*, 9444.

[256] W. T. Pollard, A. K. Felts and R. A. Friesner, "The Redfield Equation in Condensed Phase Quantum Dynamics", *Adv. Chem. Phys.*, **1996**, *93*, 77.

[257] V. May and M. Schreiber, "Density-matrix theory of charge transfer", *Phys. Rev. A*, **1992**, *45*, 2868.

[258] B. Wolfseder and W. Domcke, "Intramolecular electron-transfer dynamics in the inverted regime: quantum mechanical multi-mode model including dissipation", *Chem. Phys. Lett.*, **1996**, *259*, 113.

[259] W. B. Davis, M. R. Wasielewski, M. A. Ratner, V. Mujica and A. Nitzan, "Electron Transfer Rates in Bridged Molecular Systems: A Phenomenological Approach to Relaxation", *J. Phys. Chem. A*, **1997**, *101*, 6158.

[260] D. Segal, A. Nitzan, W. Davis, M. R. Wasielewski and M. A. Ratner, "Electron Transfer Rates in Bridged Molecular Systems 2. A Steady-State Analysis of Coherent Tunneling and Thermal Transitions", *J. Phys. Chem. B*, **2000**, *104*, 3817.

[261] E. G. Petrov and V. May, "A Unified Description of Superexchange and Sequential DonorAcceptor Electron Transfer Mediated by a Molecular Bridge", *J. Phys. Chem. A*, **2001**, *105*, 10176.

[262] H. Guo, L. Liu and K.-Q. Lao, "Non-perturbative time-dependent quantal dynamics of superexchange in electron transfer processes", *Chem. Phys. Lett.*, **1994**, *218*, 212.

[263] D. A. Micha and K. Runge, "Time-Dependent Many-Electron Approach to Slow Ion-Atom Collisions - the Coupling of Electronic and Nuclear Motions", *Phys. Rev. A*, **1994**, *50*, 322.

[264] D. Egorova, M. Thoss, W. Domcke and H. Wang, "Modeling of ultrafast electron-transfer processes: Validity of multilevel Redfield theory", *J. Chem. Phys.*, **2003**, *119*, 2761.

[265] P. Kambhampati, D. H. Son, T. W. Kee and P. F. Barbara, "Solvent Effects on Vibrational Coherence and Ultrafast Reaction Dynamics in the Multicolor PumpProbe Spectroscopy of Intervalence Electron Transfer", *J. Phys. Chem. A*, **2000**, *104*, 10637.

[266] L. Verlet, "Computer "Experiments" on Classical Fluids. I. Thermodynamical Properties of Lennard-Jones Molecules", *Phys. Rev.*, **1967**, *159*, 98.

[267] A. E. Reed, R. B. Weinstock and F. Weinhold, "Natural population analysis", *J. Chem. Phys.*, **1985**, *83*, 735.

[268] D. Andrae, U. Haeussermann, M. Dolg, H. Stoll and H. Preuss, "Energy-adjusted ab initio pseudopotentials for the 2nd and 3rd row transition-elements", *Theor. Chem. Acc.*, **1990**, *77*, 123–141.

[269] A. B. Pacheco and S. S. Iyengar, "Multistage ab initio quantum wavepacket dynamics for electronic structure and dynamics in open systems: Momentum representation, coupled electron-nuclear dynamics, and external fields", *J. Chem. Phys.*, **2011**, *134*, 074107.

[270] A. Warshel and M. Levitt, "Theoretical studies of enzymic reactions: dielectric, electrostatic and steric stabilization of the carbonium ion in the reaction of lysozyme.", *J. Mol. Biol.*, **1976**, *103*, 227–249.

[271] M. J. Field, P. A. Bash and M. Karplus, "A combined quantum mechanical and molecular mechanical potential for molecular dynamics simulations", *J. Comput. Chem.*, **1990**, *11*, 700–733.

[272] J. Gao, "Hybrid quantum and molecular mechanical simulations: An alternative avenue to solvent effects in organic chemistry", *Acc. Chem. Res.*, **1996**, *29*, 298–305.

[273] R. A. Friesner and V. Guallar, "Ab initio quantum chemical and mixed quantum mechanics/molecular mechanics (QM/MM) methods for studying enzymatic catalysis.", *Annu. Rev. Phys. Chem.*, **2005**, *56*, 389–427.

[274] H. Lin and D. G. Truhlar, "QM/MM: what have we learned, where are we, and where do we go from here?", *Theor. Chem. Acc.*, **2007**, *117*, 185–199.

[275] H. M. Senn and W. Thiel, "QM/MM methods for biomolecular systems.", *Angew. Chem. Int. Edit.*, **2009**, *48*, 1198–229.

[276] J. Tomasi and M. Persico, "Molecular-Interactions In Solution - An Overview Of Methods Based On Continuous Distributions Of The Solvent", *Chem. Rev.*, **1994**, *94*, 2027–2094.

[277] C. Cramer and D. Truhlar, "Implicit solvation models: Equilibria, structure, spectra, and dynamics", *Chem. Rev.*, **1999**, *99*, 2161–2200.

[278] M. Orozco and F. J. Luque, "Theoretical Methods for the Description of the Solvent Effect in Biomolecular Systems", *Chem. Rev.*, **2000**, *100*, 4187–4226.

[279] J. Tomasi, B. Mennucci and R. Cammi, "Quantum Mechanical Continuum Solvation Models", *Chem. Rev.*, **2005**, *105*, 2999–3093.

[280] S. Miertus, E. Scrocco and J. Tomasi, "Electrostatic interaction of a solute with a continuum. A direct utilization of ab-initio molecular potentials for the prevision of solvent effects", *Chem. Phys.*, **1981**, *55*, 117 – 129.

[281] R. Cammi and J. Tomasi, "Remarks on the use of the apparent surface charges (ASC) methods in solvation problems: Iterative versus matrix-inversion procedures and the renormalization of the apparent charges", *J. Comput. Chem.*, **1995**, *16*, 1449–1458.

[282] E. Cancès, B. Mennucci and J. Tomasi, "A New Integral Equation Formalism for the Polarizable Continuum Model: Theoretical Background and Applications to Isotropic and Anisotropic Dielectrics", *J. Chem. Phys.*, **1997**, *107*, 3032.

[283] V. Barone, M. Cossi and J. Tomasi, "Geometry Optimization of Molecular Structures in Solution by the Polarizable Continuum Model", *J. Comput. Chem.*, **1998**, *19*, 404–417.

[284] F. Lipparini, G. Scalmani, B. Mennucci, E. Cances, M. Caricato and M. J. Frisch, "A variational formulation of the polarizable continuum model.", *J. Chem. Phys.*, **2010**, *133*, 014106–014106.

[285] B. Mennucci, "Polarizable continuum model", *Wiley Interdisciplinary Reviews: Computational Molecular Science*, **2012**, *2*, 386–404.

[286] D. M. Chipman, "Reaction field treatment of charge penetration", *J. Chem. Phys.*, **2000**, *112*, 5558–5565.

[287] D. M. Chipman, "Vertical electronic excitation with a dielectric continuum model of solvation including volume polarization. I. Theory", *J. Chem. Phys.*, **2009**, *131*, 014103.

[288] C. T. Chapman, W. Liang and X. Li, "Solvent Effects on Intramolecular Charge Transfer Dynamics in a Fullerene Derivative", *J. Phys. Chem. A*, **2013**, *117*, 2687–2691.

[289] M. Marchi, D. Borgis, N. Levy and P. Ballone, "A dielectric continuum molecular dynamics method", *J. Chem. Phys.*, **2001**, *114*, 4377–4385.

[290] R. Allen, J. Hansen and S. Melchionna, "Electrostatic potential inside ionic solutions confined by dielectrics: a variational approach", *Phys. Chem. Chem. Phys.*, **2001**, *3*, 4177–4186.

[291] B. Mennucci, "Time Dependent Solvation: A New Frontier for Quantum Mechanical Continuum Models", *Theor. Chem. Acc.*, **2006**, *116*, 31–42.

[292] F. Ingrosso, B. Mennucci and J. Tomasi, "Quantum Mechanical Calculations Coupled With a Dynamical Continuum Model for the Description of Dielectric Relaxation: Time Dependent Stokes Shift of Coumarin C153 in Polar Solvents", *J. Mol. Liq.*, **2003**, *108*, 21–46.

[293] G. Scalmani and M. J. Frisch, "Continuous Surface Charge Polarizable Continuum Models of Solvation. I. General Formalism", *J. Chem. Phys.*, **2010**, *132*, 114110.

[294] M. Caricato, F. Ingrosso, B. Mennucci and J. Tomasi, "A Time-Dependent Polarizable Continuum Model: Theory and Application", *J. Chem. Phys.*, **2005**, *122*, 154501.

[295] C.-P. Hsu, X. Song and R. A. Marcus, "Time-Dependent Stokes Shift and Its Calculation From Solvent Dielectric Dispersion Data", *J. Phys. Chem. B*, **1997**, *101*, 2546–2551.

[296] M. Cossi, N. Rega, G. Scalmani and V. Barone, "Energies, Structures, and Electronic Properties of Molecules in Solution with the C-PCM Solvation Model", *J. Comput. Chem.*, **2003**, *24*, 669–681.

[297] P. Debye, *Ver. Deut. Phys. Gesell.*, **1913**, *15*, 777.

[298] K. S. Cole and R. H. Cole, "Dispersion and Absorption in Dielectrics I. Alternating Current Characteristics", *J. Chem. Phys.*, **1941**, *9*, 341–351.

[299] S. Havriliak and S. Negami, "A Complex Plane Representation of Dielectric and Mechanical Relaxation Processes in Some Polymers", *Polymer*, **1967**, *8*, 161–210.

[300] A. K. Jonscher, "Dielectric relaxation in solids", *Journal of Physics D: Applied Physics*, **1999**, *32*, R57–R70.

[301] C. J. F. Bottcher and P. Bordewijk, *Theory of Electric Polarization*; Elsevier: Amsterdam, 1978.

[302] M. J. Frisch, G. W. Trucks, H. B. Schlegel, G. E. Scuseria, M. A. Robb, J. R. Cheeseman, G. Scalmani, V. Barone, B. Mennucci, G. A. Petersson, H. Nakatsuji, M. Caricato, X. Li, H. P. Hratchian, A. F. Izmaylov, J. Bloino, G. Zheng, J. L. Sonnenberg, W. Liang, M. Hada, M. Ehara, K. Toyota, R. Fukuda, J. Hasegawa, M. Ishida, T.

Nakajima, Y. Honda, O. Kitao, H. Nakai, T. Vreven, J. J. A. Montgomery, J. E. Peralta, F. Ogliaro, M. Bearpark, J. J. Heyd, E. Brothers, K. N. Kudin, V. N. Staroverov, T. Keith, R. Kobayashi, J. Normand, K. Raghavachari, A. Rendell, J. C. Burant, S. S. Iyengar, J. Tomasi, M. Cossi, N. Rega, J. M. Millam, M. Klene, J. E. Knox, J. B. Cross, V. Bakken, C. Adamo, J. Jaramillo, R. Gomperts, R. E. Stratmann, O. Yazyev, A. J. Austin, R. Cammi, C. Pomelli, J. W. Ochterski, R. L. Martin, K. Morokuma, V. G. Zakrzewski, G. A. Voth, P. Salvador, J. J. Dannenberg, S. Dapprich, P. V. Parandekar, N. J. Mayhall, A. D. Daniels, O. Farkas, J. B. Foresman, J. V. Ortiz, J. Cioslowski and D. J. Fox, *Gaussian Development Version Revision H.36*, Gaussian Inc., Wallingford CT 2014.

[303] S. Kovalenko, R. Schanz, V. Farztdinov, H. Hennig and N. Ernsting, "Femtosecond relaxation of photoexcited para-nitroaniline: solvation, charge transfer, internal conversion and cooling", *Chem. Phys. Lett.*, **2000**, *323*, 312–322.

[304] V. M. Farztdinov, R. Schanz, S. A. Kovalenko and N. P. Ernsting, "Relaxation of Optically Excited p-Nitroaniline: Semiempirical Quantum-Chemical Calculations Compared to Femtosecond Experimental Results", *J. Phys. Chem. A*, **2000**, *104*, 11486–11496.

[305] M. A. Kahlow, W. Jarzęba, T. J. Kang and P. F. Barbara, "Femtosecond Resolved Solvation Dynamics in Polar Solvents", *J. Chem. Phys.*, **1989**, *90*, 151–158.

[306] S. Sanvito, "Molecular Spintronics", *Chem. Soc. Rev.*, **2011**, *40*, 3336–3355.

[307] A. R. Rocha, V. M. Garcia-Suarez, S. W. Bailey, C. J. Lambert, J. Ferrer and S. Sanvito, "Towards Molecular Spintronics", *Nat. Mater.*, **2005**, *4*, 335–339.

[308] J. S. Moodera, T. S. Santos and T. Nagahama, "The Phenomena of Spin-filter Tunnelling", *J. Phys.–Condens. Mat.*, **2007**, *19*, 165202.

[309] I. V. Ovchinnikov and D. Neuhauser, "Spintronics Birefringence with an Extended Molecular Loop-wire or Spiral Coupling", *J. Chem. Phys.*, **2005**, *123*, 204714.

[310] M. Rigol and R. R. P. Singh, "Kagomé Lattice Antiferromagnets and Dzyaloshinsky-Moriya Interactions", *Phys. Rev. B*, **2007**, *76*, 184403.

[311] O. Götze, D. Farnell, R. Bishop, P. Li and J. Richter, "Heisenberg Antiferromagnet on the Kagomé Lattice With Arbitrary Spin: A Higher-order Coupled Cluster Treatment", *Phys. Rev. B*, **2011**, *84*, 224428.

[312] L. Messio, B. Bernu and C. Lhuillier, "Kagomé Antiferromagnet: A Chiral Topological Spin Liquid?", *Phys. Rev. Lett.*, **2012**, *108*, 207204.

[313] A. Mielke, "Exact Ground States for the Hubbard Model on the Kagomé Lattice", *J. Phys. A: Math. Gen.*, **1992**, *25*, 4335–4345.

[314] R. Seeger and J. A. Pople, "Self-Consistent Molecular Orbital Methods. XVIII. Constraints and Stability in Hartree-Fock Theory", *J. Chem. Phys.*, **1977**, *66*, 3045–3050.

[315] P. Kurz, G. Bihlmayer, K. Hirai and S. Blügel, "Ab Initio Treatment of Noncollinear Magnets With the Full-potential Linearized Augmented Plane Wave Method", *Phys. Rev. B*, **2004**, *69*, 024415.

[316] J. E. Peralta, G. E. Scuseria and M. J. Frisch, "Noncollinear Magnetism in Density Functional Calculations", *Phys. Rev. B*, **2007**, *75*, 125119.

[317] M. K. Armbruster, F. Weigend, C. vanWullen and W. Klopper, "Self-Consistent Treatment of Spin-Orbit Interactions with Efficient Hartree-Fock and Density Functional Methods", *Phys. Chem. Chem. Phys.*, **2008**, *10*, 1748–1756.

[318] Z. Li and W. Liu, "Spin-adapted Open-shell Time-dependent Density Functional Theory. III. An Even Better and Simpler Formulation", *J. Chem. Phys.*, **2011**, *135*, 194106.

[319] G. Scalmani and M. J. Frisch, "A New Approach to Noncollinear Spin Density Functional Theory beyond the Local Density Approximation", *J. Chem. Theor. Comput.*, **2012**, *8*, 2193–2196.

[320] I. W. Bulik, G. Scalmani, M. J. Frisch and G. E. Scuseria, "Noncollinear Density Functional Theory Having Proper Invariance and Local Torque Properties", *Phys. Rev. B*, **2013**, *87*, 035117.

[321] M. J. Field, "Time-Dependent Hartree-Fock Simulations of theDynamic of Polyatomic-Molecules", *J. Chem. Phys.*, **1992**, *96*, 4583–4590.

[322] R. McWeeny, *Methods of Molecular Quantum Mechanics*; Academic: New York, 1989.

[323] J. E. Harriman, *Theoretical Foundations of Electronic Spin Resonance*; Academic Press: New York, 1978.

[324] F. L. Hirshfeld, "Bonded-atom Fragments for Describing Molecular Charge Densities", *Theor. Chem. Acc.*, **1977**, *44*, 129–138.

[325] S. Sharma, J. Dewhurst, C. Ambrosch-Draxl, S. Kurth, N. Helbig, S. Pittalis, S. Shallcross, L. Nordström and E. Gross, "First-principles Approach to Noncollinear Magnetism: Towards Spin Dynamics", *Phys. Rev. Lett.*, **2007**, *98*, 196405.

[326] L. Bogani and W. Wernsdorfer, "Molecular Spintronics Using Single-molecule Magnets", *Nat. Mater.*, **2008**, *7*, 179–186.

[327] T. D. Ladd, F. Jelezko, R. Laflamme, Y. Nakamura, C. Monroe and J. L. O'Brien, "Quantum Computers", *Nature*, **2010**, *464*, 45–53.

[328] L. Zhang, P. F. Guan, D. L. Feng, X. H. Chen, S. S. Xie and M. W. Chen, "Spin-Dependent Electron-Phonon Interaction in SmFeAsO by Low-Temperature Raman Spectroscopy", *J. Am. Chem. Soc.*, **2010**, *132*, 15223–15227.

[329] V. P. Antropov, M. I. Katsnelson and B. N. Harmon, "Spin Dynamics in Magnets: Equation of Motion and Finite Temperature Effects", *Phys. Rev. B*, **1996**, *54*, 1019–1035.

[330] V. P. Antropov, M. I. Katsnelson, M. vanSchilfgaarde and B. Harmon, "Ab Initio Spin Dynamics in Magnets", *Phys. Rev. Lett.*, **1995**, *75*, 729–732.

[331] P.-W. Ma, C. H. Woo and S. L. Dudarev, "Large-Scale Simulation of the Spin-Lattice Dynamics in Ferromagnetic Iron", *Phys. Rev. B*, **2008**, *78*, 024434.

[332] I. P. Omelyan, I. M. Mryglod and R. Folk, "Algorithm for Molecular Dynamics Simulations of Spin Liquids", *Phys. Rev. Lett.*, **2001**, *86*, 898–901.

[333] D. Perera, D. P. Landau, D. M. Nicholson, G. M. Stocks, M. Eisenbach, J. Yin and G. Brown, "Combined Molecular Dynamics-Spin Dynamics Simulations of BCC Iron", *J. Phys. Conf. Ser.*, **2014**, *487*, 012007.

[334] J. Yin, M. Eisenbach and D. M. Nicholson, "Effect of Lattice Vibrations on Magnetic Phase Transition in BCC Iron", *Phys. Rev. B*, **2012**, *86*, 214423.

[335] C. Carbogno, J. Behler, A. Groß and K. Reuter, "Fingerprints for Spin-Selection Rules in the Interaction Dynamics of O2 at Al(111)", *Phys. Rev. Lett.*, **2008**, *101*, 096104.

[336] M. Richter, P. Marquetand, J. González-Vázquez, I. Sola and L. González, "SHARC: ab Initio Molecular Dynamics with Surface Hopping in the Adiabatic Representation Including Arbitrary Couplings", *J. Chem. Theor. Comput.*, **2011**, *7*, 1253–1258.

[337] S. Mai, P. Marquetand and L. González, "A General Method to Describe Intersystem Crossing Dynamics in Trajectory Surface Hopping", *Int. J. Quant. Chem.*, **2015**, .

[338] G. Granucci, M. Persico and G. Spighi, "Surface Hopping Trajectory Simulations with Spin-Orbit and Dynamical Couplings", *J. Chem. Phys.*, **2012**, *137*, 22A501.

[339] B. Fu, B. C. Shepler and J. M. Bowman, "Three-State Trajectory Surface Hopping Studies of the Photodissociation Dynamics of Formaldehyde on ab Initio Potential Energy Surfaces", *J. Am. Chem. Soc.*, **2011**, *133*, 7957–7968.

[340] G. Cui and W. Thiel, "Generalized Trajectory Surface-Hopping Method for Internal Conversion and Intersystem Crossing", *J. Chem. Phys.*, **2014**, *141*, 124101.

[341] B. Fu, Y.-C. Han, J. M. Bowman, L. Angelucci, N. Balucani, F. Leonori and P. Casavecchia, "Intersystem Crossing and Dynamics in $O(^3P)$ + C_2H_4 Multichannel Reaction: Experiment Validates Theory", *Proc. Natl. Acad. Sci. U.S.A.*, **2012**, *109*, 9733–9738.

[342] M. Douglas and N. M. Kroll, "Quantum Electrodynamical Corrections to the Fine Structure of Helium", *Ann. Phys.*, **1974**, *82*, 89–155.

[343] B. A. Hess, "Applicability of the No-pair Equation with Free-particle Projection Operators to Atomic and Molecular Structure Calculations", *Phys. Rev. A*, **1985**, *32*, 756.

[344] B. A. Hess, "Relativistic Electronic-Structure Calculations Employing a Two-Component No-Pair Formalism with External-Field Projection Operators", *Phys. Rev. A*, **1986**, *33*, 3742.

[345] U. vonBarth and L. Hedin, "A Local Exchange-Correlation Potential for the Spin Polarized Case: I", *J. Phys. C*, **1972**, *5*, 1629.

[346] J. C. Tully, *Classical and Quantum Dynamics in Condensed Phase Simulations*; World Scientific: Singapore, 1998.

[347] J. Kübler, K. H. Hock, J. Sticht and A. R. Williams, "Density Functional Theory of Non-Collinear Magnetism", *J. Phys. F*, **1988**, *18*, 469.

[348] M. J. Frisch, G. W. Trucks, H. B. Schlegel, G. E. Scuseria, M. A. Robb, J. R. Cheeseman, G. Scalmani, V. Barone, B. Mennucci, G. A. Petersson, H. Nakatsuji, M. Caricato, X. Li, H. P. Hratchian, A. F. Izmaylov, J. Bloino, G. Zheng, J. L. Sonnenberg, W. Liang, M. Hada, M. Ehara, K. Toyota, R. Fukuda, J. Hasegawa, M. Ishida, T. Nakajima, Y. Honda, O. Kitao, H. Nakai, T. Vreven, J. J. A. Montgomery, J. E. Peralta, F. Ogliaro, M. Bearpark, J. J. Heyd, E. Brothers, K. N. Kudin, V. N. Staroverov, T. Keith, R. Kobayashi, J. Normand, K. Raghavachari, A. Rendell, J. C. Burant, S. S. Iyengar, J. Tomasi, M. Cossi, N. Rega, J. M. Millam, M. Klene, J. E. Knox, J. B. Cross, V. Bakken, C. Adamo, J. Jaramillo, R. Gomperts, R. E. Stratmann, O. Yazyev, A. J. Austin, R. Cammi, C. Pomelli, J. W. Ochterski, R. L. Martin, K. Morokuma, V. G. Zakrzewski, G. A. Voth, P. Salvador, J. J. Dannenberg, S. Dapprich, P. V. Parandekar, N. J. Mayhall, A. D. Daniels, O. Farkas, J. B. Foresman, J. V. Ortiz,

J. Cioslowski and D. J. Fox, *Gaussian Development Version Revision H.21*, Gaussian Inc., Wallingford CT 2012.

[349] X. Li, J. M. Millam and H. B. Schlegel, "Ab initio molecular dynamics studies of the photodissociation of formaldehyde, $H_2CO \rightarrow H_2$ + CO: Direct classical trajectory calculations by MP2 and density functional theory", *J. Chem. Phys.*, **2000**, *113*, 10062–10067.

[350] T. Helgaker, P. Jørgensen and J. Olsen, *Molecular Electronic-Structure Theory*; Wiley: Chichester, 2000.

[351] R. K. Nesbet, "Algorithm for Diagonalization of Large Matrices", *J. Chem. Phys.*, **1965**, *43*, 311.

[352] C. Lanczos, "An iteration method for the solution of the eigenvalue problem of linear differential and integral operators", *J. Res. Nat'l Bur. Std.*, **1950**, *45*, 255.

[353] E. R. Davidson, "Note: The Iterative Calculation of a Few of the Lowest Eigenvalues and Corresponding Eigenvectors of Large Real-Symmetric Matrices", *J. Comput. Phys.*, **1975**, *17*, 87.

[354] W. Duch, *GRMS or Graphical Representation of Model Spaces*; Springer, Berlin, 1986.

[355] P. J. Knowles and N. C. Handy, "A New Determinant-Based Full Configuration Interaction Method", *Chem. Phys. Lett.*, **1984**, *111*, 315.

[356] J. Olsen, B. O. Roos, P. Jørgensen and H. J. A. Jensen, "Determinant based configuration interaction algorithms for complete and restricted configuration interaction spaces", *J. Chem. Phys.*, **1988**, *89*, 2185.